TECHNISCHE FAKULTÄT DER
CHRISTIAN-ALBRECHTS-UNIVERSITÄT
ZU KIEL

On the Stabilization Mechanisms of Silicon Microwire Array Anodes for Li-Ion Batteries

Faculty of Engineering
Functional Nanomaterials
General Materials Science

zur Erlangung des akademischen Grades
Doktor der Ingenieurwissenschaft (Dr.-Ing.)
an der Technischen Fakultät
der Christian-Albrechts-Universität zu Kiel
vorgelegt von

Sandra Hansen, geb. Nöhren

Kiel, 12th of June 2017

1. Gutachter: Prof. Dr. H. Föll

2. Gutachter: Prof. Dr. Rainer Adelung

3. Gutachter: Prof. Dr. Ion Tiginyanu

4. Prüfer: Prof. Dr. Lorenz Kienle

5. Prüfungsvorsitz: Prof. Dr. Franz Faupel

Datum der Prüfung: 21. November 2017

Abstract

The levelized costs of energy for commercially available energy storage systems, as for example lead-acid and Li-ion batteries, are too high. These high costs are related to the high material costs as well as to the high amount of non-active material, which add up to the total weight of the battery. An analysis showed that an increase in capacity and efficiency of the battery materials could reduce the levelized costs of energy significantly. Consequently, the batteries become more efficient, attractive for the e-mobility sector, and interesting with regard to the storage of alternative energy systems. One alternative to commercially available graphite electrodes are the silicon microwire array anodes discussed in this thesis. They exhibit a four times higher gravimetrical capacity and at the same time a high cycling stability. High areal capacities, like in the case of silicon microwires, and the resulting large volume expansion of 400 % are problematic because they might induce high stresses in the silicon. This is the most common failure mechanism of standard silicon anodes. Typically, pulverization leads to material degradation and capacity fading. The aim of this thesis is to enhance the long-term cycling stability of these silicon microwire arrays. It revealed the intrinsic as well as extrinsic stabilization mechanisms of silicon leading to an efficiency increase and a time reduction of a typical charging process. Additionally, the complex interaction between this novel, freestanding array structure and the surrounding electrolyte was investigated. Another important aspect of this type of architecture is the partially integrated current collector allowing a high mechanical anode stability and reduction of the ohmic losses. Important battery parameter like size, geometry, temperature and state of charge needed to be evaluated throughout this thesis. A viscosity increase of the electrolyte leads to a very homogeneous, but flexible solid electrolyte interface around the individual wires. The interaction between this supporting layer and the silicon wires enables a constant pressure on the wires maintaining a high degree of crystallinity. The crystal structure is very important in this architecture because it facilitates high charging rates using the fastest growth direction <100> of silicon. Consequently, it prevents the typical mechanical degradation at very high charging rates of 12 minutes. These fundamental properties and requirements are not at all limited to the silicon architecture of this thesis, but could be applied to any kind of anode system. They could be transferred especially to those anode concepts, which make use of the silicon anisotropy during electrochemical etching, in order to achieve a self-supporting electrode.

Kurzzusammenfassung

Die Prozess- und Herstellungskosten für kommerziell verfügbare Speichersysteme, wie zum Beispiel Blei- oder Li-Ionenakkumulatoren sind derzeit noch sehr hoch. Zudem sind die Kernparameter wie Energiedichte und Reichweite der Speicher noch zu niedrig, was sie für den großflächigen Einsatz nicht sehr attraktiv macht. Die hohen Kosten lassen sich auf hohen Materialkosten und einen hohen Anteil nicht-aktivem Materials zurückführen. Eine Analyse hat gezeigt, dass eine Kapazitäts- und Effizienzerhöhung der Elektrodenmaterialien diese Kosten drastisch senken könnte. Nur dann können Akkumulatoren effizienter und preiswerter und somit interessanter für den Einsatz in der Elektromobilität oder der Speicherung regenerativer Energien werden. Eine Alternative zu den kommerziell eingesetzten Graphitelektroden in diesen Batterien sind die Silizium-Mikrodraht-Anoden, die in dieser Dissertation untersucht werden, welche im Vergleich zu Graphit eine viermal so hohe theoretische Kapazität und Zyklenfestigkeit aufweisen. Die hohe Flächenladungsdichte und die daraus resultierende große Volumenausdehnung im Silizium können Probleme darstellen. Sie sorgen für hohe mechanische (Ver-) Spannungen im Material. In kommerziell eingesetzten Standardanoden ist dies der häufigste Versagensmechanismus, welcher zur Pulverisierung und Zerstörung des aktiven Materials und somit zu einem Leistungsverlust der Batterie führt. Das Ziel dieser Dissertation ist es Silizium-Mikrodraht-Anoden langzeitstabil und zyklenfest herzustellen. Dabei wurden unterschiedliche intrinsische und extrinsische Stabilisierungsmechanismen dieser Drahtanoden herausgearbeitet. Dafür musste die komplexe Wechsel-wirkung zwischen dieser neuartigen, freistehenden Array-Struktur als Anode und des sie umgebendem Elektrolyten verstanden und optimiert werden. Ein weiterer wichtiger Aspekt dieser Struktur ist der integrierte Stromableiter, der für eine hohe mechanische Stabilität der Elektrode sorgt und darüber hinaus auch die ohmschen Verluste reduziert. Wichtige Batteriekenngrößen wie die Größe und Geometrie der Anode, als auch der Temperatur- und Ladezustand der kompletten Batterie wurden in intensiver Weise untersucht. Eine Viskositätserhöhung des Elektrolyten, während der Ausbildung der Festkörperelektrolytgrenzflächenschicht, führt zu einer Änderung der mechanischen Eigenschaften dieser Grenzflächenschicht. Infolgedessen können die Spannungen von dieser elastischen Grenzfläche aufgenommen werden, sodass die Drähte auch bei deutlich erhöhten Laderaten nicht degradieren. Die mechanische Stabilität der Elektrode wurde damit nahezu unabhängig von der Laderate, und eine komplette Batterieladung konnte in nur zwölf Minuten erfolgreich realisiert werden.

Diese fundamentalen Eigenschaften und Bedingungen, die durch diese Dissertation herausgearbeitet wurden, sind nicht nur auf diese Anodengeometrie beschränkt. Sie lassen sich besonders auf solche Anodenkonzepte übertragen, die ein elektrochemisches Ätzen und somit die Richtungsabhängigkeit des Materials ausnutzen können. Der Erfolg der Drahtanoden basiert auf einer selbst-stabilisierende Elektrode, die sich gegen Verfall schützt. Deshalb konnte eine vierfach höhere Kapazität und zehnfach schnellere Ladefähigkeit erzielt werden, weshalb diese Anode als eine wettbewerbsfähige Alternative dienen könnte.

Contents

Chapter 1

Introduction

1.1 Motivation

The new resolution "Transforming our world: the 2030 Agenda for Sustainable Development" of the United Nations (UN) from September 2015 calls for an international cooperation in order to reduce further global warming [1]. Suitable energy storage systems are required to replace fossil fuels and reduce the CO_2 emission. Due to high levelized costs, renewable energies have no chance to replace existing technologies, unless the existing material limitations are solved. For example, by replacing commercially available technologies and material system, thus increasing the battery efficiency. It is inevitable that something has to be done to reduce the prices for Li-ion batteries. Detailed analysis (reproduced from Lazard [2]) of the electricity price development as well as the production costs of Li-ion batteries indicate that their prices have to be drastically reduced to be competitive. As a conclusion, it boils down to a material bottleneck and availability limitation of all the raw materials in a battery like lithium, nickel, manganese, carbon etc., which dictate the battery price. These are explicit considerations, which separate completely from the material research and development. The second part demonstrates the lever one has when understanding every physical and chemical process inside a battery, which limit their performance. This thesis concentrates on the fabrication and characterization of a free-standing, purely silicon microwire architecture as novel type of anode material for Li-ion battery. By understanding how these limitations can be improved or solved, an efficiency increase of this type of battery can be realized. Thus, reducing the electricity storage price by a factor of 10 to only 23 cent USD/kWh, which is even below the current electricity price in Germany. (The abbreviation USD stands for US $.) Following this, the long-term stability of this anode could solely be achieved by understanding the complex interaction between the electrolyte and the array electrode, influencing the crystallinity of the material and the chemo-mechanical properties.

In order to get a feel for the requirements and material opportunities, the next section will concentrate on the detailed market analysis of the battery materials. Furthermore, this thesis is divided in a theoretical part in Chapter 2 which deals with the background to understand the individual characterizations before the experimental details are discussed in Chapter 3. Due to the designed microstructure of the anode, different types of battery housings and cells had to be developed for special characterization techniques. Chapters 4 and 5 deal with the detailed analysis and discussion of the anodes. Standard paste electrodes are fabricated as well with the silicon microwires as well to understand the mechanisms inside pastes and to be comparable to the standard technologies. In chapter 4, the mechanical and electrochemical interaction phenomena are investigated, which could be successfully transferred to the array configuration of the electrode in Chapter 5. Here, the details behind the successful long-term stability of the array electrodes are described depending on the advanced interaction between mechanics, structural stability, chemistry as well as electrochemistry. Finally, Chapter 6 summarizes the most important findings and shows the prospects of these silicon microwire arrays by displaying first approaches to transfer them to an industrial set-up.

1.2 Market analysis of battery storage systems

The United Nations (UN) passed a new resolution in September 2015 for the sustainable development of the earth. In total 17 aims and more than 169 targets were advised saving the world's population from hunger and poverty and the planet from the continuously growing threat of global warming. The UN's main concern is that every nation and state fulfills these aims and requirements in order to reduce the greenhouse gas emission [1, 3].

In the resolution, the UN states to rescue the planet from the continuing damage. The average temperature has increased by 0.85 K between the years 1980 and 2012 [1, 3]. The UN states that the temperature should not increase further and stay at an average temperature increase around 1.5 K up to 2 K. Furthermore, due to the increase in temperature, the rising sea level is another concern. It has increased by 19 cm in the last ten years. Therefore, the infrastructure in the individual countries should be changed in order to prevent any further damage due to the flooding, up to 2020. These climate changes are a result of the drastic increase in CO_2 emission by more than 50 % since the year 1990 [3, 4]. Consequently, the CO_2 emission has to be decreased. One way of doing is to produce and story more energy by alternative energy sources.

As one of the first countries in the world, Germany succeeded in increasing its gross electricity power supply from renewable energies to 31.5 %. In 2015, in total 376 TWh were provided only by renewable energies. This included 50 % of the power generation, 42 % of the heating sector, and only 8 % of the biofuel sector. As a consequence, the regenerative electricity production avoided 156 million tons of CO_2 emission and reduced the greenhouse effect [5]. If every country would reduce its CO_2 emission this effectively until 2030, the problem of the global warming would soon be solved. Although the regenerative energy production increased, 53.7 TWh and 23.6 TWh provided by the wind and photovoltaic sector in Germany, too little energy is used because an effective storage system is still not available. The unsteady weather conditions make it necessary to store the generated energy in, for example, Li-ion batteries. The following discussion and analysis examine if Li-ion battery technology can solve the storage problem. This analysis focuses on a) the material bottleneck and availability, and b) the price development of Li-ion batteries and their individual components. As examples, the biggest storage sectors like e-mobility as well as the power generation are discussed.

The first tipping point of the market analysis is the lithium market and availability, i.e. limitation as possible material bottleneck in the fabrication of Li-ion batteries. Lithium quality needed for battery technology is mostly Li_2CO_3 or Li_2O, like in brine or hard rock minerals. Roughly 1 t of lithium is extracted from approximately 750 t of brine. The lithium market is controlled by only five countries: China, Australia, Bolivia, Argentina, and Chile provide more than 50 % of the total amount of lithium and, therefore can dictate the prices. The total estimated amount of lithium available on earth is estimated to be in the order of 20 million tons. Nevertheless. the estimated lithium resources are always based on geological surveys dated a few years back. It is not exactly known how much lithium really exists on earth, because it is always embedded in the earth crust or rock minerals. Albemarle stated in its Global Lithium Market Outlook in March 2016 [6, 7, 8] that the lithium capacity (i.e. amount of available lithium) should be increased in Chile up to 70 MT lithium carbonate equivalent (LCE) by the end of 2022, with Chile having more than 7.5 million tons of lithium. Up to now, China and Chile can dominate and dictate the prices on the global lithium market. But nowadays, new start up companies see the growing potential to sell their lithium minerals due to an increase in demand. The price for lithium increased by more than 300 % within a year, most likely even increasing by almost a factor of 10 in the next years. This would have drastic consequences on the supply and demand situation.

If more money can be gained from enhanced lithium export by the lithium suppliers and start up companies, new ways of collecting and purifying lithium may be invented and even already existing technologies may be improved. In addition, even other countries or manufacturers may take advantage from the growing interest in lithium. It might become lucrative to try and purify even other minerals than hard rock. On the other hand, the growing importance of lithium will reduce the possible profit margins for the individual suppliers to be competitive compared to other countries. But if the price per t for lithium grows, the global lithium market will develop a highly dynamic behavior and completely depend on supply and demand. Analysts say that a higher lithium price would only lead to a price increase for the battery of 10-15 %. In fact, this directly leads to the second tipping point, known as the e-mobility. The battery of the Tesla S with, for example, 60-85 kWh contains 50.8 kg of lithium carbonate [6, 7, 8, 9, 10]. With a typical battery cost of minimum 10,000 USD, the lithium costs are only 100 USD. The number of EV (full electric vehicles) on Germany's roads increased from 2015 to 2016 by 35 % (according to statistica). In 2016, more than 70 % of the overall number of new vehicle registrations include EVs. A significant portion is attributed to the new Tesla S. The luxury e-vehicle has been sold more than 15,000 times per year in Europe, overtaking e-vehicles from Mercedes and the other European car suppliers. Tesla lead by Elon Musk has ambitious goals: The company wants to scale up its fabrication to 500,000 electric vehicles per year. A battery pack for such a Tesla S contains a minimum of 5,000 up to 7,000 cells. This means that Tesla has to increase the production capacity up to 180,000 battery cells in a year to supply all the EVs [11]. Due to the growing interest in the Li-ion battery technology, the consumption and demand of lithium will increase even more, especially with Tesla building the Gigafactory. In order to produce as many battery cells as Tesla wants to do, 24,000 t of lithium have to be provided annually. If the Gigafactory really reaches its goals, the available amount of lithium represents a material bottleneck and is probably not enough to produce high quantities of Li-ion batteries.

With lithium only taking 1 % of the total weight and price of a full battery cell, the other battery components have to be considered as well. A rechargeable battery consists of current collectors on both sides, electrolytes, and, most importantly, the electrodes with the active material accounting for the actual capacity of a battery. All these components add up to the total weight. For example, inside the Tesla S 35 % of the total weight is accounted only to the battery. The price for the Tesla S with a battery of 60 kWh is estimated to 70,000 € in Europe, which accounts for a price of a battery of this size of 24,500 € (https://www.tesla.com). A 60 kWh battery is supposed to have a range of approximately 500 km. In order to classify it correctly, a typical gasoline vehicle with a 40 l tank will generate an equivalent of 360 kWh, which is six times more than the battery of the Tesla S will generate. Although this driving range seems to be quite high, it needs to be evaluated very carefully. Naturally, this driving range depends on the number of auxiliary systems like radio, lights etc., powered at the same time, which could reduce the driving range by almost 20 %. More importantly, however, is the air conditioning and heating system. In contrast to a gasoline vehicle, those systems require an additional electrical engine, powered by the car battery, reducing the driving range drastically. Especially, the heating system reduces the range by 35 %, depending on the external temperature. The Tesla S battery has severe problems at low as well as high temperatures, being able to drive only 180 km at temperatures above 30 °C or below 0 °C, at a constant velocity of 120 km/h (auto motor sport, 12.2014, [12, 13]). Taking into account the reduced velocity at low temperatures, the battery keeps for 200 km with all auxiliary systems active. Anyhow, this temperature dependence is very strong, showing a range reduction of almost 40 %. In contrast to other e-vehicle suppliers, Tesla has the biggest problem with its battery. Another point of interest for Tesla is the acceleration power. The Tesla S can accelerate from 0-100 km in only 3-4 seconds. At first glance, the high acceleration might look good. For the battery, it means it is a high-power battery made for example for start-stop automatism and acceleration, generating lots of energy in short time. As a consequence, the batteries are almost empty after this acceleration phase, at the expense of the driving range.

The third tipping point is the photo-voltaics (PV) power generation and storage sector. The battery is not only used inside electric vehicles for e-mobility, but also to collect and store the energy from the solar or wind sector. In order to investigate the price development and how the batteries can be made more cost-effective, the levelized costs of storage analysis are considered. Lazard has conducted different studies on the energy storage for many years [2, 14]. Every year a new market analysis has been made. The numbers generated in those studies may be based on prices of the previous years, for example the prices of cent USD/kWh in the PV sector. The cost analysis in this thesis is based on the reports from November 2015 [2] and September

2014 [14]. They discussed various storage systems from flow batteries up to pure zinc batteries. As battery backup in the integrated PV systems, batteries are used to store the energy produced from the PV sector. The energy output of the PV system is not stable, but depends on weather conditions and locations. These levelized costs always contain the costs for the energy necessary to convert the collected energy to electricity and taking into account the individual capital, fuel, and operational as well as maintenance costs. Figure 1.1 illustrates the composition of the electricity price comparing different storage systems. For this thesis, the levelized costs of the PV sector (Solar OV - Utility Scale) are compared to different battery concepts (microgrid technology) [14, 4]. This allows to emphasize the prospects of the alternative battery technology proposed in this thesis. The consumer electricity price in Germany lies at approximately 27 € cent/kWh (baseline 1 in Figure 1.1). The solar PV utility price includes the installation costs to place the PV system on top of the roof and connect it, but at the same time includes the electricity costs to power this PV system. For generating the power by PV, the electricity price is nowadays below 10 € cent/kWh.

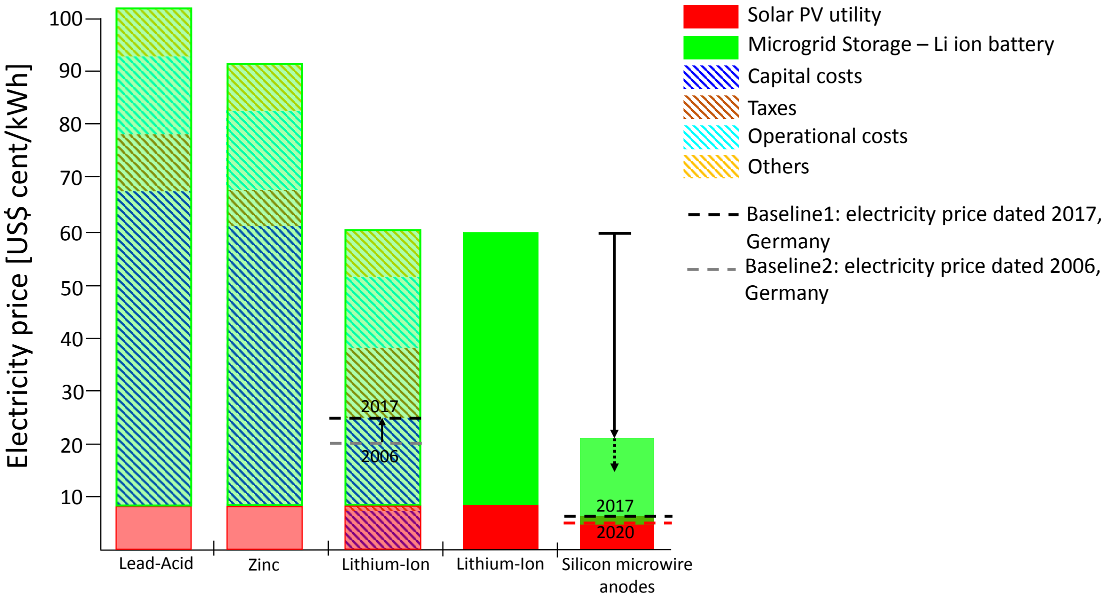

Figure 1.1: Electricity price development for different storage systems for the PV sector. Lead-acid and zinc batteries will not serve as an alternative, because the storage price is very high. Baseline 1 indicates the electricity price in Germany in 2017. It increased by 5 % in the last ten years. Baseline 2 indicates the price in 2006. On the other hand, the pure PV utility price decreased in the last years by almost 10-15 % and will decrease even more, indicated the red dashed line. The last comparison considers the prospects of the silicon microwire anode. From that comparison, it can already be emphasized that the aimed goal of the low consumer electricity price can be reached only by higher efficiency.

This price is going to decrease in the next few years to only 7-8 € cent/kWh. As illustrated in Figure 1.1, the PV utility price holds around 37 % of the costs; the rest of the costs is accounted by the costs to store the energy in a battery storage system. With a potential price reduction in the PV sector, the electricity price of the battery storage system has to be at 10-15 cent USD/kWh, in order to reach a total electricity storage price of below 27 € cent/kWh.

The levelized costs of energy components for Li-ion batteries according to Lazard for a microgrid storage system are around 56.2 cent USD/kWh. This price includes 18.1 cent USD/kWh capital costs, 14.3 cent USD/kWh charging costs and taxes, as well as operational costs of around 8.3 cent USD/kWh. In comparison, the same levelized costs for the solar PV utility scale is only at 5 cent USD/kWh in Denmark for example (Figure 1.1). For a total storage system for the PV sector based on Li-ion batteries, this would lead to a potential electricity price of 60 cent USD/kWh. From this calculation, it can be easily concluded that the price for the Li-ion battery is too high at the moment. Alternative technologies, like the lead-acid batteries, show an even higher electricity price in Figure 1.1 [14]. The storage price should stay in the range of about 10-15 cent USD/kWh. Otherwise the consumer electricity price is too high and the energy will not be stored and, therefore, also not generated by renewable energies. The same holds for the industrial electricity price for large PV systems and wind parks. There, the electricity price is estimated to be around 12 cent USD/kWh. Consequently, the price of the battery technology has to be decreased by at least a factor of five to reach these electricity prices.

Following the price development, Table A.1 compares the costs per energy output for a standard *18650*-cell with the anode production introduced in this thesis. This table demonstrates the influence of a higher capacity and energy density on the total costs of a battery. A standard *18650*-cell has a typical length of 65 cm, a diameter of 18 cm and a height of 6 cm. As shown by Menzel et al., the electrodes are sometimes smaller than their ideal dimension with an area of only 342 cm^2 [15, 16, 17, 18, 19, 20, 21, 4]. In these calculations for the price of the battery, the costs for the separators, current collectors and cathodes have to be taken into account. But these costs are comparable in both electrode systems and are not displayed in the table. In general, the separators as well as the current collectors take approximately 20 % of the total weight of a battery, wheres the electrolyte take 17 %. With an optimal electrolyte to anode interaction and ratio, it is possible to even decrease the amount of the electrolyte and thereby reducing the weight and costs of the battery. The electrolyte is a necessary part, but could be considered as dead weight, which is not active. Therefore, parts of this study also concentrates on the interaction between the electrolyte and the anode, in order to even decrease the amount and still maintain a stable capacity.

	18650-cell	Silicon Microwires
Length [cm]	57	15
Diameter [cm]	6	15
Area [cm^2]	342	243
Energy [Wh]	2.5	10.72
Capacity [mAh]	716 (2862)	3572
Charging rate	1C	5C
Costs of battery [USD]	8.5	10 (8.5)
Costs per capacity [USD/kWh]	2968	933(793)

Table 1.1: Costs per capacity comparing a standard 18650-cells with the silicon microwire array anodes, including the amount and price of the individual components in mass production. The calculations are summarized from [19, 22, 23, 16, 20, 17, 18] and additional suppliers. In brackets, the typical capacity is calculated for the standard as well as for the microwire anodes. The brackets behind the capacities for the *18650*-cells indicate the total capacity of the complete battery. Such a battery consists of four cells with the individual capacity of 716 mAh/g. Only four cells sum up to the same capacity as the silicon microwire anode with only one cell.

The costs of the anode and cathode materials account for the greatest part on the costs. For standard cells, the cathode materials like for NCA (nickel-cobalt-aluminum-oxide) or NCM (nickel-manganese-cobalt) cathodes, nickel, cobalt, and manganese, are the limiting factors [19, 22]. The electrolyte holds 17 % of the total weight and costs of the battery pack. The large portion of the costs calls for specialized designs of electrolytes for high performance batteries. If the properties of a special electrolyte align perfectly with an anode material, it would not only deliver four times higher capacity. In addition, it would reduce the time for re-charging the battery drastically by a factor of 5 to 10, as indicated in Table A.1. These effects all have a large consequence on the production costs as well as on the electricity price.

Table 1.1 introduces another class of Li-ion battery, based on the microstructure investigated in this thesis - the silicon microwire array anodes. These anodes are the first competitive application of macropores in p-doped silicon. Without going into too much detail, this process is a top-down etching process in low p-doped silicon, which allows to design the complete microstructure during macropore etching, enabling a completely free-standing anode. In contrast to other silicon anodes [24], the fabrication of silicon microwires does not need any silicon precursors.

The fabrication is designed for a re-use of the large area wafer. After layer-transfer process and removal of the finished electrode from the substrate, the structured wafer could be re-used ten times. As a result of the microstructural design, the additional material used in commercial electrodes (e.g. carbon) is not necessary, leading to a price reduction of the total battery. As far as efficiency is concerned, the main advantage of the silicon microwire array anode comes into play. These anodes show a four times higher capacity than the *18650*-cells. Another point is the enhanced lifetime of those batteries. They can be charged and discharged two to three times more often compared to standard cells with the same efficiency. Due to an enhanced electrolyte/electrode ratio, even fast or supercharging processes can be realized without significant efficiency loss. These considerations imply an increase in efficiency of these batteries by more than a factor of four for the capacity and a factor of two for the lifetime, leading to a reduction of the electricity price by a factor of 5 to 10 as illustrated in Figure 1.1. This even compensates the slightly higher production costs of the silicon microwires due to lithography processes, as indicated in Table 1.1. By scaling up the fabrication process or improving some of the process steps, it is possible to reduce these costs as well. Thereby, the newly developed anode will create a unique selling point.
In summary, for a typical cell, the material and electrolyte take the majority of the production costs. Another material bottleneck is created, leading to an even higher material price in the future if less material is available. The costs are not likely to decrease. Even a price reduction for the other components will not affect the electricity price. The cost analysis shows that the silicon microwires have four times higher capacity and could be charged faster. This means that the total price for the kWh is reduced by almost a factor of four, compared to the standard cells. Additionally, a *18650*-cells consists of four cells with the individual capacity of 716 mAh. Contrary to that, the silicon microwire anodes achieve the total capacity of a *18650*-cell (2862 mAh with only one electrode.

The proposed silicon microwire array anodes are competitive, showing superior properties, which increase the battery efficiency. These conclusions could only be made by detailed analysis and understanding of the physical and chemical processes inside a free-standing silicon microwire array anode, which is the subject of this thesis. It reveals that every chemical and kinetic process inside the silicon is a direct consequence of the mechanical stabilization and support of the silicon microwire structure. The superior performance could be understood by concentrating on every possible interface of the wires inside the battery. From this analysis, the fundamental requirements and improvements could be drawn and transported to different battery geometries. During this thesis, it is shown that the architecture of the active material, like it is composed here, is decisive for the later-on battery performance, always having in mind, that mechanical degradation is the main reason for capacity fading inside batteries.

1.3 Size Dependency

The anode as well as cathode material itself is very important, because a different kind of material, as discussed above, can improve the capacity and reduce the production costs drastically and increase the efficiency. Typical *18650*-cells have a capacity between 2-3 Ah and could be operated up to 3 V [19, 22]. The question is, what determines the capacity of a battery? The phase transformation inside the active material, when the Li ions incorporate. Those phase transformations depend on the voltage applied to the battery. For the Si-Li system, for example, at least twenty different phases and alloys exist, which form at very specific incorporation voltages (for further details refer to chapter 2.5.2). Figure 1.2 shows an example of this incorporation voltage for different silicon nanostructures (like wires, powder, film or pillars) [25, 26, 27, 28, 29, 30, 31]. This figure indicates that there might be a connection between this incorporation voltage and the wire length. It was found that the size and geometry of silicon have a drastic impact [32, 33] on the performance, not only because bulk silicon would be destroyed inside a battery. The costs for the anode and cathode dominate the production costs of a battery. If an electrode material with a different geometry delivers four times higher gravimetrical capacities and can be operated at higher current densities, the advantage over standard technologies is enormous. This leads to higher selling prices for the total battery pack, and the production costs can be disregarded. The question remains as to what geometry and size the electrode material should have. In this summary, four different types of electrode structures are mentioned, which all behave differently in a battery. The thickness is not always considered in literature. The length as well as thickness are equally important when designing battery electrode material. However, also the geometry of the electrode is crucial. The individual structures are symbolically drawn in Figure 1.2, in order to have a first indication of the delithiation voltages of the different systems. In the micrometer region, the delithiation potentials are estimated with three different exemplary scenarios of how the trend could develop. The delithiation potential is a measure of Li diffusion out of the anode and depends

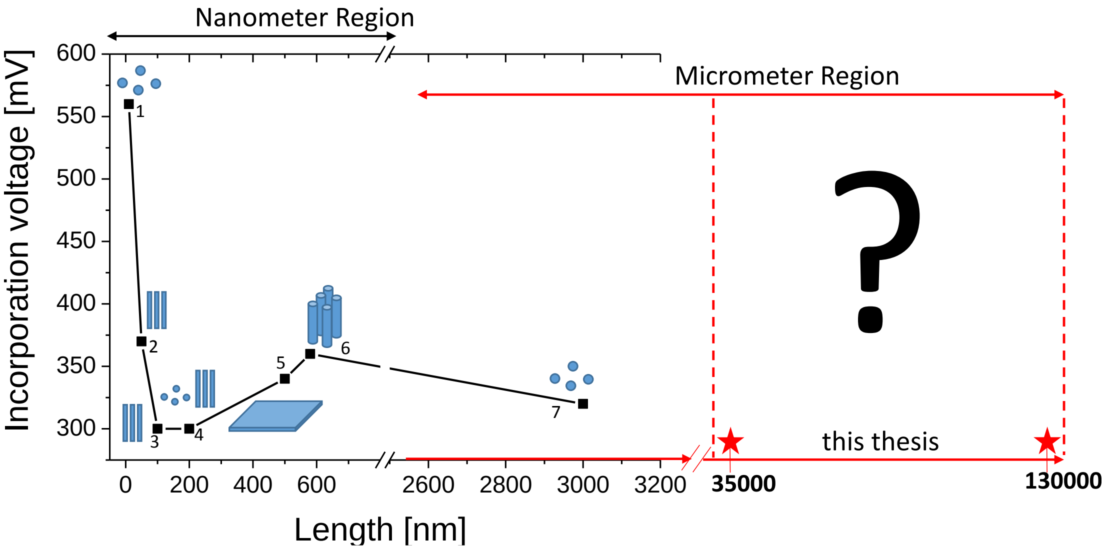

Figure 1.2: Incorporation voltage for differently sized silicon structures, reconstructed with 1:[25], 2:[26, 34], 3:[27], 4:[28, 34], 5:[29], 6:[30], 7:[31]. For the micrometer region, it is still not clear how the voltage course will continue. When comparing the delithiation potentials, it is always important to consider both, thickness and length.

on the structure. Hollow and porous structures allow easier diffusion, because there is no large resistance for the ions to diffuse. Thick and dense material on the other hand would mean that the ions have to have more energy to penetrate into those structures. This is reflected in higher voltages and capacity limitations up to a certain lithiation level. Thin films, as indicated by 5 in Figure 1.2, often have the problem of adhesion failure and are mechanically and kinetically limited. This thesis tries to answer the question of the correct sizes and demonstrates the limiting properties in batteries by varying the anode geometries. The incorporational voltage, as indicated in Figure 1.2, has another important impact: it determines the corridor in which batteries have to be cycled in order to achieve high, stable capacity (see section 4.1.).

Chapter 2

Theory

2.1 Macropore formation p-doped Si

The anode material discussed in this thesis is based on the macropore formation in p-doped silicon. Most macropore formation in silicon concentrates on n-doped silicon material. In this thesis, the macropores are formed in p-doped silicon. The back-side illumination in n-type Si generated the necessary holes for the dissolution. It is an additional degree of freedom and stabilizes macropore formation drastically. Contrary to n-doped silicon, p-doped silicon does not need any back-side illumination because here the majority charge carriers are already holes, but lacks several aspects of the stabilizing effects related to the back-side illumination.

Pore formation in p-doped silicon is still under ongoing discussion, but the fundamentals are quite clear. Macropore formation in p-doped silicon works under forward anodic bias. The general chemical reaction during silicon dissolution is formulated like [35, 36]:

$$Si + 4HF_2^- + h^+ \rightarrow SiF_6^{2-} + 2HF + H^2 + e^-$$

The silicon and pre-dominantly the pore walls are dissolved by the fluorine in the solution. If water is present in this electrolyte and if the potential during etching is increased, silicon oxide is formed at the pore walls. This silicon oxide is not working as a passivation or dielectric, but more like a catalyst for further dissolution during macropore formation:

$$SiO_2 + 2HF_2^- + 2HF \rightarrow SiF_6^{2-} + 2H_2O$$

Among the reaction products is additional water forming inside the electrolyte. If water is already prior to this reaction, the electrolyte will be enriched by this water, changing the pH-value of the electrolyte and thus reducing drastically the dissolution rate of silicon during etching. Consequently, this is a very important parameter to monitor in order to etch macropores in different electrolytic systems, as described in chapter 3.1.2. But in order to understand the pore nucleation, it is necessary to consider the electrolyte/semiconductor interface around the pores. As described already, macropore formation functions under anodic (positive voltage) bias. Thus, a space charge region forms at the interface. The width of this space charge region depends on the build-in potential, doping concentration, on the exact geometry and material to be dissolved [35, 36, 37, 38, 39, 40].

$$W = (2\epsilon V/eN_D)^{1/2}, \tag{2.1}$$

with $V = V_{bias} - V_{appl} - kT/e$. In order to achieve an accurate calculation of the width, a geometrical factor has to be considered. The most important feature, when discussing the pore formation is the difference in width of the space charge region between the pore wall and the pore tip. It is at its minimum at the pore tips. Two different cases have to be considered: a) if no bias potential is applied, there is a thermodynamic equilibrium between the diffusion and field current at the pore tips as well as the pore walls. b) If, on the other hand, the bias and potential in the pore formation region is applied, the equilibrium is shifted and the diffusion current increases because it is dominated i.e. controlled by the concentration gradient of the necessary holes. As the width of the space charge region decreases at the pore tips, the concentration gradient inside the space charge region and outside of the space charge region becomes larger (at forward potential, there are still some holes inside the space charge region). Consequently the diffusion current is always larger at the pore tips compared to the pore walls. Therefore, it is thermodynamically favored that a pore forms to compensate the current formation. A critical value for the pore formation: The distance between two pores is also controlled by space charge region width since they can overlap significantly. The process is then controlled by the space charge regions and their charge concentration gradient. The pore tips do not grow anymore. In pre-structured silicon wafers, like in this thesis, the distance of the lithographic pattern is decisive. If the distance between the pores is too large (by the defined pattern), pore branching will occur and even worth random pore nucleation might occur. Pore growth is best if no charge carriers exist at the space charge regions between the individual pores. This leads to the necessary condition, that the distance between the pores has to be twice the width of the space charge region multiplied by the pore diameter [35, 36]. In order for the pores to grow deep without any kind of branching (or thickness increase), the current density and the field strength has to be larger at the pore tips. In that case, the dissolution at the pore walls is not allowed to continue. Therefore an additional contribution to the controlled and local silicon dissolution is the passivating kinetics, which is even more pronounced in the chemical etching process [41, 42]. The surface of the pores is covered with fluorine ions. Due to the very instable Si-F bonds, the surface of the silicon pores (i.e. the pore walls) are passivated with silicon-hydrogen bonds, which are very stable. The surface of the silicon has dangling bonds. These dangling bonds are terminated, if hydrogen bonds onto silicon. The electronegativity difference between silicon and hydrogen is larger compared to the silicon and oxygen and thereby thermodynamically better if silicon and hydrogen form a stable covalent bond. Consequently, the etching process cannot continue here at the walls. At the tips, on the other hand, the field strengths is much larger and the effect dominates the etching process. In p-doped silicon, the dissolution is isotropic, leading to a global dissolution and not to pore formation. In order to have only local macropore etching, the viscosity of the electrolyte needs to be increased to improve the passitvation kinetics. As a consequence, a diffusion limitation forms inside the electrolyte leading more to an anisotropic etching. Polyethylene glycole (PEG), for example, is a good candidate [41, 42]. It tends to passivate the pore walls, thus creating locally a diffusion limitation and thereby have a defined control of the macropore etching, see section 3.1.2.

In the most general case, pore etching in p-doped silicon could only be achieved by operating in a special region of the I-V characteristic. Here, only the anodic current regions (like posiitve currents) are considered. Macropore etching is only possible if the current density during the experiment is lower than the critical current densitiy called J_{PSL}. The chemical reaction (1) is fulfilled and holes at the interface react with the silicon. If the current densities are increased and the second reaction takes place, making the dissolution reaction a bit more complicated and the consideration of the diffusion and field current get more complicated. This region highly depends on the electrolyte composition and convection, even more than in the other region. Above a maximum in the I-V-curve, the current density increases linearly up to the next maximum. This region, anyhow, does not lead to controlled, local dissolution (i.e. macro- or mesopores), but to global dissolution and polished surfaces, called electropolishing. The difference in current densities are always larger by several orders of magnitudes [36, 35, 41, 43]. Increasing both voltage and current densities even more, the I-V-characteristics change completely and instead current oscillations appear, making the dissolution more difficult. In this case, the second chemical reaction indicates that additionally to the holes, electrons are generated, which accumulate at the back of the silicon sample, leading to current oscillations. Inside this space charge region and outside of it, it is necessary that the same amount of holes and electrons are present. The current densities are more controlled by the diffusion, than by the charge transfer reactions at the interface because additionally formed silicon oxide is present in this region.

2.2 Chemical etching of Si

Wet-chemical etching of Si in aqueous alkaline solution is highly anisotropic and leads to preferential etching in silicon depending on the crystallograhic orientation, Figure 2.1. This section describes only etching in alkaline etching because this is used in this thesis, not without noting that chemical etching can be performed in different electrolytes depending on the crystal orientation and preferential etch planes.

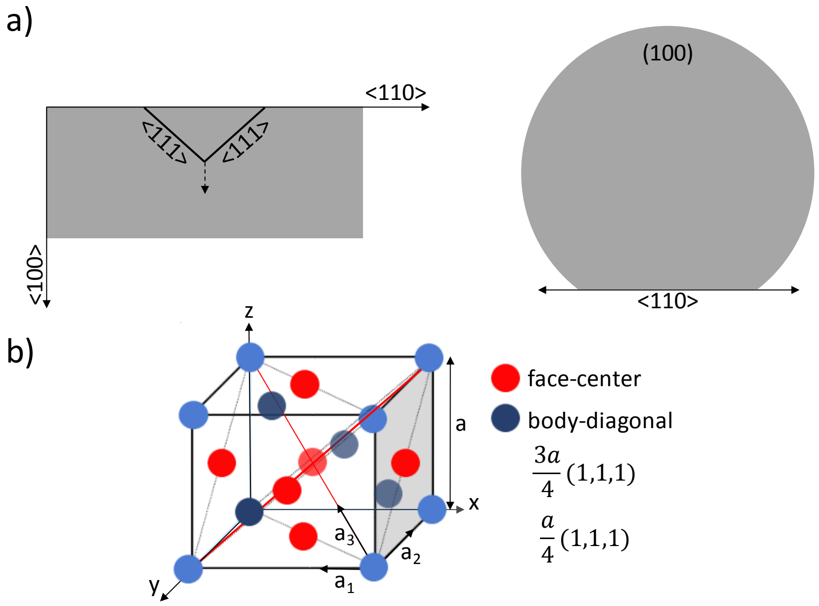

Figure 2.1: Anisotropic wet-chemical etching (KOH) depending on the crystal, diamond structure of silicon. The base of silicon is an fcc-lattice with additional four atoms sitting at the body-diagonal. They have different positions of (1/4)a and (3/4)a in the direction of the body-diagonal (with a=lattice constant). The etch pyramids are <111>-facetted (and the tip of the pyramid follow the <100> direction). The <111> direction acts as natural etch stop in silicon, because this direction shows more bonds inside the crystal, leaving less bonds facing the electrolyte and consequently chemical reactions [44, 36, 45, 46].

The chemical etching bases as well on the local dissolution of silicon. Seidel et al. analyzed in every detail the dissolution of silicon in alkaline solutions [45, 39, 40]. After immersing silicon into an aqueous KOH solution, the surface and the dangling bonds of the (100)-surface plane are saturated with silicon hydroxide formation. Consequently, the Si-Si bonds still facing the bulks silicon reduce their bond strength, allowing further dissolution of silicon. Silicon hydroxide dissociates into the formation of silicon hydroxide complex under electron injection into the conduction band of silicon. By further attack of the alkaline solution, the complex is reduced to $\mathrm{Si(OH)_0}$ and pure silicon. During this reduction process, hydrogen evolution occurs. Bubbles form and accumulate on the silicon surface, changing locally the etching rate where the bubble stays on the silicon surface [45]. The etch result during chemical etching highly depends on the etch profile on the silicon surface and on the crystal orientation of the surface. As indicated in Figure 2.1, the surface of the silicon wafer is in the (100)-plane. Different orientations of the silicon surface may lead to different etch profiles in the same chemistry [36]. The crystal orientation leads naturally to etch stops. For example, for the silicon orientations, indicated in Figure 2.1, the formed pyramids are <111>-facetted. Along this direction, silicon has more bonds facing the bulk silicon, reducing the etching rate efficiently by insufficient polarization. Along the <100> or <110> direction, the surface is saturated with $Si - OH$ bonds [36]. The etched inverted pyramids and macropores are aligned in the <100>-direction.

2.3 Band diagrams

The first step during the chemical etching is to terminate the hydrogen bonds and fluorine bonds on the surface (hydrogen passivation), but more importantly to lead to a controlled kinetic limitation. This section describes the interfaces between metals and semiconductors and if either of the materials is put into an electrolyte. Those interfaces are discussed with the corresponding band diagrams and placed into the context of this work.

2.3.1 Metal-Semiconductor contact

When a metal and a semiconducting material are placed in contact with each other, a band bending in the semiconductor occurs relative to the work function of the metal. Depending on the doping of the semiconductor, this band bending is upwards or downwards. At this contact formation, it is necessary to differentiate between an ohmic or a Schottky contact. Consequently, the work functions of the metal and the semiconductor have to be correlated: if the work function of the semiconductor is larger compared to the metal, the generated electrons can easily transfer into the conduction band (called accumulation) and a current is generated in the ohmic contact. The metal side of the contact is positively charged and the flow of electrons towards the semiconductor leads to an enrichment for continuous current flow. In the reverse case, the generated electron-hole pairs lead to a space-charge region and a depletion layer, because it is not easily possible for the electrons to transfer into the conduction band [47, 48].

2.3.2 Semiconductor-Electrolyte contact

If a metal or semiconductor electrode is immersed in an electrolyte, a double layer is formed at the interface. Across this interface, a potential difference develops. Gouey, Chapman and Stern developed three different and individual models trying to explain this double layer [49, 50, 36, 47, 51]. In summary, this double layer is a consequence of the interaction of solvents inside the electrolyte with the surface of the electrodes. Depending on the polarization of the electrode, solvent dipoles are formed at the surface and the ions are solvated accordingly. Due to the charge transfer reactions at this interface, a charge separation takes place. The models all include the differentiation between the inner and outer double layer (sometimes also called diffusive double layer), meaning that with larger distance to the electrode, the potential difference is getting weaker because the polarization and dipole-dipole interactions is less than directly at the interface. This concept is similar for both metals and semiconductors, except that directly at the interface a space-charge region is formed. For semiconductors, the potential difference induces a band bending inside the semiconductors, which depends naturally on the doping of the semiconductors. Contrary to metals or semiconductors, an electrolyte does not have discrete bands, but oxidation and reduction potentials (like LUMO and HOMO orbitals), where the electrons occupy states. If a semiconductor is immersed in a solution, as indicated in Figure 2.2 for a n-type semiconductor, a band banding in the semiconductor occurs. Under an applied potential to this interface, a shift of the band bending in the electrolyte as well as across the semiconductor occurs because the applied potential is a sum of the contribution across the semiconductor and the electrolyte, giving a rise to the bend bending and space charge region. Depending on the value of applied potential, it is necessary to differentiate between a) an enrichment layer. In that case, the concentration of electrons in the conduction band of the semiconductor is increased [49, 52]. b) If the bands bend upwards, the number of electrons is reduced and a space charge region develops.

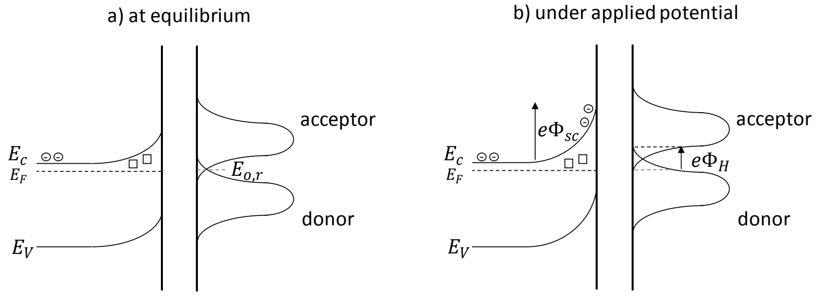

Figure 2.2: Band structure of semiconductor-electrolyte interface for an n-type semiconductor. Upon contact with an electrolyte, band banding of the semiconductor occurs (a). Under applied potential, the band bending is larger and the reduction and oxidation potentials shift as well by $e\Phi_H$(b) [49, 52].

2.4 Galvanic Cu deposition

2.4.1 Chemical Cu deposition on Si

The chemical deposition of copper on silicon wafers is based on two simultaneously running reactions. A requirement for the deposition onto silicon substrates is the usage of hydrofluoric acid (HF). The chemical deposition of copper on silicon is widely discussed (in literature) including plating properties like bath temperature, HF concentration, Cu concentration in solution and plating time. This will not be discussed in detail in this thesis. The deposition is based on a) the dissolution of silicon, b) the reduction of copper ions. Silicon substrates are dissolved by the fluorine ions in the solution, as shown in Figure 2.3. The deposition is performed in a diluted HF solution. The silicon reacts first of all with the water in the solution to form $Si(OH)_2$ [53, 54, 55, 56, 57]. The $Si(OH)_2$ is dissolved by the HF in the solution and Si-F bonds are created at the surface. In order that the reaction between the copper ions in the solution to continues, although the surface is already coated with a Cu layer, the electrons diffuse through the Cu layer and react with the atoms underneath the first layers. During the reaction, silicon tetrafluoride is formed which is a volatile component - terminating the surface by the formation of Si-H bonds. Due to this formation, the fluorine ions in the solutions are still attacking the silicon surface. Some reports indicate also the formation of complex ions like $(SiF_6)^{2-}$. This unstable anion complex reacts with the HF in the solution and decomposes by the reaction products HF and SiF_4 [58, 55, 59]. During the dissolution of the silicon, electron transfer between the silicon and the copper takes place. The silicon is oxidized during this process, thus releasing four electrons. The devilant copper ions take up the electrons and are reduced to copper that deposits on top of the surface. (Chemical) metal deposition onto silicon surfaces is preferential if the metal is more noble than the silicon. After a certain deposition time, the deposition is saturated. No more copper ions are reduced whereas the silicon dissolution is still going on. The saturation could be seen experimentally by re-deposition and delamination of the copper film on top of the silicon wafer. The deposition is independent of the HF concentration but depending on the temperature during the reaction as well as on the solution flux. The electron transfer reaction follows Fick's law. The diffusion is temperature dependent as well as the dissolution rate. The higher the temperature, the electrons are generated and travel to the copper ions. Due to the higher deposition rate, the solution gets depleted of the copper ions. Therefore, the temperature does not have a big impact on the deposition. For the deposition, only the surface atoms take place in the reaction, bulk silicon atoms ignore the reactions. If the dissolution of the silicon would dominate the deposition (and the time adjusted), the silicon would be completely dissolved. The same holds for the ions in the solution. The ions in close proximity of the sample, react with it. The remaining copper ions have to be taken into account, if the thickness of the copper has to be increased. Due to the saturation of the reaction, the thickness of the copper seed layer is only about 100 nm. The layer is called seed layer because it functions as the first sacrificial layer for the next step of the electrochemical deposition of the copper.

2.4.2 Electrochemical Cu deposition

The electrochemical copper deposition is based on the fundamental reactions inside an electrochemical cell. The electrolyte is used to transport the generated ions at the electrode sides via the solution phase to the other electrode side. One electrode is the working electrode (WE) on which the material to be deposited is reduced. This material could be any kind of material. In the case of silicon, the direct copper deposition is not possible due to adhesion problems. Therefore, as described above, an additional layer system, in the form of a thin copper seed layer is required to

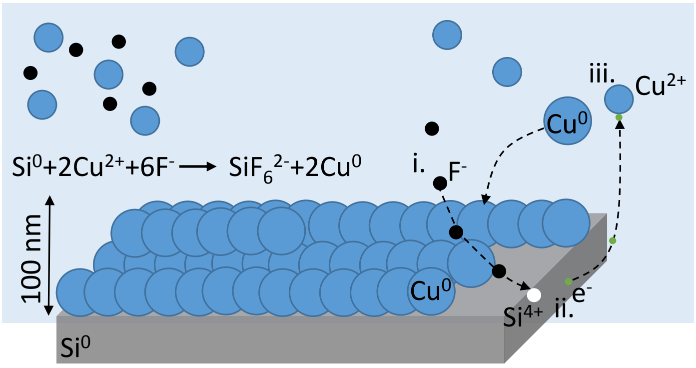

Figure 2.3: Chemical deposition of copper by galvanic displacement. The processes are divided into *i*) dissociation of the HF into fluorine ions, *ii*) oxidization of the silicon, releasing electrons for *iii*) the reduction of the devilent copper ions and the plating of the copper on the silicon [59, 54, 56].

overcome the energy barrier for further deposition. By applying a cathodic potential to the electrodes, the counter and reference electrode (CE/RF) gets oxidized. An electrochemical redox reaction takes place, oxidizing the copper electrode. The devilent copper ions go in solution and get transported on the working electrode, where they get reduced [52, 57, 49, 60, 61].

$$\text{I.: } Cu^0 \rightarrow Cu^{2+} + 2e^-$$
$$\text{II.: } Cu^{2+} + 2e^- \rightarrow Cu^0$$

This is considered as an equilibrium reaction. In the case of the silicon wires, an additional copper grid is necessary and functions as counter electrode to avoid any kind of adhesion problems.

2.4.2.1 Electrolytes

The copper deposition could be performed in different kind of electrolytes: a) cyanide solutions, b) alkaline solutions or c) acidic solutions. Acidic solutions require sulfuric acid in addition to copper salts ($CuSO_4$) to improve the quality of the deposition film. Due to the high conductivity and low polarization, the current densities during deposition can be reduced [57]. The concentration of sulfuric acid inside the solution is rather critical as it leads to the formation of precipitations if the concentration is very large. The best results in Cu deposition are achieved if the temperature is slightly increased because the redox-reaction is accelerated and more access copper is available and the solution more conductive. As for the pH-value, the phase diagram of

$CuSO_4$ and water indicates the necessary region of pH-value for the wanted Cu^0 and the electrolytes are especially designed for this region [61, 57, 49]. The advantages compared to the other two compositions are the low costs, the low toxicity compared to cyanide copper but also that it is possible to deposit copper homogeneously at low potential.

2.5 Battery Technology

Seven different battery technologies are investigated nowadays or are already commercially available. Figure 2.4 indicates the prospects of the individual battery type. Lead-acid as well as NiCd/NiMH batteries are well established batteries on the market. The low specific energies and power are a consequence of the used materials and the interaction with the electrolytes. They suffer from the classical memory effect, but also from material segregation on top of the active material. That segregation could only be prevented by deep discharging processes, which will impede even higher stress on the material. Another common problem is the electrolyte depletion in these batteries. For example, specific phases in the NiCd battery take up most of the electrolyte during its volume expansion, thereby pulverizing the complete electrode. In contrast to these technologies, Figure 2.4 demonstrates the potential of the lithium batteries. Lithium has a theoretical capacity of more than 3862 mAh/g. If the material could be used inside the batteries without chemical degradation or risk of explosion, it would be the perfect candidate to achieve high capacities. Nevertheless, this problem calls for a better solution. In the following, the different battery technologies are critically discussed in relation to the material aspects and their limitations.

Li-Air Batteries The newest member of the battery family is the Lithium-Air battery. As the name says, it is a combination of lithium as anode material and air as the cathode. The problem about this technology is the sensibility of every component in air, like nitrogen 78 %, oxygen 20 %, argon or other impurities. Another aspect is the guided oxygen diffusion through the active materials, without the irreversible oxidization of the lithium metal. Theoretically, Li-Air batteries have a very high specific energy as demonstrated in Figure 2.4 with pure metallic lithium having 3862 mAh/g. The fundamental reaction is the reaction of metallic lithium with oxygen forming lithium oxides Li_2O_2. But in reality, the specific energy and power critically depends directly on the porosity of the electrode, limiting the energy and capacity [62]. But also the electrolyte is very important because it determines the reaction products.

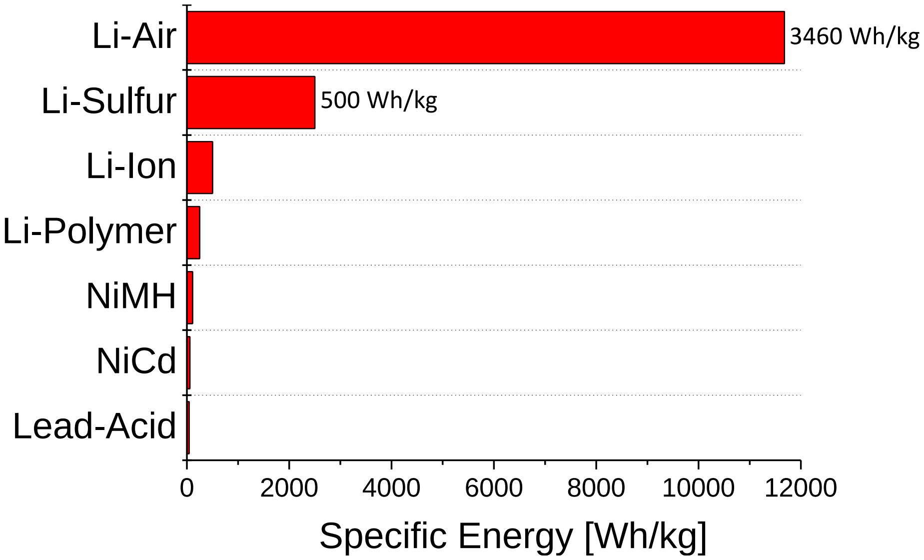

Figure 2.4: Comparison of different battery technologies depending on the specific energy. It includes the state-of-the-art Lead-acid and NiMH batteries, but also Li-Ion as well as Li-Air batteries will be critically discussed. They would have the highest possible specific energy.

Lithium oxide shows a low solubility for Li-air electrolytes. Non-aqueous and organic electrolytes are advantageous because the reaction product is only lithium oxide in contrast to acidic electrolytes. Furthermore, the electrodes have to saturate themselves with the electrolytes. Not every electrolyte with their individual viscosities allow this saturation. Zheng et al. investigated the correlation between porosities and specific energy (as well as capacity) for three different electrolyte systems, demonstrating a high degree of porosity ($> 70\,\%$), which is necessary to take full advantage of this complicated technology. Consequently, a third parameter, namely the continuous re-flow of oxygen, is crucial. Large amounts of electrolyte evaporate leading to an electrolyte depletion. This depletion hinders any further Li diffusion. Contrary to the other technologies, this electrolyte depletion is a consequence of the cell design and not due to material reactions with the electrolyte [62, 63, 64].

With respect to the electricity price (see chapter 1), the Li-Air battery with its advanced and critical demands on the electrodes, oxygen sensitive membranes and cell design is not competitive. This technology is too costly and would even increase the divergence between the production and storage price (and not reduce this gap). The anchor point is the high porosity of the anode. Typically, the anode is graphite or sodium, because of the high conductivity. Another advantage is the layered or porous structures. If this porosity is not drastically increased, the oxygen cannot diffuse through the material, and lot of material is lost, reducing the specific energy drastically. Additionally, if an oxygen sensitive sensor is not developed to filter the oxygen from the air in order to trigger this specific reaction, the battery will never be commercialized. If, on the other hand, the theoretically specific energy can be achieved together with a long cycle stability, the costs would be accepted at the prospect of the great success. In comparison, Li-Air batteries have similar energies like gasoline (13000 Wh/kg), this is the only battery which would compete with the gasoline. Nevertheless, the drawbacks are too high in order to be a real alternative for nowadays Li-Ion, Li-Polymer and Li-Sulfur batteries. The difference between Li-Ion and Li-Polymer is only small [65].

Li-Sulfur Battery

A serious competitor for the Li-ion batteries or nickel metalhydrides are the Li-Sulfur batteries, especially when using lithiated silicon as anode material (Li-Si-Sulfur batteries). As indicated, they show high energies as well as capacities with sulfur being the only cathode material with high capacities. Due to the isolating character of sulfur, the sulfur needs a conducting host materials, most commonly graphite or carbon. The limiting factor of the sulfur batteries is, on the other hand, the accessibility of sulfur and the alloy formation with Li, well-known as the shuttle-effect. Elemental sulfur exists as rhombohedral S_8. Upon lithiation, this is converted step-wise into different phases, resulting in Li_2S. The problem with this effect is that throughout the conversion insoluble products form, which agglomerate at the cathode side, blocking any further lithiation. It can be overcome by designing new types of electrolytes, but more effectively, suppressing the formation of insoluble products by using not S_8 as precursor but already polysulfides. The combination of sulfur cathodes with silicon anodes allows to form batteries with high specific energy of 500 Wh/kg and capacities of 1200 mAh/g [66, 67, 68, 69, 70]. The following sections consider the individual electrode materials and the specific requirements to achieve batteries of high capacities.

2.5.1 Designing Electrode Materials

When designing new electrode materials for any type of battery, as described above, the material and the geometry of the material are decisive. A closer look however reveals that there are some important requirements for good electrode materials [71, 72, 73, 74, 75]:

- good electronic conductivity,
- high Li diffusion coefficient,
- chemically inert towards the electrolyte,
- electrochemically stable voltage window,
- mechanically stable towards the volume expansion during lithiation/delithiation,
- (correct) specific geometry and size allowing faster and easier lithiation processes,
- high degree of crystallinity during lithiation/delithation,
- stable crystal structure during volume expansion (the oxidization state has to be maintained),
- thermally stable (also at room temperature, without the risk of safety hazards) to limit self-discharge effects,
- non-toxic and cheap,
- high availability to limit the material bottleneck for future production,
- minimal oxygen sensitivity,
- adjustable and sustainable porosity, especially for Li-Air batteries and Lead-Acid batteries,
- adjustable and sustainable pore volume, especially for Li-Sulfur batteries.
- low internal resistance,
- high operational voltages (and chemical potentials for cathodes and anode materials, in dependence of the work function of the electrolyte),
- good ohmic contact between the electrodes and the current collectors.

The following description concentrates only on the material aspects of the electrodes, neither on the economic aspect nor on the adjustments for the individual battery technology [76, 77].

2.5.1.1 Cathodes

The commercially available batteries have $LiCoO_2$ as cathode material. The layered cobalt oxide material is a transition metal oxide material, which has a capacity of up to 180 mAh/g. Due to the lack of serious alternative materials, this material is widely used but it has some major drawbacks: it is very expensive and is very toxic.

When talking about the costs, the raw material costs of both cobalt and lithium are the limiting factors for this type of cathode. Most transition metal oxides have a low electronic conductivity and low ionic diffusion. Therefore, a fast ionic diffusion is not possible during charging and discharging of the battery, which limits the cycle life. In order to increase the electronic conductivity, transition metal oxide cathodes are embedded or encapsulated with a conductive carbon network, consisting mostly of pure carbon, graphite or even CNTs [74, 70, 78, 73, 77, 79, 80]. As an alternative to $LiCoO_2$, the cobalt is replaced by manganese in layered, but mostly in a spinell crystal structure like $LiMn_2O_4$, $LiNi_{0.5}Mn_{1.5}O_4$ or even more complex $LiNi_{0.3}Co_{0.3}Mn_{0.3}O_2$, short NMC. Those manganese spinell structures have the advantage that higher numbers of Li can intercalate into the spinell structure, by occupying the octahedral positions. Thereby, different phases can be achieved, which promote the capacity of the structure. The problem with these structures is however that the structure has to remain intact with every repeated intercalation. Many efforts are done to stabilize the structures by additional surface coatings or by different cathode morphologies. Another disadvantage of the manganese cathode materials is the chemical instability of the manganese towards the electrolytes. The manganese gets dissolved by the electrolytes (similar to the dissolution of Zn in alkaline solution in NiZn batteries), destroying the cathode material, limiting from this side the battery performance. Different morphologies of the nanostructures as well as different compositions of the spinell structures are developed to limit this dissolution and crystal distortion. As an example, mesopores, nanotubes or even nanowires are fabricated out of $LiMn_2O_4$ in order to reduce the lithium diffusion paths and to allow a higher effective surface due to the increase of the surface to volume ratio. Both transition metal oxides and spinell structures are high-voltage materials of up to 4 V, but only a limited capacity with a maximum of 250 mAh/g. A new class of cathode material includes $LiFePO_4$, which crystallizes in an olivine structure and exhibits a high thermal stability in contrast to all of the other cathode materials. But similarly to the other options, also $LiFePO_4$ is limited by its low electronic conductivity. In general, all of the cathode materials are intercalation materials in contrast to most anode materials, thus incorporating the lithium into their structure like on octahedral or tetrahedral positions. In the case of layered structures, the Li forms an additional layer around the host structure. For a good cathode material the electronic conductivity of the material itself has to be increased to allow adequate Li diffusion in and out of the material. The crystal structure of the material has to allow a high degree of Li ions irreversibly destroying the crystal structure. Due to the complex structures of the spinell and olivine structures, the operational voltages for the Li incorporation is different for charging and discharging. It is easy for the Li ions to occupy the octahedral positions, but due to the volume expansion in the c/a-direction, the crystal structure gets distorted and very low voltages result. As cathodes contain lithium, they should be very oxygen sensitive, without degrading. Figure 2.5 shows an overview of the various cathode as well as anode materials. This overview shows only those materials, which have prospects to be built into a Li-ion battery. At the anode side, Zn, Al and Ti are missing in this listing because they are not very promising anode materials. For example, Zn wires or other nanostructures are still very dense and Li has problems diffusing into those structures reversibly. Aluminum, on the other hand, is a typical cathode current collector material and is typically corroded at the anode side. In order to use it for the anode side, a new electrolyte has to be designed, which allows stable Li diffusion without degradation. Furthermore, aluminum batteries are not based on the Li-Ion-Battery Technology up to now, but are more considered as typical redox-reactions. For a battery with reversible charging and discharging, the chemistry has to be modified even further.

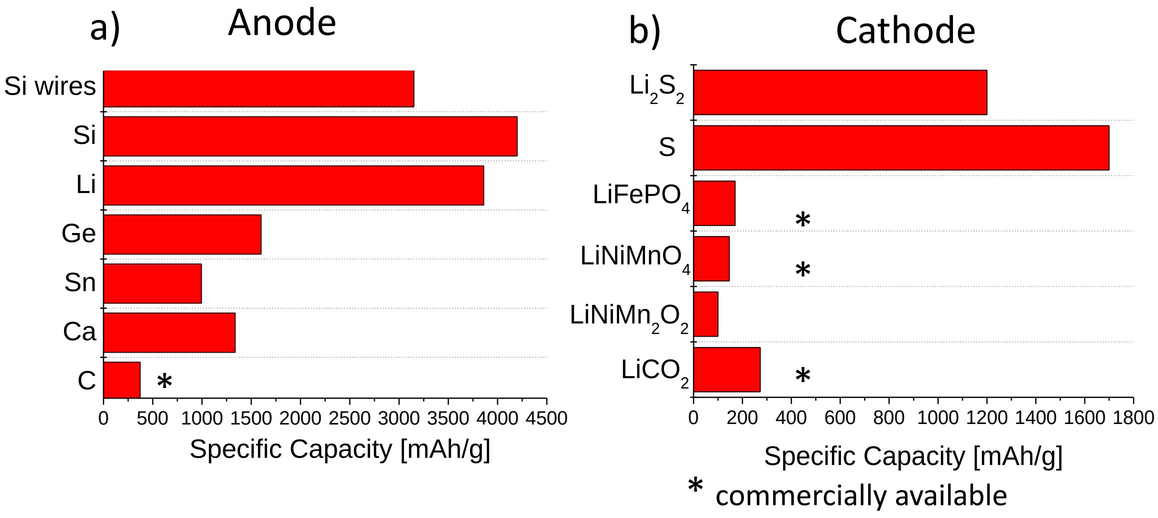

Figure 2.5: Overview of cathode and anode materials depending on their specific capacity. a) The overview shows typical anode materials. Compared to commercial available graphite, silicon as well as lithium show ten times higher specific capacity. b) The overview shows typical cathode materials, including the state-of-the-art materials. Contrary to the low capacity materials, sulfur and lithiated sulfur cathodes show a ten times higher specific capacity (which is already realized in some Li-S cells).

2.5.1.2 Anodes

The anode materials are mostly considered as (lithiation/delithiation) alloy materials, forming different phases with the lithium. In a standard battery, the cathode material is always lithiated or contains the lithium as a compound, as discussed above. Like this, the anode material can be used in its original, unique state. Commercial batteries contain graphite as anode material. This material is an exception and is considered an intercalation material as well. The layered structure of graphite is the perfect example of intercalation materials, because lithium is trapped between the layers. This material is very cheap and highly available, but has a very poor capacity of only 372 mAh/g. Not only the capacity is limiting the battery. Another weak link is the continuous reaction of the electrode with the electrolyte, superimposing a new, fresh SEI layer around the graphite structure. The growing SEI disturbs the system because the more unwanted, secondary side reactions occur, the higher the internal resistance. This leads to a dramatic capacity fading.

One alternative is pure metal lithium. It has a very high capacity of 3342 mAh/g. The problem of this electrode is the oxygen sensitivity of the metal lithium and the high risk of dendrite growth. The dendrites penetrate the separator material and form a short circuit with the anode material. The challenge in using pure lithium is to prevent the SEI formation on lithium, thus passivating the material. Silicon as anode material has an even higher capacity of 4200 mAh/g and does not have the sensitivity nor the safety problems like lithium. Silicon can incorporate four lithium ions with a coordination number of four. Due to its high volume expansion of over 400 %, silicon cannot be used as bulk material, as many cathode and anode material, and is only used as a nanostructure. Cui et al. fabricated different shapes and morphologies of silicon and even silicon/composite materials, like Si/C, Si/Ge and many more [24, 81, 77, 82, 83, 84]. The benefit of silicon is very clear: it is chemically inert, very cheap, has a good electronic conductivity and exhibits high diffusion coefficients. But not only these anode materials are the interest of research nowadays. Sn, Zn, Mg and Al might be an alternative material, although their capacity is also very low. In addition, for example, the earth alkaline materials are limited due to their high oxygen sensitivity and therefore more suitable for solid state batteries.

2.5.2 Electrochemistry of Silicon

A battery or a secondary battery after definition is a device to store charges which could be used to power a device. A secondary battery can be discharged by connecting it to a device and recharged. It consists usually out of two electrodes and an electrolyte in between them to allow diffusion of Li ions. The separator is used as mechanical separation between both electrodes to avoid short circuits. There is a lot of controversy about the definition of charging and discharging. In this thesis charging and discharging is always represented by the lithiation and delithiation process - in general by the phase transformation or formation of Li_xSi_y phases. The base of the lithiation process is the definite change in the crystal structure (amorphous/crystalline) of the phases. The specific structure or phase represents/exhibits a specific capacity which is the most important factor for the performance of the battery. The phase with the highest capacities (like $Li_{22}Si_5$) should be held as long as possible during cycling the battery to achieve long and stable cycling performance. Other phases like $Li_{15}Si_4$ show lower capacities [85, 86, 29, 27, 87, 83, 88, 89, 90]. Those phases could be suppressed (from forming) by restricting the voltage limitations during cycling. In order to avoid $Li_{15}Si_4$ for example, one possible way to restrict this, is to cycle only to the minimal voltage. The minimal voltage is the region between the last, fully lithiation peak and the scan reversal. This phase is highly unstable and only detectable in in-situ XRD-measurements. During the phase transformations from crystalline silicon to these alloys, large volume expansions exist and lots of bonds have to be broken with enhanced activation energies. This additional structural change which is imposed on the system decreases the capacity of a battery. When the alloys are formed and the capacity is reached - charges are incorporated into the material - power sources or consumers could be plugged to the batteries to use their power. Due to the physical formation of the Li_xSi_y phases (and no chemical formation), the capacities of the different types of phases have a different explanation. Lithiation and delithiation of crystalline silicon microwires is a two-step process. In comparison to amorphous or semi-crystalline structures, the Li insertion is mostly only a single step reaction resulting in different phases. The insertion in amorphous materials is still under ongoing investigation. The difference in the lithiation behavior between the two crystallographic orientations is the structural change among lithiation. Specific potential limits during voltammetric measurements or cycling experiments induce the re-orientation of the structure in specific phases like $Li_{15}Si_4$ which is accommodated with large volume changes and pulverization of the material itself. These phases have to be avoided. In order to prevent the phases to form, the limits are chosen wisely according to voltammetric measurements. As revealed in different studies like [91, 92], those phases do not exist in the silicon microwires. A typical voltammetric result of the Si microwires is shown in Figure 2.6. It resembles a typical I-V curve from photovoltaics measuring here

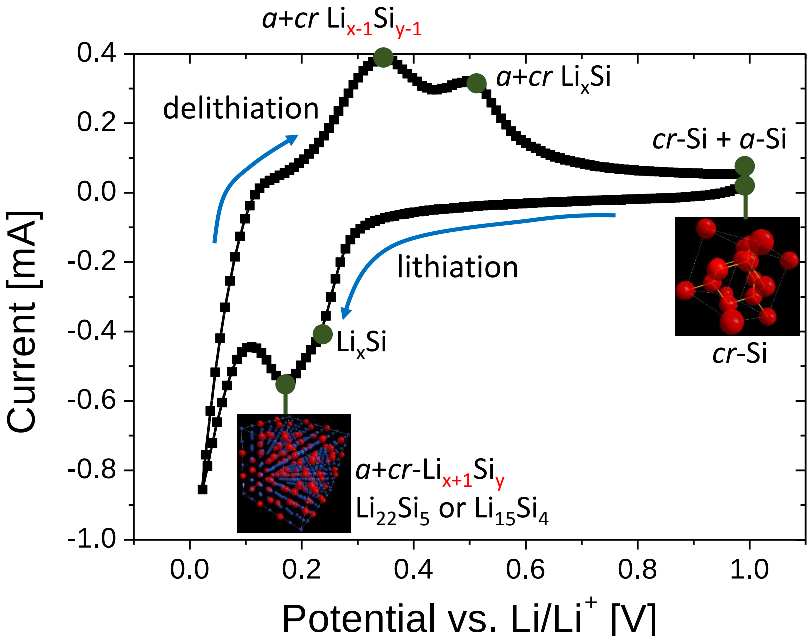

Figure 2.6: Typical lithiation and delithiation process in silicon illustrated at a cyclic voltammogram. The starting point is crystalline (*cr*-Si) in its diamond crystal structure. Upon lithiation, the Li ions incorporate into the structure and form different alloys. Typically, alloys with high amounts of Li are formed, like $Li_{22}Si_5$ and $Li_{15}Si_4$, depending on the applied potential. The crystallinity decreases and partially amorphous phases form, indicated by a+cr $Li_{x+1}Si_{y+1}$ phases with increasing cycle numbers. During delithiation, the ions are removed from the anode. If and under which conditions the crystallinity remains, is discussed in this thesis.

diffusional and phase changes according to potential change. In this figure, the resulting current is plotted versus the time of the measurement; the additional voltammogram (I-V curve) shows by the minima and maxima developments, phase transformations between the two species Si and Li. Compared to other anode materials (see Figure 2.5), Si and Li form alloys Li_ySi_x. The starting wires are crystalline. In a two-step reaction, four peaks develop and are referred to as Peak 1 to Peak 4. Lithiation behavior is described by Peaks 1 and 2 referring to the partial and fully lithiation behavior. Those peaks correspond to the phases Li_xSi and $Li_{x+1}Si_y$. That means that more and more Li ions are incorporated into the silicon wires. During the incorporation, the crystal expands and bonds are broken. The energetic as well as diffusional contributions are discussed further down. At the maximal amount of ions incorporated the fully lithiated phase is formed $Li_{x+1}Si_y$. This is in most systems either $Li_{22}Si_5$ or $Li_{15}Si_4$. By reversing the potential scan direction, the Li ions are removed from the anode and the phases are changed again. Peak 3 and Peak 4 are referred to as partial and fully delithation peak. Figure 4.1 shows as an example the correlation between the measured current and the time as well as the correlation between the potential and the current. In order to have a clear indication that peaks are referred to as phase transformations an additional voltammogram shows the LiSi-phases with the different structures. As a starting point crystalline silicon in the diamond structure is shown. In the fully lithiated state of the silicon microwires, $Li_{22}Si_5$ develops which is also shown with its crystallographic structure [85, 83].

2.5.3 Electrolytes

Electrolytes with their components play the most important role in the success and performance of batteries. As mentioned in the introduction, the electrolyte takes 17 % of the total weight of a battery. The dominating factor is the influence on the mechanical stability of the electrode. Of course, the mechanical stability is also given by the geometry and assembly of the electrode; but more important, is the formation of the SEI layer which depends and alters with the used electrolyte. By only changing the type of Li salts or their concentration, the conductivity of the electrolyte may increase but the dissociation products may lead to unwanted reactions like e.g. they reduce even more the stability of the SEI layer and surface protection. Additions of linear and cyclic carbonates (or carboxymethyl groups) to the electrolyte enhance the viscosity of the electrolyte. The diffusion could be deliberately increased to have a controlled lithiation due to a homogeneous SEI layer [93].

Battery electrolytes have to fulfill some requirements [94, 95, 77, 96]: a) Their ionic conductivity has to be high to allow fast ionic diffusion between the electrolyte to the interface between the electrolyte and the electrode surface where the reaction takes place. This requires theoretically a low viscous electrolyte in order that the reaction to take place. b) An electrolyte has to be adapted to the correct and applicable electrochemical potential range. Not every electrolyte could be applied to every potential regime without precipitations, dissociation or heat generations. For anode systems, the (electrochemical) potential regime lies between 0 and 2 V where the electrolyte is stable. c) In order to use the battery electrodes for various applications, the electrolytes have to perform at a large temperature ranges. Most electrolytes are adapted between -20 °C up to 60 °C. If the temperature range should be adapted, the ratio between the solvents (EC and DMC) changes from 1:1 to 2:1 for higher temperature ranges. Ethylene carbonate (EC) as cyclic carbonate has a high boiling point of up to 238 °C. An increase in the amount of EC leads to a more stable electrolyte at higher temperatures. This leads to the fourth requirement. d) The electrolyte consists usually of a multi-blend system of solvents like EC in combination with DMC or DEC. The solvents have to have a high boiling point and a low melting point. Hardly any single-blend system meets this requirement and therefore a combination of for example EC and DMC is mostly used. DMC has a boiling point of only 80 °C but suppresses the melting point of the blend system. In comparison to EC, DMC has a ten times lower melting point [94, 95, 77].

A battery electrolyte (no matter if cathode side or anode side) consists of a Li salt and solvents in which the salt is dissolved. On both sides the above requirements have to meet. There are only limited numbers of Li salts available for the anode (in total only five salts are used in battery electrolytes) and cathode side. The most important criteria for Li salts are the (complete) dissolution and mixing in the multi-blend solvents and its conductivity. The conductivity has to be seen in relation with the used solvents and not only alone. There exist some salts with high conductivity, but when mixing it with the solvents, the conductivity reduces and the benefit is gone. Another fact lies in the reaction and dissociation with the other components in order to build up a stable SEI layer. That means that the salt should be electrochemically but mostly chemically stable in order to prevent any unwanted side reactions during the battery performance. $LiClO_4$ and $LiAsF_6$ are good examples of non-stable salts. They exhibit higher values in conductivity as well as melting point. But for example the perchlorate in the $LiClO_4$ system is a strong oxidizing agent and reacts with the solvent to form Li_2O which deposits on the anode side. On the other hand, the reduction of AsF_6^- anions in the electrolyte lead to toxic components inside the battery packs rising safety issues. Typical solvents can be divided into linear and cyclic carbonates. Up to now, the electrolyte only contains the Li salt which has to be dissolved. The key requirement of the used solvents is of course to allow the dissolution of the salts without chemical precipitation of the salt again. For all the chemical components in the battery pack, the same requirement holds. They all have to be chemically inert towards the other in-active as well as active components of the battery. As discussed above, the melting and boiling point is critical and could be adjusted by combining different solvents. The benefits of linear carbonates are their low melting point and low viscosity. By mixing with cyclic carbonates, the melting point and viscosity could be adjusted. Ternary electrolyte systems contain three different solvents. Those systems have higher ionic conductivity over a large temperature range. No precipitation or phase transformation of the solvents exist. Additionally, those electrolytes could be applied to low temperature ranges. With the addition of for example propylene carbonate (PC), the conductivity at -50 °C remains high enough to allow Li diffusion. Ternary systems follow the Walden rule which correlates the viscosity with the conductivity of the solvents. The electrolyte could be seen as a series resistance model where every new component with its viscosity adds up to the system. the same holds for the dielectric constants in the mixture [77].

The electrolyte has one most important function: to form a stable and homogeneous SEI layer around the structure of the active material [94, 97, 98]. The composition and the stability of the SEI layer could be triggered with the used electrolyte and most especially with the used solvents. Propylene carbonate was mostly studied for graphite electrode adding the PC into the standard electrolyte. When cycling the graphite electrodes with this electrolyte, the capacity faded irreversibly very quickly. This phenomenon is understood now in every detail. During the dissociation of the PC, the dissociation products (like dicarbonates, propylene gas) co-intercalate into the graphite structure before the passivation layer is build up. Propylene gas forms, rises the internal pressure and induces cracks in the graphite structure which leads to exfoliation and destruction of the structure. The isolation of the active material leads to percolation losses and to capacity fading in the battery.

The basic difference in the reduction mechanism of PC lies in the existence of the methyl group attached to the cyclic ring. Upon breaking of the CO double bond and electron uptake, the radicals form. Two kinds of terminations are possible with the PC: a) radical termination with the formation of alkyl dicarbonates and b) the formation of propylene gas and propene. The difference between both scenarios is supposed to be concentration dependent. At low concentrations of PC, mostly propylene gas, propene and Li_2CO_3 form as additional products in the passivation layer. PC with its dynamic reactivity is very sensitive to traces of electrolyte impurities or oxygen and reacts dynamically with lithiated surfaces [99, 77, 100, 101].

Electrolytes are usually designed for a specific temperature range. In order to use batteries in different applications like in aerospace technology where temperatures of $-80\,°C$ exist or the other extrema for using cars in the desert at extremely high temperatures, the electrolytes have to withstand those temperatures. Standard anode electrolytes in a co-solvent system (EC and DMC) with $LiPF_6$ as lithium salt have their limitations at those temperatures. By adding and varying the ratios of both solvents as mentioned above, adaptions could be made. Ethylene carbonate with its high boiling point and large viscosity ($\eta = 1.9$) hinders the application at low temperatures. If the viscosity is too high, diffusion limitations due to enhanced passivation kinetics hinder the formation of a stable passivation layer and lead to capacity fading. It leads to phase separations of the solvent. The amount of linear carbonates is therefore increased to benefit from their low melting and boiling points [94, 102, 103, 104, 105, 106, 77, 107, 108] At higher temperatures, the solvents are not stable anymore. The dissociation is thermally activated and leads to a ring opening process of the EC and PC. Those products react with the linear carbonate DMC in a transesterification [94] to DMDOHC. The dissociation of the Li salt forms the anion PF_5^- which reacts with the cyclic carbonates in the electrolyte. The new formed products influence the SEI layer stability drastically because the probability of HF development increases with temperature. At even higher temperatures of up to 120 °C, the SEI layer itself starts to decompose. A dissolution of the SEI layer means additional non-faradaic currents which superimpose on the electrochemical system and a complete loss of the mechanical stability of the structure.

For characterizing a non-aqueous (polymeric) electrolyte, it is necessary to model the conductivity and viscosity. The diffusion coefficient D is directly correlated with the Stokes-Einstein equation to the viscosity of an electrolyte [109]

$$D = kT/6\pi\eta r_0, \tag{2.2}$$

with η being the viscosity of the electrolyte and r_0 the radius of the ion inside the electrolyte, here considered lithium. Another contribution is the ionic conductivity of an electrolyte, which has to be as high as possible to allow ionic diffusion inside the electrolyte and allow phase transformation of and inside anodes. The conductivity σ follows

$$\sigma = (q^2c/kT) * D, \tag{2.3}$$

with q being the charge, c the concentration. In order to adequately describe an electrolyte for Li ion batteries, another equation has to be considered. Electrolytes may contain certain type of solvents, which might undergo polymerization reactions. Therefore, an electrolyte might also be considered polymeric, thus following the Vogel-Fulcher temperature dependency. It is a common equation relating the conductivity with the temperature under which an electrolyte might be operated [109, 77]. This is a non-Arrhenius law,

$$\sigma = A\sqrt{T}exp(-B/(T-T_0)), \tag{2.4}$$

with A and B being constants. The most important parameters are the temperature dependencies with T_0 as the reference or glass transition temperature for polymers. Nazri et al. showed the temperature dependence of common, standard battery electrolytes, which show clearly an increase in temperature compared to room temperature by a factor of two [77, 110, 94, 71, 111, 112, 113]. Another important aspect is the viscosity. Viscosity is usually related to the diffusion coefficient and to the rate constants. In general, viscosity is correlated to the shear stress inside a fluid, being able to transport particles in a medium from one point to the other. High viscous fluids are honey or gel with high stress, where more material is taking while a particle moves. Thus, viscosity is a property of a fluid describing the ability and amount of material being transported. Battery electrolytes are always designed in such a way, that the ionic conductivity is the highest and therefore, the viscosity rather low. The energy band diagram shown in Figure 2.7 of the electrolytes in combination with the electrodes summarizes the necessary requirements, when designing both electrode materials as well as electrolytes. An anode material with a potential μ_A higher than

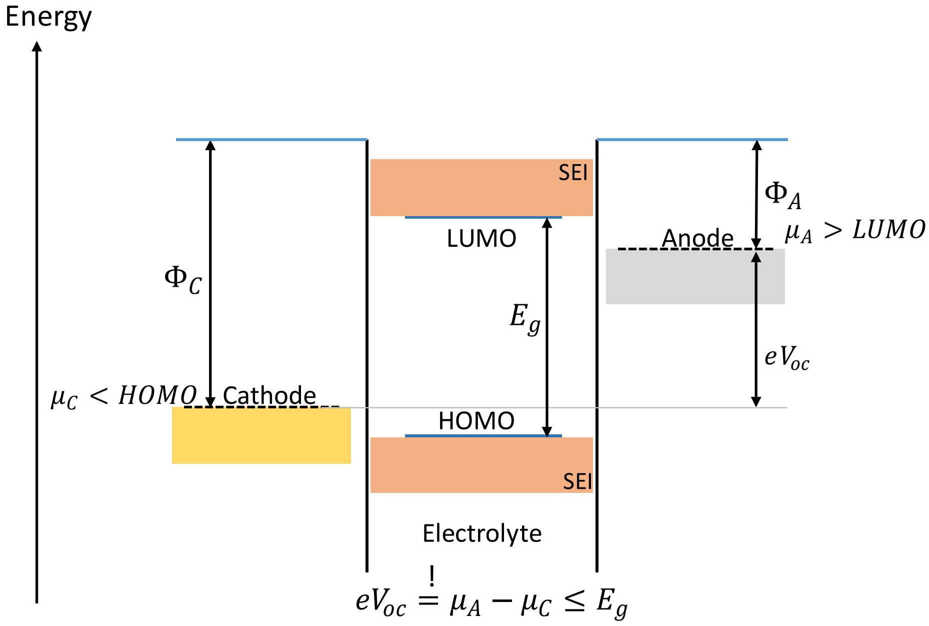

Figure 2.7: Energy band diagram of the electrolyte-electrode interface. In contrast to the electrodes (metals or semiconductors), an electrolyte does not have discrete energy bands, but acceptor and donor levels in solution. E_g is the electrochemical voltage window, in which an electrolyte could be operated. In other words, it is the distance between the lowest unoccupied and highest occupied energy level. μ_A as well as μ_C are the electrochemical potentials of the anode and cathode materials [75, 71, 114].

the LUMO level of the electrolyte tends to reduce the electrolyte. In order to avoid this irreversible reduction, an additional energy barrier forms in form of the SEI layer at the electrolyte-electrode interface. The same happens at the cathode side, if the potential μ_C is below the HOMO level. Consequently, the potentials of the individual anode and cathode materials has to be equal or lower than the E_g of the electrolyte, in order to have a thermodynamically stable electrolyte [75, 52, 74].

2.6 Electrode kinetics

The electrode kinetics was found to be the most important parameter, when analyzing battery performances because it happens at the direct interface between the electrode and the electrolyte. The reactions happening at this interface are the rate-limiting steps because they decide between good ion diffusion through this interface into the electrode material and consequently about good electrochemical performance of the battery.

2.6.1 Solid-electrolyte interface (SEI)

The solid-electrolyte interface layer forms a passivation layer around each electrode in contact with ionic liquids or battery electrolytes [115]. This happens at the electrolyte/semiconductor interface, described in chapter 2.3, on both the cathode and the anode sides. Although this point is often neglected in the discussion about the SEI, it also forms in the same way on the cathode. Upon dissociation and decomposition of the individual solvents and salts inside the electrolyte, their reaction products agglomerate at the electrode surface, allowing only Li diffusion and blocking any side reactions with the electrode. For the most common non-aqueous, organic electrolyte (Selectilyte LP 30) the SEI products include for example a) PF_5, b) LiF, c) LiO, d) and carbonates as well as esters due to the dissolution of ethylene carbonate and dimethyl carbonates. Those dissociation products highly depend on the exact composition of the electrolyte as well as the electrodes. Therefore, the SEI might change due to the chemical nature and electron transfer reaction of the chemical components. In the case of moisture inside the battery or electrode, water will lead to further reduction of the salt and forms hydrofluoric acid (HF). Not only HF might form, but also LiOH, which oxidizes the metal lithium. For detailed reduction mechanisms of individual electrolyte components, consider [94, 97, 116, 95, 77]. The reason for the exemplary reduction mechanism is to quantitatively discuss the impact of the products on the electrode interface and, with it, on the electrode performance. Especially, in the case of silicon, a high fluorine concentration (not bound in a salt) in the electrolyte will lead to an unwanted surface oxidization. As a consequence, more and more silicon is lost as active material. Another example are the reduction products of the solvents, which is even more important, considering that they could react to long-chain polymers, thus influencing the diffusion and kinetics in the battery.

Whereas the SEI formation is continuous on graphite electrodes leading to partial exfoliation on those electrodes, it has a fixed thickness on silicon electrodes. For that matter, the SEI formation is the result of the electrochemical stability of each solvent and salt. If the composition changes inside the electrolyte due to a temperature change inside the battery, consequently, the solvents are influenced. In general, there is a direct correlation between the chemical and thermal stability of the solvents and salts on the composition of the SEI layer. Mostly, the SEI formation happens in the first cycles i.e. at the first contact between electrode and electrolyte. Depending on the specific conditions of the charging/discharging like for example long-term cycling or temperature increase, the SEI layer can alter its composition and chemical stability.

The composition needs to be monitored by either IR- or Raman-Spectroscopy. If the temperature is increased, the SEI layer is less stable mainly due to the thermal instability of the electrolyte components.

Naturally the question arises, why this is an important aspect. The answer is quite simple: a passivation layer is an additional layer around a material and thus has to be considered as such. In the case of layer structures, the correlation between chemistry and mechanics has to be investigated. By analyzing the surface chemistry, inorganic and organic reactions can be triggered in order to enhance (if necessary) the chemo-mechanical properties of exactly the additional layer.

2.6.2 Temperature dependent electrode kinetics

Temperature has a number of influences and consequences on an electrochemical system. In a battery system, when characterizing anode or cathode materials, temperature not only influences the charge-transfer kinetics, it also ages the electrolyte, thus influences the interface between electrolyte and electrode. In chapter 2.6.1, the influence of temperature impact and long-term stability of the SEI layer has already been described. Electrolytic aging means for example an enhanced decomposition of electrolytic salts like $LiPF_6$. Such decomposition triggers unwanted side reactions, which might lead to a decomposition of the SEI layer. The most common result of a temperature increase is the evolution of hydrogen, carbon dioxide or even HF [108, 94, 111, 104, 102, 117]. But a functional and intact SEI layer is a requirement for a high capacity anode or cathode material. The protection at the interface is needed especially at higher temperature. Otherwise it will lead to the well known self-discharge effect. This effect is based on the accelerated charge transfer process because the reaction rates depend exponentially on the Boltzmann factor which scales with temperatures [117]:

$$k = Aexp(-E_a/kT) \tag{2.5}$$

As a consequence of the temperature increase, the Li diffusion inside a silicon crystal for example also increases because it has the same temperature dependence. The diffusion is directly correlated to the mobility of the ions by the Einstein-Schmucholsky equation:

$$D = \mu kT/q = Aexp(-E_a/kT) \tag{2.6}$$

Enhanced diffusion is directly accompanied with enhanced ionic mobility with an increase in temperature. Consequently, more ions need incorporated into the anode, thus creating a higher concentration gradient at the electrolyte/electrode interface.

2.7 Electro-analytical Characterization Techniques

2.7.1 Cyclic Voltammetry

Cyclic voltammetry is a typical electro-analytical characterization in chemistry to analyze solvent solutions in order to determine reaction rates, kinetics and redox reactions. Furthermore, it is used to analyze if organic or aqueous solutions are electrochemical and chemically stable, by analyzing current peaks. For battery technology, cyclic voltammetry is an important tool to analyze a) the occurrence of phase transformations, b) chemical stability at the electrode/electrolyte interface, c) electrochemical stability of electrode materials towards the electrolyte and between the electrode materials, and additionally, d) to calculate reaction kinetics. Those properties could be analyzed by the current change and peak formation. They are a consequence of the charge transfer kinetics and the mass transport. In the most general case, a thermodynamic equilibrium reaction is established at the surfaces between element A and B, which are oxidized and reduced in the appearance of the electrolyte.

The charge transfer kinetics at the interface between electrode and electrolyte also obey the Butler-Volmer equation. Consequently, the current depends on the concentration gradient at the surface and on the diffusion layer, which forms due to the formation of the contact. This diffusion layer thickness depends on the sweep rate and controls the mass transport. The sweep rate is a key parameter because it controls how much material is passed. Typically, measurements are performed at a low sweep rate to measure at steady state conditions. Additionally, the diffusion layer thickness has to be penetrable for the solvents in order for them to react with the electrode surface. This allows insights in the transfer kinetics and rate constants. When analyzing voltammetry results, typically three cases have to be differentiated: In the reversible case, the reactions are only diffusion controlled and the mass transport is critical. The reactions are triggered by the establishment of concentration gradients at the electrode surfaces. In an irreversible case, peaks only show up either the anodic or cathodic side - the reactions are dominantly happening at one side of the electrode and no thermodynamic equilibrium is established. The reactions are only limited by the charge transfer at the individual electrode surfaces, because the diffusion is completely limited. For example in the battery analysis, an irreversible peak shows up during discharging because the electrolyte decomposes. This peak does not reappear during charging. Another example is the appearance of side effect reactions of the electrode materials with each other.

A typical case for battery technology is the quasi-reversible case, where both diffusion and kinetics have to be considered in order to fully characterize an electrochemical system. This means that both the current amplitudes (of the peaks) as well as the potential differences and absolute potentials have to be calculated. The potential differences and absolute potentials are necessary to calculate rate constants and estimate charge transfer processes [118, 119, 120, 50]. Another important aspect when talking about surface chemistry and voltammetry are the individual currents: Faradaic currents are the result of the charge transfer reactions and directly correlated to the material information and phase transformations. But simultaneously, a current is driven through the double layer formation, charging the corresponding capacitance and ionic solvation at the interface. Both currents have a different time dependency. Consequently, the answer of the recorded current of the voltammogram has not only the necessary material information, but is falsified by secondary processes [118, 120, 47].

2.7.2 Staircase Voltammetry

Instead of linear potential ramps, a second way of measuring electrode kinetics is staircase or step voltammetry. In this case, constant steps are incorporated, where the potential is kept constant for a certain time period. This allows the secondary processes to relax, because they decay faster than the faradaic processes. This voltammetry type is used pre-dominantly, if the sweep rate cannot be reduced effectively. Anyhow, this method has another advantage: it allows to analyze relaxation phenomena of the reacting species. The biggest disadvantage of this type of voltammetry for characterizing kinetics for batteries is that a constant potential step influences the state of charge of batteries. Therefore, the time of the potential steps has to be as short as possible to not change the reactions too much, but also long enough to allow the secondary processes to decay [121, 119, 118, 120].

2.7.3 Fast-Fourier-Transform Impedance Spectroscopy (FFT-IS)

Impedance is the complex property relating the complex parameters of current and voltage. It is a linear response analysis, when a sinodical signal is superimposed on the applied current or voltage [122, 123]. In order to measure accurately, it is necessary to be in the linear region - minimizing the current and voltage amplitude. The specialty of Fast-Fourier-Transform Impedance Spectroscopy is the transformation from the frequency into the time region. As a result, the measurement speed is increased drastically allowing to measure simultaneously over a wide frequency region (10 Hz up to 20 kHz) within a second. The frequency region is transformed into the time region, allowing directly to correlate kinetics and diffusion to time-dependent processes. Compared to standard EIS technology, the frequencies are all applied during one measurement, reducing the time with the same sensitivity. For this technique, Nyquist plots are not analyzed in order to see changes in the resistances, but rather seven individual parameters like time constants, capacitances and resistances are displayed depending on the time. Those parameters indicate all the necessary information, especially for electrode characterization. The analysis of Nyquist plots gives only qualitative information, but the direct correlation between time constants and phase transformations indicate kinetic and diffusional parameters by modeling the interfaces inside the battery or in general electrochemical cell. The recorded data is fitted to a special equivalent circuit model, consisting of resistances and capacitance (and

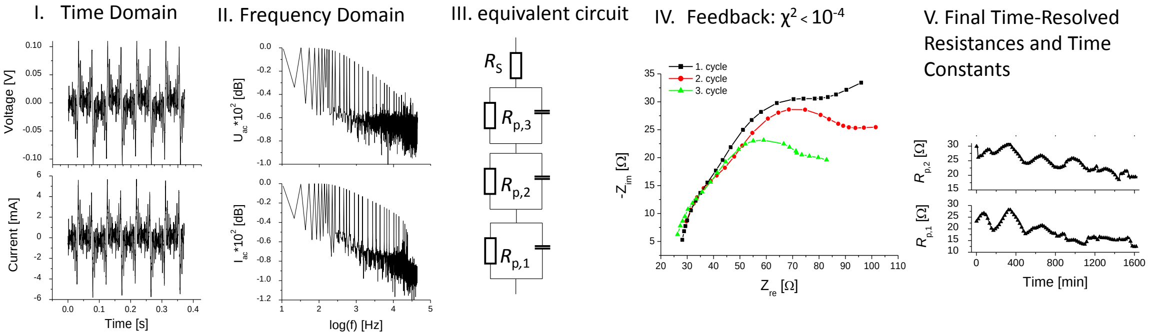

Figure 2.8: Measuring and fitting routine of FFT-IS analysis. I. The data is collected and transformed from the time domain into the frequency domain (II.). According to the correct equivalent model, which is applied to the recorded data (III.), Nyquist plots are fitted (IV.). The feedback of the quality of the fit is measured by the least square deviation. The deviation should be in the order of 10^{-4}. The characteristic resistances and time constants are plotted versus time (V.). Consequently, those resistances (and the corresponding time constants) describe the physical parameters inside the electrodes of a battery.

sometimes even of inductance) in parallel or series to another. If one RC circuit or several circuits describe the data the best, it is always evaluated with the least square deviation χ^2. This parameter is modeled by standard least square minimization routine. In order to measure those impedances in-situ simultaneously to different electro-analytical characterizations, 10 Hz is the lowest frequency [124, 122, 123, 125, 126]. Figure 2.8 shows the measuring and fitting routine for the FFT-IS measurements.

2.8 Instrumentation

2.8.1 Hard X-ray Transmission Microscopy (TXM)

X-ray Transmission Microscopy is widely used in biology to penetrate and image biological tissue. This technique is now growing in different fields of application, it is used to image nanoscale structures and make 3D tomography analysis. This microscopy technique is divided into soft x-ray microscopy and hard x-ray microscopy. Soft x-rays are in the order of 100 Å and only used to image biological tissue. On the other hand, hard x-rays have the highest energy and can penetrate deeper into the material (<2 Å) [127, 128]. These hard X-ray microscopy technique is used in this thesis, in cooperation with the Stanford Synchrotron Radiation Laboratory (SSRL, beam line 6-2), Stanford University, CA, USA. This technique is very beneficial to analyze the different structures of nano- or micromaterials due to its high local resolution of below 30-40 nm [129]. This allows a detailed structural analysis of different regions on a specimen, even in-situ.

By using a monochromator, the beam could be precisely focused. With the help of a special motor, the samples can be moved very precisely in every direction. The synchrotron radiation source consists of a Wiggler with additional mirror collimator, which is then directed towards a monochromator, which defines the energy resolution of the beam line. The beam line can be operated at different voltages, depending on the application ranging from 5 to 14 keV [130, 128, 131]. The detected signal is then projected and aligned towards a scintillator which is detected by a CCD camera [130]. With this technique and the high energy, sample thickness of around 40-60 µm can be radiated and analyzed. For more detailed information consider [130, 128, 131].

If radiation transparent samples are analyzed, a phase ring is added into the beam line. This phase ring is based on the Zernike phase contrast and is a special phase contrast, also used in standard light microscopy, for materials lacking of a self-contrast for biology [132]. During in-situ battery analysis, the working and counter electrodes are connected with a potentiostat, which allows to monitor structural changes during charging and discharging of the battery [129, 133]. The sample is placed in a special aluminum set-up with a pin hole of 14 µm diameter. In contrast to for example Transmission Electron Microscopy, for TXM no special preparation technique is necessary to thin the samples in order to be electron transparent. The only modification is a specially designed sample set-up for the in-situ analysis, see chapter 3.3.

2.8.2 X-ray Diffraction (XRD)

X-ray Diffraction is a standard technique in chemistry and materials science to analyze (poly-, mono-) crystalline materials. This technique allows to determine lattice parameters and unit cell parameters of the individual atoms in the material, thickness measurements of thin films and gives a complete elemental mapping of the analyzed samples. The detailed analysis of the diffraction position and peak width allows among other things to determine the sizes of the crystals or grains. The diffraction intensity depends mostly on the thickness of the material and the atomic form factor. This form factor specifies, which hkl-planes and diffraction pattern are allowed and which of them do not appear in the diffraction pattern [134, 135, 136].

The diffraction is based on elastic and inelastic scattering of the incoming, monochromatic beam with the atoms. During inelastic scattering, the energy and momentum of the incoming electrons is transferred and leads to multi-scattering inside the material. The energy is not sufficient to leave the atom. In contrast, the electron does not change its momentum during elastic scattering. When the X-rays penetrate a parallel crystal arrangement, they get diffracted and reflected at the lattice planes obeying Bragg's reflection law. Typically, $\Theta/2\,\Theta$ scans are performed. During these scans, the incoming and reflected beams are both varied in relation to the sample surface plan, but kept equal. If the incident beam is projected through the sample, the angle between the projected direction to the sample would be as well Θ, which makes in total the $2\,\Theta$ scan [136, 134, 137]. Those angles are related to the d-spacing - the distance between the atomic planes inside a material and gives direct insight in the corresponding {hkl}-planes of the material. Problems with the analysis are mostly subjected to the misalignment of the sample before diffraction. This leads to a peak shift in the diffraction pattern and it may accordingly lead to a different elemental analysis. Another sort of problem is related to the Lorentz factor, polarization factor and absorption factor, which lead to a variation of the diffraction intensity [138].

The XRD patterns in this thesis are recorded in cooperation with the Stanford Synchrotron Radiation Laboratory (SSRL, beam line 11-3), Stanford University, CA, USA. In contrast to standard XRD technique, the spot size is very small with $1.5 \times 1.5\,cm$ with a high energy of $12.7\,keV$. This small spot size is necessary to investigate small areas of nano-structured areas. Reference patterns are performed with Seifert XRD 3000 PTS 1997.

2.8.3 Raman and IR-Spectroscopy

Raman as well as IR-spectroscopy are both based on molecular vibrations and therefore will be discussed in the same section. Both techniques are mainly used in chemistry to detect known and unknown species in a material, to investigate the type of bond and its bond strength as well as to analyze the influence of the concentration of a solution on the variation in a material. Not every material is Raman active and at the same time IR active. Therefore, it is necessary to clarify and set conditions, when a molecule or in general a material is either Raman or IR active. For IR spectroscopy, dipole moments have to be induced and changed. A Raman material has to change its polarization [139, 140, 141, 142]. A molecule has translational and rotational degrees of freedom, but the bonds in between can also bend or stretch giving rise to the vibrational modes. In order that a given vibration contributes to the IR (absorption) spectrum, those vibrations have to induce an asymmetric configuration, leading to a change in a dipole moment (considering the difference in electronegativity of the molecules involved). For example, double bonds between C and O will lead to a high absorption peak because the high electronegativity difference leads to stretching of the bond and therefore to a dipole change. In, on the other hand, a linear or symmetry bond (like C-C bond), it is rather weak in IR because no dipole can be induced. An electrical field will displace the positive and negative charges and induces polarization. If this happens, the molecule is Raman active [143, 144]. Infrared Spectroscopy (IR) is based on the absorption of photons, which induces vibrations. The Raman spectroscopy is based on the scattering of photons, where the incoming photon is in-elastically scattered and transfers the energy and momentum. The energy from the incoming and scattered photon is different. Those energy differences induce vibrational transitions inside the material.

Raman analysis uses a monochromatic laser, whereas IR spectroscopy uses a polychromatic laser in the 10^3 - 10^5 nm range. The IR measurement relies on the principle of the attenuated total reflectance (ATR), to measure solids or liquids in chemistry. In contrast, transmission IR measurements are limited for thick samples because the beam has to be transmitted completely through the sample. Therefore, the sample has to be specially modified and prepared to actually to be analyze the sample. The ATR sampling method is beneficial because the (standard) sample does not need any special preparation. The most important requirement for a good measurement is a good contact i.e. interface between sample and the ATR crystal of high refractive index. This is necessary because the incident beam is guided into the ATR crystal and is subjected to multiple reflections. In general, Snell's law has to be considered. If an incident beam of a certain angle travels through a medium with the refractive index n_1 and hits the interface between the two media of different refractive indizes, the beam gets refracted and travels in the second medium with a different angle. If, on the other hand, the incident angle is too steep, it leads to a total reflection inside the material, where the beam cannot pass the interface. This is also the principle of the ATR. The incident beam cannot penetrate into the sampling medium, but gets refracted internally. Although the wave cannot penetrate, an electrical field (i.e. evanescent wave and field) develops at the interface of the two media, underneath the sample (directed towards the sample at the contact). This field cannot penetrate the sample completely, but exists only at the interface. The sample absorbs specific energy of the incident infrared spectrum, which changes the electrical field and wave at the interface. This change is transferred back inside the crystal. The multiple refracted infrared beam is then guided through the crystal towards a detector. The detector records the changes in the absorbed spectrum [145, 146, 147].

Chapter 3

Experimental Details

For preparing battery anodes based on silicon microwires, fundamental aspects have to be understood and applied in order to achieve large scale, homogeneously etched anodes which are (mechanically) stable for long term applications. The fabrication of the wires include the pre-structuring, the macropore etching and the chemical over-etching. The wires could, in general, be used for all kinds of applications like filters, drug delivery in medicine etc. For the application in this thesis, the etching of Si is the first step in the process line. In order to fully characterize the wires, different kind of wires in different electrolytes are fabricated and especially optimized with respect to the I(t) profile for the macropore formation. Battery application or electrical application in general, need electrical contacting. For the anode side, copper is galvanically deposited between the silicon wires. The galvanic deposition is discussed for small and large samples. The up-scaling of the anode area was successfully done in previous studies. Nevertheless, the only part missing was the galvanic copper deposition for large area samples, which has been realized in this thesis and is under patent protection. In order to fully characterize the silicon wires, they are tested as anodes in different kind of battery set-ups which are specially designed for different characterization methods like cyclic voltammetry, impedance spectroscopy, cycling tests but also for (in-situ and ex-situ) characterizations using synchrotron radiation.

3.1 Silicon microwire fabrication

Silicon microwires are fabricated in several (etching) steps. The starting point of the process is the pre-structuring to have a highly-ordered lattice structure with precise distance all over a 6' p-doped Silicon wafer with a resistance of 15 - 25 Ω*cm and a surface orientation of (100). By photolithography, a simply cubic pattern of circles with a diameter of 1.5 µm, and a pitch distance of 3 µm is transferred to the wafer, 45 degree to the flat (Figure 3.1 a). Two steps in the following processing will not work, if inhomogeneities show up:

1. the macropore etching itself, which is controlled by the over all current, and thus,
2. the detachment of the finished microwire array from the substrate, which will fail, when in some parts on the wafer no pyramids are formed or their depths is reduced.

If the lithography does not work "close to perfect", sometimes many steps later on in the anode fabrication will not be successful. Consequently, the array is not mechanically stable and it might be that the wires do not have their proposed length. Since for a contact lithography using these sizes of the mask, 1.5 µm windows are already principally challenging, a cleaning of the mask is indispensable to guarantee a free-standing wire array.

The lithography step is a positive step where the exposed areas (the photosensitive compound in the resist) are soluble in the developer. For the positive resits, the pattern on the mask is the same pattern as on the photoresist (and with that on the wafer). To obtain the desired structure, a 1 µm thick layer of a positive photoresist AZ 6612 (Microchemicals) is deposited at 4000 rpm in 30 seconds. The volatile components of the photoresist are removed during the pre-baking at 110 °C for two minutes. To achieve a high resolution for the small spot size of 1 µm for a 6’ wafer, the sample is exposed to the UV light (UV characteristic at 405 nm at vacuum contact. In this contact, there is hardly any alignment gap (10 µm) between the wafer and the mask. The sample holder consisting of a vacuum chuck with additional sealings provides an internal vacuum. The wafer is directly pressed onto the mask. Different exposure modes like hard or soft contact have a minimal alignment gap of 100 µm in between and lack of resolution at this spot size. The exposure takes only 4 seconds. This value is calibrated and calculated by the dosage of the photoresist and the UV intensity distribution of the mask aligner Suess Microtech MA6. The soluble parts of the photoresist are removed during the development process. The adhesion of the structured photoresist with the pattern from the mask is enhanced by a post-baking step at 125 °C.

3.1.1 Dry and wet chemical etching

The pre-structuring continues with the dry chemical etching process. This etching step is a pattern transfer process. In comparison to wet chemical etching techniques, no undercutting between the photoresist and the silicon takes place. The reactive ion etching process is a plasma etch process consisting of two parallel processes: the physical etching by ion bombardment i.e. collision in SF_6 atmosphere and the chemical dissolution of the photoresist in Ar atmosphere. Both gases are initiated in an optimized ratio of 2.5 SF_6 to 7 Ar for 3 minutes. If the etching is not homogeneous, the photoresist delaminates from the silicon wafer at the edges. The pattern transfer is performed at high power of 300 W and a bias voltage of 54 V. The high bias voltage results in a high energetic ion bombardment on the wafer. During this process, small nearly spherical holes are etched into the circles with a depth of 1 µm. The small holes are the starting points for the pyramid etching in a wet chemical etching process (Figure 3.1 b). In order to have a homogeneous etching, the wafer is warmed up in a solution of pure deionized water at 50 °C and then transferred to the passivation solution. The deionized water is necessary to avoid any surface contamination The passivation step is done at 50 °C in a 5 wt. % of polyethylene glycole (PEG) solution for 30 minutes. In a 3.5 M KOH solution with 1 wt. % PEG, pyramids are etched inside the wafer at 50 °C for 45 minutes [148, 41, 125]. During silicon dissolution, hydrogen evolves in form of small bubbles. Those bubbles act like a passivation layer on the surface. Underneath those bubbles, the dissolution rate is reduced which can lead to an inhomogeneous pyramid etching. In order to prevent this, a pneumatic tilting table is connected to a hotplate. During the etching, this tilting table guarantees enhanced electrolyte flow over the surface. It produces an electrolyte wave that destroys any bubbles that form in an up and down movement. Additionally, the etching solution is constantly stirred. Figure 3.1 shows a top view of the resulting structure. The amount of PEG in the chemical etching solution is high. After the etching the PEG sticks to the surface of the wafer. The PEG coats the surface of the wafer completely. Therefore, several cleaning steps for the surface are applied. During two temperature controlled cleaning solutions - one at 50 °C and one 25 °C - the PEG is removed from the surface. The final inverted pyramids have a sharp tip. Due to high electrical fields around the sharp tip, the perfect starting point for the macropore etching as described in section 2.1. The formation of the etch pits depends on the crystal anisotropy, described in section 2.2.

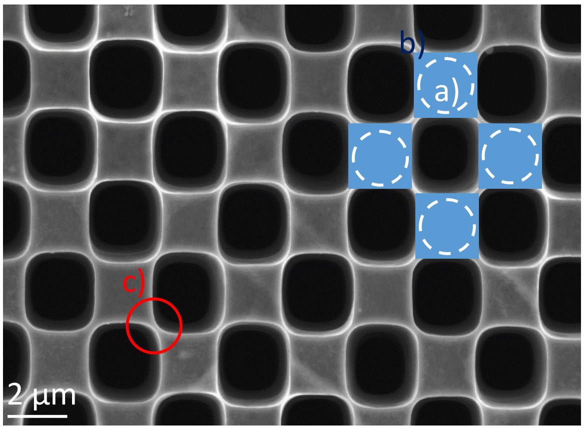

Figure 3.1: Top-view of silicon structure after complete pre-structuring (including macropore etching). a) The circles indicate the simple cubic lithography structure, which turns to squares during the KOH etching in b)., c) After the pore etching, the pore walls are dissolved, in order to obtain the wire arrays.

3.1.2 Electrochemical macropore etching

3.1.2.1 Electrochemical etching cell

The electrochemical etching of the macropores is performed in a four-electrode cell setup. The cell is made of PTFE, a chemically inert material which is not effected by the hydrofluoric acid (HF) in the electrolyte. The etching cell has four electrodes. The working electrode (WE) is the p-doped Si sample which is directly electrically connected to an aluminum stripe. The silicon wafers have a conductive aluminum backside. The aluminum side is coated with a paste - a standard solar cell coating step known as AluBSF, performed at ISFH using the standard technology for p-type solar cell metallization. The decisive part in forming a good (ohmic) contact between the aluminum and the silicon is a high temperature sintering step at 900 °C. Figure 3.2 shows the electrochemical etching cell with its connections. A reference electrode (REF) is placed from the electrolyte close to the silicon surface, without touching it. The REF electrode is a non-conducting Pt wire where hardly any current is flowing. The Pt wire as reference electrode balances and levels the measured potential. Using a different kind of reference electrode would produce large currents, which would disturb the macropore etching itself. The counter electrode (CE) is placed far away from the sample. This electrode is woven like a net of non-conductive Pt wires. The last electrode is the sense electrode (SE). This electrode compensates the voltage losses which occur over the electrolyte, the electrical connections between the potentiostat and

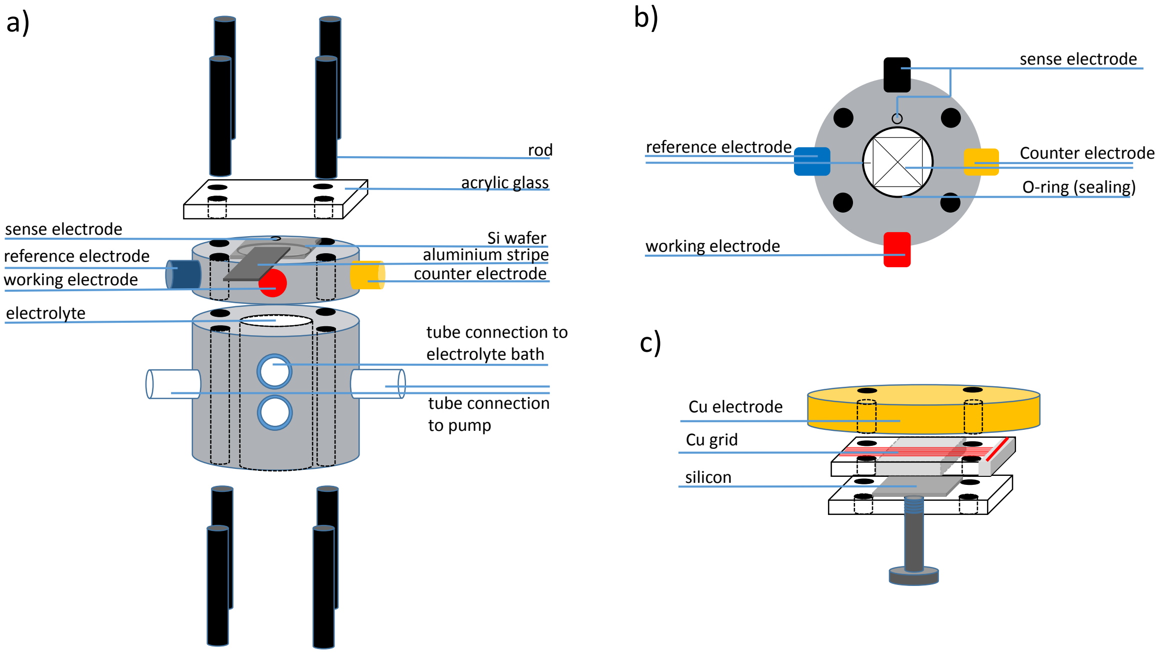

Figure 3.2: Four-electrode set-up for the electrochemical etching cell. The four electrodes connect the silicon sample (a-b), which is placed with the pre-structured side on the orifice for a good contact to the electrolyte. c) For the galvanic deposition, the etching cell is modified by the copper electrode and additional copper grids, which act as working and counter electrodes by simply depositing copper on copper.

the electrochemical etching cell. It separates the voltage from the current measurement. The silicon sample is placed with its pre-structured surface on top of on orifice, an opening to the electrolyte bath. In order to maintain a good adhesion and a minimum electrolyte leakage, an O-ring sealing of a diameter of 1 cm is placed in between. For the etching, the electrochemical cell is turned by 180 degree to obtain a continuous and homogeneous electrolyte contact towards the sample. The electrochemical etching cell is connected via (chemically resistant) tubes to a microprocessor controlled peristaltic pump which controls the electrolyte flow direction and allows to pump the electrolyte from the cell back into the electrolyte bath. The electrolyte bath is made of a double walled PTFE tank. The electrolyte bath and the etching cell are in two independent circulations. The bath is temperature controlled by additional Peltier elements inside the electrolyte bath. The Peltier element is connected to the potentiostat (galvanostat) developed by ET & TE GmbH. In addition, the etching cells with their four electrodes is connected and controlled by the potentiostat, whereas the etching profiles as well as the temperature are adjusted by the software SiPor.

3.1.2.2 Etch parameters & Electrolytes

Macropore etching in n-doped Si is well understood and the pore geometry can be adjusted by backside-illumination/current-density modulation. Nevertheless, etching in p-doped silicon, which is used in this thesis, is still investigated. Therefore, the choice of electrolyte is crucial and discussed here also in detail. The electrolyte is responsible for the selectivity of dissolution and pore diameter modulation. The benefit of p-doped silicon lies also in the price for possible up-scaling of the battery production. As indicated in the introduction (see chapter 1), solar cell silicon could be used with a possible price reduction by a factor of three for the complete battery.

As far as pore diameter modulation is concerned, it is the most crucial part for a free-standing microstructure. The pores etched in this thesis are based on two different types of electrolytes, taking advantage of the individual prospects and further understanding of the pore modulations. The role of pore modulation, when creating free-standing anodes based on pores and wires, is important, because a diameter variation of the pores act as a) diffusion layer stop for galvanic current collector deposition, b) mechanical support to allow free-standing microstructures, without the help of any precursor material and c) as a releasing agent to remove the finished electrode from the substrate. This section emphasizes the dependency of the current density modulation in p-doped silicon on the electrolyte composition and on the diameter variation. The basic principle behind macropore etching is already described in section 2.1, thus being the pore wall passivation as well as the higher dissolution rate at the pore tip [40, 39, 35]. Anyhow, achieving these advanced pore diameter as well as length variations for the intended application needs further discussion about the electrolyte composition.

Because the dissolution current has to be larger at the pore tip compared to the walls, the walls have to be passivated in order for a pore to grow deep with a high dissolution rate. With an increase in HF concentration it is possible to achieve high etching rates with high current densities. Nevertheless, this will lead to an unstable pore growth. Another contribution is the enhanced dissolution rate of the solvents which might lead to decomposition reactions inside the electrolyte [40, 39, 41]. Therefore, the HF concentration in both electrolytes in this thesis is reduced to only 12 wt. % HF (45 %).

a) *mixed-aqueous electrolyte*: The pores for the paste electrodes are etched in an aqueous electrolytes. The benefit of mixed aqueous electrolytes is a higher dissolution rate, based on silicon oxide formation, which reduce the etching time for the wires.

b) *organic (water-free) electrolyte*: The pores for the array configuration are etched in a pure, organic electrolyte. The advantage of pure organic electrolytes is the controlled diffusion limitation allowing long pores and enhanced pore modulation.

The mixed aqueous electrolyte consists of 6 wt. % HF in a dimethyl formamide (DMF) and deionized water solution with 2.5 g of PEG (M 3360 g/mol). The water in the solution oxidizes the pore walls and forms SiO_2, increasing the enhanced oxidization power. The added HF dissolves the SiO_2 and the reaction proceeds faster. This facilitates the electrochemical but also the following chemical etching step. The etching is temperature controlled at 18 °C. In comparison to the etching performed in organic electrolytes, here, the enhanced current burst leads to an increase in diameter during the etching process i.e. to continuous pore wall dissolution and increase in pore diameter. During this study, etch profiles in aqueous electrolytes are modified so that the pores have a constant diameter with bulging at the top and bottom part of the pore, for different lengths. Those presented profiles in Figure 3.3 A are typical examples, optimized for paste electrodes and show significant differences compared to pores etched in organic electrolytes. The direct comparison of both electrolytes in Figure 3.3 B indicates the change in the profiles, also in regards of the application.

Figure 3.3 A shows exemplary the etching profile for macropores with 60 µm lengths. The small 3 mA current at the beginning of the experiment and the correspondingly small applied voltage only starts the Si-dissolution at the tips of the inverted pyramids (the etch pits), i.e. allowing stable pore nucleation. After the first nucleation, the current increases to 19 mA. Macropores with length scales from 35 µm up to 75 µm are produced as well. Due to higher dissolution rates, the current profile has to be modulated to keep the diameter constant. This is implemented by additional constant steps at 9.3 mA for one minute in the reverse and forward current step. The pore modulation is done at two steps along the pore length, always indicated by constant current steps. The schematic indicates the pore diameter modulated. These are called stabilization planes. As the pore walls are dissolved in the subsequent etching step, the remaining silicon keeps the array standing, leading to a mechanical stable structure. For varying the lengths of the macropores, the complete profile has to be adapted in certain parts to a) keep the diameter constant along the enhanced length of the pore and b) change the time of the etching accordingly (see Figure 3.3 A a). As a summary for the length variation (deeper pores), the time for the constant

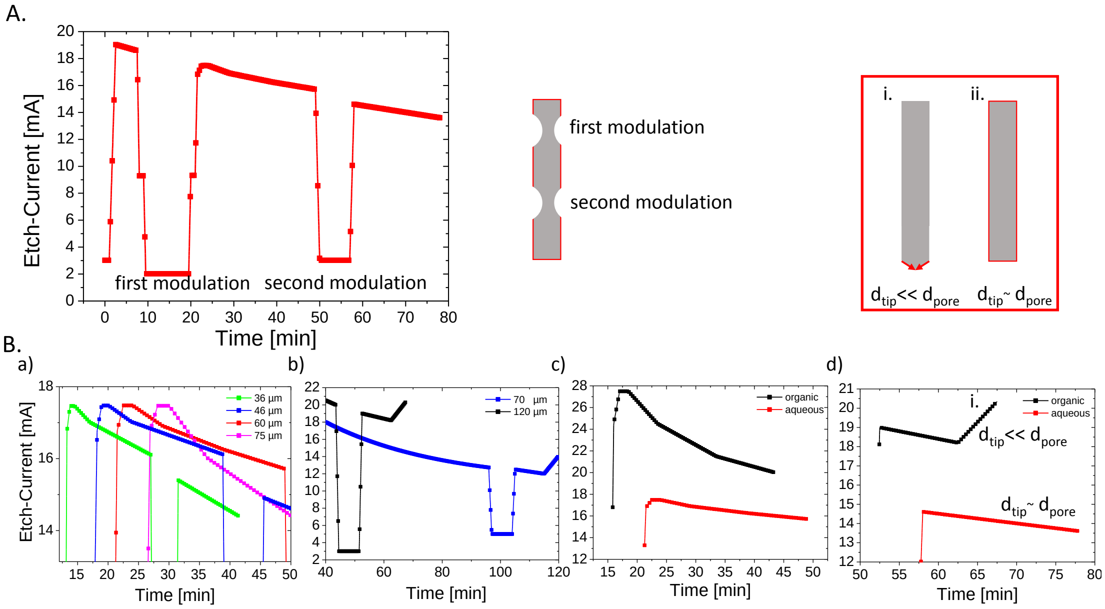

Figure 3.3: Pore modulation in p-doped silicon during macropore etching depending on the type of electrolyte. A. Typical etch current profile with two diameter modulations. B. Macropore modulation in length a-b) as well as in diameter for the desired application c-d). The specific comparison of different parts along the profile indicate the complexity of the macropore etching [125, 33, 149].

steps during the pore modulation is increased, to allow still efficient silicon dissolution. If this part is not adjusted correctly, the diameter of the pore is not constant but reduces from top to bottom of the pore. With increasing pore length, the etching becomes more difficult due to diffusion limitations.

For the macropore etching, precise temperature control of the electrolyte is necessary. The etching rate scales with the Boltzmann constant and the temperature. Thus, an increase in temperature during etching will generate an increase in dissolution rate. As a consequence, it will lead to a change in the pore geometry. Mostly, Joule heat is present during electrochemical etching process, which scales directly with the time and current density. Meaning, for very long pores or larger etching areas, this effect is even worse and needs additional external cooling. Those considerations have to be taken into account, during up-scaling of the complete anode. An etching cell needs to be constructed in such a way, that the electrolyte flowing across the surface area has a constant temperature and the generated Joule heat is discharged immediately. Because of this, an active feedback control is implemented with additional temperature sensors directly at the etching cell, monitoring the complete electrolyte flow from the electrolyte tank to the etching cell. In the case of organic electrolytes, the temperature control is even more important because organic electrolytes have a small heat capacity. Which means that even small amounts of generated Joule heat will lead to a large temperature increase of the electrolyte. Because this temperature cannot be dissipated accordingly, it will lead to an increase in the etching rate. Another important factor of the electrolyte is the added PEG. The role of the PEG is essential for the chemistry because it locally slows down the diffusion. It is a self-supporting process because a reduced diffusion slows down the etching rate locally, especially responsible for the pore modulation. The viscosity increase of the electrolyte due to the added polymer enhances the diffusion limitation, which is essential in the pore modulation of p-doped silicon. Whereas in n-doped silicon, it is easier to locally modulate the pore diameter due to the generation of electron-hole pairs by modulation of illumination or sinodical current density, for p-doped silicon it can only be achieved by deliberately changing the kinetics during etching by viscosity increase. The reaction rate is directly proportional to the diffusion coefficient, which is decreased in this case. By adding PEG to the electrolyte, the viscosity of the pure organic electrolyte increases drastically. For the mixed aqueous solution, the PEG is dissolved and the viscosity increase is reduced. Whereas in aqueous solutions, the main contribution to the pore growth is the indirect pore wall dissolution due to the oxide formation, the oxidization power in organic solvents is almost negligible. Therefore another contribution to the pore wall passivation is needed to have a controlled pore modulation. On the one hand, the pore walls are H-terminated, but the polymeric chains of the PEG agglomerate at the pore walls and form a passivation layer. Inside the electrolyte, they increase the viscosity. Because the viscosity is anti-proportional to the diffusion coefficient, the relationship is perfectly clear, leading to diffusion limitation. Consequently, the fluorine ions in electrolyte cannot dissolve directly the pore walls with the same speed as without the PEG, having a more precise control of the pore diameter [150, 41, 151].

The organic (water-free) electrolyte contains 12 wt. % HF in a pure DMF solution with 2 g of PEG. The etching is done at 17 °C. Figure 3.3 B b-d) shows the difference in pores, compared to the aqueous electrolyte. The profile is different at the pore tip. While the current is reduced and has a steep slope for the aqueous etching, the etch current profile shows an increase again in the end. The adjacent schematic indicates the influence of this diameter decrease at the pore tip. This is the biggest difference between both pore geometries, depending on the application. The diameter at the pore tip is very narrow compared to the bulk pore, allowing an easy detachment of the wire array from the substrate. If, on the other hand, the diameter at the tip is still the same as the pore, a complete detachment will be difficult without partial destruction of the wire. Second, pore modulation especially at deeper pores lead to the stabilizing planes, necessary to keep the wire array standing.

3.1.3 Chemical etching

During the chemical etching, the pore walls are dissolved and determine the wire thickness. The complete process is optimized to produce different wire thicknesses in order to analyze and demonstrate the size influence on the cycling potential as seen in Figure 3.4.

Prior to the chemical etching, the silicon sample is immersed in a 0.015 M aqueous PEG solution for thirty minutes. PEG enhances the viscosity of the electrolyte and locally at the pore walls. As a consequence, the etching process is kinetically limited leading to an interface passivation at the pore walls. This process enhances the selectivity of the etching. Without this additional step, the subsequent chemical etching would not be homogeneous at every point along the pore length and even without diameter modulation. Wet-chemical etching of silicon is performed in an 0.08 M aqueous, alkaline KOH solution, with additional 2 wt. % of PEG with a molar mass of 3360 g/mol. The etching rate highly depends on the temperature, as described in section 2.2. Therefore, the process is performed at 50 °C. Figure 3.4 shows examples of the 70 µm long silicon wires. The SEM images indicate diameter modulations for enhanced mechanical stability of the complete wire array. Figure 3.4 a) shows in a cross-sectional view that the pore walls are completely dissolved. In Figure 3.4 d), the wire tips are illustrated for both types of etch pores. In the case of pores etched in a mixed electrolyte, the pore diameter remains constant, whereas pores etched in an organic electrolyte the diameter is reduced to a minimum, which is necessary for the successful removal of the anode from the substrate. The thickness is controlled by the time of the etching. After 30 minutes, the thickness of the wires is 1.8 µm. At even shorter etching times, the pore walls are not completely removed. The wires are not completely formed yet. On the other hand, longer etching times have severe consequences on the mechanical stability of the wires because the diameter at the wire tips, illustrated in Figure 3.4 d) 3.3, would be drastically reduced. The wires would collapse and not remain standing. The thicknesses analyzed in this thesis scale with time ranging from 30-60 minutes corresponding to a thickness range between

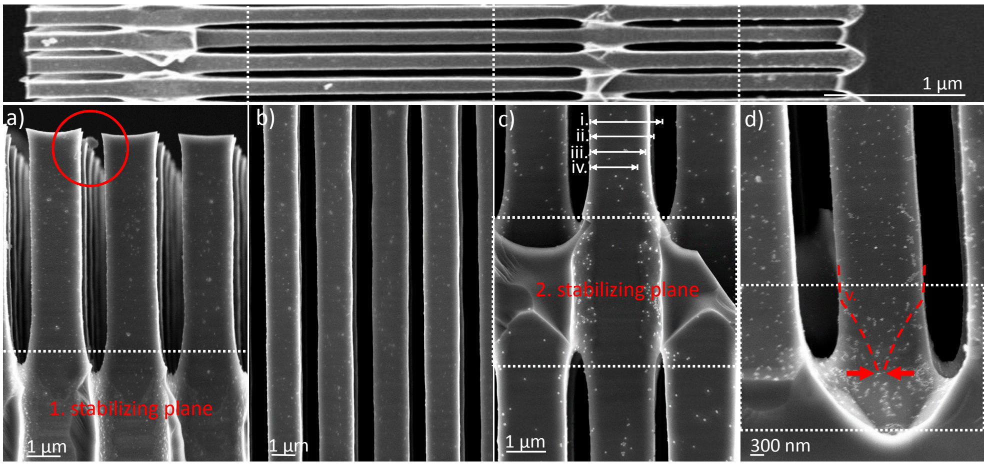

Figure 3.4: Anisotropic wet-chemical over-etching of macropores to obtain silicon wires. Four different SEM images show the individual consequences of the pore modulation on the wire geometry during macropore etching. The images indicate a) the top part with the first stabilizing plane, b) the length of the wire in the middle, c) the second stabilizing plane with the four different thicknesses and d) the individual diameter modulation at the pore tips for the Si-arrays. This modulation is also indicated in Figure 3.3 B d) and shows the specific differences in the current modulation. As a comparison, the complete wire lengths (70 µm) is shown above.

1.8 µm, 1.6 µm, 1.4 µm and 1.2 µm. The electrolyte during macropore etching shows its consequences during chemical etching. The enhanced oxidation power due to the additional water inside the electrolyte enhances the dissolution rate due to the formed silicon dioxide [151]. This layer does not function as a dielectric, but acts as a sacrificial and accelerating layer. As a consequence, the pore wall dissolution is faster and results already after thirty minutes in 1.8 µm thick wires. Anyhow, pores from organic electrolytes have to be etched half an hour longer to result in the same wire thickness, as for the mixed electrolyte.

3.2 Galvanic Cu deposition

For a good electrical and mechanical contact, all Si wires within the arrays, are contacted with galvanically, deposited Cu in the top region of the microwire arrays, as outlined in Figure 3.5. The advantage of galvanic copper deposition, compared to CVD or other sputter deposition techniques, is that the copper can be deposited between the structure with a high aspect ratio. For example, during sputter deposition, as indicated in Figure 3.5 c), a thin layer of copper is deposited mostly on top of the

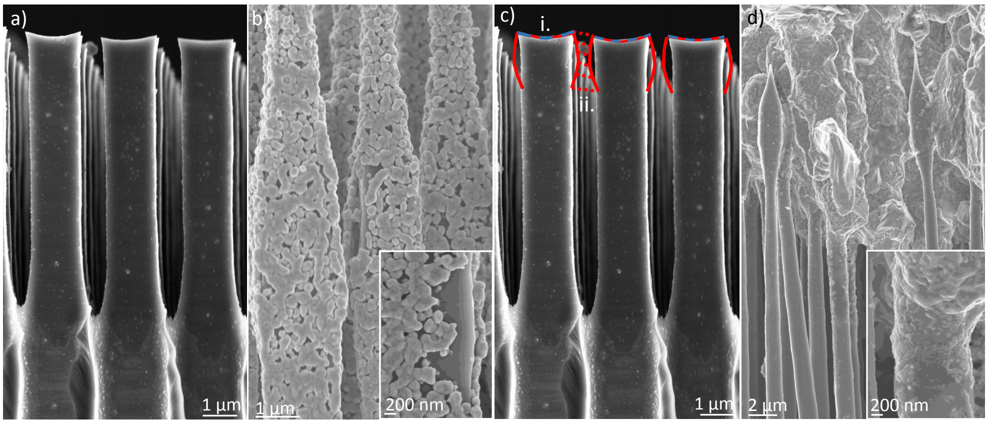

Figure 3.5: Two-step galvanic metallization process. After the chemical etching process a), the two step copper deposition includes b) a chemical copper deposition step, where a thin seed-layer is deposited on top and along the wires. The inset shows how the layer grows around the wires. c) The schematic illustrates two standard deposition techniques i) evaporation and ii) sputter deposition, in order to emphasize the need of galvanic metallization. d) A thick current collector is integrated in between the wires, enabling a good mechanical stability of the complete anode.

wire. The schematic shows the copper deposition techniques following the chemical over-etching, emphasizing the array in the background. In addition, it is possible that the copper deposits on the first 1 µm of the wire walls. But due to the edge coverage of the copper from both sides between the wires, it only leads to a reduction of the hole and a closing of the possible deposition hole. The copper will not penetrate further between the wires. Standard evaporation techniques are even worse because they would only follow the contours of the wires, forming a thin layer on top, but would never penetrate in between the wires.

Nevertheless, this is crucial for this application. As mentioned, the wires are formed still attached to the substrate material. For the wire preparation no precursor material is necessary because the complete process is a top-down process. In order to have the current collector deposition in a cost-effective manner (even scale invariant), the process is designed in that way that it is directly deposited on the substrate material with the etched wires (without an additional transfer step before the galvanic). Consequently, the current collector has to be electrically conductive, but calls for good mechanical properties. In contrast to the galvanic deposition, the evaporation or sputter deposition techniques do not allow good mechanical properties to remove 70 µm (and even longer) deep wires with a high aspect ratio over large areas. Therefore, a silicon/copper contact is formed in between the individual wires, enabling a good mechanical stability to remove the complete wire array from the silicon substrate with enough force. If this interface is weak, like for small thicknesses or in the case of CVD or sputter deposition, it would lead to a simple layer removal of copper without the wires. The copper is integrated in between the wires up to 12 µm (Figure 3.5 d)). The current collector has a thickness of about 35 to 45 µm. Due to the fact that the wires have a minimal lengths of 70 µm, the force to detach this layer (in a transfer process) has to be strong. Otherwise, only the thin copper layer is removed but the wires will not stick to it. Of course, this good silicon/copper interface influences the ohmic contact as well because it defines drastically the ohmic resistance losses inside the battery.

3.2.1 Chemical Cu deposition

The chemical Cu deposition (Figure 3.5 b) is necessary to enhance the adhesion between the silicon wafer and the thick copper layer, see Figure 3.5 b). It is done in a 2.1 wt. % aqueous HF solution with 1.9 wt. % of copper(II)sulfate at 50 °C as seed layer for five minutes [149, 33, 59]. Constant stirring during the deposition enables a continuous electrolyte flow over the sample. In this step, 100 nm of copper are deposited homogeneously on the sample. The reaction needs elevated temperature control because it needs activation energy for the oxidation and reduction steps. Increasing the deposition time to longer than five minutes will lead to a delamination of the already formed layers and re-deposition on top of the previous layers due to the continuously increasing layer thickness. The seed layer is not homogeneous anymore.

3.2.2 Electrochemical Cu deposition

To achieve a thick Cu layer, a galvanic deposition step is used. It is performed at constant current of 35 mA/cm^2 in an aqueous 17.7 wt. % sulfuric acid solution with additional 2.5 wt. % copper(II)sulfate, designed for a pH-value between 9 and 10 (see 2.4). For improving the copper film homogeneity, the process is temperature controlled at 22 °C (see 2.4). The resulting voltage lies in the region between 0.2-0.3 V. If the voltage is too high, additional deposition is taking place for example at the backside of the sample or at the assembly holders. As discussed in 2.3.3, the deposition needs a counter electrode and a connection to the working electrode. For this set-up, a Cu grid is used as counter electrode (under cathodic bias), as shown in Figure 3.2 c). The sample is placed on the copper grid made of parallel aligned and fixed copper wires. During deposition, a copper film is formed directly on the wires i.e. electroplated. Due to the contact between the copper grid and the silicon sample and the direct deposition on the grid, a copper film is formed on the silicon substrate as well. Copper is deposited on every wire of the sacrificial grid, increasing locally the thickness of the copper from both sides between the grid wires. At some point, the layers form interconnections and a complete layer on the silicon substrate. As mentioned, the grid acts as sacrificial electrode to enhance the deposition rate and improve the film homogeneity on the silicon because direct deposition is complicated due to adhesion loss. Therefore, the silicon has a seed layer, which allows for the copper film i.e. interconnections between the grid wires to stick on the silicon. SEM images indicate that the deposition starts from small islands or agglomerations, which allows for a high aspect ratio deposition, even at these dimensions (pitch size of 1 µm and 12 µm in z-direction). This adhesion allows the deposited copper to integrate between the wires and the layer-transfer process works. As mentioned before, the current collector has to withstand forces in order to remove both the copper with the integrated wires completely. Therefore, the thickness of the collector is optimized to be in the range between 35 µm and 45 µm. The deposition rate is 62.5 nm/minute.

3.2.3 Chemical Cu dissolution

For some applications or characterization techniques like in-situ XRD or TEM analysis, the thickness of the current collector is too large to be electron transparent. Therefore, the thickness has to be reduced in a subsequent step by a factor of five (70 % of the thickness is etched off). This dissolution step can be considered as an additional etching step. Therefore, it is necessary to protect the already finished silicon wires. They are covered with a typical photoresist ARP 3100, which is chemically stable in this chemistry. The photoresist is dried at 120 °C for 30 minutes prior to etching. As previously motivated, the removal of the complete stack from the substrate needs force, which cannot be provided by thin (5 µm - 10 µm) copper layers. Consequently, the thick copper layer is dissolved by chemical dissolution in an aqueous 1 wt. % sodiumpersulfate solution at 50 °C. The weight loss is constantly monitored during the chemical dissolution, taking into account the additional weight of the photoresist. The remaining photoresist is subsequently removed.

3.2.4 Large area metallization via gel matrix

The above described deposition set-up and processes are optimized for samples up to a 2 cm^2 area. For larger areas a different approach has been developed. This process is aimed for scale-invariant processing suitable for large area contacting of up-scaled silicon wire etching. With larger contacting area, the lateral potential differences across this area increase. Furthermore, the applied currents increase proportional to the diameter. For small samples with 1 cm^2 the applied current is 35 mA. (For large areas the current would be in the order of 2 to 3 A.)
The idea is to have a dried polymeric matrix, where the copper deposition can be initiated by contacting the silicon wafer and the matrix with water. As the chemistry for the copper deposition is already embedded and dried in the matrix, it is an ideal current collector matrix for role-by-role processing. As pre-defined nucleation points, copper filaments are incorporated insie the matrix, where the copper deposition starts. As the layer thickness grows, the film spreads across larger area and a closed copper film results (Figure 3.6). The size of each template can easily be 20 cm × 20 cm or even larger. By just placing a dry template on a top of a Si wire array and adding water (so-called layer-transfer-process), a Cu-seed layer and a close connection between the

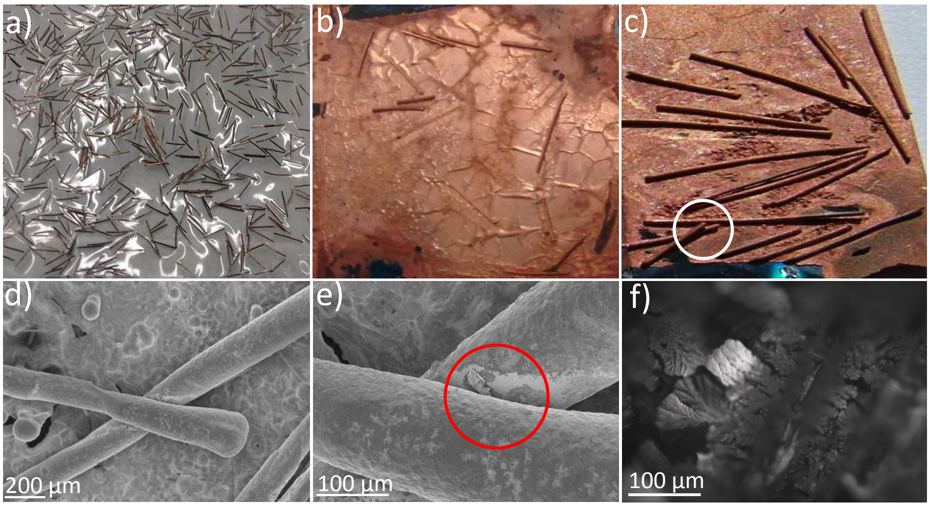

Figure 3.6: Scale-invariant copper metallization initiated in gel matrix. The metallization requires a gel that is chemically stable in HF and mechanically flexible to allow a layer-transfer process in the dry state. a) Dried gelatin matrix with embedded copper filaments, b) Partially dissolved gelatin matrix after chemical copper deposition, c) Final metallization after electrochemical deposition, d-e) SEM images of the metallization directly at the interconnections. f) SEM image of the dendritic growth inside gelatin.

Cu network and the Si wire array is formed due to two reasons: a) the wet hair effect, b) incorporation of the necessary chemistry i.e. Cu-sulfate in the gel. This approach is obviously applicable to large samples, can be useful e.g. to from metallization on solar cells as well and therefore has been patented (WO2016/037610 A1 - 17.03.2016).

In detail, the copper deposition can be initiated via a gel matrix with embedded copper filaments [152]. As illustrated in Figure 3.6, several templates have been produced, varying in a) number and length of copper filaments, b) gel type and c) chemical composition. Figure 3.6 a) shows a dried gel matrix made of gelatine. The advantage of these gels is their swelling and drying process. The hydrogels swell upon contact with water or other solvents. Upon drying, the water evaporates leaving a flexible gel membrane behind (in the dry state), keeping the incorporated filaments in place. They replace the copper grid, described in 3.2.2. The copper filaments are arranged in the dry state in order to touch each other at small, local interconnection points. The purpose of those filaments is to act as nucleation points for the copper deposition, see Figure 3.6 b-e). As the deposition proceeds, the copper thickness on and around the filaments increases leading to a homogeneous layer around each filament. The filaments should be arranged in that way that the next filament is in direct contact. This allows the copper which is formed around each filament to touch forming an homogeneous layer on the silicon substrate. In this way, the filaments form a percolating network. Nevertheless, the correct order of filaments is essential. If many filaments overlap, the copper thickness increases locally on the filaments (in z-direction), but no film forms on the silicon surface (x-y-plane). The size, geometry and thickness of the filaments has been evaluated as well and found to be crucial for the copper deposition i.e. nucleation center. Thin filaments have the disadvantage that only thin copper layers are formed (in the nanometer range). Hence, those filaments predominantly form islands and could not be dispersed individually, leading to island growth and not to layer growth. Optimal filament thickness was found to be at 70 µm with lengths ranging from 5 mm to 1 cm. The SEM images in Figure 3.6 d-e) indicate how the copper is deposited at the filament interconnections. Focal microscopy analysis indicated the thickness increase around these interconnections, acting as film nucleation. A network of these interconnections is best and successfully implemented by using pure electrostatics to arrange the filaments in a correct order.

In order to take advantage of the wet-hair effect of the gel, the gel should re-solve in contact with water, but not completely dissolve or decompose. In addition, it should be chemically inert or stable enough to maintain the mechanical stability towards the filaments and the silicon substrate. Accordingly, different gel types and compositions are evaluated in Table 3.1.

The evaluation showed that the water content is crucial and influences the flexibility and layer thickness of the resulting dried gel matrix. If the water content is too high, the membrane swells too much and is too flexible after drying or even leaving residual water in the matrix hindering the drying process. But the layer transfer process relies on a membrane which is completely dry (the water content is nearly zero after drying). It is even possible to incorporate the same, necessary chemistry for the chemical deposition like $CuSO_4$ inside the gel, thus initiating the copper deposition by only wetting the matrix. Hydrogels are stable in HF environment, enabling even the incorporation of fluorine ions inside the matrix. This allows to store and initiate the chemical deposition in-situ by water contact. During this process, the fluorine ions adsorb at the copper filaments and a thin copper forms, while swelling again. Due to the in-situ process, large areas of dried matrices with incorporated chemistry can be produced without an additional chemical deposition step like before. The amount of $CuSO_4$ was not crucial for the deposition process and the same amount, as for the standard chemical copper deposition, could be maintained. Among the proposed hydrogels in Table 3.1, gelatine is the most suitable candidate because a) it exhibits a high mechanical stability, but the chemical stability is limited in such a way that the layer-transfer process of the matrix with the copper is guaranteed, but the gelatin is dissolved during the electrochemcial etching process.

Gel	Gel Type	Composition (Gel:$CuSO_4$)	Water [ml]
Gelatine	Protein gel	1:2.5	4
Gelatine	Protein Gel	1:3	4
Gelatine	Protein Gel	1:5	4
Polyacrylamide	Polymer	1:2	8
Polyacrylamide	Polymer	1:4	8
Polyacrylamide	Polymer	1:5	20
Alginate	Alginic Acid	1:2	10
Alginate	Alginic Acid	2:1	20
Alginate	Alginic Acid	20:1	20

Table 3.1: Overview of gelation behavior depending on gel type.

This flexible membrane is placed on top of any silicon wafer and contacted by wetting the layer with water. Upon that contact, the membrane adheres perfectly to the wafer due to the wet-hair effect. This wet-hair effect is the advantage of this technique. Upon wetting the gel swells, but does not dissolve completely. If the chemistry for the chemical deposition is already integrated in the gel, subsequent chemical deposition is not necessary anymore. As a result, this process is cost-effective and time saving. Because the process relies purely on dry processing, the gels can be prepared and stored. Such gels with the embedded chemical components form thin copper layers and still need the electrochemistry to form thick copper layers. Anyhow, the electrochemistry takes advantage of the growth mode of copper initiated in gelatin. Upon electrochemical deposition, small dendrites grow, see Figure 3.6 f). By redirecting the dendrites, the deposition rate in gelatin is enhanced from 62.5 nm/min to 210 nm/min, reducing the total time for the metallization by a factor of four, making this process attractive for commercial or industrial applications. The dendrites do not necessarily grow perpendicular to the silicon surface, but also at very narrow angles, leaving space for the copper to grow around and on top of the dendrites, and thus, accelerating the metallization. During this deposition step, residual gel is completely dissolved.

While the chemistry is not changed, the deposition parameter are adapted to this process. It is necessary to incorporated a potentiostatic step in the beginning of the deposition. It allows to keep the filaments and the matrix in place, while immersing the set-up in the electrolyte. Without this additional step of five seconds, it might be that a mechanical separation between substrate and matrix occurs, if a water bubble remains at the interface and hinders the wet-hair effect.

3.3 Electrode fabrication

The anodes as half cells vs. Li in this thesis are tested via electro-analytical characterization methods and performance tests. In order to do that, two different anode configurations are tested throughout this work. First, paste electrodes are fabricated. These electrodes are comparable to the standard electrode fabrication process and allow to monitor the most common degradation mechanisms in this type of electrode. It allows to detect limitations of the diffusion and kinetics of the pastes. The length and thickness of the silicon wires can be deliberately adjusted by the macropore etching process. Therefore, it is not necessary to discuss any contribution to the kinetics of differently sized spherical silicon particles. But the analysis concentrates on the interaction of silicon wires with the paste due to the random distribution of the wires. Second, a freestanding array electrode structure is tested because it eliminates all the disturbing and well-known problems of pastes due to a highly-oriented silicon structure [33, 125].

Not only the performance is of interest, but also the structural change during lithiation processes is investigated within this thesis. Therefore, the anodes are characterized by ex-situ and in-situ techniques for which specially designed half cells and wire arrangements are required.

3.3.1 Si-Paste electrodes

The paste electrodes analyzed in this work have the same composition as standard graphite paste anodes, just replacing graphite by micrometer-sized Si wires [33]. On industrial scale, such pastes are transferred by roll-to-roll processes. The pastes are mixtures of two or more components casted or glued to the current collector. Silicon nano-/microparticles are mixed with a conductive additive and a binder. Conductive additives are used in this process to enhance the conductivity of the anode. Most commonly carbon black (CB), graphene, graphite etc. are used for this purpose. As the name indicates, binders have the task to bind the particles together without reacting with the active material and changing their chemical structure. During volume expansion of the anode the particles expand and contract. If the binder would not exist or withstand that in the matrix, the particles would loose their connection between each other and to the current collector [153, 154, 87, 155, 156, 157]. No percolation would exist anymore and no charges could flow. The role of the binder and its function is discussed in more detail later in chapter 4.1. Figure 3.7 shows exemplary an SEM image of the wires, embedded in the carbon black matrix. The paste electrodes based on silicon microwires for this thesis use carbon black, Super P (Sigma Aldrich) as conductive additive and carboxylmethylcellulose (CMC) as binder (if not indicated otherwise). The finished silicon microwires are scratched off from the silicon wafer substrate. The wires are mixed with carbon black in a ratio of 1 : 1 45 wt. %; the remaining 10 wt. % is the binder. A homogeneous mixing is achieved by adding 3 microdroplets of water to the paste to reduce the viscosity. The samples are casted on a 1 cm^2 area sample and dried in a vacuum oven at 75 °C over-night. If the amount of the silicon wires is increased up to 75 wt. %, the adhesion inside the paste is weak and no homogeneous film is formed. For this ratio, the amount of binder has to be increased to have a good adhesion between the particles. The increased amount of binder leads to delamination of the current collector during the

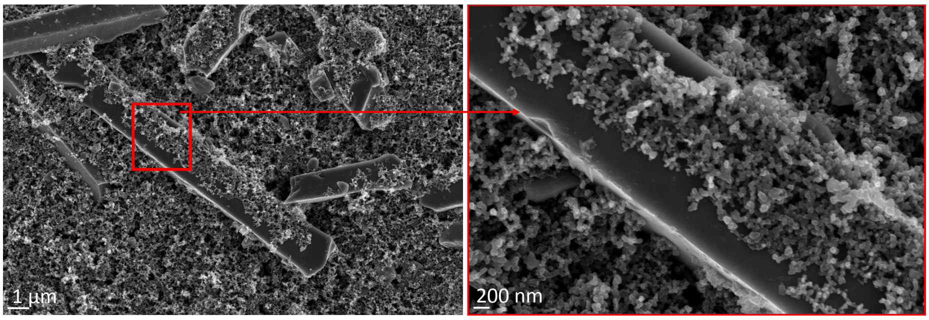

Figure 3.7: SEM image of a typical paste electrode with silicon microwires embedded in a conductive carbon matrix. These paste electrodes are similar to the commercially available graphite electrodes, just replacing the graphite with silicon. The binder is completely adsorbed on the silicon surface, therefore, it is not optically visible. Sodium residues from the cellulose (sodium cellulose) are found in the subsequent EDX analysis, which show that the binder exists and is adsorbed. Carbon black surrounds the wires and connects it from every side to the current collector [33]. The SEM image demonstrates the good quality of the binder, carbon black interaction with the silicon.

drying process. Furthermore, the conductivity of the samples is small. If on the other hand, the amount of carbon black is increased, the conductivity of the samples is high enough but the electrochemical signal is rather weak because less active material is used. Additionally, also here the amount of binder in the paste is crucial in order to avoid delamination.

3.3.2 About half-cell formation

In contrast to paste electrodes, Si-array electrodes investigated in this thesis do not need any conductive additives. As illustrated in Figures 3.3 and 3.4 the diameter at the end of the wires are very thin to facilitate the removal of the anode from the substrate after the galvanic deposition of the current collector. In order to avoid any oxygen or moisture contamination, the half-cell preparation is always performed in an Argon filled glovebox. Stainless steel housings are used as battery housings to avoid any influence of the housing material due to possible corrosion or side reactions. A glass fiber membrane (from Whatman company) is used as mechanical separator of cathode and anode electrode. The glass fiber membrane has an average pore size of 1.5 µm and a thickness of 625 µm. With those membranes, it is possible to avoid dendritic growth. The anodes are tested in half-cells. Those test cells are beneficial because only one electrode is characterized whereas the counter electrode is a well known reference: metallic lithium. During the electrochemical characterizations, every value is calibrated to lithium.

The half cells need counter, reference and working electrodes. The working electrode is the silicon anodes which is characterized. The separator is placed above that and rinsed with the battery electrolyte LP 30 from BASF. The metallic lithium (Sigma Aldrich) with a diameter of 1 cm^2 is placed on top and acts as reference and counter electrode. In the stainless steel housing additional springs increase the pressure on the electrodes to enhance the contact between them.

3.3.3 Pouch cells

In contrast to a stainless steel assembly, (standard) pouch cells are prepared with polymer pouches. Polymer pouches are polymer membranes made of polyethylene or polypropylene. The flexible arrangement allows to investigate oxygen sensitive electrodes via XRD and TXM. Compared to other pouches (which are laminated with Aluminum tape for contacting), these pouches are transparent, for the electron beam to pass through the polymer and to have a local control, where the characterization takes place. Optically and X-ray transparent polyester pouches (provided by Ampac) are used which exhibit high tensile strength and are chemically and heat resistant. Additionally, they are flexible and vacuum sealable because for standard characterizations they have to fit in preparation assemblies which are (sometimes) very small. For actual measurements, no air or humidity is allowed to come into contact with the electrodes. Otherwise they will oxidize and a high risk of explosion occurs. Pouch cells with anodes for in-situ as well as ex-situ measurements are prepared as follows (seen in Figure 3.8). The beam needs to be focused through a small hole in a sample holder exactly at the edges of the sample, which makes the preparation difficult. The small pouch cells have a length of 6 cm and a width of 4 cm. As indicated in Figure 3.8, two configurations of pouch cells are prepared/needed for the in-situ measurements. Figure 3.8 a) shows the standard way of contacting pouch cells. First of all, external negative terminals as current collectors are used for pouch cells. They form the external contact between the electrodes and the potentiostat. They have a width of 3 mm and are 60 mm long. The electrodes are placed in between the current collector tabs. On the anode side, the tabs contact the copper and on the cathode side, they are in direct contact with lithium. In order to avoid short circuits, they are not allowed to touch each other. In contrast to the "standard characterization" in chapter 4, an electron and X-ray transparent cell needs to be optimized to allow for accurate measurements,

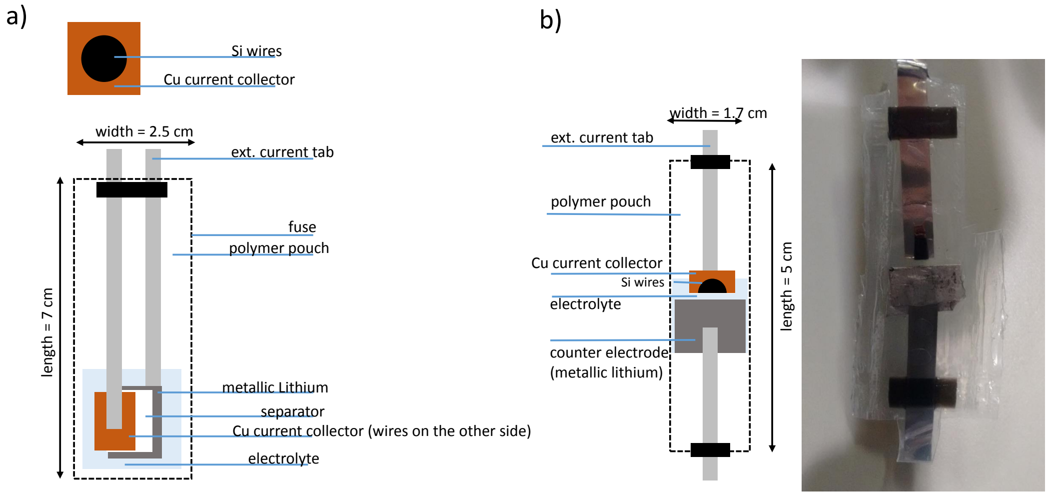

Figure 3.8: Specialized pouch-cells for in-situ and ex-situ pouch cells. a) Standard pouch cell configuration for in-situ as well as ex-situ XRD measurements with synchrotron radiation. b) Special designed pouch cell configuration for in-situ TXM measurements for synchrotron measurements

which are neither negatively influenced by a thick current collector nor separator material. Therefore, the separator material is changed to PP/PE double layer Cellgard filter of 25 µm thickness. The pouch cells are also only half-cells, using the same metallic lithium as counter and reference electrode. In order to allow diffusion inside the pouch cell between the electrodes, small amounts of electrolyte wet the separator. The external tabs are chemically inert and do not influence the experiment. Figures 3.8 b) and 3.9 illustrate the second pouch cell configuration for in-situ synchrotron characterization, like TXM. TXM has a very high local resolution, see section 2.8.1, and allows to monitor crystallographic and structural changes on the nanometer or sub-micrometer range of individual Si-wires along the length of a wire. As a result of the perfect alignment of the wires along the <100>-direction across the surface, a configuration as shown in Figure 3.8 a) would only lead to an integral analysis across the surface i.e. wire tips, but not to detailed local analysis along a wire (Figure 3.9). Consequently, a special electrode configuration was developed. The wires are bent. Thus, some wires at the edge lie perpendicular to the surface. That way, locally resolved measurements at specific points could be performed, indicated by the white square in Figure 3.9. Compared to the first configuration of pouch cells in Figure 3.8 a), the external tabs are not parallel to each other, but placed in-line to each other, leaving only a small area in between for the sample. The area in between the tabs has to be as small as possible to limit resistance losses during the measurement. As

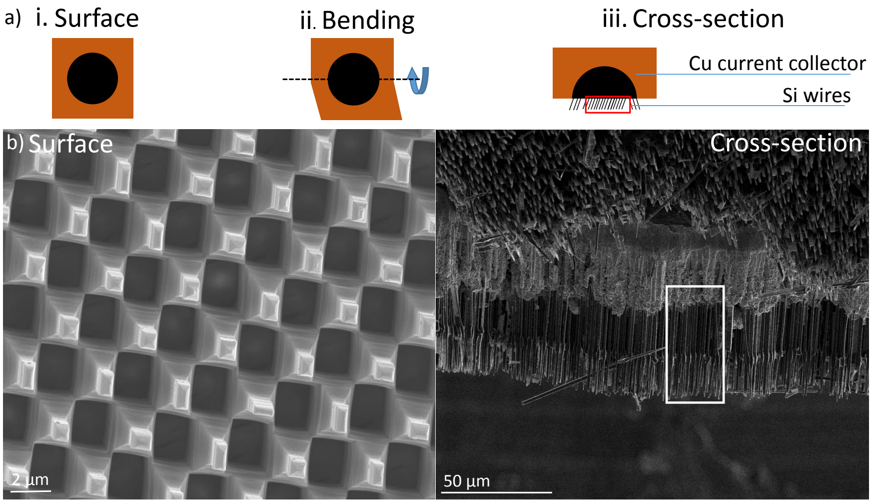

Figure 3.9: SEM images of the wire array configuration inside pouch cells by bending the sample. a) The schematic shows the idea of the wire configuration for the structural analysis. The corresponding SEM images in b) emphasize the highly-symmetric structure, which makes a different cell and wire design necessary. On the left side, the wire arrays are shown in a top view. The cross-sectional view after bending shows that only some wires stand in one direction whereas others stick out.

indicated, the distance between both tabs is around 0.3-0.5 mm.

3.4 Cyclic voltammetry

The most common ex-situ characterization method is the cyclic voltammetry measurement, explained in section 2.6. The voltammetric set-up used in this thesis is based on the electrodes in the half cells and the connected potentiostat build by ET & TE GmbH. The basics of the voltammetric set-up is a three electrode configuration. The working electrode (WE) is the sample to be analyzed where the voltage is applied to. The counter electrode (CE) closes the circuit. An additional third electrode is the reference electrode (REF), to control the applied voltage. The counter and reference electrode are connected together and act as one electrode. Thus, the measured voltage is always referred to the standard potential of metallic Lithium which acts as the counter and reference electrode in half cells. The three electrode configuration is necessary to compensate the additional losses occurring within the electrolyte, cables and of the electrical connections.

The anodes have been cycled between 1 V and 20 mV. Lower voltages than 20 mV are not suitable because metallic lithium would be deposited on the anode surface. All experiments were cycled from 1 V and 20 mV and back to 1 V, using mostly slow voltage sweep rates $v = E_2 - E_1/t$ of 0.1 mV/s, in order to reach nearly steady-state conditions for the whole cycling experiments, i.e. one scan takes 163.3 minutes. Typically, at least five cycles have been measured. The half cells are covered with an additional double walled stainless steel housing. Water cooling of the stainless steel housings was used to change the temperature during the experiment. An additional PT-100 temperature sensor connected to the housing was used to control the temperature in the range between -5 °C, 0 °C, 20 °C, 40 °C, 60 °C and 80 °C.

3.5 Cycling

The long-term cycling and performance measurements are done with a potentiostat/galvanostat from Astrol Electronics. This potentiostat/galvanostat has eight independent (grounded) channels to perform eight measurements simultaneously. It can measure in a current range between 5-200 mA with an accuracy of ± 0.08 % and in a voltage range of ± 12 V with an accuracy of ± 0.01 %. The measurements are controlled via a CCCC software. Again the temperature was controlled typically to 20 ° C, as described above by water cooling of the housing.

The anodes are tested by a characteristic cycling program which includes potentiostatic and galvanostatic steps. The schematic in Figure 3.10 illustrates the capacity and weight calculation with the individual properties of the wire. For that, the active

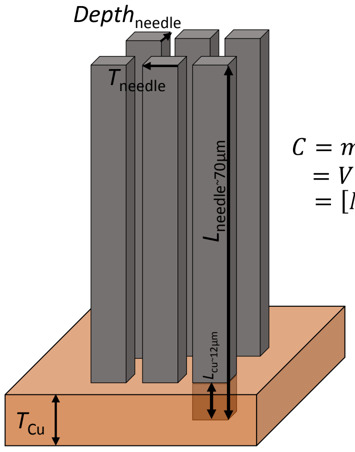

$$
\begin{aligned}
C &= m * C_{theo} \\
&= V * \rho_{Si} \\
&= [N_{needle} * T_{needle} * Depth_{needle} * (L_{cu} - L_{needle})] * \rho_{Si}
\end{aligned}
$$

Figure 3.10: Capacity calculation based on the wire geometry. The wire has a simple cubic base and is partially embedded in the copper. These properties have to be considered for the exact capacity calculation C. The theoretical capacity of silicon is 4200 mAh/g.

material weight $\mathrm{m}_{needles}$ has to be calculated, depending on the thickness $T_{needles}$, length $L_{needles}$ and number of $\mathrm{N}_{needles}$ of the wires. The wires are partially embedded in the current collector. For the calculation, only the active material has to be considered. Therefore, the total length of the wire needs to be calculated without the part embedded in the copper current collector. In those programs, the state of charge (SOC) and additional parameters are optimized and adjusted for each measurement and purpose.

Chapter 4

Results and Discussion - Part 1: Paste Electrodes

Paste electrodes are the most common, industrial way of fabricating electrodes for Li-ion batteries. The active ingredient (e.g. graphite for commercial anodes) is embedded in a "paste" containing different functional materials, like conductors (carbon additives and binder materials. Here they contain silicon microwires. The general problem in industrial fabrication is a large spread in the average particle size; the actual size varies typically between 2 µm to 100 µm. This inhomogeneous distribution is mirrored in a local spread of the physical and chemical properties. A local property spread, in turn, does not allow to identify the exact processes for the Li incorporation into the silicon from external measurements like FFT impedance analysis. With the macropore etching process in silicon as introduced in chapter 3, it is possible to precisely adjust the thickness as well as the length of each and every wire in an array. Utilizing thin necks as pre-determined breaking points, uniform cylindrical Si particles are obtained for the creation of well-defined paste electrodes. This chapter elucidates why (industrial) paste electrodes with silicon do not perform well and which effects have to be considered in order to understand the exact processes. With the precise thickness and length variation of the silicon wires, it was possible to demonstrate a "geometrical" disintegration of the paste, rather than a chemical decomposition. These physical processes were investigated by in-operando impedance measurements in section 4.2. From the outside, a battery represents a black box with just external connections to the power supply or load. This allows characterizing currents and voltages, but it is impossible to record physical and chemical properties directly. From the cycling results of current and voltage, one can draw some conclusions about what happened during charging and discharging by comparing measured data with model simulations afterwards. With in-situ FFT-impedance spectroscopy, as utilized in this chapter, it is possible to record a range of time-resolved parameters tied to the relevant individual processes simultaneously. With a specialized fit model (typically several connected RC circuits), the physical processes can be assigned to resistors, capacitors, and in particular to time constants, allowing deep insights into the various processes taking place. The slowest time constant in this system, for example, is linked to the charge transfer process into the silicon, which thus turns out to be the rate-limiting process. This time constant is directly correlated to the movement of the paste and the void formation because of the volume expansion of silicon, attributed to the fastest time constant. The paste does not change its volume in synchrony with silicon increasingly insulating the silicon because the mechanical properties of the binder material are limited. Consequently, the void formation and the slow charge transfer result in a drastic capacity fading.

This analysis demonstrates that impedance spectroscopy is currently the only tool to assess the internal working of the “black box” and can indeed record defect formation and the ”health” status of paste electrodes during the battery operation. In conclusion of chapter 4, the problems of Si paste electrodes can be traced to a purely mechanical problems and not, as usually assumed, to problems of the silicon battery electrochemistry.

4.1 Length and Thickness Influence of Si Microwires on Lithiation Potential

As already discussed in chapter 2.5 in more detail, a typical charging and discharge curve for silicon, recorded during cyclic voltammetry, has four peaks, responsible for the lithiated and delithiated silicon formation. Figure 4.1 shows the correlation between the measured current, time and potential as well as an example of the corresponding voltammogram typical for silicon. For the silicon microwires, no additional peaks are recorded, relative to Si-C pastes discussed in literature [81, 24] . Lithiation behavior is described by Peaks 1 and 2 referring to the partial (intermediate) and full lithiation behavior. Those peaks correspond to the phases Li_xSi and $Li_{x+1}Si_y$. That means that more and more Li ions are incorporated into the silicon wires. By reversing the potential scan direction, the Li ions are removed from the anode and the phases are changed again. Peak 3 and Peak 4 refer to the partial and full delithiation peaks. The figure indicates the applied potential as well. Every point of the current response in the time resolution relates to a certain potential. This allows to define changes in the time resolution directly to voltage changes, which might correspond to phase transformations or even to changes inside the electrolyte. Further details of the paste electrodes and the mechanisms during lithiation are discussed in chapter 4.2 as well as chapter 5.2.

4.1.1 Length Dependency of Si Microwires

As demonstrated in Figure 4.1, the peaks correspond to a certain potential. The peaks, which are indicated in the figures, are taken for each size, recorded according to cycle number and change upon that and compared. Figure 4.2 shows the lithiation and delithiation potential dependency on the wire lengths for the third cycle. Due to the very precise structuring i.e. etching method of the wires, it is possible to vary the

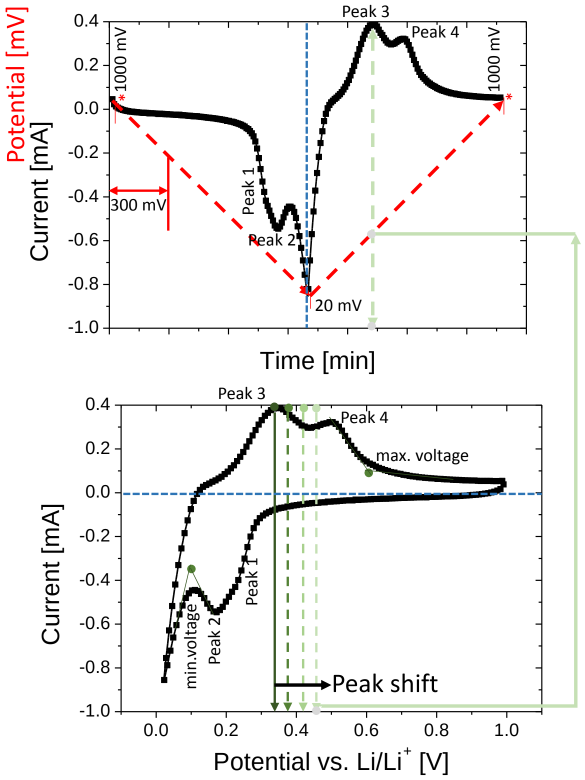

Figure 4.1: Example of a typical voltammogram in correlation with the current-time profile. This correlation illustrates how the current relates to the applied voltage and emphasizes how the peak shift is investigated. The lithiation peaks are referred to as peak 1 and peak 2 for the partial and full lithiation peak. The delithiation peaks are referred to as Peak 3 and Peak 4 (see chapter 2.5). Both diagrams show the same information, but are displayed in a different representation.

length and thickness of the silicon wires. This makes a detailed analysis of the sizes and the corresponding lithiation potentials possible. Different lengths and thicknesses of the wires are produced ranging from 35 - 75 µm with a constant thickness of 1.4 µm as well as thickness variations ranging from 1.2 µm up to1.8 µm with a constant length of 60 µm.

To analyze the lithiation process, the partial and full (de-)lithiation peaks are analyzed separately (Figure 4.2 a-d). As discussed in chapter 2.5, delithiation means the removal of the Li ions from the anode, which might have an effect on the silicon microstructure and needs to be determined, refer to chapter 5.3. The x-axis represents the lengths of the wires. When the wires are getting longer, the delithiation peak potentials increases almost linearly, i.e. in a standard cyclic voltammogram (IV-curve), the peak position shifts to the right. The difference between the shortest and the longest wire in terms of delithiation potential for the full delithiation peak is 60 mV. As discussed in section 2.5, the lithiation potential can be translated into a incorporation voltage i.e. the voltages, which are needed for the Li ions to go into the crystal structure

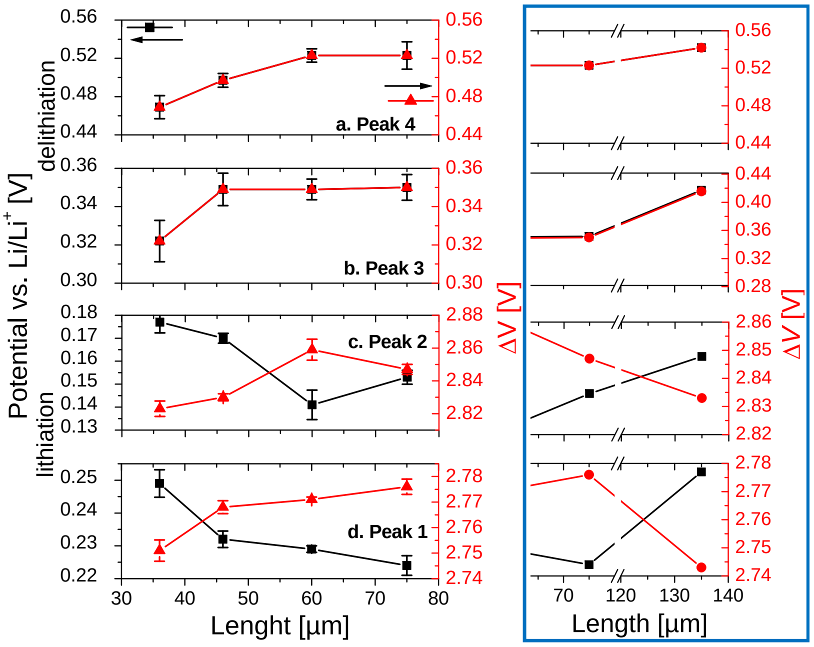

Figure 4.2: Influence of lengths on lithiation and delithiation potentials. The lithiation potentials can be transferred into incorporation voltages, by taking the starting and end point of the individual potential scan into account. With increasing length of the wires, more voltage is needed to incorporate the ions across a large surface area. The error bars indicate the changes for the number of cycles as standard deviation [33]. Additionally, the figure contains very long wires of 135 µm to estimate how the lithiation and delithiation potentials develop.

of Si. Those incorporation voltages are calculated by taking the scan direction during the cyclic voltammogram into account:. For the lithiation process (scan direction between 1 V and 20 mV, the open circuit potential U_{oc} is taken as reference, the open circuit potential of a battery after assembly. The tested half cells with the silicon microwires have an open circuit potential U_{oc} of 3 V. Lithiation is performed between 1 V and 20 mV. Therefore, to calculate the incorporation voltages for the lithiation, the open circuit potential U_{oc} is subtracted by the peak positions of the Peaks 1 and Peak 2.

For the delithiation, the scan direction is changed from 0 V to 1 V. The voltage is then calculated by the difference between the peak positions 3 and 4 and the scan reversal at 0 V. The right y-axis in Figure 4.2 shows exactly the trend of the incorporation voltage. According to the delithiation behavior in Figure 4.2 a-b), the incorporation voltage increases as well with the length of the wire. The longer the wire, the more voltage is needed to remove the ions from the anode - to destroy the $\mathrm{Li}_x\mathrm{Si}_y$ alloy, which forms during the lithiation process. Figure 4.2 c-d) shows the tendency of the lithiation peaks versus the wire length. The curves for the partial (Peak 1) as well as the full lithiation peaks (Peak 2) decay exponentially with the length. The longer the wires, the more flat is the lithiation curve. There is a saturation and the lithiation potential decays slowly. As indicated by the definition for the incorporation voltages, the smaller the value for the lithiation potential is, the higher are the values for the incorporation voltage. This length dependency could be understood by using a simplified network of series and parallel resistors describing the wire resistance, shown in Figure 4.3. The additional series and parallel resistors account for the length L and thickness T inside the different paste electrodes. An additional series resistance $R_{contact}$ is added in series to account for the contact formation with the surrounding matrix. When the wires are embedded into a conducting matrix of CB and CMC, the wires are homogeneously electrically contacted from every sides by the conducting matrix. This matrix functions as a percolation network between the silicon microwires inside the paste electrodes and as contact to the current collector. Li ions can diffuse from all three directions to the wires (except for the one side facing the current collector) and incorporate into the wires.

As previously described in chapter 3.3, inside the different set of paste electrodes the same amount (in g) of silicon wires is used. Consequently, when increasing the wire length to $2\,L$, the overall amount of wires is N. This means that inside the pastes with wires of length L, twice as many wires exist. Long wires could just be broken in the

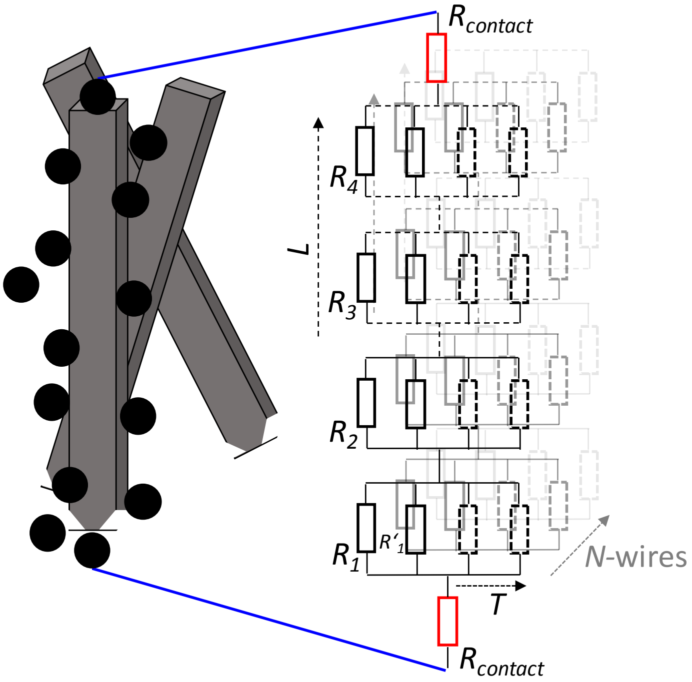

Figure 4.3: Model of size differences of Si microwires in paste electrodes during lithiation and delithiation according to a resistance model [32, 33]. The schematic shows how the thickness of the wires can be described by the number of parallel resistances. The length can be described by the number of resistances added in series. For more wires, this equivalent resistance model can be applied for N wires. An additional series resistances indicate the electrical (ohmic) contribution due to the adhesion of the silicon wires to the carbon matrix and the current collector.

middle and the small wires would remain. As a result, the total volume and surface area of the silicon wires (for the complete pastes) are the same. Due to the same surface area, the diffusion path remain also the same. Thus, they should behave completely similar. Nevertheless, the voltammetric results indicate (repeatedly) a strong voltage increase with longer wires. Exactly these set of pastes or experiments allow to decouple possible geometrical effects from diffusion and kinetics. Thus indicating that it might not only be a geometrical effect. For an increase in wire length, the number of series resistors increases. In order for the same current to flow through wires of different length, the resistance across this wire is increased. Therefore, the incorporation voltage increases almost linearly.

Strong hints are directed towards the ionic transport inside the wires and the contact formation lengthwise of the wires. This could be emphasized by looking at the length change during lithiation. The wire expansion by a factor of four indicate a direct correlation between the length increase and the consequence on the diffusion length. During this change, the diffusion length for the ions become larger for long wires, compared to short wires. Figure 4.3 indicate a homogeneous integration of the silicon wires. In order to point out the problem, it is necessary to consider the worst case of contacting: if only the ends would be contacted to the matrix, the resistance at the interface would be infinitely small. With an increase in wire length, the resistance increases drastically until the wire is no longer in contact to the matrix and thus looses ohmic contact. The wire would no longer be in contact to the current collector because less contact points exists to the paste. This means only half of the long wire would be contacted, resulting in a loss of active material. Consequently, it is a reduction of the wire length with the same number of contact points. This could be considered as the effective surface contacting. With increasing length of the wire, the probability increases that more Li ions incorporate into the silicon at different positions along the wire. The number of incorporation positions increases. Consequently, the increased, local incorporational positions need higher energy to break the still existing bonds resulting in higher incorporation voltages in Figure 4.2. Figure 4.2 shows additionally an estimation of the potentials for very long wires of 135 µm length. Longer wires cannot be produced with the used mixed, aqueous electrolytes. Only by modifying the electrolyte and using pure organic electrolytes allows to fabricate even longer pores and wires. This size dependency demonstrates the importance of these defined incorporation voltages. The trend for the delithiation potentials is similar to the already discussed results of the other wire length; it increases more. More voltage is needed because the ions have to be removed from even longer wires, across a larger surface.

The lithiation behavior changes for really long wires. This change is illustrated already between 60 µm and 75 µm. Up to 60 µm, the incorporation voltage for the full lithiation peak in Figure 4.2 c) increases. For even longer wires, the incorporation voltage decreases, facilitating the alloy formation and ion diffusion. The same can be seen in Figure 4.2 d) for the partial lithiation peak. For longer wires, the second contribution dominates the lithiation behavior. There are much more local incorporation points for the Li ions. Not all travel with the same velocity and distance towards the silicon interface. Some are already incorporated forming lithiated Si alloys. Additional ions still need to incorporate into the structure. Some ions move forward into the structure, compensating the additional energy required for the first lithiation. Therefore, the voltage is reduced. Another contribution is the adhesion to the conducting matrix. Another import contribution is the electronic conductivity of the carbon black because there are larger areas of only carbon black in the electrode. This contribution reduces the lithiation potential [125]. This phenomenon is supported by additional FFT-IS analysis in chapter 4.2.

This size-dependency analysis shows that the length of a silicon wire has a direct impact on the lithiation and the delithiation potentials. This has a direct consequence for the cycling of these wires. Anodes and cathodes are cycled within a specific voltage range, designed for the electrochemical voltage window of the material and electrode side. Quiroga et al. showed that the voltage ranges are very different depending on the structure, shape and material [91]. A large range of voltage limitation, for example between 1 V and only 20 mV, for a silicon system during cycling has a direct impact on the cycling behavior. As indicated in this cyclic voltammetry analysis, the peaks appear for silicon between 100 and maximum 800 mV. Consequently, the phase transformations happen only in this voltage range. Thus, it would be beneficial if the anodes would only be cycled in this range. Cycling in a larger voltage range means that the electrode needs this additional voltage to achieve higher capacities. This has a severe drawback and adds on the series resistance losses on the anodes. In order to illustrate the drastic influence of this size dependency on the specific voltage ranges, the minimal and maximal voltages i.e. the voltage limitations for the discussed length and thickness variations are shown in Figure 4.4. It shows directly that the length and thickness changes both voltages. The minimal voltage increases linearly. Consequently, if the size is not at all considered during cycling, these will not be ohmic resistance losses, but diffusional losses, which limit the anode. Therefore, it is necessary to adapt the voltage ranges according to the specific length and thickness as well.

4.1.2 Thickness Dependency of Si Microwires

The lithiation as well as delithiation potential depends directly on the length of the wires. Now, the thickness dependence is discussed as shown in Figure 4.5 as well. The delithiation process for different wire thicknesses is represented in Figure 4.5 a-b). Both curves show a similar tendency. They decay almost exponentially with increasing thickness. The right y-axis shows also here the translation into incorporation voltages. The larger the thickness of the wire, the smaller is the voltage which is needed to incorporate Li ions inside the anode. The incorporation voltage decreases for thick wires about 60 mV compared to very thin wires for both the partial and full delithiation peaks. For the lithiation - the incorporation of the Li ions into the silicon - both peak

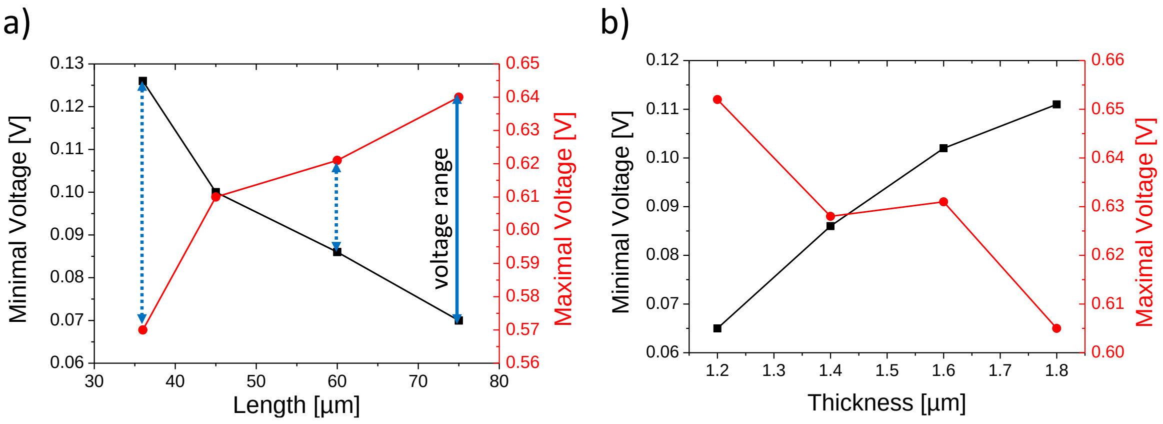

Figure 4.4: Size-dependent voltage limitations for cycling silicon microwire anodes. a) The figure indicates the minimal voltages with varying wire length. The left y-axis indicates the minimal voltage for cycling. The minimal voltage means it is the voltage after both lithiation peaks. The maximal voltage, right y-axis indicates the voltage after both delithiation peaks. These specific voltage limitations are indicated by arrows for each length and thickness of the wires b).

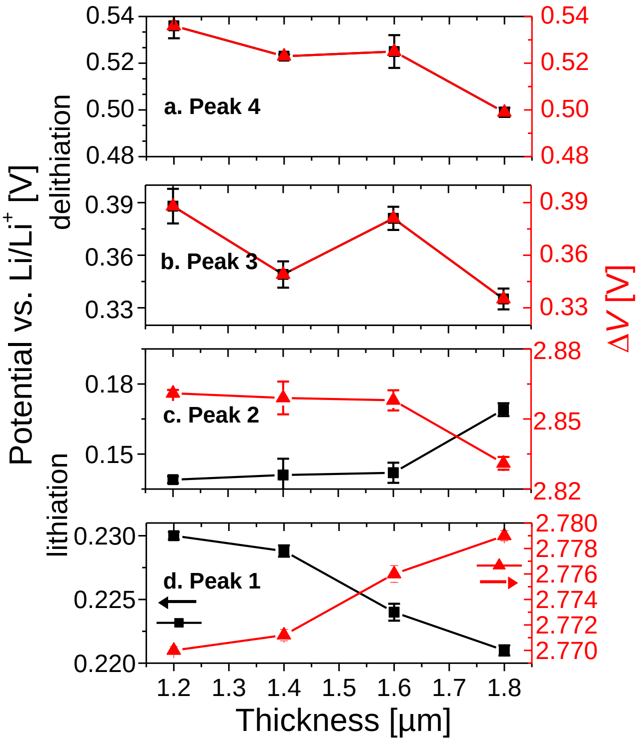

Figure 4.5: Influence of thickness on the lithiation and delithiation potentials. The partial and full lithiation potentials show reverse behavior due to differences in kinetics in the first lithiation. The error bars indicate the deviation for the number of cycles as standard deviation [33].

tendencies have to be discussed separately. Figure 4.5 c) describes the behavior of the full lithiation peak. The lithiation potential increases first almost linearly with the thickness up to 1.6 µm; the curve changes the slope significantly when the wires get thicker. The peaks shift to larger values. This implies that less voltage is needed for the ions to enter the silicon wires. Also here the difference between the thin and the thick wires is 60 mV. Summarizing, both delithiation peaks as well as the full lithiation peak show the same tendency for the incorporation voltage for thick wires.

The partial lithiation, on the other hand, shows completely the reverse behavior. As indicated in Figure 4.5 d), the lithiation potential decreases. The peaks shift to smaller values for thick wires. The incorporation voltage $\Delta\,\mathrm{V}$ increases. Li ions need much more voltage to incorporate into Si wires, if a critical wire thickness is exceeded. In this case, the difference in lithiation potential lies around 100 mV. In order to understand the lithiation behavior for the different wires, several contributions have to be taken into account.

The network of series and parallel resistances, proposed in Figure 4.3, is taken to describe the thickness contribution inside paste electrodes as well. For the thickness contribution, additional parallel resistors are applied to the network. For thicker wires, the cross-sectional area increases and thus the number of parallel resistors (since the wire resistance is inversely proportional to area) i.e. simply speaking, a thick wire is a parallel arrangement, thus parallel resistors, of thin wires. Due to the parallel arrangement of the resistors, it is clear that smaller voltages are necessary to allow the same current to flow to trigger the reaction. When using thick wires, the effective surface contacting area needs to be considered as well as the diffusion inside the wires. For thick wires, the effective surface area is larger and thus the ohmic transport towards these wires is better because there are more points to the matrix.

Anyhow as indicated in Figure 4.5, the partial lithiation of Li inside the silicon wires needs more voltage. In the beginning of the first lithiation process, Li ions have to diffuse into the purely crystalline silicon wire. The covalent bonds of the Si crystal are stronger than those of the Li-Si alloys. At that interface of the enhanced cross-sectional area, the bonds have to be broken and activation energy has to be provided to do that. For thick wires, radial diffusion has to be taken into account as well as large stress during lithiation. The ions diffuse first to the interface of the silicon and react there. The already lithiated phase diffuses further into the silicon with time; but the core remains crystalline. The energy for the covalent bonds of the silicon is larger than those of the already lithiated phases. The crystal reorientation between crystalline and amorphous silicon leads to large volume expansion inside the silicon. Those expansion of the crystal disturbs further incorporation of ions. Stress upon the anode structure reduces further lithiation. Especially, for very thick wires only the outer part is lithiated. Therefore, it is necessary to overcome this additional energy to transfer the already lithiated phases and incorporate more ions. The part of the remaining crystalline silicon is larger than in thin wires. This additional energy due to the diffusion limitation in thick wires is translated in higher lithiation voltages in Peak 1. This is explained by enhanced lithiation induced compressive as well as tensile stress inside the already lithiated front. This stress scales with the surface area, as explained in [33, 158, 88] and is inverse proportional to the square of the radius. As indicated, the stress during lithiation is critical and lead to an accumulation of surface charges and a large concentration gradient at the interface to the silicon wires. The diffusion is limited at that point and the additional energy and the stress needs to be relaxed in order to allow further diffusion. If stress pile up, it might also be that no futher lithation takes place because the reaction front stops growing. As indicated in the voltammograms, this is the case only during the first incorporation, intermediate state between the purely crystalline and the full lithiation state. Of course, this so-called radial diffusion happens as well with different wire length. But for this model proposed by [158] the effect surface area i.e. the circumference is necessary when discussing the interfacial reactions, because the radius as well as the circumference directly are accounted by this model.

4.2 Chemo-mechanical interactions inside paste electrodes

In-situ FFT-IS data are recorded simultaneously to cyclic voltammetry measurements. All our experimental results with respect to the behavior of individual silicon wires in a paste can be summarized by three mechanisms: a) the chemo-mechanical interaction of the silicon wires with the surrounding conducting matrix, b) the SEI layer formation around the wires and on the matrix and c) the charge transfer reactions. The rate limiting step for these processes is most probably the charge transfer reaction, which is found to be the slowest process with the largest time constant. Anyhow, the chemo-mechanical interaction of the silicon wires with the surrounding binding material has a severe influence on the charge transfer reaction, especially to the cycling stability

[149, 98, 123, 159, 160]. Therefore, those two correlations are discussed here in detail, with respect to the different lengths and thicknesses of the individual wires (see Figure 4.6). The dashed and solid lines emphasize the potential change (blue dashed line), the change between lithiation and delithiation in the current (red dashed line), but more importantly the green solid line as the peak formation and phase transformation. Here, only the length variation is discussed. A detailed thickness analysis is performed in Hansen et al. [125]. Figure 4.6 a) indicates the difference in time constants with time. Firstly, it is necessary to discuss the fastest time constants τ_1. The time constant shows periodical minima and maxima throughout the measurement, exactly at the potential scan direction reversal. At the phase transformation, the time constants either increase or decrease. Looking at the corresponding resistance, it decreases with time having the highest values during the first cycle. These are strong hints that the fastest time constant is correlated to the interaction between the silicon wires and the binder in the surrounding matrix. The polymeric chains of the CMC binder adsorb

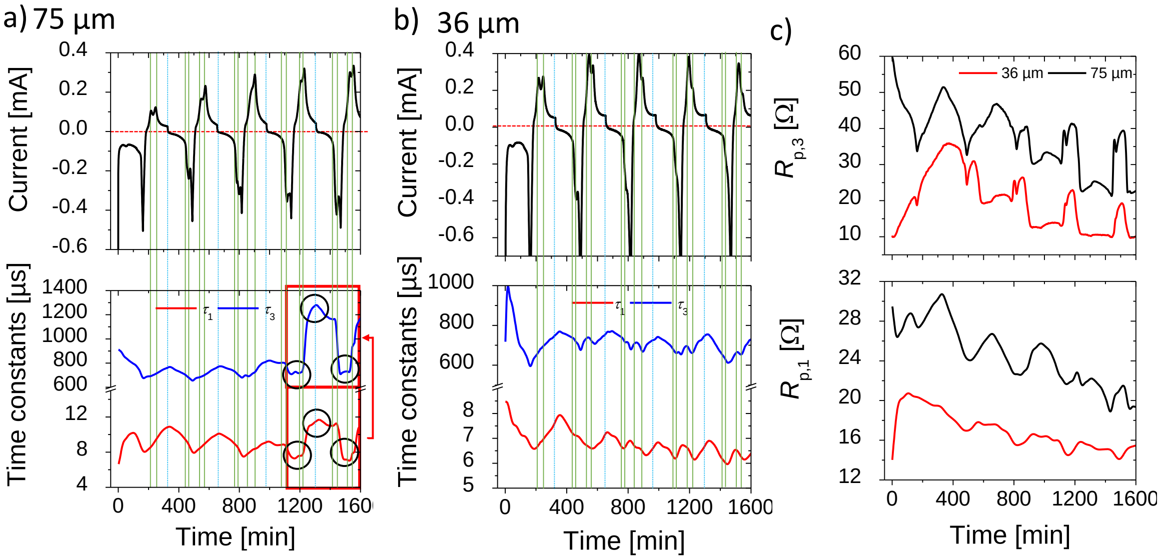

Figure 4.6: FFT-IS analysis of silicon wires embedded in paste electrodes with regard to different length of the silicon wires. Here, CMC is used as binder material. The dashed blue line indicate the potential scan reversal. The other vertical lines indicate the individual phase transformation. In order to clarify the correlation between phase transformation and time constants, those lines are also visible in the time constant representation. As indicated, the current time representation is a typical curve resembling the voltammograms in Figure 4.1. In order to simplify these plots, the use of points and lines is avoided. a) Development of time constants for long wires (75 µm long and 1.4 µm thick wires), in comparison to short wires 35 µm long and 1.4 µm in b). c) It shows the corresponding resistances for the time constants in comparison to the different lengths [125].

on the silicon surface and bridges between the individual wires and the carbon black particles. If the wires expand during volume expansion, they push the surrounding matrix. Upon delithiation, the wires retract again. The surrounding carbon matrix does not retract with the same speed as the wires, thus, probably creating voids in between. The voids do not contain any silicon anymore and create a lateral distance between the silicon and the carbon. Although the polymeric chains act like "springs" to mechanically move the conducting network back in contact with the silicon, it is not possible to close the gap instantly [157, 154, 161, 156, 24]. The difference in both time constants is evident, but nevertheless the fast process highly influences the slow charge transfer process. If the gaps between the individual wires and the carbon black still remain also after repeated lithiation and delithiation processes, they are not longer connected to the current collector and cannot contribute to the capacity or in general to the battery performance. Probably a lot of active material is getting lost due to the interaction between the binder and the silicon wires. This is even more astonishing since cellulose is known to have the advantage, compared to alternative binding materials like Polyvinyldifluoride (PVDF), that it forms spring-like contacts between the wires and the carbon. PVDF, on the other hand, forms only a thin net around the active material and do not chemically bind with silicon at the surface. For detailed comparison refer to Appendix A3. The disadvantage of PVDF is that it swells upon contact with the battery electrolyte, allowing for the silicon wires to move around the matrix and creating even larger uncovered areas and disconnected wires. The void formation is enhanced with this type of binder due to the swelling of the polymeric chains [153, 154, 87, 155, 156, 157, 162].

When comparing the fastest time constants for short and long wires, another contribution needs to be taken into account. As stated previously all the paste electrodes contain the same amount of wires. The total surface area is the same in the different sets of electrodes (for wires with twice the length, the number of wires is N, whereas for half of the length it is twice the number creating the same total volume and surface area). Paste electrodes with long wires contain larger areas with pure carbon black, thus rising the time constant due to an enhanced conductivity. Figure **??** shows a cross-sectional schematic of silicon in contact with carbon black, binder and the electrolyte. Before cycling, the silicon is homogeneously contacted everywhere to the paste. During cycling, anyhow, voids along different spots at the wires form due to the volume expansion. The bond between cellulose and silicon is often represented with springs, that adhere to the silicon. These bonds tend to form again with every

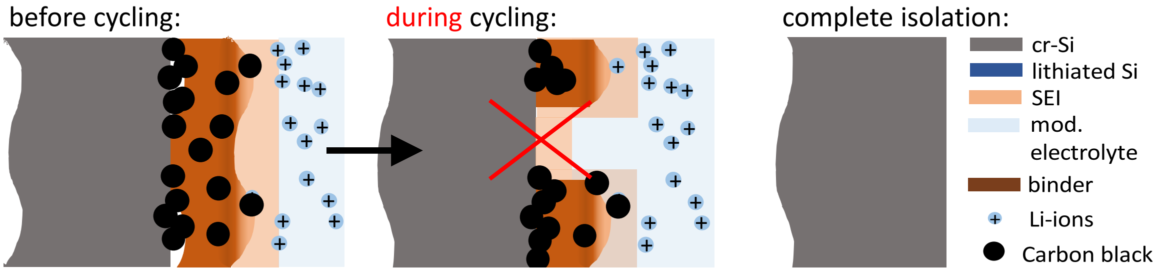

Figure 4.7: Chemo-mechanical interaction as rate-limiting step inside paste electrodes identified by FFT-IS. The schematic shows the cross-section of the paste electrodes before cycling. During cycling, the volume expansion of the silicon wires leads to a void formation at the silicon surface. The paste cannot retract at the same time with the silicon, leaving the silicon particles electrically insulated and locally isolated. The binder material CMC acts like springs around the active material; retracting the paste back to the wires [157, 163, 164]. Appendix A3 discusses the impedance data for different binder materials.

lithiation and delithiation process and still remain attached to the silicon surface. The periodic minima and maxima in the impedance data indicate that the number of voids increases. This is evident during the fourth and fifth cycle because both time constants for long wires increase. Due to the high aspect ratio and its length, the cellulose tries to cover the complete wire and connect it across the complete area to the matrix. Especially in the beginning, the time constant shows periodically maxima and minima, with almost the same height. The minima and maxima occur every time when the potential is reversed. Such a change in the potential correlates to a large volume expansion because the physical behavior behind the potential scan changes. In the fourth cycle, the formation of the maxima and minima seems to stabilize. The void formation enhances from that moment on. Additional maxima form in this cycle, exactly corresponding to the partial and full lithiation peaks. This (maybe) sudden maxima formation can be explained by the reduced influence of the SEI formation. The SEI is stable at that point, as indicated by τ_2, meaning that this formation does not contribute to the silicon/paste interface anymore. The minima and maxima correspond to enhanced mechanical activity inside the paste and around the wires. This means that more charges incorporate, more lithiated phases form and enhanced volume expansion is necessary. The additional peaks in the fastest time constant have a direct impact in the slowest time constant τ_3. In cycle four, the additional peaks appear also here and correspond to enhanced charge transfer inside the anode. More charges correspond directly to more current output. The peaks of the voltammogram tend to stabilize with time of measurement.

The next cycle demonstrate the consequence of the void formation on the charge transfer process. Both time constants show a large increase, resulting from the mechanical interaction inside the paste. Larger values indicate slower processes. While the increase for τ_1 is only low, the impact on the slowest time constant is rather high; it increases by a factor of two. It is evident that the adhesion to the current collector and between the silicon wires has a big influence on the battery performance. The slowest time constant is directly shown in the same figure, in order to compare both effects directly. By taking the corresponding resistance into account, the correlation gets more pronounced: If more material gets lost and disconnected from the matrix and from the conducting network, the ionic diffusion and incorporation inside the material will be more difficult as well.

In other words, due to the unexposed areas and disconnected areas, the SEI layer is likely to be destroyed, which has to be formed again, giving rise to the time constants because it takes longer to penetrate through a thick diffusion layer. During cycle four and five, additional peaks appear in the resistance curves which correspond to the two-step phase transformation. For long wires, the interaction with the matrix is more pronounced. They are longer and have consequently more contacts to the surrounding matrix. This contact has to be maintained throughout the lithiation and delithiation process. As stated in Hansen et al. [125], this is problematic because the length change of long wires may lead to an even enhanced void formation and consequently to loss of active material. In order to clarify the consequence of the void formation, the silicon wires get isolated both electrically and locally (figure 4.7). This lost silicon cannot contribute anymore to the overall capacity of the battery. Figure 4.8 demonstrates how the charging capacity fades drastically. The galvanostatic charging curves indicates two voltage plateaus in the first cycle.

The plateaus represent a phase transformation, during which the Li is incorporated into the Si. If this phase formation is finished, the voltage increases again until the next phase is starting to form. With increase in cycle number, no plateaus remain at the expense of the charging capacity. This capacity fading is a direct result of the disintegration of the silicon paste electrode.

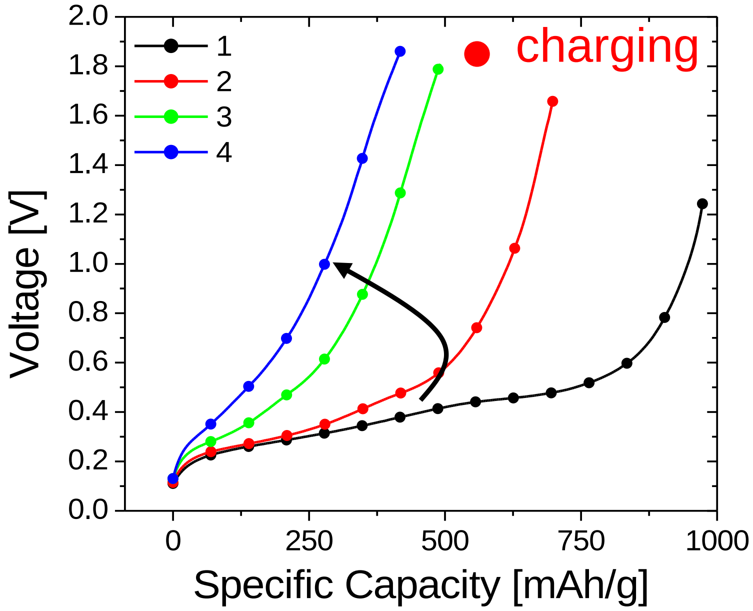

Figure 4.8: Galvanostatic charging capacity of paste electrodes with silicon wires. With number of cycles, the capacity fades drastically as consequence of the complete disintegration of the electrode and the void formation around each single silicon wire.

4.3 Relaxation Phenomena in Si wires

As discussed in the last section, the fundamental investigation of the physical parameters inside paste electrodes with Si microwires as active material revealed a size-dependency. The FFT-IS analysis demonstrated how the mechanics plays an important role at the interface between the silicon wires and the surrounding paste medium. Void formation is a consequence of large volume expansion during cycling in a paste with a low elastic modulus of the binding material. This investigation concentrated on the diffusion and kinetics and is inevitable when analyzing anodes. To learn more about the relaxation phenomena within the paste, a specially modified step-voltammetry was performed.

As discussed earlier, constant steps at the phase transformation alter the state of charge and shows how the system adjusts back to the equilibrium. By analyzing the transients, relaxation time constants are quantified. Thus e.g. diffusion processes can be analyzed which have time constants significantly larger than one second (the largest time constant, which can be analyzed with the FFT-IS approach is discussed in section 2.7.3). Figure 4.9 indicates when the steps are applied. They are always applied at the maximum voltage peaks. Jumping from the maximum peak positions to the end

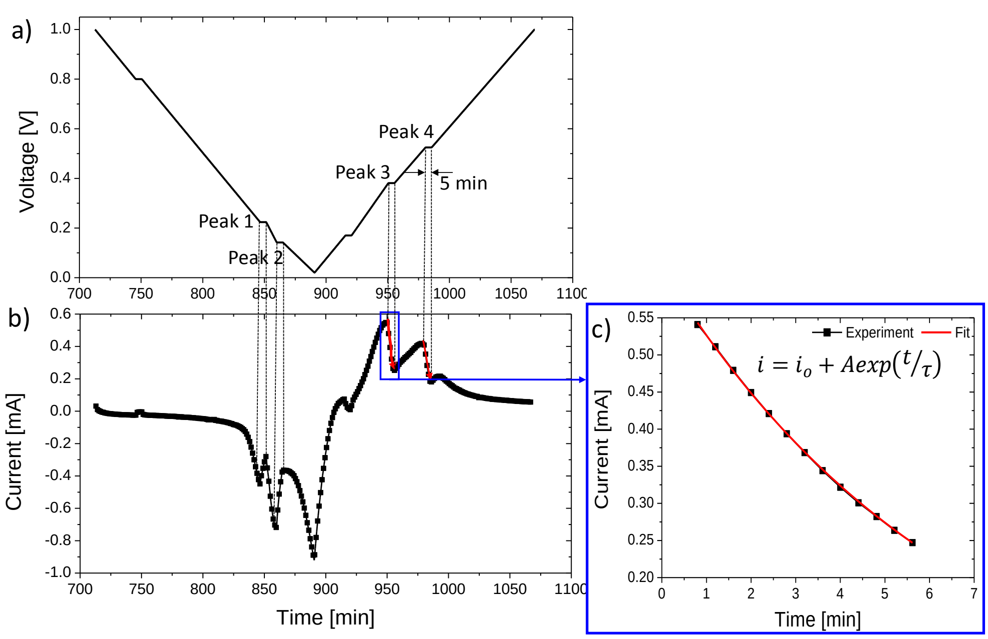

Figure 4.9: Applied modified step voltammetry and transient measurement. a) The constant voltage steps are applied directly at the maximum of the voltammetric peaks - directly at the phase transformations. b) The response of these voltage steps is seen in the current-time characteristics by current transients. c) The current decay can be fitted by an exponential decrease. The corresponding quality fit χ^2 value is in the order of 10^{-4} [33].

of this peaks shows directly how fast locally a wire can be charged or discharged, or in other words, how fast Li ions can diffuse into the wire.

Figure 4.10 indicates that the relaxation times are much larger than in FFT-impedance spectroscopy. It could be explained by kinetic limitations. Slower time constants would destroy or negatively influence the measurements by pure drift (diffusion), but like this, it is simply possible to record the (absolute) velocity and kinetic limitation of the Li ions. For the lithiation Peak 2, for example, the constant voltage steps jump from the maximum peak position to the end, revealing the velocity from a non-charged to a charged anode. The process shows the total time constant of the complete charging process (including faradaic and non-faradaic charging processes). As a consequence and requirement of step voltammetry, non-faradaic charging currents decay much faster, compared to the faradaic currents, the sum of the time constants mostly include only the contribution of the charge transfer kinetics [120, 118, 165, 166]. Summarizing these results, the modified step voltammetry indicates the kinetics of the maximal amount. Furthermore, from these results, it can be deduced how many charges per time can be incorporated and how fast this happens. Figure 4.10 shows the relaxations times for the thickness and length variation of the wires, divided

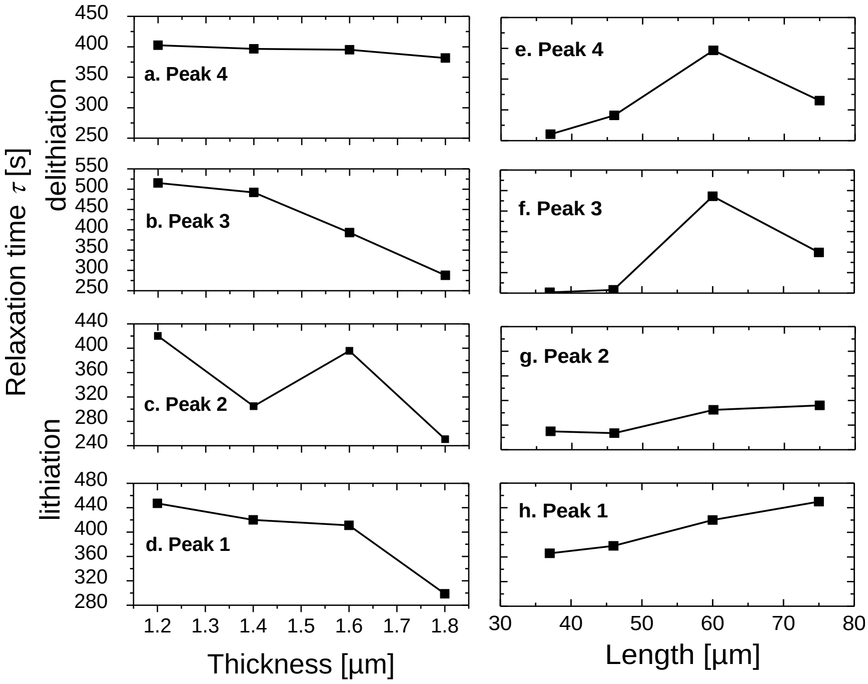

Figure 4.10: Relaxation times for wires of different lengths and thicknesses. The relaxation times recorded with modified step voltammetry are four orders of magnitude higher than those recorded by FFT-IS. The inset shows the results of the FFT-IS discussed in 4.1.2. It describes diffusional behavior of the electrode [33].

into lithiation as well as delithiation behavior. As mentioned above, the constant voltage steps are applied to all four of the peaks and the corresponding current transients are recorded individually. By comparing the peaks, the relaxation times have always the same order of magnitude for the partial lithiation/delithiation and the full lithiation/delithiation. Figure 4.10 a-d) shows the thickness dependency on the relaxation time. The here discussed characteristic shows surprisingly the smallest relaxation time for thick wires. With the above explanation that means that for thick wires the time for the complete charging process might be the slowest. Furthermore, it indicates that the kinetics for the maximal amount of Li ions inside thick wires could be the fastest. Taking into account the previous FFT-IS analysis, the contact formation around silicon wires and the interaction with the surrounding matrix has a direct consequence on these transient measurements. Whereas the relaxation times for the thickness variation show always the same tendency, for the length analysis in Figure 4.10 e-h), τ increases for the lithiation, but decreases for the delithiation. Especially, the relaxation time for Peak 1 increases almost linearly for long wires; the difference is $120\,s$, scaled with the amount. For Peak 3, the value is almost twice as high for long wires. The kinetic processes for wires with varying lengths are much slower compared to the thickness variations. Also here, the previous discussion can be considered: the contact between the surrounding matrix and the wires have to be maintained or established first across a larger local surface area, espacially because the voids created during volume expansion create additional mechanical loss to the matrix and thus show an effect on the kinetics.

Chapter 5

Results and Discussion - Part 2: Array Electrodes

Creating a high performance battery (high C-Rate, high capacity, high energy density and high cycling stability) requires large amounts of silicon, which is not possible with paste electrodes due to mechanical disintegration of the paste ingredients. Chapter 5.1 presents a replacement solution for the unreliable paste system: a precise spatially controlled silicon wire array, where the distance, the thickness, and the length of the individual silicon wires across a large surface are everywhere the same. These arrays require neither carbon additives, nor binders, which limit their performance.

In order to fulfill the above-mentioned requirements, it is necessary to understand what happens at the electrode-electrolyte interface as described in chapter 5.2. Typically, rate-limiting processes like oxidations and electrolyte decompositions are found at this interface, often leading to a drastic capacity fading. Although the SEI is well investigated for graphite electrodes, no detailed information exists for silicon. Consequently, for the first time, function and formation of a solid electrolyte interface is analyzed for such high-density silicon anodes. The SEI and its morphology are still not completely understood and are further investigated by in-situ FFT-IS, Raman measurements as well as SEM and TEM analysis. In order to understand the influence of an SEI layer to the cycling performance of silicon anodes, the electrolyte is varied as the SEI layer is highly depending on the used electrolyte solvents.

Among the tested electrolyte additives and solvents, the evaluation contained well-known solvents like propylene carbonate from graphite electrodes. In the graphite electrodes, neither successful cycling nor protective SEI formation was possible. Instead, a complete destruction followed. Due to the new approach of using pure silicon anodes (without any graphite), propylene carbonate turned out to be an advanced solvent. This solvent allowed decreasing the necessary charging time for a fully charged battery to only twelve minutes (5 C). Furthermore, the SEI layer improved its morphology completely. In standard electrolytes, the SEI appears wrinkled and rough. With the addition of PC, the passivation layer is smooth, which is similar to the silicon surface before cycling. This is one of the reasons why fast charging of the silicon wire anodes is possible.

Another pre-requirement for stable cycling is understood by the systematic analysis of the SEI layer formation, the cycling parameter as well as the dependence on the state of charge in chapter 5.1 and 5.2. Silicon wire anodes need pre-conditioning in the first four cycles during the SEI formation at slow C-rates. Chapter 5.3 shows for the first time how the wire microstructure changes with varying C-rates using coherent X-ray diffraction during in-situ synchrotron XRD as well as TXM measurements at the Stanford University, SLAC, USA.

These measurements revealed that the silicon wires re-organize in a single crystalline structure in every cycle after cycling. The prerequisite for this is a seed crystal, and the Si encased in the copper conductor acts as that. Since it cannot expand, it does not incorporate Li and stays fully crystalline throughout a cycle. This holds for many cycles if the charging speed is slow ($C/10$) during the SEI formation. No crystalline silicon peak could be detected anymore if cycled fast from the beginning at $C/2$, too fast for a stable SEI formation. This indicates that the SEI layer is very important for the re-crystallization as single crystalline silicon. The SEI layer enforces a constant pressure from the outside on the individual wires to ensure crystalline silicon.

For most electrolytes, fast C-rates during pre-conditioning results in a thin and rough SEI. This SEI does not withstand the pressure during volume expansion, leading to its destruction over time. The pre-conditioning of batteries with the optimized, PC-containing electrolyte is significantly faster, because the growth of the SEI is enhanced.

In order to use the potential of the novel silicon anodes and their excellent cycling performance in full cells, the areal capacity of the cathode material has to match. Sulfur electrodes fulfill this requirement, but raise new problems. Chapter 5.5 reveals the problems when cycling silicon with typical ether-based electrolytes used for sulfur cathodes. Up to now, the silicon-sulfur chemistry in batteries is still new. Sulfur as conversion material is usually available in its elemental form; not bonded or alloyed in a solid solution. This calls for complicated chemical reactions like sulfur dissolution, sulfur precipitations or SEI layers including sulfide groups.

Electrolytes for the anodes cannot be used in combination with sulfur because carbonates undergo multiple nucleophilic attacks with sulfur. Thus, it would lead to decomposition reactions before even cycling the battery. This chapter highlights the possible electrolytic limitations, like oxygen-containing SEI layers as well as the accompanied microstructural change of silicon. According to detailed impedance spectroscopy, it was possible to find an optimal ratio between viscosity and electrochemical dynamics of the electrolyte, which facilitates the fabrication of silicon-sulfur full cells.

Another critical point for batteries is their thermal stability in a broad temperature range, discussed in chapter 5.6. Otherwise, internal processes could trigger a chain reaction leading to thermal runaway. Most types of batteries and their electrolytes are only stable up to 60 °C, but with severe restrictions for the cycling stability and fast charging capability. Chapter 5.6 demonstrates how the thermal stability of silicon microwire anodes can be significantly improved. By coating boron nitride nano-platelets in between the individual wires as thermal coating, it is possible to cycle these arrays even at high C-rates with applied temperature of 80 °C, which is 20 °C higher than without.

5.1 Entropy or How Silicon Wire Arrays Perform

The highly ordered Si array anodes, i.e. a closed-packed arrangement of equally shaped, parallel Si wires, all connected to a copper current collector, tend to reduce the degree of disorder. The entropy is the most important and crucial parameter in materials science and engineering. Thus, the extremely small entropy of the anode directly after fabrication implied an entropy barrier hard to overcome, leading to the high cycling stability of the anode. Some negative aspects of a reduced symmetry have been already discussed, when using the same Si wires inside paste electrodes. The aim of the two completely different electrode types was to evaluate exactly this symmetry effect and to investigate how paste electrodes work. Inside these paste electrodes, as discussed, the silicon wires are completely randomly distributed. For that type of electrode, a chemo-mechanical interaction between the silicon wires and the surrounding conductive medium is the rate limiting process. The previous chapter showed not only the difference in symmetry, but more importantly, gave insights into paste electrodes (comparable to commercial graphite paste electrodes), which help to analyze common problems. Figure 5.1 shows the cycling performance of both anode configurations. This comparison indicates how important size, geometry and order in an anode can be. As described in chapter 3.5, the cycling parameters were improved to

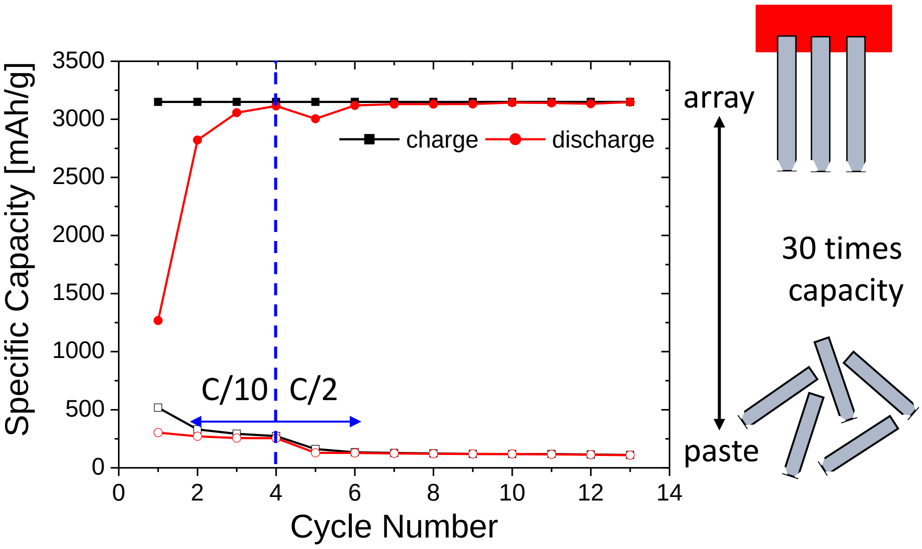

Figure 5.1: Cycling performance of silicon wires of different assembly (arrays and paste electrodes). Highly-symmetric silicon wire arrays show a constant capacity of 3150 mAh/g for large number of cycles (300 cycles). Paste electrodes with silicon wires show a significant decrease in the capacity by a factor of 30.

have slow cycling in the beginning with $C/10$ and then increased to $C/2$ for the wire array, according to [149]. Contrary to the array, paste electrodes cannot withstand high C-rates like this. In pastes, the individual wires are completely, randomly distributed. During volume expansion, the wires can expand in all directions inside the paste and are not fixed in one direction like the wire arrays. Those electrodes show a 30-times lower capacity and need to be cycled slower. This is essential to consider because the silicon/paste interface changes during cycling. Voids form around silicon wires, separating the paste from the silicon. The difference can be explained by considering the in-situ FFT-IS analysis for both configurations.

5.1.1 Comparison of Time Constants from FFT-IS for wire arrays and paste electrodes

The impedance spectroscopy can directly reveal the most important mechanisms, which contribute to the difference in cycling performance between the already discussed paste electrodes and the array electrodes. The proposed mechanisms have a direct consequence on the performance. Figure 5.2 a) and b) compare time constants extracted from FFT-IS for identical experiments using identical Si wires in paste electrodes and in highly-ordered array electrodes. The underlying fitting model as described in section 2.7.3 contains one series resistance R_s and three parallel RC elements. Similar measurements applying constant currents and voltages have already been published by Quiroga et al. [91]. Here, in contrast, several complete charging and discharging cycles are performed during cyclic voltammetry measurements, while measuring impedance analysis. The advantage of this type of measurement is to directly correlate time constants with voltages and phase transformations according to Figure 4.1. The time dependence always enables the possibility to detect changes of time constants and processes with time. In the beginning, processes may be dominated by the SEI formation. Later, the processes show a more direct connection to kinetics and diffusion. The impedance analysis is fitted according to the same model as for the paste electrodes, in chapter 4.1.2. It has a series resistance R_s in series with three RC circuits containing parallel resistances R_p. The three semicircles in Nyquist plots (not shown here) correspond to three interfacial effects, revealed in the discussion, see also chapter 2.7.3. Paste electrodes as well as wire arrays use wires of the same length, and having 1.2 µm wires. Here, only the basic difference between both configurations are discussed.

As a reminder, the most important properties of wires embedded in paste electrodes, previously revealed by FFT-IS, is the void formation around the wires due to a strong interaction between the electrolyte and the binder, especially during volume expansion. These voids (see Figure 4.6 and **??**) form pre-dominantly around long and thick wires. Figure 5.2 b) shows again all three time constants. As they have been discussed in detail in section 4.2 as well as in [125], the discussion here focuses on the comparison.The geometry of the wires (or, in general, of the active material inside paste electrodes) is important for the amount of free volume around the wires. They form as a result of the change at the interface between silicon and the paste. The paste contains a polymer binder CMC. The functional groups (OH-bonds) of the binder adhere to the wires and form a chemical connection between the paste and the silicon. During volume expansion, this interface changes: The wire expands to every side homogeneously, pushing the matrix away. Enhanced void formation around long wires means that all along the wires surface area voids are formed. These voids lead to a disintegration and disconnection to the conducting paste. The ions have problems to incorporate into the wires. Under those conditions, the polymeric chains have no time to retract in time. The retraction of the paste to the wire is necessary to keep all the wires in contact to guarantee high percolation and still guarantee a good adherence to the current collector. A lack of adherence means loss of active material, which negatively contribute to the capacity. But it is not enough to consider only the extrema, like long and thick wires, as the best geometry for an electrode. It is also necessary to consider additional effects, discussed in this chapter. In contrast to the paste electrodes, silicon microwire arrays do not need any non-active binder material. These anodes exhibit exceptionally high capacity during long-term measurements. The following discussion describes the performance of the wire arrays and points out why highly-symmetric wire arrays, like we produce them, show extraordinary performance. In this discussion, not every small parameter is revealed. But during the thesis, the processes seen in this early FFT-IS analysis are understood. The discussion mainly concentrates on revealing the differences between both configurations. At first glance, every time constant is larger by at least a factor of two. This can be explained by the different structure itself. In the following, the details about the different processes are discussed in detail. In correlation to Quiroga et al. [91] and Hansen et al. [125], τ_1 represents the conductivity of the electrolyte, τ_2 is correlated to the SEI formation and τ_3 corresponds to the charge transfer process. For the array electrodes, the first time constant τ_1 corresponds directly to the influence of the electrolyte i.e. ionic conductivity on the silicon/electrolyte interface. This time constant shows how the electrolyte reacts with the wire. In further discussions, this time constant becomes more important in order to obtain even higher cycling performances. Together with the second time constant, they give clear information on how the SEI forms and how the electrolyte influences that formation. In paste electrodes, the effect of the electrolyte is always buffered due to the addition of non-active material and conducting agents. The electrolyte reacts first with the additional material and only indirectly with the wires, changing the silicon/electrolyte interface. Inside paste electrodes, there are large interconnected carbon sections, which contribute with higher electronic conductivity to faster time constants at the anode/electrolyte interface. τ_1 for the array shows a stabilization as well, here already after two cycles. The over-all appearance of this time constant stays similar in both systems, though. The height and amplitude of the minima and maxima stays constant over time, after the stabilization. The difference lies in the development of the additional maxima. For pastes, those maxima came up late in the measurement during the fourth cycle. They correspond on the one hand to the scan reversal from 20 mV to 1 V, but they result also from the lithiation. The peak at 54 minutes is translated in a major increase in the time constant τ_2 and τ_3. This increase in the time constant is very pronounced for the array configuration because the SEI has to be formed over large surface areas without any additional material. It

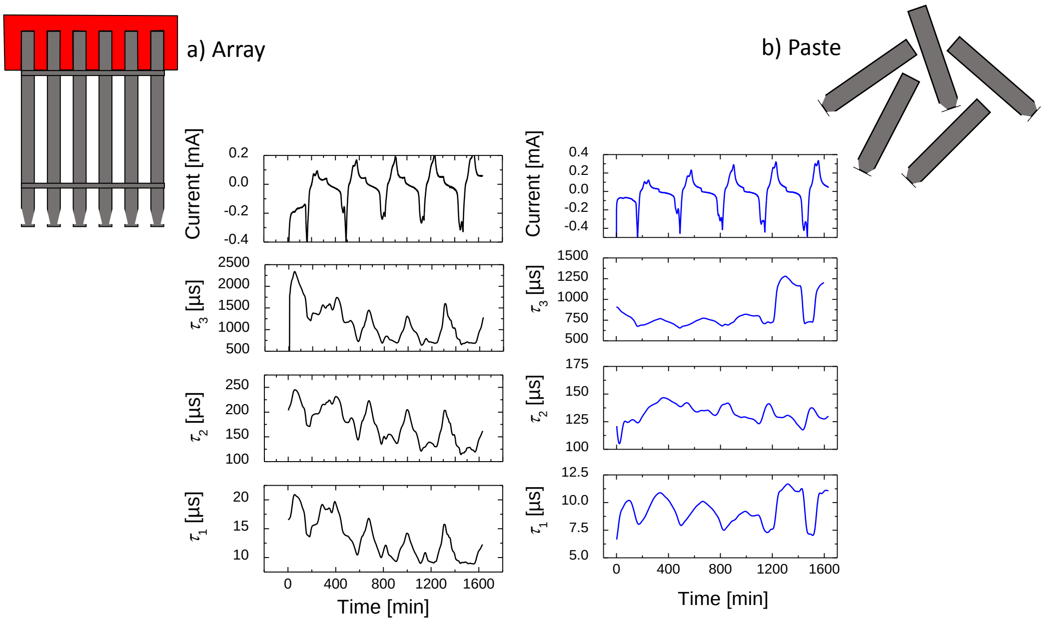

Figure 5.2: FFT-IS analysis of silicon microwire arrays. In order to compare the results, the used wires in both configurations have the same length. The three time constants correlate to different processes. The similarities in time constants and processes are discussed during detailed discussion

contains only silicon wires. The electrolyte can flow to every area through and around the wires and everywhere the SEI has to be formed. At every phase transformation, a new maximum forms in the time constant slowing down the SEI formation until the SEI formation is stabilized.

The trend in both τ_1 and τ_2 is coupled with the dissociation and decomposition of the electrolyte and the first reactions with the fresh silicon (which was never in contact with the electrolyte before). The answer of this behavior is displayed in the non-stable trend in both time constants. Additional maxima and minima form, as the result of the individual components decomposing, changing the ionic conductivity inside the electrolyte. Those tendencies seem to stabilize after the stabilization at the interfaces. Like in the paste electrode system, the third and slowest time constant represents the charge transfer process inside the wires. The increase around the phase transformation results from the volume expansion of each wire. As stated before, the volume expansion is laterally pinned in one direction. But still the SEI forms which makes it harder and is slowed down if the thickness of the wire increases parallelly. During that formation when it is not stabilized it is possible that the SEI is not stable and breaks. Only until it is stabilized, it stops growing. The stabilization is reached when the time constant keeps constant. τ_3 represents the slow charge transfer process. The trend is similar for both electrode configurations. For the array, they are just much slower, which reflects the difference in the charge transfer mechanism. Exactly at the peak positions of the voltammogram, the time constant shows local minima. Directly before these minima, the process is much slower. It reflects directly the incorporation of Li ions into the silicon structure. During the first cycle, the process is still slow because the crystalline silicon is in contact with the electrolyte for the first time. Additionally, it is still crystalline silicon. The activation energy for the first lithiation processes are higher than for the later on incorporation. A concentration gradient of Li ions induces pressure on the wires in the beginning of the formation of lithiated phases. This is seen in the time constants with the slow time constants in the beginning. As the lithiation proceeds, it gets easier with time. In this thesis, the lithiation problem will be discussed in more detail, taking the function of the SEI into account.

Additional peaks appear with time because the delithiation becomes more pronounced with cycle number. More charges get incorporated and removed. Charge transfer is accompanied with high volume expansion. The array system is perfectly symmetric. The charges can directly and only incorporate into the wires. The charge transfer is kinetically not limited by additional carbon like for graphite electrodes for example. For that, the additional graphite lithiates partially as well. The signal from this time constant is influenced by this contribution as well. The incorporation of the ions and alloy formation is not only limited to one potential. Although the peaks form at that potential, the system changes constantly and especially around the two step lithiation or delithiation processes. The ions have to find their way through the structure and this is constantly. Therefore, the time constant is always a bit higher around the phase transformation peaks. In this time constant, the order or symmetry of the electrode is also reflected directly. The charges in this array have to incorporate from every direction over a large surface area, slowing down the processes. This slow process corresponds to an entropy minimization. This entropy minimization helps to incorporate the ions without additional influences or additional activation energy to form the alloys.

A very decisive difference is the increase of the time constant after the third cycle for the paste electrodes. That does not happen for the array electrode. As already discussed, the increase is a consequence of the high disorder of the wires in the system. Because they can expand in the matrix to every side. The ions can also incorporate from every side. But the void formation around the wires leads to active material loss with time. They create more disorder in the anode i.e. the entropy increases. An increase in entropy disturbs the equilibrium in such systems shifting the incorporation potentials and making the phase transformation harder. The disintegration of the electrode is a consequence of the missing mechanical stability of the electrode. For the array system, the charge transfer is established and on-going. This results from the geometry and mechanical stability of the electrode. Due to the high mechanical stability of the integrated copper no wires are lost; all the active material stays intact and the charge transfer process is stable. This fact leads to high cycling stability of over 300 cycles. This FFT-IS revealed that the electrode configuration plays an important role in the discussion about performances. The cycling test revealed the big difference. The three time constants showed that they add up and influence themselves. Therefore, it is crucial to discuss all the contributions to performances separately.

To sum up the performances, if the C-rates for paste electrodes is reduced by a factor of four ($C/40$), the void formation might be limited because the system may have time enough to cope with the different material influences and the SEI formation. At high C-rates, the incorporation process is superimposed by the influences of the matrix and the interaction i.e. the non-faradaic effects during cycling are too high.

Only if the SEI is allowed to form homogeneously around each wire, reliable and stable performance is guaranteed. Because this parameter is very important and crucial, it is discussed in even more detail in the next section.

5.2 Role of the SEI - Electrolytic Influence on Charge Transfer

As discussed in section 2.5.3 and 2.6.1, the electrolyte as well as the SEI layer are essential for anodes in Li-ion batteries and it is even more important for the silicon microwire arrays, as discussed further in this section. The electrolyte has very important properties and plays the most important role facilitating electronic and ionic transfer processes only realized in good conducting media [114]. The decomposition and transfer reaction of the Li ions happen at the electrode/electrolyte interface. Therefore, it is essential to investigate the electrolyte influence on the SEI layer and on the silicon microstructure. The standard battery electrolyte Selectilyte LP 30 is a multi-blend electrolyte composed of different carbonaceous solvents, namely ethylene carbonate (EC) and dimethyle carbonate (DMC) (in a 1:1 ratio, with 44.1 wt. %), provided by BASF. As previously described, this electrolyte is the "working horse" in the battery technology, but not the only available electrolyte. This section describes the influences of an electrolyte by changing the different solvents and discusses their influences on the interaction with silicon. It is necessary to remember that the SEI layer is a passivating layer forming during battery cycling due to the decomposition of the electrolyte. Thus, it is not sufficient to concentrate the discussion only on the (initial) solvents, but more importantly, on the interaction of the already decomposed and aged solvents with the silicon surface. With the aid of a long-term experiment illustrated in Figure 5.3, the limitations of this standard electrolyte, mentioned above, are emphasized. As previously reported in [149, 91], the wire arrays have an areal capacity of 4.25 mA/g and under the correct C-rate conditions ($C/10$ and $C/2$), it shows very high capacity of 3150 mAh/g. The capacity is limited to 75 % of the SOC of silicon, that is very high for the high amount of active material inside the anode. The capacity remains stable for 300 cycles. This is an exceptionally high value for the capacity. In comparison to commercially available graphite electrodes, the C-rates for this silicon array system are much higher than that for graphite. For example, $C/10$ in this system translates into 5 C for graphite electrodes. That means that silicon wires have to withstand much higher stress, strain and more importantly currents during their charging process compared to graphite electrodes. The wires here in this thesis are 70[µm] long and still have to withstand high currents, whereas graphite is only a layered structure and cannot withstand high currents or C-rates without complete exfoliation. Still the silicon anodes of this thesis are able to last 300 cycles. Looking closer at the SEI layer, it forms completely homogeneously around each wire. It expands with the wires, but it is not destroyed during cycling. If on the other hand the SEI layer broke, new reactions would occur at the interface to silicon leading to possible micro-structural changes, as discussed later on. Anyhow, as will also be discussed later on, the homogeneous coating of the SEI layer is not alone the key parameter or successor of the high capacity. Figure 5.3 shows two limitations: a) at larger cycling numbers > 400, the capacity fades. The reason might be either dendrites forming or that the stresses on the wires accumulated during the over-all 400 cycles and that they start to degrade. This might be a result of the amorphization process. With ongoing amorphization process, it is known that there forms a sharp edge between amorphous and still crystalline silicon leading to a phase separation of the SEI layer and the already lithiated phase from the silicon wire. This is further discussed in 5.3. The inset in Figure 5.3 illustrates another limitation. It indicates the first cycles. During those cycles, the SEI forms. The formation of the SEI means a disturbance for the battery i.e. for the electrochemical system that expresses in series resistance losses during the first cycles. The irreversible losses are very large during these cycles. Nevertheless, it is not clear how they form and why. Therefore, the following section concentrates on the modification of the already existing standard electrolyte and discusses the consequences on the SEI layer and the cycling performance. It also emphasizes another problem when cycling the silicon anodes in standard electrolytes.

5.2.1 Propylene Carbonate (PC) as additional cyclic carbonate

As shown in Figure 5.3 as well as in [92], silicon microwire array anodes show superior cycling behavior with standard, non-aqueous EC-DMC electrolytes, as already mentioned above. They show long-term stability, but suffer from irreversible losses at the first contact with the electrolyte during the first cycles. Those losses may add up to more than 70 %. The losses stabilize once the electrolyte decomposes completely and forms a stable SEI layer around the wires. Or expressed differently, once the interaction between the silicon surface and the decomposition products stabilize, the losses reduce. Anyhow, this process has a consequence on the cycling performance. If the stabilization of the SEI layer is not guaranteed for high C-rates, the wires are either destroyed or the anode cannot reach its full potential [92, 24, 167, 168]. Additionally, the anodes cannot be charged faster than within an hour. Faster C-rates lead to destruction of the highly-symmetric wires due to the high pressure. The question arises what the reasons behind these losses or restrictions are, for example, either diffusional

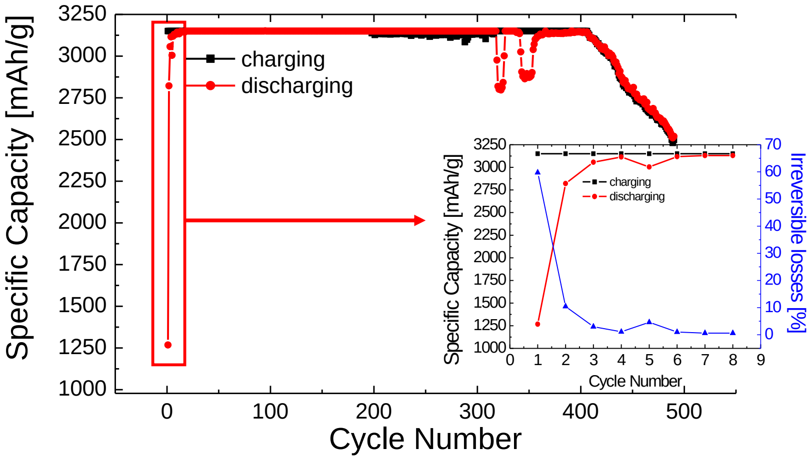

Figure 5.3: Long-term cycling experiments silicon microwire arrays with standard non-aqueous multi-blend EC-DMC electrolyte Selectilyte TM LP30 (BASF) for 500 cycles. The high capacity of 3150 mAh/g stays for over 300 cycles. After that the capacity fades by 20 % and is still higher than comparable electrodes. The wires in this array configuration have a length of 70 µm. The inset shows the first cycles. The discharge capacity slowly increases and therefore the irreversible losses in this region are rather high (70 %).

problems or ohmic losses occurring with time. In order to commercialize the anodes, the charging and discharging rate should be as fast as possible without destroying the anode. Electric vehicles need anodes with even higher areal capacity, like 12 mAh/cm^2 for start-stop applications with high power output. This is an increase by a factor of three. In order to reach this goal, the length of the wires has to be increased further, which has an impact on the battery. A battery can only work if a correct combination between active material, current collector and especially electrolyte is established. For this systems with higher areal capacity, the amount of electrolyte has to be increased in order to guarantee a charge transfer. More electrolyte means additional weight for the complete battery pack and consequently higher prices. This impact can only be minimized if a) the silicon/electrolyte interface and the formation is understood very well and b) the diffusional problems are minimized (or at least understood). This calls for a new design of electrolytes by evaluating the electrolyte properties like ionic conductivity and viscosity. The ionic conductivity plays an important role at least for anodes with high areal capacity. Otherwise, the system will impoverish and no ions can flow.

In this thesis, the electrolytic influence on the cycling behavior is investigated by adding different solvents to the standard electrolyte. This section discusses the electrolyte influence on the diffusion, demonstrates how the SEI layer forms and demonstrates the different nature of solvents on the silicon/electrolyte interface.

Propylene Carbonate (PC) has been studied as standard electrolyte additives for graphite electrodes for years. With its low melting point, but high flash and boiling point, it is a well-known fact that it is a good candidate for temperature applications of batteries [77], where it adjusts the necessary electrolyte properties. Nevertheless, for graphite, PC leads to enhanced exfoliation by intercalating into the layers and destroying graphite [77, 169, 170]. Therefore, this type of additive is no longer used for cycling graphite electrodes. Furthermore, PC is also not used when cycling standard silicon and carbon paste electrodes. Hence, due to the chemical degradation of the PC in combination with the carbon, it leads to a well-known degradation process of silicon as well. Consequently, this additive is no longer used in silicon and/or graphite electrodes [171]. The reduction mechanism of PC leads to a pronounced formation of LiF as well as HF, which leads to a common pulverization of silicon electrodes. The chemical structure is very similar to EC, which is already included in the electrolyte. Due to the well known stereoisomerism of PC, this cyclic carbonate is chemically very interesting for the electrolytes because it tends to increase the ionic conductivity inside the electrolyte. Unlike the standard silicon and carbon paste electrodes, the silicon wire array (in this thesis) do not use any additional carbon or graphite and thus this additive is used here to modify the intrinsic properties of the electrolyte [172, 173]. This thesis demonstrates the impact of this additional cyclic carbonate to an already existing alkyl carbonate electrolyte by changing the composition of the electrolytes. As a consequence, the influence on the long-term cycling experiments for silicon are evaluated.

Additional 5 wt. % of PC is added as co-solvent to the already existing electrolyte combination EC-DMC (0.5 M PC solution). In order to check for the electrolytic influence on the cyclic performance, the anodes are cycled with different C-rates ranging from the standard slow C-rate $C/10$ to fast charging of 5 C. Each C-rate is tested for five cycles in a first experiment. After the fast charging, the C-rate is decreased again to the value in the beginning, to check if fast charging damages the electrode irreversibly. Figure 5.4 shows the results of the cycling tests with PC, in comparison to the standard (EC-DMC) electrolyte system. The capacity stays constant for every C-rate, as well as for 5 C - 12 minutes charging is possible. Due to the high symmetry of the wires, 5 C translate into 35 C for comparable graphite electrodes. The currents, the wires have to withstand, are very high and nevertheless they cope those stresses without collapsing. Compared to the standard EC-DMC

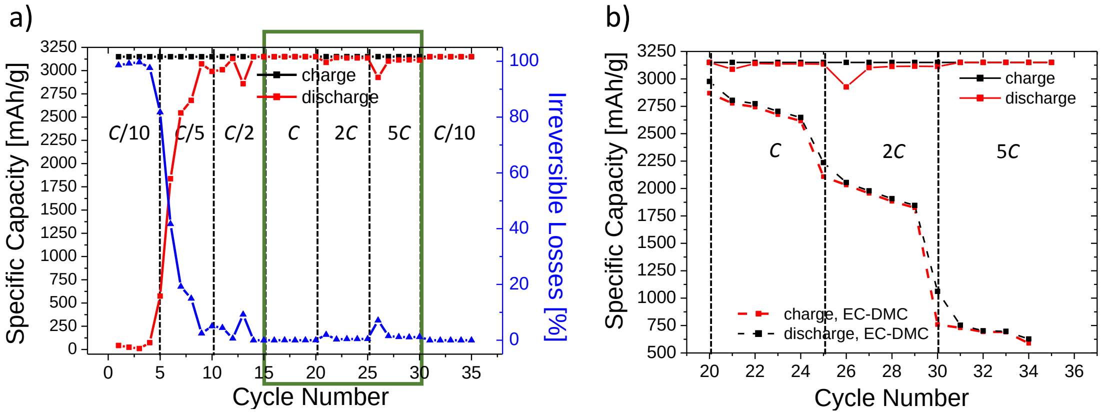

Figure 5.4: C-rate dependent cycling with 5 wt. % PC electrolytes. Every C-rate is tested for five cycles. The low C-rates are found to improve the stability of the SEI formation. 15 times higher C-rates allow charging and discharging the battery in only 12 minutes, without destroying the electrode. The comparison with the standard electrolyte system shows the significance of this additive. Without adding this cyclic carbonate to the system, fast charging was not possible.

system, the capacity decreases if the C-rates are higher than 1 *C* [91]. As visible in Figure 5.4, with PC as electrolyte additive, it is possible to achieve stable cycling with five times higher capacities and at the same time be ten times faster. Additionally, the irreversible losses decrease drastically in the first cycles during the SEI formation. Further improvement of this electrolyte showed only 25 % irreversible losses during the first cycle, reaching already a capacity of over 2300 mAh/g. This is an increase in capacity by almost a factor of two, compared to the standard electrolyte. Postmortem SEM as well as EDX analysis in Figure 5.5 and 5.6 show the elemental composition of the anode and SEI layer after cycling. As mentioned above, the SEI is a crucial factor for the performance of the anode. The SEM images in Figure 5.5 show typical SEI layers around cycled silicon wires with PC additives. The SEI covers homogeneously the wire, as for the EC-DMC system [149]. Particularly, the morphology of the SEI changed. The passivation layer seems to be porous, having small holes on the wires surface. The pores are integrated into the layer (are part of the layer) which stabilize the structure during the volume expansion of the wires. This indicates that the expansion of the wires, which are covered with a porous and flexible network is easier in comparison to a thick dense layer. If the layer is dense during volume expansion it could form cracks and openings to the silicon material underneath the SEI layer. Another advantage could be easier diffusion of the ions into the silicon wires. The SEI has different mechanical properties compared to the standard system. As mentioned

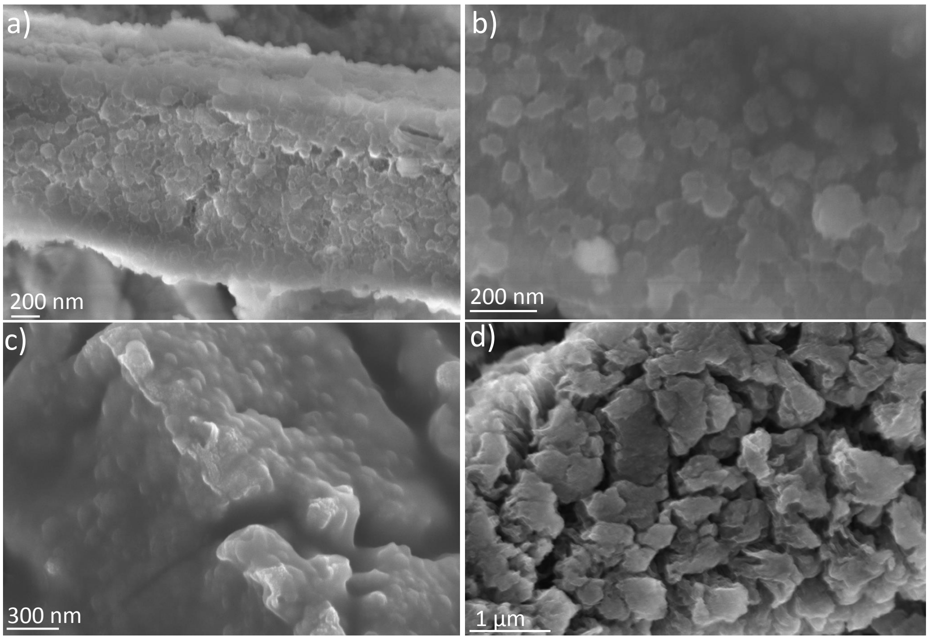

Figure 5.5: Postmortem SEM analysis of high performance array electrodes cycled in 5 wt. % PC. The SEI is penetrated with pores which enables higher charging and shows elastic mechanical behavior of the passivation layer. c) With increased PC concentration, the flexibility is lost and the meshes are covered. d) In contrast to the very smooth, but semipermeable SEI layer in the case for PC electrolytes (a), here, the SEM image indicates a very rough surface in standard electrolytes.

the irreversible losses are reduced in this modified PC electrolyte. Those losses are directly correlated to the SEI formation.

EDX reveals carbon and fluorine on the silicon surface. The amount of carbon is increased compared to the standard EC-DMC system due to the increase in carbonate reduction. The amount of fluorine in the solution or on top of the Si wires decreased. Fluorine ions are a result of the decomposition of the $LiPF_6$ salt. The reduced amount of the fluorine ions gives hints about the reduction mechanism of the PC. In order to understand the PC reduction (electrolyte reduction) after cycling, postmortem Raman spectroscopy was performed for different stages and types of electrolytes, which will be discussed even further during this thesis (refer to section 5.2.3.1).

In order to investigate the influences on kinetics and diffusion in more detail, voltammetry measurements are performed. Figure 5.7 a) shows the voltammetric results with 5 wt. % PC. The lithiation behavior is very stable, the current increase with cycle number is negligible once the SEI is formed (indicated in Figure 5.7 a), cycle 2 to 5). As it is well known, the area underneath the peaks can give strong hints about

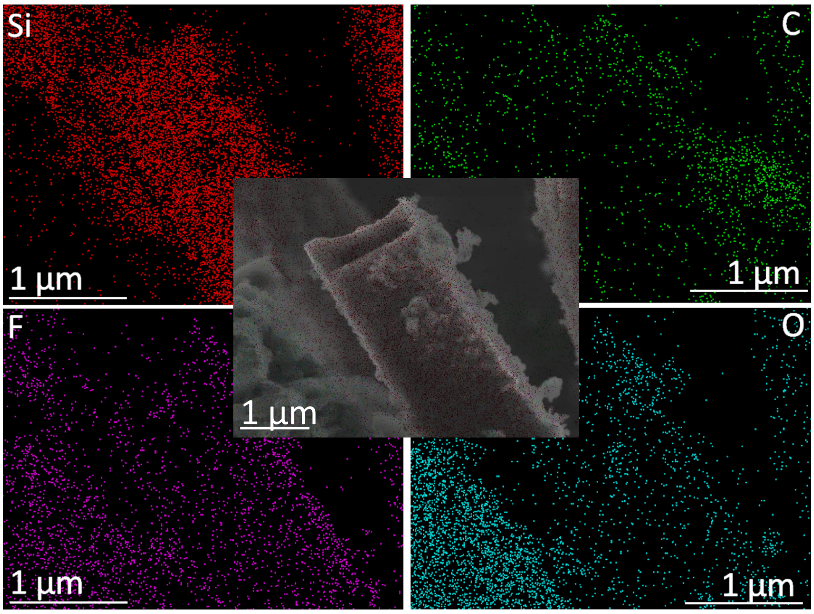

Figure 5.6: Postmortem EDX analysis of high performance array electrodes cycled in 5 wt. % PC. The spectra show an increase in fluorine on the surface of the silicon wires. The core of the silicon wire is still crystalline and not oxidized after the cycling.

the diffusional behavior i.e. the velocity of the diffusion. This is supported by the change of the peak shape (always in comparison to standard EC-DMC electrolytes). For PC electrolytes, the peaks become very broad. Consequently, these results may be interpreted as slow diffusional processes [120, 118].

With increased PC concentration up to 50 wt. %, the shape of the voltammogram changes. As indicated in Figure 5.7 b), the current increases with every cycle. Compared to 5 wt. % PC, the peaks become very narrow. During cycle 3, the delithiation peak current increases. The partial delithiation peak diminishes over time. This behavior resembles a peak overlap. The base of both delithiation peaks is the same. All of the lithiation as well as delithiation peaks are very narrow. This is a strong indication, that the diffusion of the ions in the high concentrated electrolyte is faster. The ions are very mobile and want to incorporate. This resembles the case for fast sweep rates and could be correlated to faster diffusion. It might be interpreted as a kinetic limitation for the structure, which cannot accommodate the high pressure due to faster diffusion. This is also indicated in the peak shift. As discussed earlier in chapter 4, a peak shift during voltammetric experiments may indicate kinetic changes during cycling. With high PC concentration inside the electrolytes, the experimental results show a peak shift for the delithiation process to higher potential values. This translates directly to higher voltages to remove the ions from the structure. The same holds for the lithiation. More voltage is needed to incorporate the ions into the anode. When comparing the first cycle of the low and high PC concentrations (Figure 5.7), an additional peak arises, which is usually attributed to the SEI formation. At high concentrations, anyhow, not only one peak appears, but two peaks. The latter gives first indications of the electrolyte reduction mechanisms at the interface. This type of peak depends on the electrolyte potential. For the standard electrolyte, it occurs between 0.7 V and 0.8 V. In this case, it could be a result of the excess reduction of PC.

If the PC concentration increases (Figure 5.5 c) the morphology of the SEI layer changes again. The meshes are no longer visible, indicating a possible saturation of the decomposition products or the formation of additional components, which are accounted for the roughness change of the SEI layer. Raman analysis indicated even unreacted PC molecules remaining after cycling. Only a limited amount (like in the case of 5 wt. % PC) seems to be enough to promote the elasticity change. The postmortem SEM analysis in Figure -d) already indicated, how the morphology of the silicon wires change with increased PC concentration. A thicker SEI layer was formed and the meshes seen by only small amounts of PC are no longer visible. It might be that new layers of decomposed PC deposited on top of the already existing SEI layer. This alters the mechanical properties of the SEI layer. It may become more stiff and cannot accommodate the fast volume expansion of the anode at 5 C. In general, the SEM images show the same morphology of the SEI layer. It is obvious that the meshes of the net are fully covered due to the enhanced PC concentration. The gap between the wires is completely covered with the electrolyte products, limiting the volume expansion more than it is comforting the mechanical stability of the wires. The electrolyte might become unstable; the internal reactions between PC and the lithium salt $LiPF_6$ dominate [174]. Those reactions change the silicon/electrolyte interface. Contrary to the low concentrated electrolyte, the PC does not contribute to the mechanical support of the wires anymore. Due to the correlation between the ionic conductivity and the diffusion coefficient, the change in the electrochemical behavior recorded in the experiments may be interpreted as faster diffusion. Nevertheless, at this point three reactions take place simultaneously. Due to the faster diffusional processes as reaction of the enhanced ionic conductivity, an enhanced reaction between the silicon and the electrolyte takes place. This phenomena is counteracted with the increased chemical reaction between the lithiated surface of the silicon and the

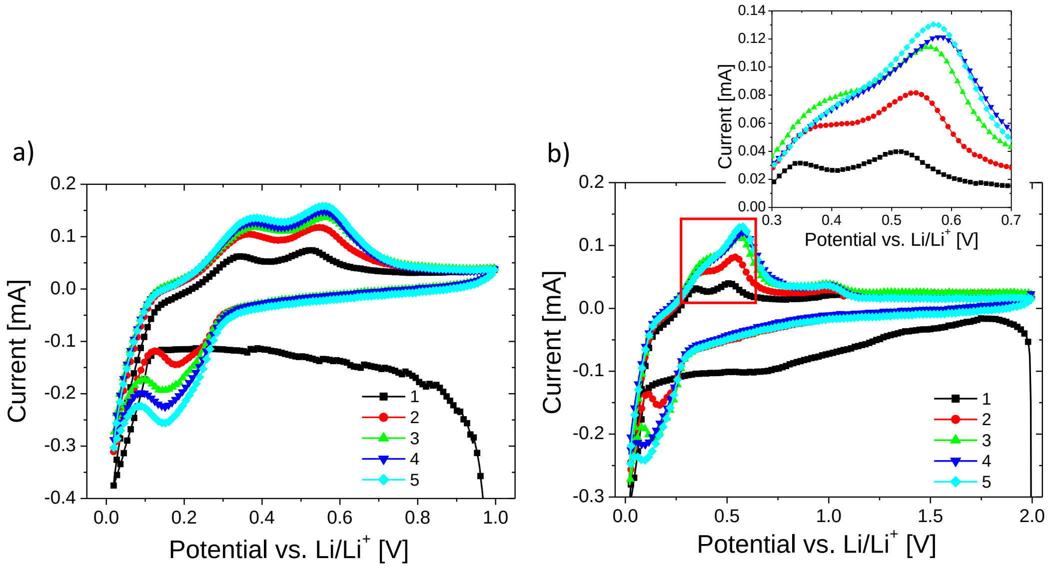

Figure 5.7: Voltammetry results with varying PC concentration in the electrolyte. a) The voltammogram for low PC content (5 wt. %) shows stable and reversible lithiation as well as delithiation behavior. With increasing amount (50 wt. %) of PC b), the delithiation behavior is dominant and the diffusion increases due to the increased reduction reaction of PC.

dissociation/reduction products of the PC which effects the SEI on the surface of the wires. With increased PC concentration, also refer to 5.2.3, the capacity shows repeatedly a wavy-like fluctuation during cycling at 5 *C*. The capacity is not stable at 3150 mAh/g, but reduces to maximal 1000 mAh/g. In summary, the maxima and minima in the capacity result from the opening and closing of the SEI layer. Due to the very fast charging as well as discharging process, the stress upon the wires exceeded a critical value upon which the SEI layer broke. This leads to a capacity fade. When the SEI grows again, it closes the gaps like a band-aid; thereby increasing the capacity again.

5.2.2 Linear Organic Solvents

As shown in the last section, additional cyclic carbonates inside the electrolyte change the structure of the SEI layer, allowing an increase in C-rate by a factor of 10. This section summarizes the influences of linear solvents, either ether based or carbonate based linear solvents. Usually, they are added to the electrolytes to influence the melting as well as boiling point of the electrolytes, simultaneously reducing the viscosity of the electrolytes. The investigated solvents include also typical sulfur electrolyte solvents like dimethyl ether (DME) as well as Tetraethylene glycol dimethyl ether

(TEGDME). This section contains only an excerpt of the complete analysis of the linear solvents. Another part of this analysis is postponed to the electrolytic analysis for the full cell compatibility. The direct comparison of all the tested ethers or carbonates is summarized in Figure 5.8 in their voltage curves, always in relation to high C-rates.

The individual differences are directly seen in these cycling tests. Thus, it is evident that using electrolytes composed of only linear solvents is not sufficient to allow fast charging processes. Further discussion of the used solvents will indicate the electrolyte properties and will allow to better correlate these results. When comparing the analyzed solvents DMC, DEC and DME, an essential difference can be concluded (Figure 5.8 a): a) With this type of electrolyte, the predefined voltage limitation is reached too early. As a consequence, the capacities are limited. Following this, the internal resistance increases drastically, and superimposes on the irreversible losses.

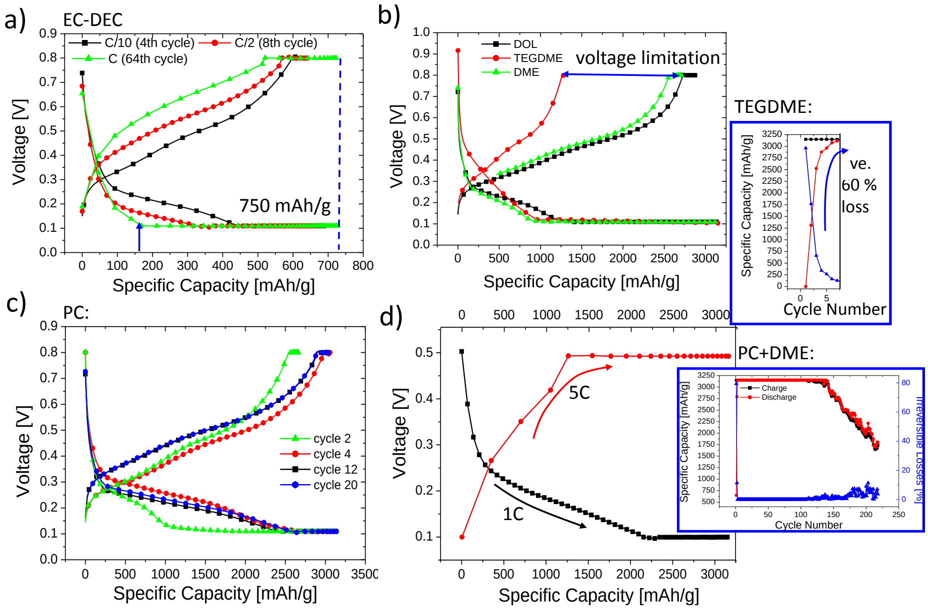

Figure 5.8: Detailed solvent investigation depending on C-rates based on the capacity vs. voltage curves during cycling. a) It describes the cycling performance inside EC-DEC electrolytes and indicates the limitation. From the course of this plot, it can already be deduced that the lithiation is not a two-step process. There is no plateau, but instead the voltage decreases exponentially. b) The summary with varying ethers and carbonates indicate the reason behind possible electrolyte depletion behavior in TEGDME electrolytes. The low viscous medium together with other electrolyte limitation leads to a severe loss in the first six cycles, combined with a disturbed SEI formation. c-d) Both figures describe the exceptionally good performance at high C-rates with the addition of PC and DME to the electrolytes.

DEC leads to a completely different chemical and structural behavior, compared to the others, especially during the SEI formation process. Cycling experiments show that no stable SEI formation is possible, which has a direct consequence on the capacity fading throughout the measurements because the irreversible losses were high throughout the experiment. Postmortem TEM as well as Raman spectroscopy indicate the structural change of the silicon wires, when exposed to DEC electrolytes. The wires start to be in an "intermediate" state between crystalline and completely amorphous [175]. Locally at the interface between the silicon wire and electrolyte, the chemical decomposition reaction of this type of electrolyte leads to an exothermic reaction due to the enhanced OH-groups inside the electrolytes and subsequently to an enhanced, local oxidization [176, 177, 178]. The capacity-voltage curves indicate a switch from galvanostatic into the potentiostatic state already below 500 mAh/g in the third cycle, which is unusual for cycling silicon wires. It is necessary that the galvanostatic mode is longer active, in order to reach high capacities. The capacity does not stabilize anymore, especially at high C-rates. As indicated, DEC partially oxidizes the silicon wires and leads to structural re-orientation and partially amorphization leading to a lack of mechanical stabilization of the free-standing anode. Figure 5.8 b) shows another comparison between TEGDME, DME and a mixture of DOL and DME (like it is standard for sulfur electrolytes, [179, 180, 181]). It indicates the limitation of the glyme electrolytes (TEGDME): During charging this electrolyte, it reaches the voltage limitation already at 1000 mAh/g, whereas the other solvents can be cycled up to 3000 mAh/g, without reaching this limit. This means that the internal resistance is too high for the battery and needs higher voltages with every new cycle to push the reaction forward. Problems when cycling TEGDME are a direct consequence of the low viscous fluid, which is even more diluted with the addition of DME inside the electrolyte. TEGDME is a standard solvent additive for Li-S or Li-Air batteries. This low viscous medium around the silicon wires leads to an electrolyte depletion and consequently to a disintegration of the silicon wires. In direct comparison, TEGDME with its low viscosity cannot transport a lot of medium while the ions are diffusing to the wire interface, thus producing high amounts of losses, as indicated, with an average loss of more than 60 %. As indicated in the thesis, the higher the viscosity during SEI formation is, the lower the losses. DOL enhances the reaction due to the cationic polymerization reaction at the interface to the wires, reducing the losses in the beginning. Concluding this investigation, when changing only the linear carbonate inside a standard, non-carbonaceous electrolyte, no cycling stabilization, especially at high C-rates, could be observed. Only when adding the additional PC, the reaction inside the electrolyte could allow faster C-rates during charging, thus, stabilizing the electrolyte.

5.2.3 FFT-IS Analysis of pure electrolytic systems (electrolysis)

With a modified and novel FFT-IS measurement technique, the electrolyte as well as the SEI formation could be analyzed without the need of a silicon electrode. This measurement may be considered as electrolysis. This measurement is designed to eliminate all the disturbing influences and interactions, like transport phenomena through the silicon wires, between the silicon-electrolyte interface or the copper-electrolyte interface. If the active material is still inside the battery, the SEI forms due to the interaction with the silicon wires. It is possible that some reactions are slowed down or even triggered because of the reactive interface with silicon. This analysis is done as well, but only after being able to differentiate the measured impedance data for the silicon from the influence of the pure electrolyte. By using inert electrodes for examining the electrolytes, an artificial SEI layer forms on top of these inert electrodes. Thus, the impedance data is not falsified by the individual interactions with the silicon and is a pure result of the dissociation and reaction between linear and cyclic carbonates. With detailed knowledge about the electrolytes and their behavior, it is possible to understand the previous battery performances and if necessary adjust the electrolytes.

In order to understand why and how the PC addition to the electrolyte leads to this drastic performance increase, it is analyzed with the FFT-IS analysis always in reference to the standard, carbonaceous electrolyte Selectilyte LP 30, indicated in Figure 5.9 by the pre-dominant functional groups EC-DMC. Here, the focus is only on the series resistance R_s, representing kinetic transport processes at high frequencies (20 kHz). Figure 5.9 a) shows the series resistance of both electrolyte systems. The first part (up to 600 minutes) is the first cycle of the cyclic voltammetry measurement. During this electrolysis, $LiPF_6$ dissociates into Li^+ and $(PF_6)^-$. The $(PF_6)^-$ dissociates further into $(PF_5)^-$ and reacts either with the linear carbonates or, which is most likely under ring opening with EC. It is well accepted, that EC reduces according to the one-electron transfer reaction [171, 116, 77, 182]. This dissociation is followed by a viscosity change with time. Principally, the dissociation is similar in all of the three investigated electrolytes, because they contain all the same base electrolyte. The

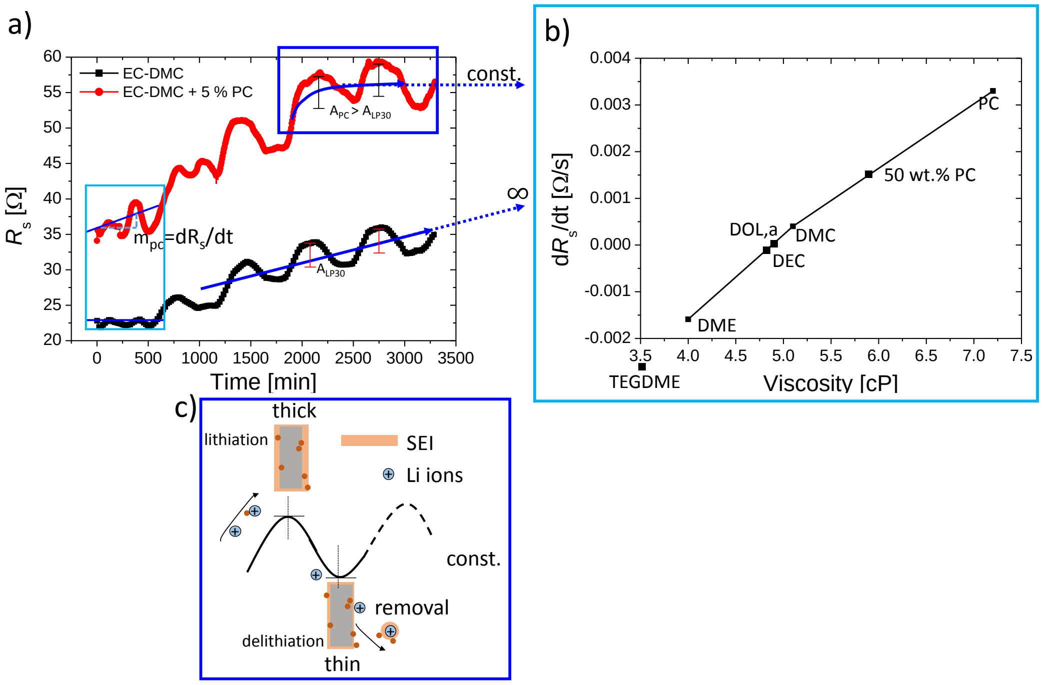

Figure 5.9: FFT-IS-Electrolysis of battery electrolytes. The series resistance during this measurement is characteristic for each electrolyte system. a) It shows in a comparison the different electrochemical dynamic of the electrolytes. The average slope can be extracted by fitting the curve to straight lines using multiples of full periods. Thus, probably the slope of the linear fit in the first region can be attributed to the viscosity of the electrolyte. The changes of the slopes b) for each electrolyte are plotted in dependence of the calculated (literature values) viscosities. c) The schematic shows the occurrence of the amplitudes in the series resistance. The maximum indicates how the Li ions diffuse towards the wire during lithiation and carry electrolyte material. During delithiation, the ions carry some with them leading to a thin SEI layer [98].

addition of PC changes the electron reduction reaction to a two-electron reaction, leading most probable to different reaction products [116]. Anyhow, the first part differs in its slope, indicated by a linear fit (Figure 5.9 a). For the standard EC-DMC system, the linear fit is almost parallel to the x-axis with a very small slope ($m_{EC-DMC} = 0.000069$). Although the ionic conductivity should increase with the addition of PC [77], the series resistance increases. The offset in R_2 is larger compared to the standard electrolyte as well as the slope of the linear fit of the first cycle (by a factor of 35). For the DME system, the slope is even slower than the standard system ($m_{DME} = -0.00146$). Figure 5.9 b) shows exactly this linear fit. PC and DMC are not the only solvents under investigation. When taking all investigated solvents (linear as well as cyclic carbonates, ether and esters) into account, a clear correlation to the individual viscosities during cycling could be made. In order to support this theory, literature values for the viscosities of each solvent component [180, 94, 95, 113, 162] are used in order to calculate the total viscosity of the examined electrolytes. This calculation is based on the Walden rule and on equation 5.1 [180]:

$$\eta_{electrolyte} = \eta_{solvent,1}^{1-x_{solvent,2}} * \eta_{solvent,2}^{x_{solvent,2}}, \tag{5.1}$$

where η_x are the viscosities of the pure solvents, x_n the molar fractions of the solvent compositions i.e. ratio between the solvents inside the electrolyte. The results of this calculations are indicated in Figure 5.9 b). The fit corresponded perfectly to the slopes of the impedance data, demonstrating the correlation between the viscositites and the series resistance in the beginning of the electrolysis.

What does this mean now for the electrolytes? In general, viscosity is a synonym for the resistance of a particle (ions in this case) to move. It is a force perpendicular on a system or particle diffusing through the electrolyte, upon shear stress. While diffusing from point a to point b, it carries material with it, depending on the viscosity of the surrounding medium. A particle would carry more material, if the viscosity increases, as in the addition of PC. In the case for the Li ions for the battery electrolyte, the ions diffuse through the electrolyte and to the silicon/electrolyte interface, where the passivation reactions take place. For higher viscous electrolytes the ions carry more material to the interface, forming a different, more elastic SEI layer. There, an enhanced reaction between the ions, the dissociated solvents and silicon takes place. This influences the morphology of the SEI and consequently the measured series resistance. Both curves increase after 600 minutes. For the standard system, the curve continues to increase periodically with a large amplitude in series resistance. This is indicated in the Figure 5.9 a) by the infinity sign. When adding PC to the electrolyte, not only the slopes change, but the second part changes as well. The total amplitude of the series resistance increases. But in contrary to the standard electrolyte, with time this electrolyte reaches a steady-state. This steady-state means that the electrolyte is not continuously decomposed. A continuous decomposition or dissociation of the Li salt would maybe lead to an even higher increase in the series resistance, as supported by measurements of an electrolyte, which is already decomposed (Appendix A1). Considering the applied voltage characteristics as well when looking at R_s, the amplitude modulation could be explained by the transport process with respect to the viscosity. The maximum of the series resistance curve (in the last region) is the part, where the Li ions incorporate into the silicon wires. Like discussed previously, if the Li ions diffuse through the electrolyte towards the silicon-electrolyte interface, it takes material with it, which is deposited at this interface. Exactly this behavior is represented here in this transport resistance. The minimum of the amplitude is attributed to the opposite. If the Li is extracted again from the silicon anode, material is removed from the interface, when the wire contracts. Thereby, the solvation shell and the SEI layer is thinner because the surface area is getting smaller. Due to the fact that the total amplitude of this region is larger for PC electrolytes, it could indicate larger transport processes and restoring forces occurring around the silicon wire. Additionally, if the viscosity increases the transport processes are slower represented in a lower diffusion coefficient. Nevertheless, as shown in the experimental results, the increase in series resistance is nothing bad, but actually beneficial because it correlates to an enhanced inner elasticity of the SEI layer (Figure 5.9). The schematic indicates the transport of material to the silicon wire interface. The maxima appear because the SEI layer is more thick due to larger transport to the wire interface and therefore more resistant. During delithiation, the ions transport the material leading to thin SEI layer and a less resistant state [98].

This stabilization is necessary to allow an SEI layer with modified mechanical properties. The dynamics of the electrolyte show that a standard electrolyte concentrates on the continuous passivation and establishment of the SEI layer. The high slope in the series resistance of the electrolyte with PC corresponds to higher viscosity (that forms during charging). Viscosity and dynamics are directly correlated to each other. The viscosity increase supports the silicon wire array, making the electrolyte dynamic very stable. The very low R_s value for the ethers and esters is also a consequence of the transport processes. Due to the enhanced OH-bond formation at the silicon surface, it leads locally to a surface oxidation and a very thin SEI layer. The complex decomposition reaction like proposed by Campion et al does not lead to a stable SEI formation on silicon surfaces, but result in many oxygen-containing electrolyte components like OH, CO_2 and oxygen production will change the series resistance behavior in the impedance data [175, 178, 177, 176]. A similar behavior in the second region is obvious with DOL solvents. In combination with DOL, there is a larger tendency that OH-groups form or are split off the reaction. Summarizing these results, the first part of the series resistance curves are a result of the viscosity change of the electrolytes. The higher the viscosity change, the more material is transferred to the SEI layer. The second part of the series resistance indicates the electrochemical dynamic of the electrolyte and the restoring force of the resulting SEI layer could be estimated. For the high performance electrolyte, the series resistance stabilizes and does not increase anymore. A too high resistance in the long term means that the ionic conductivity of the electrolyte is lost, slowing down diffusion mechanisms. If, on the other hand, the conductivity remains stable, the ions can move in and out of the electrode without kinetic limitations. Additionally, it implies that the lithiated salt is not irreversibly decomposed and remains coordinated in the electrolyte. The correct amount and concentration of PC helps to coordinate the lithiated salt, mainly due to the delocalized methyl groups of PC (i.e. stereoisomerism). Viscosity can be expressed as difference in mechanics of the SEI layer. Consequently, it is necessary to understand the mechanics or in general the physics behind the SEI layer.

5.2.3.1 Chemical electrolyte analysis

The reason behind the viscosity increase and the difference in performance is very difficult and multifaceted. Raman analysis could indicate some important reduction mechanisms, which will be shortly summarized in this section. The reduction of an electrolyte with PC follows principally two different electron-reduction reactions, which are well known on graphite electrodes [183, 184]: the one-electron reduction and a two electron-reduction reaction. In order to fully characterize the possible reduction mechanism of PC, it is necessary to consider the experimental facts as well as the possible reaction products, which might actually lead to a viscosity increase of the electrolyte.

- *one-electron reduction reaction*: One PC molecule reacts upon ring-opening under electron release. During this reaction, it is possible that either an longer chain molecule forms or lithium alkyl carbontes form. This kind of electron transfer reaction is highly unlikely, because the PC molecules react with each other, thus being molecule molecule interaction.
- *two-electron reduction reaction*: It is well accepted that PC reduces along a two-electron reduction reaction (at least on graphite electrodes). For this type of reduction, there are several reaction mechanisms. Upon ring-opening, two PC molecules open up and form an oligomer. An oligomer would then lead to a higher viscosity because the chain length increases. On the downside, LiF forms and segregates. LiF is a solid and forms usually small particles. The EDX analysis, on the other hand, on the silicon surfaces revealed that the fluorene concentration reduced, compared to the standard electrolytes. Additionally, no signs of spherical particles were found on the silicon surface. LiF is usually found on graphite electrodes. It is supported by additional experiments using a silicon-carbon black mixture, where exactly these small amounts of fluorine particles appear. But due to the fact, that the silicon arrays do not need additional graphite, either this reaction path is not happening or what might be highly likely that the lithium salt $LiPF_6$ further reacts. There is an equilibrium reaction between $LiPF_6$ towards PF_5 and LiF. This reaction is likely to shift towards the products and to an enhanced PF_5 concentration in the electrolyte. PF_5 is a strong Lewis acid, which is a well-known initiator for radical polymerization [94, 174, 185, 186]. In this case, the Lewis acid triggers a polymerization reaction between the PC molecules or between PC and the linear carbonates, leading

to a longer chain molecule. As non-aqueous electrolytes consist mostly of organic solvents, organic chemistry needs to be discussed. Lewis acids act as initiating agents for cathodic polymerization reactions. Upon ring-opening of the cyclic carbonates PC and EC, the polymeric chain of the new build monomers propagates (upon reaction with the linear carbonates). The polymerization velocity highly depends on the polarity of the solvents, which is higher for PC. PF_5 is the end product of the decomposition reaction of the lithium salt. In the first step, the radical PF_6^- forms. This peak is detected in the Raman analysis. In general, this peak appears at $738\,\mathrm{cm}^{-1}$ (Figure 5.10). For the PC electrolytes, this peak slightly shifts to higher values, resembling to a weak coordination of this radical. LiF is not detected directly in the Raman analysis, whereas it might still form, but that the peak is not detectable in either Raman nor SEM, because they are not sensible to lithium. Due to the fact that graphite (or in general additional carbon) is missing, it is more likely that not LiF forms, but Li_xPF_y in addition. The viscosity increases due to the reaction of EC and PC with the linear carbonates [174, 116, 113, 172]. Upon ring-opening, the cyclic carbonates react with the linear carbonates and form long-chain polymers or oligomers. This formation of a long chain polymer stabilizes the reaction of the solid electrolyte interface. Depending on the chain length of the polymer, the electrolyte will become unstable, because it completely polymerizes and hardens. For enhanced PC concentration, the viscosity increase and change of the SEI is not beneficial anymore, as discussed in chapter 5.2.1. Following the above explanation, the polymerization reaction might be either too fast or due to a lack of PF_5 it leaves un-polymerized functional groups inside the electrolyte. As for PC, Table 1 A in the Appendix summarizes all the necessary data for the analyzed electrolytes. Although PC does not seem to be structurally very different to EC (except an additional methyl group), the viscosities and dielectric constants are very different. Thus, implying, that the overall viscosity of PC leads directly to a viscosity change of the SEI due to cationic polymerization. The task is to locally enhance the viscosity during the SEI formation, but still be electrochemically stable in the long term (and not harden completely) [94, 170, 169, 174, 187].

- There are additional possibility of reaction path. Nevertheless, those reactions take up water and form volatile components like CO_2 inside the battery. Raman analysis could not reveal any sign of water (no hydrogen peak, coordination with OH). Any pressure build up inside the cell would be obvious in form of (at least) gas bubbles during cycling. These ways could be excluded. The previous experiment revealed that the viscosity oft he SEI layer increased. That is precisely the reason why the reaction path with only short chains is also highly unlikely. Lots of small chains would not lead to a higher viscosity of the electrolyte [171].

- In general even LiO might form at the silicon surface and therefore leading to surface oxidation in DEC electrolytes for example [175, 177]. This peak would appear at 603, 605, 609 and 612 cm^{-1}. During the electrolyte variation, on the other hand, this peak did not appear. Neither for the PC variation nor for the DEC electrolytes. Nevertheless, this reaction could not be completely excluded, but is not very likely. LiO is kinetically very unstable and decompose further into different components. Due the instability, it might be that the EDX analysis did not detect this as LiO formation.
- In correlation to the radical PF_6^-, which is found in PC electrolytes, the stereoisomerism needs to be considered. PC has the ability to form different coordination around the lithium salt. Nie et al. reported the different coordination depending on the electrolyte viscosity as well as number of free lithium molecules. The PC molecules are highly mobile inside the electrolyte. Therefore, it has the tendency to coordinate by different geometries like tetra or tre-bonded coordination. As reported the EDX analysis shows reduced fluorine concentrations. In agreement with Nie et al., it might be that the PC forms a tetra-coordination with a solvated PF_6^- around this complex. This solvated PF_6^- is weakly bonded. Taking the coordination into account and the cationic polymerization reaction, it is highly possible that this is the reason for the viscosity increase at the silicon-electrolyte interface [171, 116, 171, 111, 182, 94].
- As it forms this tetra-covalent bonding or coordination, the PC forms so called bond bridging and tends to "drag" the lithium ions away from the usual bonding between EC and $LiPF_6$. The last to points represent the peak at 721 cm^{-1}. The shift in peak 712 cm^{-1} resembles exactly this difference in coordination, as it is usually a bond bending [188, 189, 171, 111, 182, 94].
- The peak at 898 cm^{-1} is unaffected in the PC electrolytes, anyhow, a slight shift and an additional peak is noticed when using the standard electrolyte as well as for the DEC electrolytes. As a summary, this is attributed to a ring opening or ring breathing of the EC inside the electrolyte, meaning a solvent-solvent interaction might appear in these electrolytes [175, 177] (Figure 5.10).

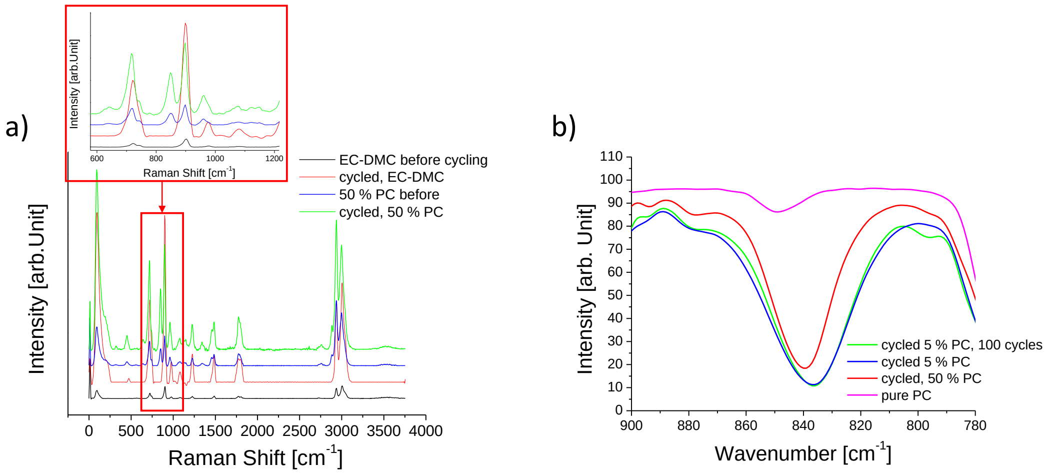

Figure 5.10: Raman and IR analysis of the cycled electrolytes of different PC concentrations. a) The overview shows examples of the analyzed electrolytes before and after cycling. The y-axis is shifted vertically in order to clarify the different spectra. The inset shows the most important PC peaks for high concentration of PC. b) The additional IR analysis of the cycled 5 wt.% PC shows a shift and a splitting of the $LiPF_6$ absorption peaks, normally attributed at higher molar concentration and consequently to high viscosities, like observed during cycling. It also includes the long-term cycled electrolytes, which does not show any significant change anymore. With these changes in the absorption peaks, the solvation and coordination of Li and PC changes and less PC could be coordinated around it. This coordination on the other hand allows reversible cycling with the analyzed viscosity increase.

The concentration of the measured PC electrolytes is at 50 wt. % inside the electrolytes. To some extend, there exist non-reacted, free PC molecules inside the electrolyte even after cycling. It tends to reach a saturation concentration, above which, the viscosity does not change anymore and it even tends to dilute. As a result, the cycling performance reported previously is not very good, but instead shows additional maxima and minima in the capacity curves. Subsequent, IR analysis of only 5 wt. % PC electrolytes (Figure 5.10) shows an additional contributions, which is coherent to the first cationic polymerization reaction.

- Cycled 5 wt. % PC electrolytes show an additional absorption peak as well as a shift of the $LiPF_6$ absorption peak, which appear at $835\,\mathrm{cm}^{-}$ as well as at $877\,\mathrm{cm}^{-}$. These two absorption peaks usually appear at higher molar concentration of $LiPF_6$. At these concentrations usually the number of PC molecules bound with Li decreases and not the tetra-, but a tre-coordination appears. If this type of coordination appears, the solution structure changes with the solvation. In this case, as there is no graphite, that would form either LiO, Li_2CO_3 and LiF, the complete fluorine molecules contribute to the higher concentration of the

> $LiPF_6$ and the further reduction in order to result in the proposed cathodic polymerization. Kondo et al. invested in this case a drastic viscosity increase with higher concentration of $LiPF_6$, detected by the peak shifts at $835\,cm^{-1}$ [174, 171, 190, 113, 99].

As a conclusion, the electrolyte analysis with Raman as well as with IR is a very complex and complicated process. By considering both methods, the coordination change between 5 wt.% to 50 wt.% could be detected, thereby changing the inner viscosity and elasticity of the SEI layer around the silicon wires. The next section now uses this analysis of the electrolytes and transfers it to the silicon-electrolyte interface trying to identify and simplify the reactions inside silicon anodes. Without the physics of the SEI layer and the direct contribution to the charge transfer process, no qualitative analysis of the cycling performance can be performed. The mechanics and the charge transfer process are correlated for highly-ordered systems as well as for paste electrodes. The importance to model electrolytes according to their change in viscosity is multi-faceted because a) the best parameters can be adjusted without the necessary electrode, thus reducing production and battery costs, b) the exact electrolyte parameter variations are not falsified by an additional interface interaction and c) it is possible to produce large amounts of specialized electrolytes in advance. In addition, even artificial SEI layers can be produced by deliberately considering polymerization processes with even different solvents like 1,3-dioxolane (DOL). DOL as standard solvent for sulfur electrolytes is further discussed also regarding the electrolyte compatibility for full cells in chapter 5.4.2. The importance of the electrolyte degradation and the possibility to detect it as well with the impedance spectroscopy is discussed further in detail in Appendix A2.

5.2.3.2 Impact of Viscosity on SEI

The electrolytic impact on the SEI formation can be modeled by introducing the viscosity and elasticity change on the wires. Upon cycling and (with the use of a different electrolyte), the viscosity of the electrolyte changes from fluid-like behavior to more viscous electrolytes. The viscosity plays an important role in the function of the SEI layer. The SEI could be modeled with two separate systems: First, it works like a zip of a jacket. To close the jacket, the zipper has to be tightened from below, narrowing the body inside the jacket. This is comparable to the SEI layer. The SEI forms from below and then zips the wire up - it forms homogeneously around it. Due to the viscosity change, the SEI layer changes its mechanical properties. The elasticity changes. It behaves like an elastic fisher net made of different mesh sizes.

Figure 5.11 shows in postmortem SEM images a typical example of the very unusual morphology of the SEI layer around the cycled silicon wires, when cycled in viscous electrolytes like PC. When cycled in this type of electrolyte, meshes form inside the SEI layer around the silicon wires. This only happens in the specialized PC electrolytes. The SEM image shows the meshes inside the SEI around the wires. This behavior is shown exemplaryly in Figure 5.11 b). The very elastic SEI layer around the wires adapts every movement of the wires. It is around the wires like a second skin. At high C-rates, there is a large overpotential and high currents, which might damage the silicon wires. Even at standard conditions, the currents are higher than for normal silicon or graphite electrodes. With the even higher C-rates, the currents are now increased by a factor of 10 (compared to $C/2$ conditions).

Another possible effect might be that the time for a complete recrystallization is not possible. When the wire expands very fast due to the fast C-rates, the SEI layer tolerates that volume expansion perfectly. The meshes inside the net together with the elasticity are very important. A stiff layer around the wires can maybe

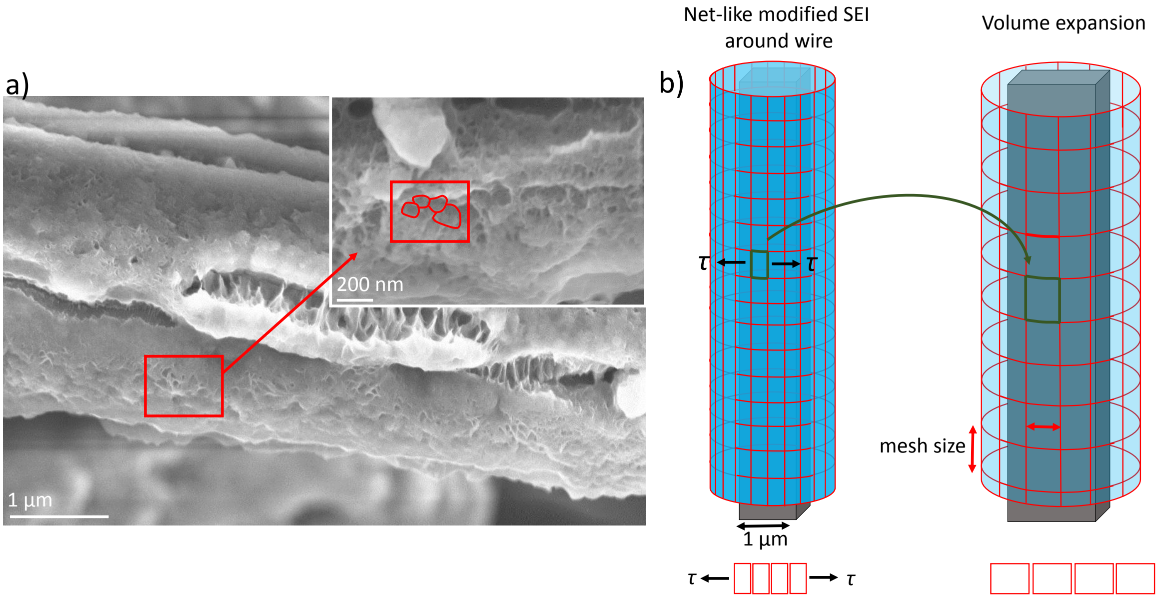

Figure 5.11: Model of the elastic and viscous SEI behavior in PC electrolytes. The SEM image shows how the SEI layer looks like after charging and discharging silicon microwire arrays with 5 wt. % PC. b) The right schematic shows a net with various meshes, that expands more elastic compared to the SEI in the standard EC-DMC system and can adapt the behavior and movement of the wire like a fisher net in the water.

cope with moderate volume changes, like $C/10$ up to $C/2$ for the standard EC-DMC system. If the SEI layer around the wires is stiff, it is hard to adapt the movement of the wires without breaking. This effect is well known from literature [81, 163]. A SEI layer around spherical particles or differently shaped geometries, for example, behaves exactly like this. It breaks or opens, not completely, but in parts. This leads to enhanced electrode/electrolyte contact, which might locally lead to enhanced oxidization or disassembly of the electrode.

The viscosity change of the electrolyte and the modified SEI layer around the silicon microwire arrays protects the wires and allows fast charging. TEM analysis showed that the inner core of the wires stayed completely crystalline after charging it with 5 C. Around the wires, there is only a small area, which shows amorphization. Normally, with repeated number of cycles at higher C-rates, silicon amorphizes faster. This demonstrates even more the mechanical stabilization of the SEI layer. The function of the SEI layer is not limited to a chemical barrier, but it works predominantly, as mechanical stabilization of the wires. The wires in the array are very narrow and need special mechanical protection. They are exposed to very high currents, which would lead to a destruction of the wires, if they are not stabilized intrinsically with the SEI layer. The fisher net, which forms around the wires, keeps the crystallinity of the wire. It allows to store the crystalline structure from the initial state or enables the initial state conditions to be repeated. The amorphization is slowed down and delayed for the crystalline phases to stay longer. The crystalline phases provide high capacities because they can store much more Li ions. In combination with PC and DME, it is possible to realize high alternating C-rates (5 C as well as 1 C), compare Figure 5.8. This could only be realized by giving the electrodes enough (optimal) time to recrystallize. The drawback would be, if the silicon structure does not have enough time for the recrystallization, it would get amorphous during cycling. Amorphous silicon is mechanically very instable. Thus, the highly-oriented silicon wires would loose their stability and would eventually break during cycling with these high current densities. This type of pulverization is very common for silicon electrodes because the volume expansion of the material is this high. The cycling behavior is exceptionally good and could only be realized with the additional mechanical stabilization of this type of electrolyte. With this combination, it was possible to achieve even long term stability with the alternating C-rates (5 C as well as 1 C). Using only PC does not result in long cycling experiments because of the different coordination possibilities of PC. But in order to show what is possible Figure 5.12 shows another very impressive experiment when cycling these wires with $C/5$ during discharging and $5\,C$ during charging. The cycling experiment in Figure 5.12 exhibits the maximum capacity up to cycle 20, and then the capacity drops to 1500 mAh/g. This transition is correlated to the change of the C-rates. The charging process is performed in only 12 minutes. In contrast to that, the discharging or the lithiation process takes 5 hours for the first part, and then 2 hours for the last cycles. The corresponding voltage-capacity curves (for $C/5$ and $5\,C$) indicate how the cycling experiments worked for three different cycles. The discharging curve has two slight voltage plateaus, corresponding to the two-step lithiation process. Almost the complete experiment is performed at galvanostatic charging. The potentiostatic step is only activated at high capacities. Consequently, this rate is not kinetically limited. The charging process, on the other hand, is performed within one step galvanostatically up to 2000 mAh/g. The third cycle shows first hints of the limitation of this type of cycling. The voltage drops or saturates before it reaches its voltage limitation. This might indicate irregularities in the corresponding current. When charging the anode with a faster discharging rate, the charging currents cannot follow anymore and the capacity drops. This could have two explanations: This version of experiment directly follows a very different cycling profile. It is discharged really slowly, in order to really get the lithium in to the correct silicon phase, followed by a very fast charging. The difference in current densities

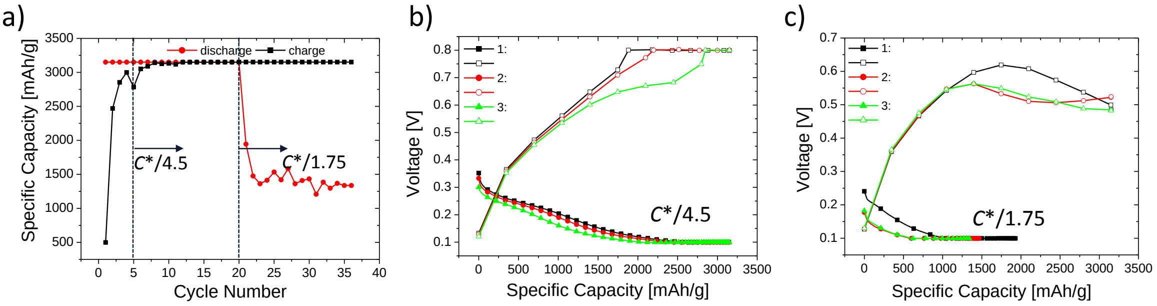

Figure 5.12: Potential of cycling silicon wires with slow and fast charging rates. a) The cycling experiments indicates the maximum capacity up to cycle 20, and then the capacity drops to 1500 mAh/g. This transition is correlated to the change in C-rate from $C/5$ to $C/2$. The charging process is performed in only 12 minutes. b) The corresponding voltage capacity curves (for $C/5$ and $5\,C$) indicate how the cycling experiments worked for three different cycles. The discharging curve has two slight voltage plateaus, corresponding to the two-step lithiation process. c) The last discharging experiment is performed within two hours, as well with high charging rates. This point emphasizes the limitation of the alternating C-rates, supporting the necessity of (re-)crystallization. C^* indicates that the imposed C-rates and the real C-rates (after the experiments) are not the same, but rather the discharging process is slightly faster than 5 hours.

is enormous. For $C/5$, the current densities are usually approximately 0.84 A/g, whereas the charging process has current densities of more than 21 A/g. Following these results, it is evident that the difference in current density could destroy the silicon wires in combination with the high volume expansions. The wires would not be intact anymore and lead to enhanced amorphization and therefore to mechanical failure. Like this, the silicon wires can withstand 140 cycles with the high cycling rate. The reason behind the alternating charging rates is based on the two models. Due to sandwiched silicon and the continuous flow of (the correct amount of) crystalline silicon, enough crystallinity (i.e. crystalline silicon) is available to keep it also at the enhanced volume expansion. The limitation is here the discharging process, which is perfectly understood. The silicon system needs the time to keep the crystallinity and to re-crystallize as discussed with the in- and ex-situ experiments in chapter 5.3. The advantage of this highly-oriented structure with the embedded metallization is the key requirement to allow the crystallinity and re-crystallinization. If, on the other hand, the same high C-rate is applied during the lithiation process, not enough crystalline silicon can diffuse into the rest of the wires of the array. During every lithiation process, a small part of disorder i.e. entropy increase is induced into the system. Furthermore, it demonstrates the strength of the silicon microwires as anodes, because they can withstand these current densities and stress. As a summary, the complex system of charging rate, electrolyte and crystallization needs an optimal configuration in order to maintain the crystallization, enable a mechanical stabilization of the individual wires and still allow fast charging times. The capacity fading in Figure 5.12 c) might not only be an historic effect of the previous cycling, but it also means that the time for the recrystallization is not enough in this type of electrolyte. These experimental facts rely not only on the modified electrolyte, but also on the intrinsic crystal structure during charging. These contributions will be discussed further in a later chapter 5.3.2.

5.2.4 FFT-IS Analysis of silicon-electrolyte interfaces

In order to understand how the newly designed electrolytes perform with silicon, the FFT-IS analysis is also applied to silicon anodes. The results from the previous FFT-IS-electrolysis directly influences this discussion. The viscosity change, the difference in ionic conductivity in the multi-blend electrolytes all have to be taken into account to discuss the resulting time constants. The strategy of this new developed investigation is based on the reduction of all the unnecessary electrodes. The FFT-IS-Electrolysis analyzed the pure electrolyte. All those indications are transferred to the silicon-electrolyte interface. Gaberscek et al. [160, 191, 162] evaluated that every component in a battery should be seen as an interface. Particularly, FFT-IS-Electrolysis revealed the interface between the electrolyte and inert electrodes; thus stating only changes of the electrolyte. With the increase in dielectric constant the conductivity increases and with it the series resistance of the system decreases. This translates into reduced ohmic losses which fall over the electrolyte because the conductivity and, in consequence, also the ionic mobility inside the electrolyte is enhanced. Figure 5.13 shows the impedance data for silicon microwire arrays for different electrolytes. The standard system on the left is already discussed in chapter 5.1. Therefore, only the difference between the electrolyte with the new background information about them is discussed here. When comparing the three time constants, τ_1 and τ_2 follow a similar curve, whereas the slowest time constant shows a completely different behavior. In contrast

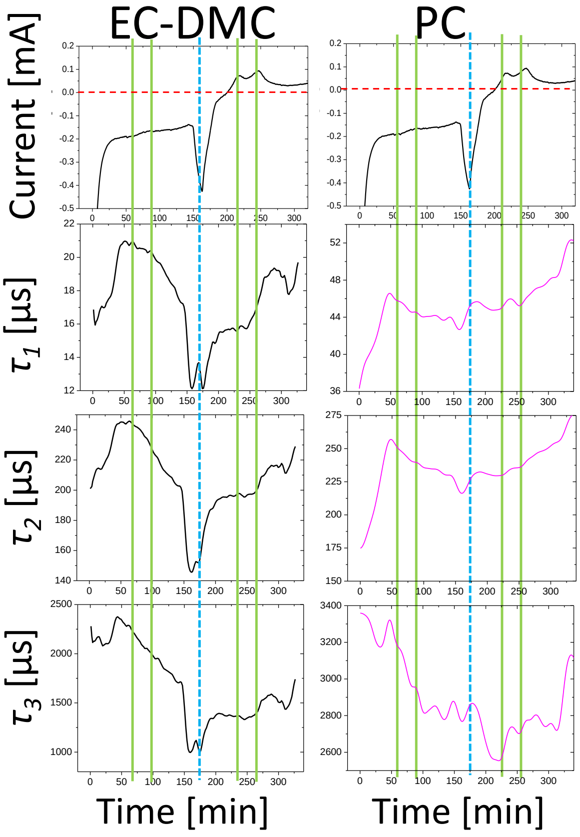

Figure 5.13: FFT-IS analysis of silicon microwire arrays in different electrolytes. The high performance electrolyte with the addition of PC is compared to the standard Selectilyte LP 30. In order to show how the time constants correlate to the recorded voltammograms and the phase transformations, the current is plotted as reference.

to the standard electrolyte, it is also slightly slower. This can be explained by the viscosity increase during the SEI formation and the complex interaction of the chemical components with the silicon surface. Especially in the beginning when the lithium salt dissociates and reacts with the silicon surface, the charge transfer reaction shown in τ_3 is slowed down. The second time constant, which is explained by the SEI formation, does not show any decrease, it stays nearly constant during the first cycle. At the first phase transformations, this time constant starts to increase again, indicating that this process is slowed down again. Particularly during the phase transformation, which means enhanced volume expansion it increases again. Having the coupling with the viscosity increase of the SEI layer and the slower charge transfer reaction, this process with the high performance electrolyte can be considered as local diffusion limitation to actually enhanced the controlled way of incorporating the ions into the silicon wires. Without this diffusion limitation at least only locally at the wire interface to the electrolyte, high C-rates would not be possible. This process resembles a lot the macropore etching and the dependence on the electrolyte, see chapter 3.1.2.

5.3 Role of Copper Current Collector on Crystallinity

The previous discussion based on the interaction between specially designed electrolytes with the silicon microwires. This study revealed high artificial mechanical stability during the SEI formation, accompanied by homogeneous coating around every wire from top to bottom. This chapter analyzes the impact of different cycling parameter on the silicon microstructure. Postmortem TEM analysis on those samples after more than 100 cycles indicated still a high degree of crystallinity [192, 193].

As discussed in the paper from Quiroga et al. [148], the success of the cycling performance strongly depends on the correct and slow charging conditions during the first cycles. Fast cycling within two hours from the beginning (starting with a fresh, crystalline silicon sample) will lead to immediate capacity fading. The same holds when cycling the silicon to the maximum possible capacity (100 % SOC). It is not yet clear what impact this C-rate variation in the beginning has on the individual silicon microstructure.

In order to verify and characterize this C-rate dependency on the cycling durability, different in-situ as well as ex-situ characterization techniques are performed (see chapters 2.8 and 3.8 for details in instrumentation and sample preparation). The silicon wires are cycled in standard electrolytes.

This specialized measurement technique involved the development of a new pouch cell design, described in section 3.3.3. Like this, it was possible to have a high spatial resolution (40 nm) along the individual wires in order to monitor their crystallographic changes during cycling. Ex-situ experiments of the Si wires are difficult, since even in the delithiated state, the silicon contains roughly 13 % of Li. Any exposure to air, the disassembling of the anode and the transfer into the measurement unit can easily introduce artifacts, difficult to identify.

Figure 5.14 shows the in-situ XRD measurements for varying C-rate during the SEI formation in the first four cycles.

Figure 5.14a show exemplary results of the in-situ XRD measurements using coherent X-ray diffraction at different stages during the measurement at slow C-rate. As mentioned before, the samples are embedded into polymeric pouch cells, which show additional peaks in the XRD spectra. The individual peaks and their corresponding materials are highlighted in the spectra. An attached goniometer continuously rotates the diffraction angle about plus and minus 5 degrees. By that, synchrotron radiation

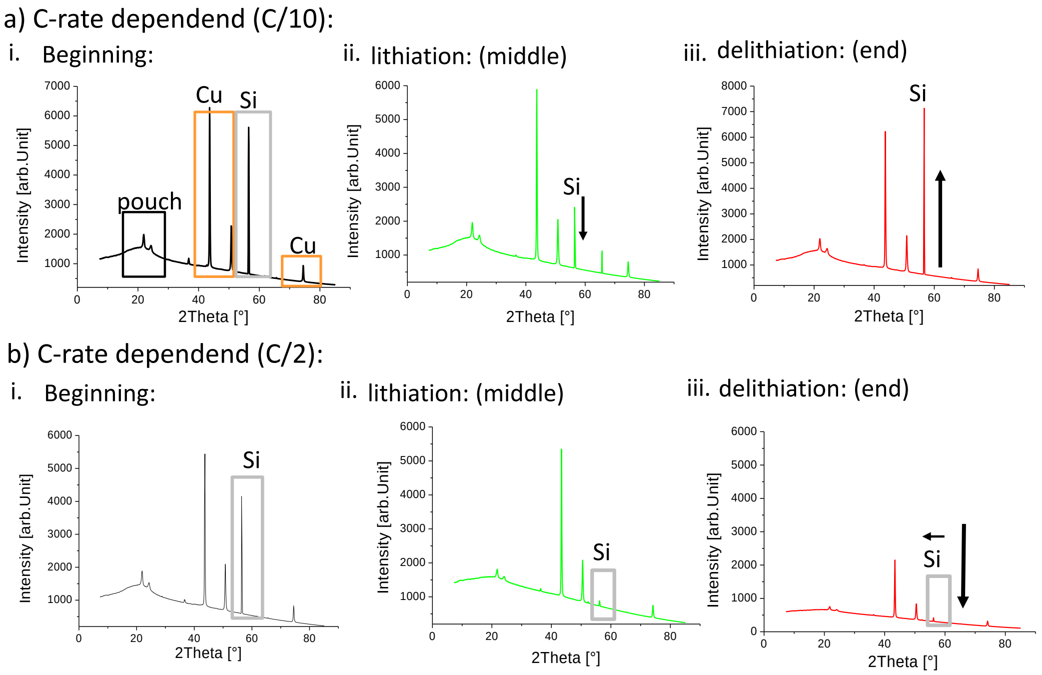

Figure 5.14: In-situ X-ray diffraction using coherent synchrotron radiation. The silicon microwire arrays are cycled at different charging rates and the microstructural change is monitored in-operando. a) Silicon microwire arrays are cycled with a slow C-rate of $C/10$ at 75 % SOC. This is a pre-conditioning step to form a homogeneous SEI layer around the individual wires. i-iii. indicate the structural change displayed by the different diffraction patterns. During lithiation, the intensity of the silicon peak decreases. But it completely recovers in the end of the delithiation. b) Silicon microwire arrays are cycled with high C-rate of $C/2$ at 75 % SOC. i-iii. demonstrate how the crystallinity changes during cycling. The crystalline silicon peak vanishes completely.

hits more and more wires during lithiation. During lithiation, the intensity of the silicon peak decreases because Li-Si phases form (Figure 5.14a i-iii). This peak gains in intensity after the delithiation process again.

In contrast, Figure 5.14 b) shows how the XRD pattern changes when cycled at $C/2$. In the beginning of the experiment, the peaks are very similar to those discussed before. During lithiation and delithiation, on the other hand, the silicon peak cannot be detected anymore. This indicates that the silicon microstructure completely changed from crystalline to amorphous. Apparently, the charging rate has an impact on the crystallinity of the silicon wires. This is verified by ex-situ TEM and TXM measurements in Figure 5.15, on different spots on the individual wires. The ex-situ TXM measurements in 5.15 a) shows how a slowly lithiated silicon sample looks like. As reference, the inset shows a non-lithiated sample. Due to preparation, the figure shows only individual wires. They are scratched off the array. The remaining

silicon wire looks transparent. The results indicate that the wires remain completely crystalline after the cycling procedure at the slow C-rate. There is some electrolyte left at the edges of the wires. The non-lithiated wires are as transparent as the wires cycled in $C/10$. There is no difference.
Ex-situ TEM measurements support this measurement. The almost transparent part at the edges of the silicon wires is the thin SEI layer Figure 5.15 b). The SEI layer is amorphous because it is purely composed of organic compounds from the electrolyte, as indicated by the diffraction pattern (not shown here). Figure 5.15 c) shows that the wires are perfectly crystalline after cycling at $C/10$. The attached diffraction pattern shows no amorphous rings, but very pointy crystal plane reflections.

Additionally, the DF-TEM images show different kind of defects, because of

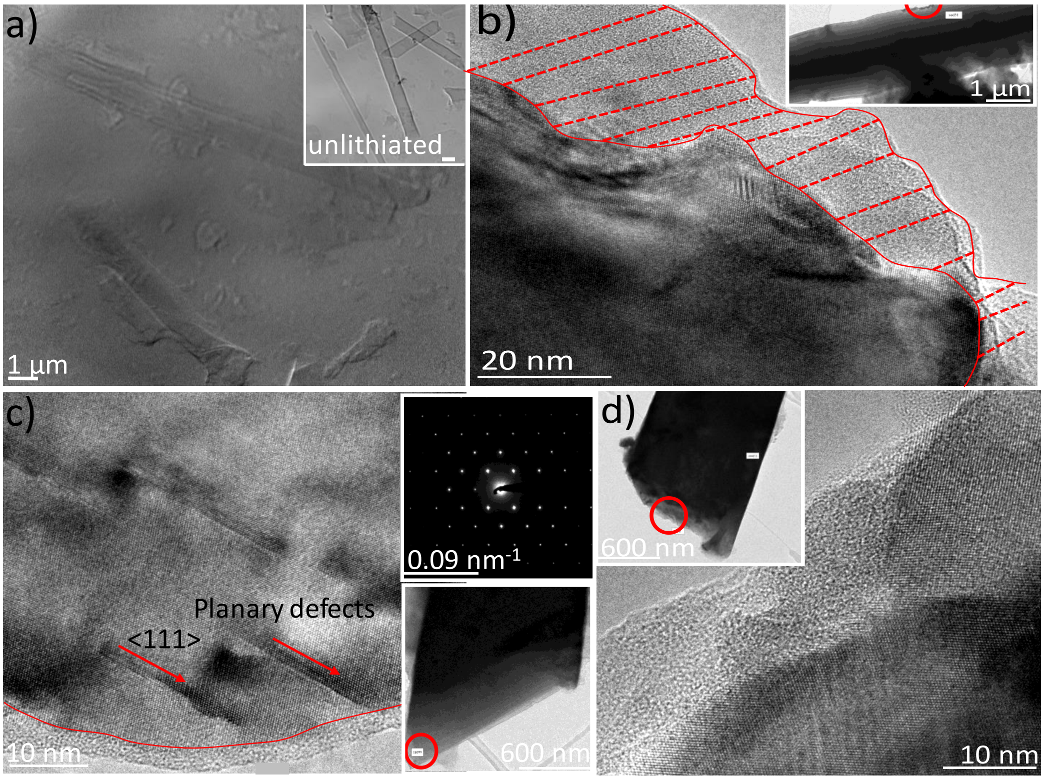

Figure 5.15: Ex-situ TXM and TEM characterization with varying charging rates. a) TXM results on slowly lithiated wires. The inset shows non-lithiated wires and both types look very similar. No change in colour and structure can be detected. b-c) Ex-situ DF-imagess indicate a perfectly crystalline silicon sample, covered with an amorphous SEI layer. d) At the corner of an individual wire, the crystal structure shows three differently, oriented parts. These parts are amorphous, if cycled at $C/2$. The analysis of the attached SEI layer shows even crystalline parts, resulting from the destruction of the silicon wires due to the high currents. For more information, refer to [192].

the charging process. These planar defects are re-crystallization planes of differently oriented crystal structures. This means that upon lithiation the crystal goes from crystalline to amorphous and re-crystallizes again according to this observation, supporting the synchrotron measurements. Upon slow lithiation and delithiation the crystal structure remains crystalline and more importantly re-crystallizes again.

At higher C-rates, ex-situ TEM measurements indicated that the silicon became amorphous Figure 5.15 d). The DF image indicate even differently oriented silicon regions, which are in an intermediate state between crystalline and completely amorphous. Due to the sharp amorphization front (area between crystalline and amorphous silicon) at this C-rate, parts of the silicon wire detached and diffused into the SEI layer [168]. The high current density during the SEI formation is too high leading to mechanical and structural disintegration of the silicon wire. There is no conditioning step for the homogeneous SEI layer formation because it is disturbed by the enhanced volume expansion of silicon. Thus, it breaks and needs to form again. At the same, this could trigger new and unprotected reactions at the silicon-electrolyte interface, which will be discussed even further in the next chapters. This demonstrates a clear correlation between the charging rate, the SEI formation and the crystallinity change of the silicon wires. All of the three properties and parameters influence the cycling stability. For highly-oriented silicon wire arrays, the first five cycles are the most important cycles to enable long-term cycling stability. The silicon re-crystallizes during lithiation and delithiation if the charging rate is adjusted to a slow and homogeneous SEI formation.

5.3.1 Role of the Current Collector

After previously discussing changes in crystallography and the re-crystallization of the silicon wires, here the results clarify the role of the Cu-Si layer further. These results are necessary to discuss the cycling stability of the silicon wire anodes. Figure 5.16 shows in-situ TXM investigations on different areas (a-c) of the silicon wires, embedded in the pouch cell, see section 3.3.3. The wires, shown in figure 5.16, are cycled with $C/10$. Figures b) and c) show parts of the wire, which are partially embedded into the current collector. Small, parallel lines in the TXM images indicate the silicon wires, whereas the dark part is the copper. Copper, or metals in general, cannot be investigated with the synchrotron radiation and appear very dark in these images. Nevertheless, the most important point can still be concluded. At the Cu-Si interface,

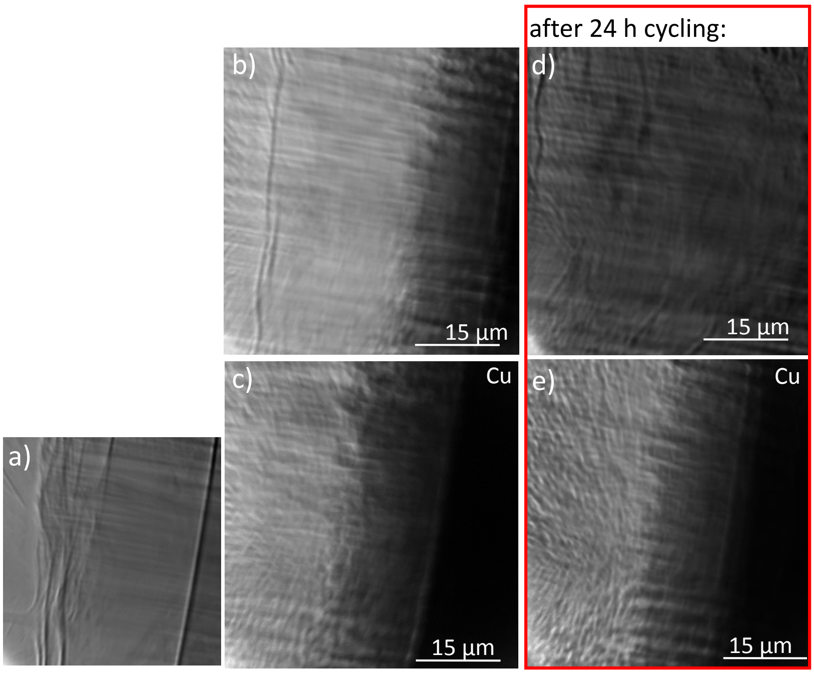

Figure 5.16: In-situ TXM investigations on silicon microwires. a) It shows the down part of the silicon wires, which are embedded inside a pouch cell. The polymer could be seen by different wrinkles. b-c) The figures emphasize how the silicon wires are partially integrated into the copper (the black part on the right). d-e) After cycling the silicon wires for 27 hours, the embedded silicon part remains the same. The rest of the silicon wires, on the other hand, shows drastic changes on the crystallography. The silicon, which was transparent in the beginning, gets grey during cycling.

the silicon wires do not take part in the lithiation mechanism. They are completely sandwiched in between the copper and no Li ions can diffuse through the metal. In order to proof this hint, the same TXM images after 27 hours of cycling show also no signs of crystallographic change of the embedded silicon (Figure 5.16 d-e). The active part of the silicon, facing the electrolyte, changes at the outside due to the SEI layer formation and the outside amorphization, depending on the C-rate. As a summary, a partial copper integration keeps parts of the silicon deliberately crystalline, which is very important for a high cycling stability as will be discussed in the next sections.

5.3.2 Self-organizing and self-supporting single crystal growth

The following interpretation allows to understand the high crystallinity of the silicon wires after charging and discharging processes, as described in section 5.2.3.1. The TXM results showed that the silicon embedded into copper matrix remains crystalline

(Figure 5.17). During lithiation, the completely crystalline silicon wire reacts with the lithium at room temperature forming Li-Si alloys. These are usually amorphous after the first cycles. Nevertheless, during cycling of the here discussed silicon microwires, no amorphous silicon is detected in the end, but a single crystalline phase remains. Thermodynamically, this is a transition between a system with low energy and (almost) perfect order (as a perfect single crystal, Figure 5.17 a) and a system of maximal entropy and disorder. With ongoing delithiation, the recrystallization front propagates through the silicon wire, as shown in Figure 5.17 a-c). At the phase boundary, two conditions co-exist of a lower entropy dominated by the bond strength. The difference in bonding strength and energy is decisive for the process as well as the entropy barrier. The bond strength and bond dissociation enthalpy of a Si-Si bond is much smaller compared to the Li-Si bond. Therefore, the silicon atoms in the solid solution will bond covalently to the already existing silicon single crystal. Consequently, the silicon will lower the energy and entropy of the complete system, by (homo-)epitaxial growth of the single silicon crystal. This case could be called entropic purification. As a consequence, the crystallization behavior of the silicon wires during cycling resembles a solid solution and a (common) purification process of metals, alloys as well and metallurgical silicon [194, 195, 196]. However, this metallurgical silicon contains a certain concentration of phosphor used during crystal growth as nuclei. Nevertheless, these phosphor impurities are not wanted for the final product and need to be removed by fractional distillation. By repeated distillation or purification, the impurity concentration of phosphor atoms is decreased step-wise. The comparison shows that this process is commonly used in silicon crystal growth.

Basically, it is possible to explain the lithiation process during cycling with basic thermodynamics of the phase transformation and application of the lever rule, Figure 5.17 d). The Li-Si alloy is a two-phase region inside the binary phase diagram. By continuing the lithium reaction, the re-crystallization front propagates through the silicon wire and shifts the phase boundary forward. The more perfect and crystalline the wire is, the higher the entropy barrier becomes. With increased lithiation, the lithium concentration increases shifting the lever to the left inside the phase diagram. For the opposite case, the lever would be at the far end with a high concentration of Si. Thus, entropy is withdrawn from the system providing more energy by the crystallization and homoepitaxy (by Si-Si bonds and lowering the entropy of the crystal). In this way, the lithiation and delithiation process uses thermodynamic. According to the segregation coefficient, it is possible to calculate the concentration difference at the specific phase boundaries between the solid (or perfect crystal in silicon) and the liquid phase (Li-Si). It directly relates to the Gibbs free energy of the system and thereby to the entropy. Thus, the phase transformation is the transition between the state, where the bond strength is important compared to the entropy. The recrystallization process of Si or differently speaking, the solidification process, has a certain aspect of life because it combines many different aspect. The epitaxial growth of silicon inside the solid solution is only possible if a specific amount of seed crystal survives repeated cycling. Since a part of the silicon wire (17 % of the wire length) is squeezed into the copper matrix and does not take part in the lithiation or delithiation, it remains in its initial, freshly crystalline state and acts as seed nucleus (crystal). This process is comparable to homogenous nucleation during a solidification process. Normally, the nuclei inside the melt needs a critical minimum size. Otherwise the surface energy change would dominate the Gibbs free energy and the nucleus

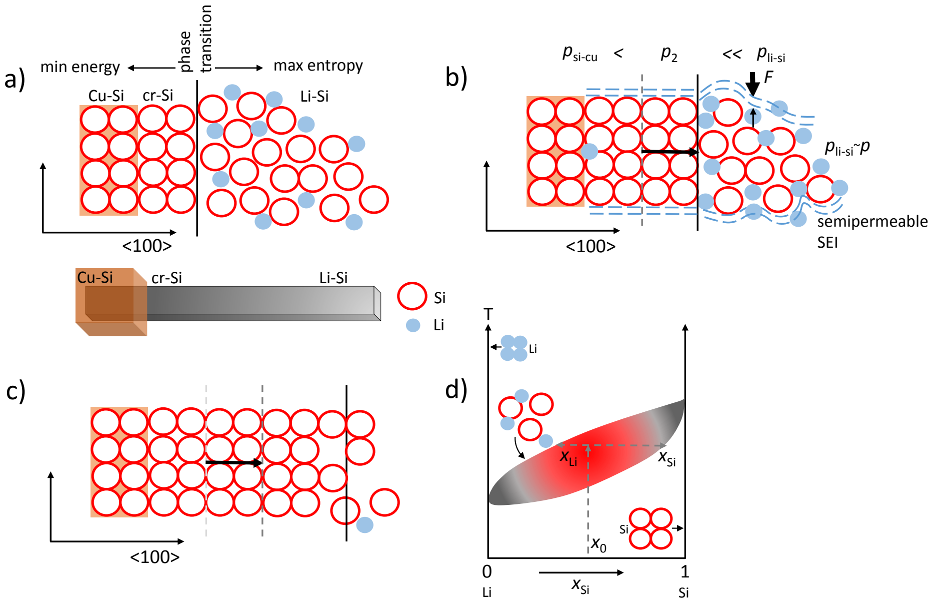

Figure 5.17: Model of the re-crystallization of the silicon during cycling. a) The figure shows the perfect single crystal with an energy minimum and a solid solution of Li and Si with maximum entropy. b-c) During delithiation, the phase boundary shifts and the recrystallization front propagates through the silicon wire. The Li-Si phase could be described like a liquid and Raoult's law applies, upon which the partial pressure has to be equal. Due to the volume expansion, the liquid tends to dissipate. In order to avoid this, the SEI layer around the liquid has to build up enough restoring force to level out the increase in partial pressure. d) The change from Li-Si phases to cr-Si, and vice versa, can be described similarly to a binary phase diagram, comparable to typical fractional distillation [197, 198, 199, 158, 200, 194].

cannot grow anymore. Consequently, the free energy barrier for the nucleation would be too high to be overcome and the nucleus would collapse. The same applies for the case of the silicon epitaxial growth. Only in this case, no new nucleus grows inside the melt, but the silicon grows epitaxially layer-by-layer on top of the seed crystal (the silicon wire embedded in the copper matrix). Therefore, the homo-epitaxy of silicon and the critical size has to be considered as well.

The velocity of the crystal growth (or the solidification process) directly corresponds to the dendritic growth direction inside silicon. The <100>-direction is the fastest and most stable direction for the silicon dendritic growth. Exactly this direction, as indicated in Figure 5.17 and 5.20, is the direction of the macropores and consequently of the freestanding wires. Therefore, the re-crystallization can keep up with a high C-rate. As charging could be realized in 12 minutes, it means that the crystal growth proceeds at 5 µm per minute by deliberately using the fastest growth direction of silicon. It is commonly known, that the lithium diffusion in silicon depends on the (incorporation) direction and is anisotropic [199, 201, 202, 87]. Exactly this <100>-direction is the slowest for lithium diffusion [197]. This combination of fast silicon growth and slow lithium diffusion helps the kinetics.

The recrystallization of silicon and lithium could be easily modeled as a liquid, i.e. an ideal solution, where the silicon and lithium atoms are highly mobile. Like that, the necessary mechanisms become clear and Raoult's law applies. In thermodynamic equilibrium, the temperature as well as the total pressure are constant. In thermodynamic equilibrium, the cycling is not kinetically limited. The partial pressure of every component inside the liquid is locally everywhere the same. During lithiation, the volume is not constant, but increases by a factor of four and it is not longer considered as thermodynamic equilibrium. In this case, different partial pressures set in, as indicated in Figure 5.17 b). The copper matrix maintains always the same pressure on the embedded silicon wire. The volume expansion of the silicon, on the other hand, leads to a drastic increase of the partial pressure p_{Li-Si} of the Li-Si ideal liquid solution. Now, these pressure differences have to be leveled out by the elasticity of the surrounding SEI layer. Consequently, a force has to be applied from the outside in order to avoid the dissipation of the liquid. The SEI around the liquid has to maintain as much force to equalize the partial pressure at this point. If, on the other hand, amorphous silicon is present in the beginning, the partial pressure would increase significantly. Thus, the force on the silicon wires has to be increased or in other words the SEI has to tolerate these pressure differences without breaking. The function of the SEI layer becomes clearer underlining the preservation of the single crystal and the excellent performance of the complete wire. The mechanism behind the performance could be described like a self-organized and self-supporting crystal growth.

As a summary, in thermodynamic equilibrium the partial pressure should be everywhere the same. During cycling, the partial pressure increases leading to a high pressure difference between the solid solution with higher Li concentration and the perfect single crystal. In order to still maintain the same partial pressure everywhere, the SEI has to restore the partial pressure by its modified, more elastic layer around each Si wire. It builds up an opposing pressure, but at the same time, it has to be permeable for lithium. Exactly this permeable membrane structure could be realized using PC as additive as shown in the SEM images after cycling in Figure 5.11. As discussed previously in section 5.2, the morphology of the SEI layer changes, having more of a net character (Figure 5.5). TEM images supported that even at ten times larger C-rates with PC, the silicon remains single crystalline. The reduction of the irreversible losses during the first cycles indicate that the SEI formation is much more stable. Optimization allowed fast charging only after one or two pre-conditioning cycles. Thus, the SEI enforces high pressure on the silicon wires already after short time, which allows the recrystallization behavior. If this force is not large enough, it will lead to segregation or in other words, the structure will no longer be able to convert into a perfect single crystal.

5.3.3 Charge Transfer Dependency upon C-rate and SOC

In order to investigate how the observed change or stability of the crystallinity of the silicon wires influence the charge transfer kinetics (discussed in 4.1.2), SOC variations are analyzed by cyclic voltammetry measurements. This allows a good correlation between the structural change and the electrochemical processes for lithiated samples. 3.4 as well as 3.5 in the Experimental Details describe only the standard process of the cyclic voltammetry measurements. These processes are adapted to simulate what happens after the first lithiation process, like during cycling. Therefore, the arrays are pre-lithiated. That means that they are first cycled under the standard cycling conditions (same C-rate and capacity limitation) for only one cycle followed by cyclic voltammetry measurements.

SOC variations are investigated in a fundamental characterization, using silicon wires in paste electrodes. The impact of the state-of-charge variation can be directly seen in a potential and current shift, recorded by cyclic voltammetry measurements [203]. The SOC is varied between 0 and 75 % SOC. 4.1 discussed the size-dependency without pre-lithiation at 0 %. When increasing the SOC up to 50 % (2100 mAh/g), the delithiation potential decreases almost linearly. The shortest wire shows the smallest delithiation potential. The longest wire needs more delithiation potential at that state-of-charge. The length variation depends linearly on the potential changes. If the SOC is increased even further, the potential shifts and the tendency changes. Partial delithiation peaks show potential shifts to large values for short wires. They need more voltage to remove the ions if the state-of-charge is at the standard SOC for cycling the wires. Figure 5.18 shows the difference in lithiation and delithiation for long wires, depending on the state-of-charge. At 75 % (i.e. 3150 mAh/g), a high amount of charges are incorporated into the silicon anode, which means that high energy has to be provided to let them in. Due to that behavior, the ions form lithiated silicon alloys. The lithiated phase is pushed towards the core of the silicon, shifting the concentration gradient. This amount of charges leads to a change in crystal structure, changing from crystalline to amorphous. Especially for short wires, the lithiated area surrounds the wires encapsulating the inner core. The ions are incorporated across a smaller surface area, leading to higher diffusion and concentration gradient towards the core. Larger wires on the other hand need to be first incorporated on all of the

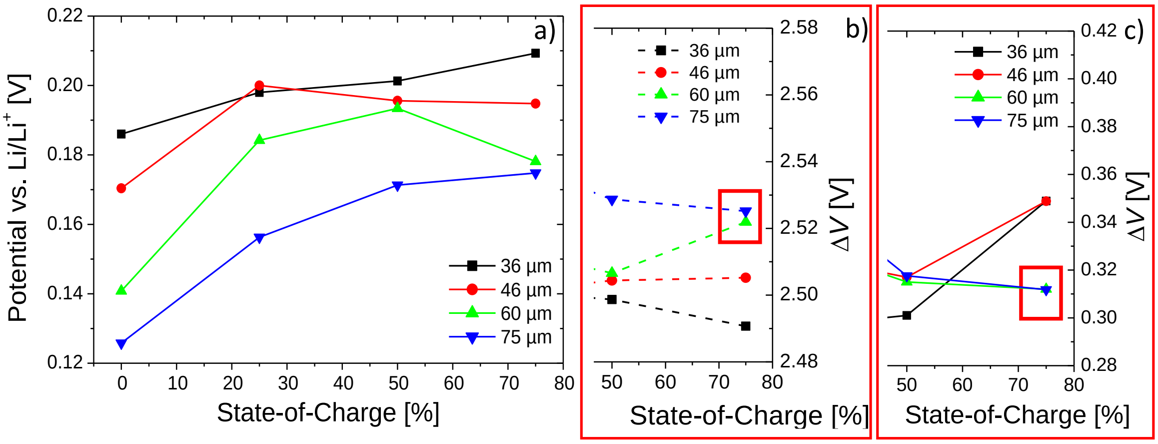

Figure 5.18: Influence of State-of-Charge on lithiation and delithiation behavior for wires with different length and a thickness of 1.4 µm. a) The full lithiation peak (Peak 2) shows small values for long wires, which translates into large incorporational voltages in b). The 60 µm long wires are important to consider, because they are used in wire arrays. Although they need larger voltages to incorporate the ions, c) indicate less voltages to remove them during delithiation (Peak 3) (roughly 50 mV) in contrast to shorter wires. For these comparison, only the voltage is considered, in agreement with the discussion in chapter 4.1.

surface area. The crystalline structure change in short wires leads to an increase in the delithiation potential because it needs more time to remove the ions from already amorphous silicon. In contrast, longer wires have a larger, still crystalline area. The lithiation process needs higher voltage with increasing length and SOC. A detailed analysis of the other peaks is shown in [203].

The thickness variation indicates the essential parameter for cycling silicon wire arrays. It indicates that the thin 1.2 µm show the smallest delithiation voltage at the standard 75 % SOC. The delithiation peaks during cyclic voltammetry analysis shift to even lower voltages, compared to the thick wires. Figure 5.19 shows the tendency of the lithiation and delithiation behavior. In all of the lithiation and delithiation peaks, the incorporational voltages decrease with decreasing thickness. At high degree of pre-lithiation, less ions can still incorporate into the wires. Due to the fact that all the necessary bonds were broken beforehand, less energy is needed. For this discussion, the surface to bulk ratio is critical. Thin wires have a larger surface to bulk ratio, in principle they have more active sides for the ions. Therefore, they need more voltage if they are not at all lithiated. This can be explained by considering the diffusion layer thickness, which depends on the state-of-charge and on the degree of the lithiated phases. With higher degree of lithiation, as in the case for the 75 %

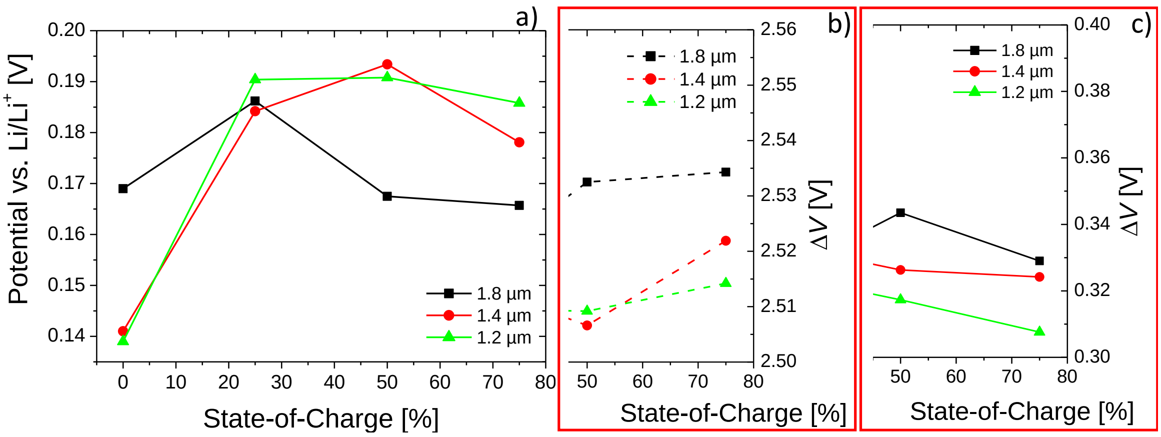

Figure 5.19: Influence of State-of-Charge on lithiation and delithiation behavior for wires with different thicknesses with a constant length of 60 µm. a) The full lithiation peak (Peak 2) indicates an increase in potential for thin wires, which translates in small incorporational voltages b) for the same peak. Even for the delithiation behavior (Peak 3) in c), they need the smallest voltage to remove the ions. Therefore, those thin wires are used in the array electrodes. These tendencies support the cycling parameters and shows that cycling behavior might be best at high SOC values. For this comparison, only the voltage is considered, in agreement with the previous discussion in chapter 4.1.

SOC, the diffusion layer around the surface area of thick wires is also thick, caused by the enhanced Li ion diffusion. This indicates that a larger area has to be penetrated (this diffusion layer) in order to contribute to the capacity and leads to an increase in incorporational voltages. This is also reflected by the current increase, discussed by the Cotrell equation. Here, the current depends directly on the concentration gradient (correlated to Fick's law) and of course on the diffusion itself, refer to [204]. The concentration gradient decreases with the amount of charges already integrated into the anode. This means that the current amplitude decreases as well exponentially.

5.4 Modified Lithiation Model

After discussing every point of the anode structure as well as the structural changes for silicon, which occur during cycling, this section summarizes these findings with a lithiation as well as mathematical model. Compared to the most common chemical etching methods like MACE (Metal Assisted Chemical Etching) for example, this macropore etching with structured silicon wafers allows a well defined pore modulation and structuring, which is absolutely necessary for this type of application. The individual wires have only limited space in between each other, where they can expand during cycling without hindering each other. This is absolutely necessary to avoid constrictions of the SEI and total failure. Due to the limited space between the individual wires, another brick and solid stabilization in form of the next wire minimize the constriction of the SEI. Instead it stabilizes the next neighboring wire and its SEI layer. The current collector is found to be also very important because first, it enhances the mechanical stability of the complete electrode. Second, it provides the necessary pressure from the outside on the silicon wires, in order to preserve the single crystal structre as seed crystal for nucleation. In order to fully reconstruct the contributions (current collector, electrolyte and SEI layer) on the crystallinity, it is necessary to transfer it to the lithiation process inside silicon. Most models [168, 158, 205, 206, 199, 207, 90] agree, that the lithiation process is a co-existence between a kinetic reaction and the diffusional-controlled process of the Li ions trying to incorporate into the silicon. Figure 5.20 shows schematically the silicon wire array inside an electrolyte, where the Li ions move around. The magnifying glass on the wires symbolizes the processes around silicon wires on large scale, taking into account all the discussed results. The results could be modeled according to the tensile and compressive stresses inside the material. Very importantly, the SEI layer is taken into

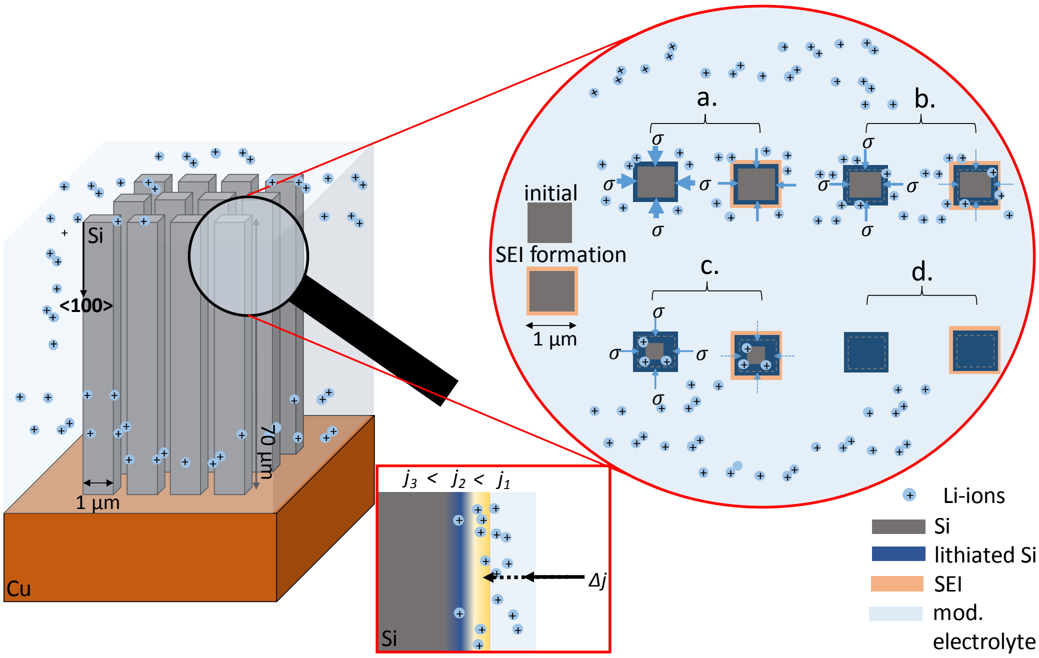

Figure 5.20: Model of the compressive stress on silicon wires during lithiation. This model shows the kinetic and diffusional processes of Li ions, when incorporating into the silicon wire in two scenarios. The incorporation process induces compressive stress on the wire upon which the driving forces for further lithiation are reduced. The modified SEI ensures the mechanical support around the wires. The difference in compressive stress is indicated by differently sized arrows. Large and thick arrows indicate a high stress level; the smaller the stress, the thinner the arrows [158, 205, 199, 90].

account. The left hand inside the magnifying glass shows the initial state of the silicon wire and also the state after the SEI formation. The SEI is shown as additional square, because it forms homogeneously around each wire. Here, no details are given about the SEI formation, but the mechanical properties of the SEI layer are considered, like discussed before for the lithiation. The processes are exemplary considered for only one wire. But it is assumed that it happens around every wire in the exact same way. The SEI formation is the first process that occurs when applying voltage on a battery. The next process is that Li ions diffuse through the electrolyte and towards the interface between the crystalline silicon and the electrolyte. At that interface, the Li ions have to diffuse additionally through the SEI layer. The bond dissociation energy of Si-Si bonds is approximately 340 kJ/mol. Li ions with an atomic radius of 167 pm have a slightly larger radius compared to silicon with only 111 pm. When Li diffuses into the diamond crystal structure of silicon, the dissociation energy of Si has to be overcome and provided [87, 199]. Furthermore, the crystal structure is widened - the lattice constant of diamond is increased. These are the first structural

changes. The second process changes the kinetics. Upon lithiation, a concentration gradient of Li ions is formed. Figure 5.20 indicates the concentration gradient Δj directing from the electrolyte to the wire. The individual currents are labeled by j_1 to j_3 according to the different regions. The external current induces the diffusion towards the silicon by forming alloys, upon which a concentration gradient of Li ions is induced. This concentration gradient produces compressive stress on the silicon and on the already lithiated phase. Arrows indicate the direction of the stress. In the beginning, the stress is very large. Consequently, if the stress grows, the driving force for further lithiation reduces drastically in order to cope with the induced stresses. That influences the kinetics of the lithiated alloys. Compressive stress usually induces cracks or local defects in the material and would lead to loss of active material, like in this case, the silicon would rupture from the rest of the wire.
This scenario is indicated in Figure 5.20 a) on the left hand side. It describes the influence of the elastic SEI on the compressive stress during lithiation. As indicated, the elasticity of the SEI helps to reduce the compressive stress during lithiation upon which the driving forces for further lithiation are not limited. It provides exactly enough force on the silicon wires, in order to compensate the large volume expansion of the Li-Si phase for the silicon seeds to survive. With the modified, more viscous electrolyte, the moving ions take material with them to the interface of the silicon wires and build up a SEI layer with high enough restoring force. If that happens, the velocity of the Li diffusion stays (almost) constant, until the wire is completely, reversibly lithiated without loosing its high degree of crystallinity. After analysing also the SOC contribution to the lithiation behavior and considering the models for the single crystal, another point could be deduced: The cycling performance might be nearly independent of the SOC limitation (75 % SOC) because of the intrinsic regulation of the crystal growth. This prevents to obtain instable phases like $Li_{13}Si_4$, which is considered as metastable phase accompanied with high volume expansion. Moreover, the growth speed of the single crystal and the movement of the lithiation front is an intrinsic effect (in thermodynamic equilibrium).

All the necessary parameter can be summarized in the following mathematical equation in equation eq:simulation and Figure 5.21. It shows the engineering and optimization procedure, starting from the experiment [208, 209], leading to an optimization routine. The consequences of the modified electrolytic system on the performance of the silicon wires are described by the total differential in equation 5.2:

$$\frac{df(x(t),t)}{dt} = \frac{\delta f}{\delta x}\frac{\delta x}{\delta t}dt + \frac{\delta f}{\delta t}dt \tag{5.2}$$

The equation includes two basic properties of the complete discussion: first, every property like the mechanical stabilization of the SEI layer, its formation, the amorphization process due to chemical additives could be all expressed by the first derivative of this total differential. The electrolyte is modified in such a way, that the viscosity as well as the ionic conductivity is in an optimal range to support the wires during cycling. As a consequence, the irreversible losses during the SEI formation are minimized. Consequently, it might also be possible to cycle silicon anodes already after one formation cycle, i.e. slow C-rates in the beginning. As a result, the wires show an enhanced mechanical stability. Even the amorphization process, which is a result of some electrolytic additives or higher C-rates, could be attributed to a modified SEI layer with optimal thickness and morphology. By adjusting the viscosity of the used electrolyte and understanding how the copper current collector contributes to the performance, it was possible to stabilize the wires to achieve even high C-rates. The second part of this total differential includes only time-dependent behavior, which

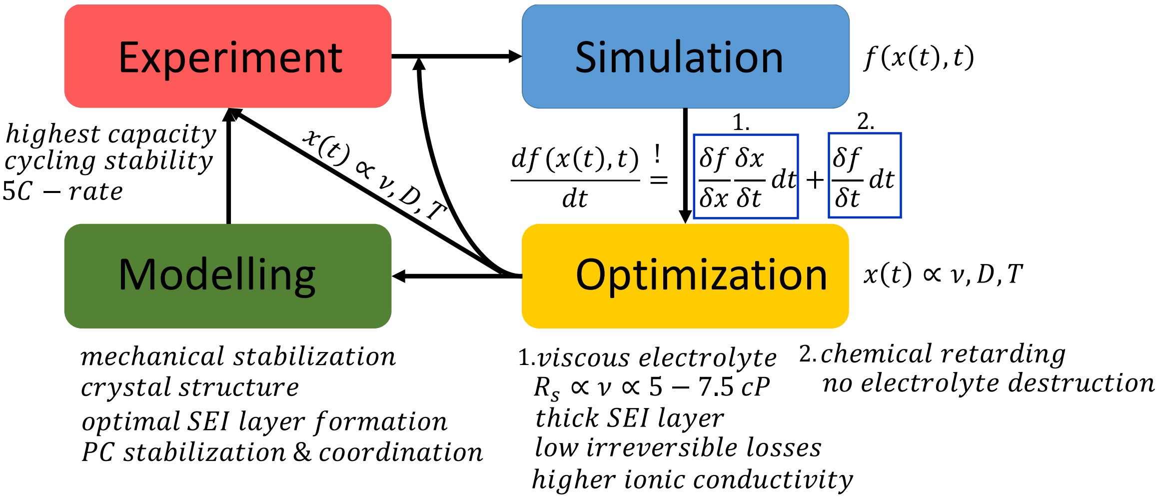

Figure 5.21: Schematic of the optimization procedure for high-capacity silicon wire electrodes. A total differential of the function f could be fitted and modeled to the experiments, including the two important components necessary to describe the results. One contribution is the artifical mechanical stabilization by modifying the electrolyte and the SEI layer formation. Every property and cycling performance would result from an optimal electrolyte viscosity. The second part is the purely time-dependent contribution, which does not lead to this mechanical stabilization. This includes the chemical retarding and coordination of the PC leading to a stable electrolyte during long-term cycling experiments [208, 209].

is not necessarily attributed to the SEI layer formation. This includes the chemical retardness and stability of the electrolytes by adding PC. It changes the coordination and complex around the Li ions, thereby even enhancing the ionic conductivity of the electrolyte. Another contribution is the dendritic growth of silicon in the <100>-direction, in which a single crystal growth fastest and more stable, leading always to a single crystalline seed crystal.

5.5 Electrolyte Compatibility for Lithium-Silicon-Sulfur Full Cells

Up to now, all the reactions are analyzed in half cells. The electrode, which should be analyzed is cycled against metallic lithium as reference and counter electrode. The gained knowledge and understanding is now transferred to complete batteries with cathode and anode materials (full cells). As already described in the Introduction and in chapter 2, the silicon wire arrays are a very promising anode material for Lithium-Sulfur (Li-S) cells due to the highest possible areal capacity. In those full cells, the wires would be combined with sulfur cathodes. Sulfur cathodes are typically a carbon host matrix with infiltrated elemental sulfur, described in [210, 211, 212, 213], which is not subject of this thesis.
Therefore, it is necessary to test the electrolyte compatibility i.e. if the electrodes perform well with the specially designed electrolyte for full cells. In contrast to the already discussed carbonaceous electrolytes (combinations), typical sulfur electrolytes consist of a two-blend solvent system with 1,3-dioxolan (DOL) and DME with a lithium salt, called Bis(trifluoromethane)sulfonimide lithium (LiTfSi). This electrolyte itself does not contain any additional (elemental) sulfur i.e. S_8; but only the sulfide functional groups of the salt, which will become relevant in the subsequent discussion of the cycling performance and investigation of these electrolytes in chapter 5.4.2. Typically, sulfur electrolytes additionally contain small concentrations of $(NO_3)^-$ ions. For a full cell with sulfur, this is very important because it reacts with the insoluble polysulfides inside the electrolyte and traps those sulfides [211, 214, 181]. Furthermore, for a sulfur cathode, it should increase the ionic conductivity. Compared to $LiPF_6$ electrolytes, the ionic conductivity of LiTFSi electrolytes is three times lower [215]. For batteries with the insulating sulfur cathodes, the ionic conductivity has to be increased intrinsically by adding $LiNO_3$. This section tries to identify the problems when cycling silicon microwire arrays with sulfur electrolytes. In addition, it shows the consequence of $LiNO_3$ inside the electrolytes on the cycling performance of the silicon wires, but also demonstrates how the electrolyte components interact and (negatively) contribute to the SEI formation.

Figures 5.22 a) and b) show the cycling behavior with $LiNO_3$ containing electrolytes [216, 217, 212, 66]. They show how the capacity fades drastically by almost 50 % at higher cycle number, when cycled in the sulfur electrolyte with $LiNO_3$. This capacity drop together with the highly fluctuating behavior is a typical example of the cycling behavior, which was only observed in this type of electrolytes ([66] as well as in the "AlkaSuSi" final project report [218]). Although this behavior is not new, it is not yet evident why the silicon does not perform stable in this environment.

The first four cycles are cycled with a slow C-rate of $C/10$ and afterwards increased to $C/2$ (Figure 5.22 b). Special attention is directed towards the first cycles, also in comparison to electrolytes without $LiNO_3$. Taking into account all the discussed results up to now, a long-term cycling experiment only reflects the history of the first cycles. Thus, a stable SEI formation in the first cycle could lead to a repeatedly high capacity. For pure LiTFSi electrolytes, the losses in the first cycles are really low. This indicates, that the effects which accompanied the SEI formation are not that severe as compared to the other sulfur electrolytes. The inset shows the slow increase in the discharge capacity. In the beginning, the capacity increases very slowly. When the C-rate increases by a factor of five in cycle 5, the capacity decreases again, trying to stabilize during cycling. A closer look at the galvanostatic and potentiostatic charging modes indicated additional contributions. This type of representation is a typical characteristic when discussing about battery charging. Obrovoc et al. demonstrated in several publications [85, 163, 219] how the lithiation and delithiation capacity correlates to the voltages. Voltage plateaus - constant voltages - during the lithiation (with a slight slope) indicate a phase transformation between the already lithiated Li_xSi_y and the remaining Si inside the anode. This plateau is considered always with a slight slope, because the highest possible LiSi alloy [85, 163] should have a capacity

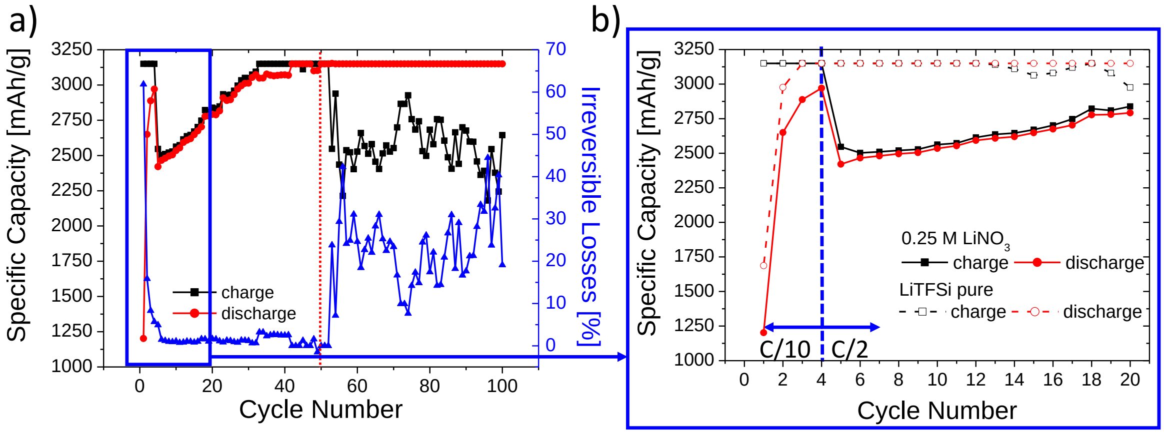

Figure 5.22: Cycling behavior of silicon microwire arrays with $LiNO_3$ containing electrolytes a) for 100 cycles and b) for the first cycles, to direct the attention to the problems during SEI formation. A comparison without this co-salt emphasizes even more the effect on the cycling stability and the stable SEI formation.

of about 4200 mAh/g. Upon delithiation, there exist several plateaus, in agreement with the recorded cyclic voltammetry measurements. They indicate also a two-step delithiation process, until the voltage increases further for a complete removal of the Li. In addition, Figure 5.23 shows how the currents and voltages develop during the measurement. This is very important because it demonstrates which process (potentiostatic or galvanostatic charging) dominates the cycling. All the cycling experiments during this thesis are a combination of potentiostatic and galvanostatic charging. Upon lithiation, the voltage reduces until it reaches its pre-set voltage limit of 110 mV; with a galvanostatic step simultaneously, where the current is constant. When the voltage reaches the limit, the cycling mode changes to potentiostatic and the current increases step by step. Consequently, the current increases until it is reduced to only 10 % of the starting value; indicated by the red squares. After that the charging (delithiation) process starts with again a mixture of galvanostatic and potentiostatic steps. For all cycling tests, this is the standard cycling procedure (unless mentioned otherwise).

According to those tendencies, the limits of the battery with this type of electrolyte are identified. More importantly, it reveals how and when the series resistance changes during the measurement. The consequence of this current and voltage dependency is shown in Figure 5.23 d). This type of representation correlates indirectly the voltage to the phase transformations (different representation than cyclic voltammetry) in voltage plateaus. Figure 5.23 a) shows the cycling behavior of cycle 49 up to 55. The capacity starts to fade exactly during these cycles. Therefore, the potentiostatic and galvanostatic cycles are shown in order to indicate how the current changes upon cycling. The capacity fade can be correlated directly to the voltage/current curves here. Until cycle 50, this combination can be reversibly seen in the current and voltage curves. From cycle 50 to cycle 51 (292 hours), the current does not reduce anymore to 0 mA. Figure 5.23 b) enlarges this scenario. The cycle before shows still the galvanostatic and potentiostatic modes, whereas the next cycle changes its voltage and current behavior. The blue dotted line indicates the behavior how it should be. This allows a very detailed comparison. The voltage does not reach its limitation at 700 mV and does not change into the constant potentiostatic mode anymore. As a consequence, the current does not drop exponentially, but switches instead from the positive limit directly to the negative galvanostatic limit for the new cycle. For cycling silicon microwire arrays, potentiostatic steps are necessary to allow high cycling stability with high capacities. If this step is missing, the anode cannot reach high capacities.

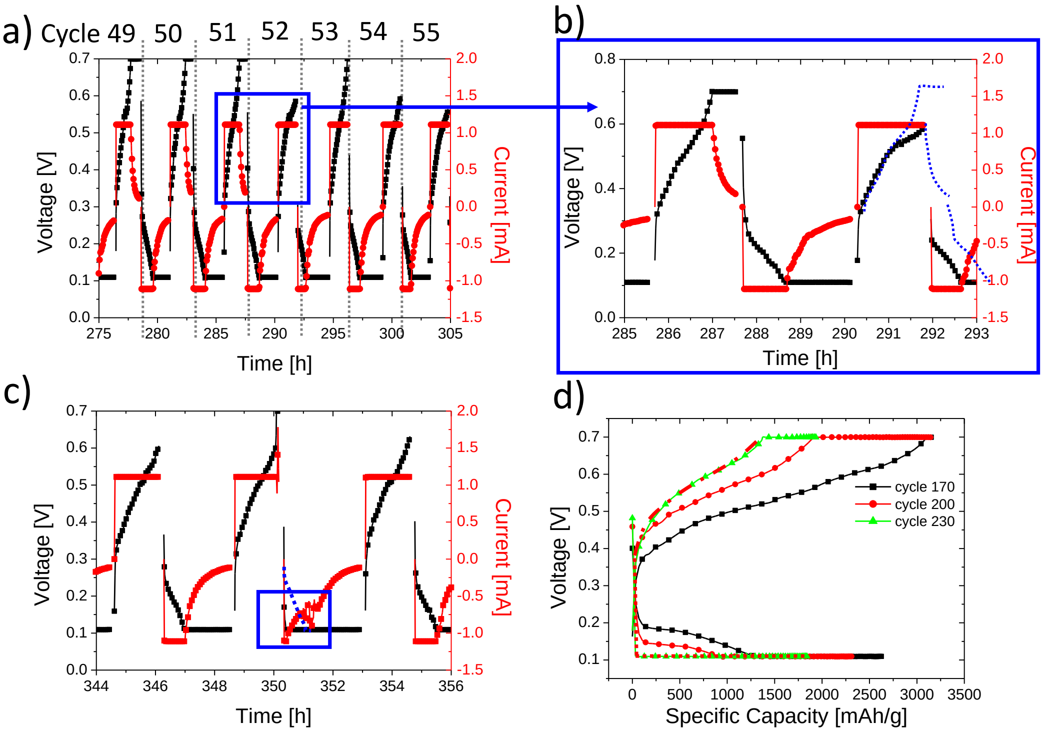

Figure 5.23: Cycling experiments with $LiNO_3$ containing electrolytes, by looking closer at the currents and voltages during cycling The analysis shows which charging process dominates and how the current and voltages change with cycle number. This dependency is very powerful because it demonstrates how the battery fails and could indicate resistance losses inside the battery. a+b) It shows the behavior at cycles 49 up to 56. As indicated in Figure 5.22, at cycle 50, the capacity starts to fade. This is seen in the time scale at 292 hours in a) and b) in the missing current decrease as a consequence of the missing potentiostatic (constant voltage) part during the charging. c) In the same kind of representation, it shows how the current during the discharge is unsteady. This is a consequence of the long potentiostatic charging. d) As a consequence, the capacity fades completely at high cycle numbers and is triggered purely galvanostatically.

Figure 5.23 c) indicates the voltage and current behavior for higher cycle numbers (cycle 65 - 68). Here, the missing potentiostatic step is predominant. Between cycles 65 to 68, (349-351 hours), the voltage increases almost up to 700 mV. In the following cycle, the galvanostatic mode is very short during discharging. As a consequence of this missing galvanostatic step, the current shows spikes (parasitic reactions). This is the first indication of an unwanted reaction inside the battery. With higher cycle number, the current shows more and more of these parasitic reactions i.e. the current increases by a factor of three, leading to the large capacity fade indicated in Figure 5.23 d). The capacity drops to 50 % of its initial value. The drastic current increase is the first sign of the degradation mechanism of the anode with this type of electrolyte.

It is the consequence of the missing potentiostatic mode i.e. the battery cannot reach its limit anymore. If the battery is triggered towards this limit, it will induce cracks inside the wires leading to more loss of active material. These current peaks do not appear during every cycle; at first at cycle 66 and repeatedly at cycle numbers higher than 100. These are strong hints of the length scale of the degradation mechanisms. It has to be an effect that it is a slow but steady reaction with large time constants, because it seems to become more effective at higher cycle numbers.

As indicated, Figure 5.23 d) shows indirectly a correlation to the phase transformations. For the galvanostatic lithiation in Figure 5.23 d) at cycle 200, it indicates a very low voltage plateau. For that interpretation, it is important to notice that this mode changes already at 1000 mAh/g. This small voltage plateau already gives first hints that the silicon is almost completely converted into amorphous silicon. It only has one single, very small voltage plateau. It emphasizes that there is hardly any crystalline silicon anymore. The estimated capacity cannot be reached by this mode anymore. The same behavior is observed during the delithiation. There is only one voltage plateau followed by an increase in voltage. This increase is necessary for the complete removal of the lithium out of this already amorphous alloy. The one-step conversion supports that the formed LiSi alloy is amorphous and no additional step is needed to extract the lithium out of a crystalline alloy.

The cycling performance of silicon microwires with $LiNO_3$ electrolytes indicate degradation after 200 cycles, induced by missing potentiostatic plateaus, which lead to parasitic reactions in the current. This effect is a slow effect with a large length scale because the consequences are observed first at higher cycle numbers. In the beginning, the anode performs well with high capacities. Therefore, the degradation effect has to have slow time constant to leads to this large degradation. This slow time constants appear due to collective phenomena and not only locally, where usually the time constants are faster.

5.5.1 Copper Degradation

As indicated, the length scale for this degradation phenomena is quite high. The capacity fade occurs first after a long cycling period. Due to the fact, that the current increases drastically, there are strong hints that parasitic reactions occur. Parasitic reactions might be first signs of the degradation mechanism of the copper current collector. This means that the ohmic contact between the silicon wires and the current collector starts to fail. The silicon wire anodes have a current collector with a thickness of 45 µm. Due to the integrated contact between the wires and the copper, series resistance losses are imposed on the anode. The current collector cannot carry the change in the current due to the galvanostatic and potentiostatic modes anymore and starts to fail. In order to verify, if this degradation mechanism is related to series resistance losses at the ohmic contact, corrosion tests are performed.

The amount of $LiNO_3$ inside of a standard battery test is 0.0086 g for a 0.25 M $LiNO_3$ solution. The corrosion tests contain five times this amount to accelerate the corrosion and simulate what could happen to the current collector with time. These tests are performed in a transparent glass tube, forming the battery housing, with two inert electrodes on both sides as counter electrodes. The test slide (working electrode) has a similar diameter like the real copper current collector, but with a reduced thickness of 25 µm (half the thickness of the real anode current collector). Figure 5.24 indicates how the copper slide reacts with the dissolved $(NO_3)^-$ ions. Camera-based imaging during the corrosion tests revealed the complete corrosion and dissolution of the copper test slide. The separator shows a color change from white to blue and green. The color change is characteristic for the formation of $Cu(NO_3)_2$. This color change is also visible at the surface of the copper slide. The slide itself is pulverized in several pieces. Even parts of the slide are completely dissolved by the used electrolyte during this corrosion mechanism. The results indicate that the copper is dissolved by the electrolyte additive. Due to the high amount of additive, the corrosion was fast within 24 hours time. The diameter of the copper slide was reduced by a factor of 1.5 (from 1 cm reduced to 0.67 cm) with a thickness change of about 10 µm. The dissolution rate during this experiment is higher than during the standard cycling test. If the dissolution rate with increased amount of $LiNO_3$ is approximately 0.5 µm per hour; in a cycling experiment with 5 times lower amount of this corrosion catalyst, the dissolution/etching rate is also slowed down. The same experiment with reduced electrolyte indicated that only the circumference of the copper slide (on the edges) turned green i.e. oxidized. Another severe consequence has the oxidization on the copper-silicon interface. The thickness of the real current collector of the anode is twice as thick as the test slide. This concludes that the corrosion i.e. degradation of the current collector of the anode plays an important and crucial role. The reduced dissolution rate has a high length scale on the system and imposes series resistance losses on the ohmic contact at the interface between the copper and the electrolyte. There, locally at this interface the complete current collector starts to oxidize. This is

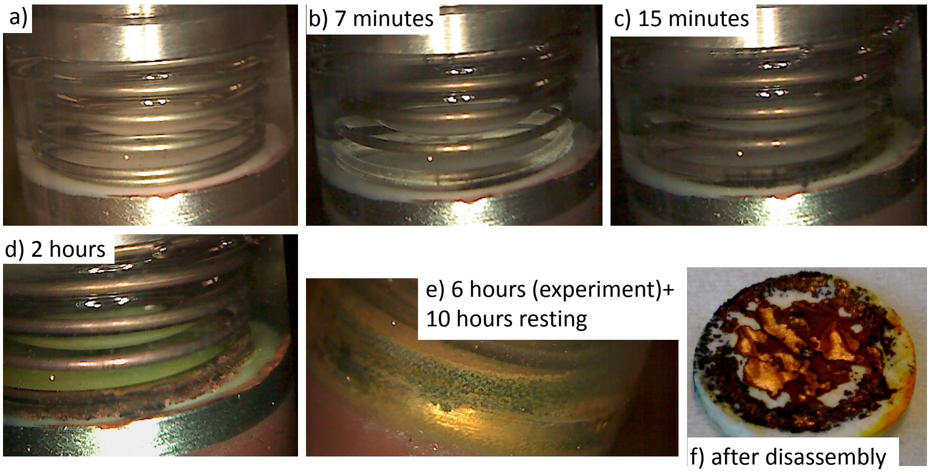

Figure 5.24: Corrosion of the copper current collector by in-situ camera-based imaging of the electrode. The corrosion test is performed in a specially designed transparent cell, in order to investigate possible corrosion in a color change of a copper slide. a) It shows the original, starting experimental set-up as reference for possible reactions. b-c) Due to the high amount (0.043 g) of $LiNO_3$ inside the electrolyte, first signs of corrosion at the copper/electrolyte interface are visible at the copper side already after several minutes. d-e) With time of the corrosion test (approximately 2 hours), the reaction products of the oxidation of the copper can be seen in the electrolyte. This can be seen in the change of color of the electrolyte from transparent to green due to the formation of $Cu(NO_3)_2$. f) After disassembly of the electrode, the separator as well as the copper show severe signs of degradation and complete destruction of the copper slide.

reflected by the comparable corrosion experiment (Figure 5.24), where in 24 hours only the interfaces and edges of the copper slide were predominantly corroded due to the reduced amount of additive. These parts are in direct contact with the electrolyte. Transferring this to the complete anode structure, the main part of the current collector of the anode (Figure 3.5) is covered by the silicon wires, buffering or retarding the oxidization of the copper.

If the ohmic contact is damaged and degrades over time, parasitic reactions occur and the observed current increase occurs. If the current collector oxidizes, the copper-silicon interface is crucial because the oxygen and nitrogen ions from the oxidization may start to oxidize silicon. As a possible consequence, the sandwiched silicon may become amorphous and no (new) crystalline silicon is transported into wire. The sandwich structure is for this electrolyte the weak link. Looking further ahead, the electrochemical reaction continues and the remaining, crystalline silicon wires still expands by a factor of four. The now amorphous sandwich, on the other hand, has problems during this volume expansion and is a mechanical limitation. Especially, if nitrogen and oxygen ions continue to diffuse along the wire and start to change the crystal structure, the complete mechanical stability of the free-standing structure weakens. Complete amorphization of the wires lead to a drastic capacity fading, as a result of different (activated) silicon alloys.

5.5.2 Viscosity Influence of Electrolyte

First, the current collector-electrolyte interface was discussed and hence the related degradation of the current collector was revealed. But the electrolyte not only has an effect on the current collector, it also effects the silicon wires directly. This is the most important interface because the silicon wires are the active material which have to work with the electrolyte in a Li-S cell. In order to differentiate between already known influences on the silicon array and completely new and special phenomena in this type of electrolyte, the electrolyte itself (pure without the electrode) is investigated following the FFT-IS-Electrolysis for the standard electrolytes (refer to chapter 5.2). The detailed investigation of the electrolyte is essential, in order to produce a high performance full cell. Up to now, the electrolyte (as well as the low areal capacity of the cathode) is the limiting factor in a high performance and durable full cell, either limiting the necessary anode performance or depleting the complete full cell due to complete absorption of the electrolyte by the cathode [66, 212].

The main concern here is the electrolyte compatibility with the anode because usually pre-lithiated silicon anodes are used in full cells. Nowadays, pre-lithiated sulfur cathodes are used as an alternative to the pre-lithiated silicon anodes as well. Consequently, the silicon wires are in contact with the electrolyte already during the SEI formation. Exactly this formation and the consequences for silicon have to be evaluated because it might allow to design a specialized electrolyte for silicon and sulfur electrodes. As discussed previously, the SEI is the most crucial property in batteries and has to be maintained also in full cells. Chapter 5.2 already showed the electrolytic influence on the cycling performance. There, it was elaborated that the viscosity and the ionic conductivity of the electrolyte are crucial properties, which contribute to the anode performance. The basic difference between the cyclic carbonates used in the previous electrolytes and in this sulfur electrolyte (1,3-dioxolane, DOL), is the lack of an additional CO double bond, as in the case of EC. Another difference is the change in lithium salt. LiTFSi is found to be less stable, compared to $LiPF_6$ and reduces the ionic conductivity. Figure 5.25 indicates the series resistances of the sulfur electrolytes, recorded again by the FFT-IS analysis.

The addition of PC to the standard carbonaceous electrolyte system is already discussed in detail in chapter 5.2. In order to understand the differences to that electrolyte system, it is shown here as well. Important to mention is, that sulfur electrolytes (Table A2) are tested in a different voltage region. The series resistance in Figure 5.25 can be divided in three parts: I. represents the viscosity change during the SEI formation, II. shows the electrochemical dynamic of the electrolyte and III. emphasizes the dynamics and kinetics of the electrolyte. The first part is the most important one (Figure 5.25 a). The resistance increases for PC almost linearly in part I. For $LiNO_3$, the series resistance decreases, instead of increases, indicating a negative slope. Following the above discussion, there is no significant viscosity increase. Compared to standard anode electrolyte, sulfur electrolytes with the added $LiNO_3$ show low viscosities of only $1\,cP$ [212, 217, 220]. By deliberately aging electrolytes, they can be tested, if they will perform with highly-oriented silicon wires or not. The reduced viscosity for $LiNO_3$ electrolytes indicate a very low material flow to the electrode/electrolyte interface, which corresponds to a thin SEI layer. This reduced viscosity needs to be taken into account when discussing the

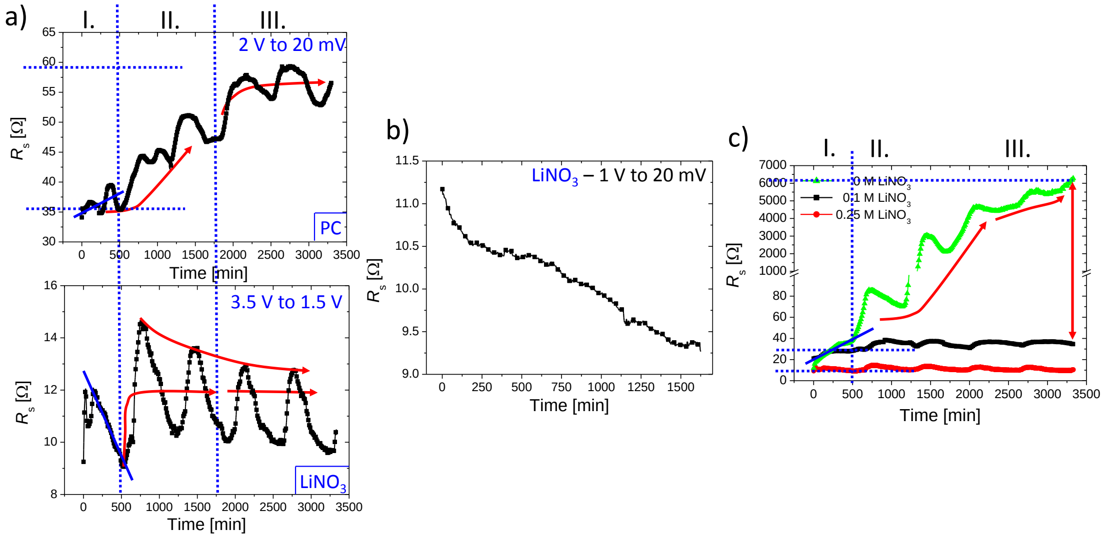

Figure 5.25: FFT-IS-Electrolysis of sulfur electrolytes with $LiNO_3$. a) The comparison of two different electrolytes PC (above) and $LiNO_3$ (below) shows the dynamic of the electrolytes and the necessary viscosity change. $LiNO_3$ electrolyte is cycled between 3.5 V and 1.5 V. In contrast to that, b) shows the series resistance of the same sulfur electrolyte exactly in the same voltage range, as the other electrolytes. c) When changing the composition of the electrolytes, severe differences are obvious. Electrolytes without nitrates show an increase in series resistance about two orders of magnitude.

long-term cycling experiment, shown in Figure 5.22. There, very high irreversible losses occurred with up to 70 % in the first cycles. Taking into account the previous discussions, the reduced capacity in the beginning is a result of the changed SEI formation. Not only the decomposition products of the electrolyte on the silicon wires changed, but also the influence of the solvent changed. As it is well-known, DOL is a Broensted acid and can also be seen as initiator for cationic polymerization (BASF, [221, 94, 222, 185, 186]). Due to the reduced reactivity of DOL without $LiPF_6$, the polymerization reaction is reduced and the viscosity is consequently not increased. Consequently, if a polymerization takes place, it only forms short polymeric chains. But also this polymerization is negatively influenced by the co-salt $LiNO_3$. In comparison to the other cyclic carbonates EC and PC, DOL has initially a very reduced viscosity and cannot contribute this effectively to a higher degree of polymerization. Due to the addition of a common linear carbonate for sulfur electrolytes, namely DME, the already low initial viscosity is even more decreased i.e. diluted (refer to Figure 5.25). In order to explain the capacity fading at higher cycle numbers, the second and third part of the series resistance plots have to be taken into account, (as well as the copper degradation). The co-salt $LiNO_3$ is only electrochemically stable for voltages above 1.7 V. Below this limit, it is irreversibly reduced on the anode surface. This reduction is observed during cyclic voltammetry measurements as additional peak at 900 mV. The co-salt reduces mainly to Li_xNO_y phases on the surface of the anode and disturbs the stable and homogeneous SEI formation. [217, 220] observed around silicon mainly surface films containing a high amount of oxygen and less amount of fluorine. The $LiNO_3$ hinders the dissociation of the main-salt LiTFSi, resulting in only a small amount of LiF inside the SEI. The dissociation of the standard electrolyte LP 30 (mainly consisting of alkyl carbonates EC-DMC) contains mostly [220, 94, 95] Li_xPF_y, LiF and Li_2CO_3 (and many more). This reaction is even more disturbed because the nitride agglomerates at the silicon surface. The influence of the nitrides on the silicon surface are unclear up to now. One suggestion is that it forms an isolating, dielectric layer around the wires; first in form of agglomerates which grow into each other. By enhanced agglomeration, it might be that locally the current increases drastically, destroying the wires.

During the cycling experiments, the C-rate is increased after the first four cycles. At this point, there is a sharp decrease in the capacity. Due to the reduced thickness of the SEI layer, it takes more time to build a complete SEI layer around each wire. Compared to others [217], the amount of active material is very high. Not only is the amount high, but also the aspect ratio because the length of the wires with 70 µm is rather high as well. That means, if the SEI formation is not finished during these four cycles, the capacity will fade because the volume expansion is increased by the C-rate. The SEI layer has to expand as well and induces holes, which have to be repaired in the following cycles. This is reflected by the cycling experiments. The second and third part of the series resistance describe the dynamics of the electrolyte. The series resistance of the high-performance electrolyte with the addition of the PC is twice as large and shows a stabilization in the third part. The sulfur electrolyte with $LiNO_3$ does not show such a resistance increase. The electrochemical behavior of the electrolyte is completely different. The series resistance switches from the viscosity change directly to the last and final part: to an almost constant series resistance. The amplitudes for the resistances stabilize, which means that for every cycle the height is the same with clearly, defined large minima and maxima. Postmortem analysis of the silicon wires showed a high depletion and consumption of the electrolyte after cycling. There was too less electrolyte during cycling the anodes with that type of electrolyte. They were completely dried. No ionic conduction could be established anymore due to the enhanced depletion. This was supported by the multi-step reduction of the electrolyte and the reduction of the cyclic and aprotic solvents [219, 94, 216]. It is known already that the first reduction or in general reaction of nitrides with DOL lead to enhanced depletion of the electrolytes. With higher cycle numbers, this change in electrochemical dynamic is seen in slower diffusional processes due to electrolyte depletion. Higher voltages are needed with every new cycle, either to incorporate or remove the ions from the anode. Although the series resistance is quite low compared to the standard electrolytes, the ionic conductivity of these electrolytes is twice as low. In this voltage regime, the byproducts are still soluble and still contribute to the reaction inside the electrolytes. But the partially reduction of the co-salt $LiNO_3$ is still triggered because the voltage is swept at 1.5 V. That means, that the salt dissociates and reduces partially in the first cycle, but forms reaction products with the co-solvents at higher voltages. With ongoing cycles, higher degree of reduction is achieved. It can be deduced from the electrochemical dynamic of the electrolyte that the salt is not completely reduced after these five cycles because the maxima and minima stabilize. There are also no agglomerations or insoluble products, which would drastically reduce the impedance.

The compatibility of sulfur electrolytes with the electrodes is quite new and not discussed in every detail. Therefore, the FFT-IS analysis is decisive for the full cell technology. Figure 5.25 b) shows the FFT-IS analysis for the same type of sulfur electrolyte with added $LiNO_3$, but analyzed in the same voltage range as for the standard EC-DMC electrolyte (anodic region), in order to test the electrolyte compatibility. The series resistance decreases almost linearly with time. It shows neither the viscosity increase nor the maxima and minima in the resistance. This clearly demonstrates the dynamic of this electrolyte in this voltage regime. The reduction shows that the electrolyte is not electrochemically stable. Both impedance curves (in both voltage regimes) can be explained by looking at the chemical reduction of the electrolyte ingredients. The electrolyte is only electrochemically stable above 1.7 V. That means that lower voltages irreversibly reduce the co-salt $LiNO_3$ in NO_2 and Li_xNO_y, feeding the conductivity of the electrolyte. The co-salt is reduced every time again, and completely consumed. It cannot contribute anymore to the ionic diffusion, lowering the resistance every time even more. The behavior can be extrapolated to zero, if the experiment would only take long enough. At those voltage regimes, reactions between $LiNO_3$ and the co-solvent DOL lead to enhanced decomposition of the carbonates inside the electrolyte, by shifting the equilibrium more the decomposition products. Those reaction products agglomerate and are not soluble again in the rest of the electrolyte. They block further reactions [217, 223, 220, 212, 216].

$LiNO_3$ concentration variation (0 M - 0.25 M solution), as indicated in Figure 5.25, clarify the salt influence on the electrolyte performance [217, 215]. Electrolytes without $LiNO_3$ show a completely different behavior and resemble more those already discussed in chapter 5.2.3. The basic difference is the drastic increase in series resistance after the first region. This is a result of the low ionic conductivity with LiTFSi. Nevertheless, Region I. shows a large increase in R_s, which is accompanied by a viscosity increase of the SEI layer. Cycling behavior supports this necessary increase in the resistance because it can be (almost) directly correlated to the minimized irreversible losses in the first cycles. As mentioned, during these cycles the losses are always higher than for higher cycles, because of the SEI formation. The impedance measurements now indicate that this is more stable and that it helps the cycling process. This reaction is so stable due to the increased viscosity or expressed differently to the reduced ionic diffusion in this part. For the long term cycling, the critical part is the increase in resistance and its ongoing increase, which might again limit the reversible, high behavior. If the ionic conductivity is lost at some part, no diffusion could be established. The effect of $LiNO_3$ inside electrolytes is still under investigation.

5.5.3 Influence of the electrolyte on the mechanical stability

Having a closer look at the silicon interface after cycling, SEM as well as EDX analysis revealed the consequence of the individual components in Figure 5.26. The EDX analysis revealed a severe oxidation of the silicon surface. The shape of the silicon surface is not at all typical after cycling. Usually, it is flat or covered with a smooth surface, like the ones shown in Figure 5.5. Large amounts of oxygen are recorded. TEM analysis verified the oxygen contents and revealed a nearly complete amorphization as a result of this oxidation. A complete comparison of the TEM results with varying electrolyte is located in the Appendix A5. The total ratio of the detected signal of silicon and oxygen is almost 1:2, indicating a very high oxygen concentration accompanied with a dielectric silicon oxide formation. With the combination of DOL and $LiNO_3$, the reaction is shifted towards more oxygen-containing sulfur species like mentioned above, for example NO_2, or LiS_xO_y and short oligomers with lots of oxygen functional groups. If a small layer of oxide forms directly at the interface, it is a catalyst for further oxidation [175, 177]. As discussed earlier, a high degree of

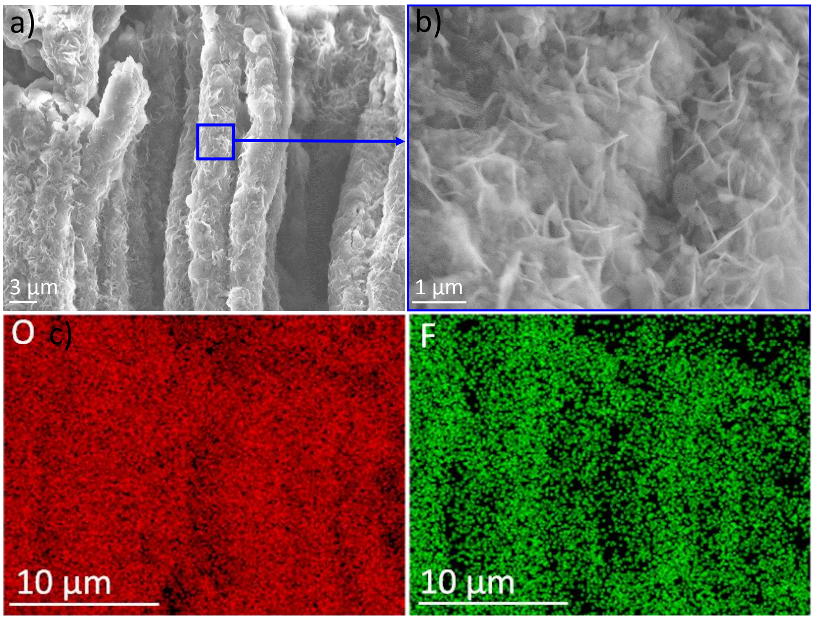

Figure 5.26: Silicon surface after cycling in $LiNO_3$ electrolytes. a+b) The surface of the silicon wires show small spikes, which is not typical. c) An extract of the EDX analysis shows severe oxidation of the silicon surface. Sample preparation artifacts can be excluded because the oxidation is demonstrated independently by Raman spectroscopy as well. Those measurements are performed in an argon-filled and sealed pouch cell, without contact to oxygen.

crystallinity is a requirement for the good cycling performance. An amorphization as in this case results in a capacity fading. At this point, again the lack of the mechanical stabilization of the silicon wires is important: with ongoing amorphization, silicon cannot withstand the volume expansion anymore and is prone for crack formation and mechanical failure. If the stress is inhomogeneously distributed inside the amorphous layers, cracks are induced and are likely to propagate, leading to a phase separation of the amorphous and crystalline silicon and therefore to mechanical failure of the silicon wires [168, 206, 224, 225, 226, 227, 199]. Even if only small cracks exist inside this amorphous layer or at the interface between amorphous-crystalline silicon, the Li ions are likely to diffuse exactly to those spots and start new chemical reactions with the silicon. Locally they break additional (still crystalline) silicon bonds and lead there locally to enhanced tensile stress and crack propagation. Thus, the capacity fading described in Figure 5.22 might be a combination of two facts: a) the ohmic loss and mechanical disintegration of the silicon wires and b) the almost complete amorphization of the silicon wires. Coming back to the self-organized crystal growth, for the sulfur electrolytes, the SEI layer is not elastic enough and cannot maintain enough restoring force on the silicon wires. This leads to an amorphization. In addition, the electrolyte and decomposition products of the electrolyte accelerate this effect. There is still a seed crystal embedded inside the copper. But there is a major drawback: a) these seed crystals are also partially oxidized due to the $LiNO_3$ and the copper corrosion. As a consequence, the seed crystals do not necessarily survive the long-term cycling process, which have momentous damage on the wires. If an amorphization takes place, the partial pressure difference between the quenched (copper-silicon sandwich) silicon part and the rest, amorphous parts increases and the SEI layer has to withstand large amounts of pressure. Due to the very thin layer, it cannot accommodate this very easily (Appendix A5).

5.5.4 Potential of FFT-IS-Electrolysis

In order to point out the power of this type of measurement (see chapters 5.2.3 as well as 5.4.2), an additional example is the investigation of the possible current collector oxidation, as in the case of $LiNO_3$ and copper, with the electrolytes. The course of the curve in Figure 5.27 illustrates the oxidized current collector as a result of the redox reaction. In analogy to Gaberscek, this oxidization is considered as an additional interface reaction between the current collectors and the electrolytes with a parallel resistance. (The fit of these data is related to one RC circuit, as indicated in chapter 2.7.3.) Every increase in the resistance is directly correlated to a defined local corrosion process. After complete oxidization, the resistance increases over many orders of magnitude. The resistance is directly correlated to the current. After complete oxidization, the system undergoes a short circuit and the current decreases to zero. In summary, all of these FFT-IS-Electrolysis results show the importance of

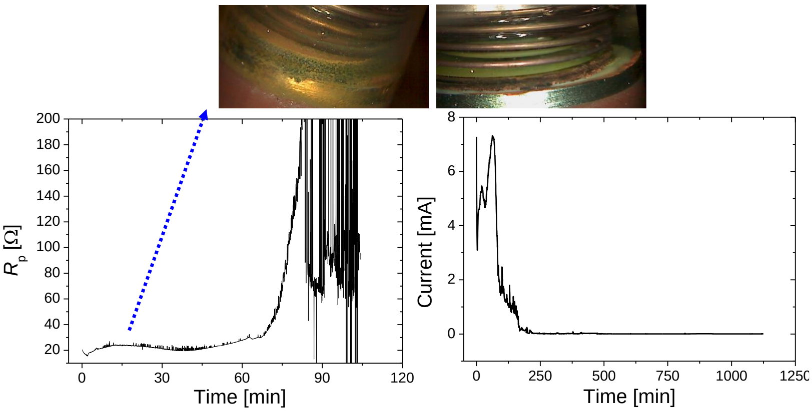

Figure 5.27: FFT-IS analysis of the current collector-electrolyte interface. By analyzing also the current collector, it is possible to detect possible oxidization and redox reactions before cycling a complete battery in this type of electrolyte. The corresponding photographs illustrate the oxidization, accompanied by an increase in parallel resistance.

this measurement technique, which should be done on a routine basis.

5.6 Kinetic Limitation in High-Temperature Cells

It is already well known that temperature is the worst enemy of batteries. The enhanced self-discharge leads to a complete failure of the battery. Even Tesla's batteries, with Tesla being the largest e-vehicle supplier, suffer the most from a driving range reduction of around 30-50 %, if the temperature is not constant at ambient temperatures (auto motor sport, 12.2014, [12, 13]).

Up to now, all experiments are performed at room temperature. In order to investigate the temperature influence on the silicon wires, temperature profiles are recorded and applied to the half cells. Cyclic voltammetry as well as corresponding FFT-IS analysis emphasize the kinetic influences on the silicon wires. This fundamental study is necessary to understand how the silicon microwire array anodes can be improved to perform at high temperatures as good as at ambient temperatures.

Figure 5.28 indicates the temperature profile, which is applied to the anode at the same time during long-term cycling experiments. Of course, the C-rate is varied as well in order to estimate the limits of the silicon microwire arrays. Astonishingly, after immediate C-rate increase from the starting value, the capacity fades drastically. The step-like character in the capacity curves perfectly reflects the (external) change

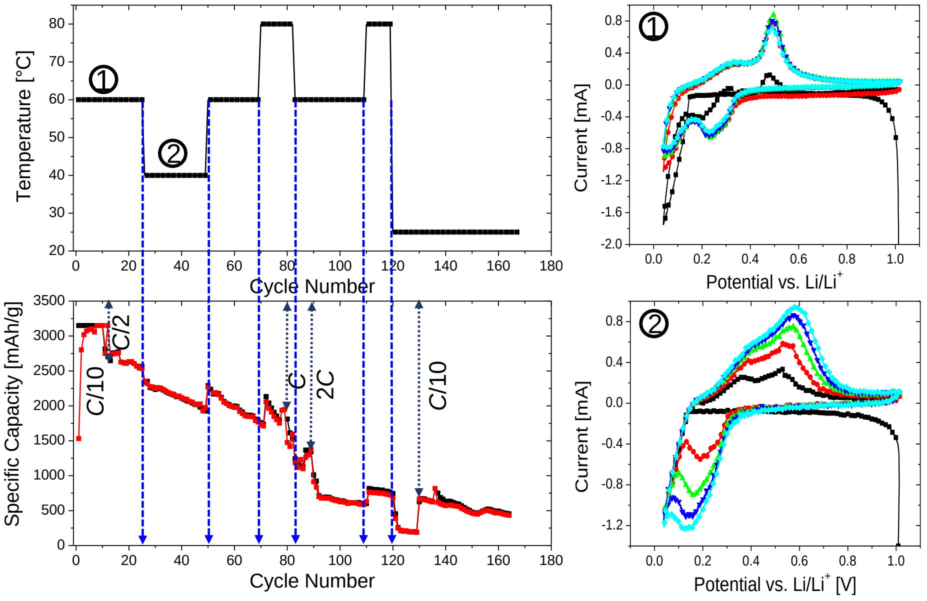

Figure 5.28: High-temperature cycling with silicon microwire arrays indicate a high capcity loss with varying temperature. The adjacent voltammograms in the same temperature range, as indicated with 1 (60 °C) and 2 (40 °C), show an enhanced reaction at the expense of the partial lithiation and delithiation process.

on the system, either by temperature variation or by C-rate modulation. The capacity keeps decreasing drastically by nearly 80 %. Possible explanations can be drawn from the enhanced diffusion rate and kinetic limitations. As discussed in chapter 2.6.2, the reaction rate increases exponentially with temperature. A higher number of ions move i.e. diffuse to the individual wires and try to incorporate into the anode. The adjacent voltammograms, recorded at 40 °C and 60 °C, support this mechanism. The current keeps increasing to the expense of the partial lithiation and delithiation peaks, indicating a higher number of charges flowing. This means that almost no two-step conversion exists anymore. Consequently, the structure might accelerate to amorphize completely, thus losing its characteristic high degree of crystallinity. Another aspect might be that the structure completely loses its stability with the temperature impact due to the crystal re-orientation. Postmortem TEM analysis show that the wires break in small pieces (refer to schematic in Figure 5.30) or that cracks are induced. The surrounding SEI layer partially keeps the individual parts together.Thus, the mechanical properties of the free-standing electrode are lost or at least changed dramatically. These cracks might be a consequence of the inhomogeneous distribution of the generated heat at the silicon interface in combination with potential amorphization. Because of the higher diffusivity of Li towards the cracks and higher local, tensile stresses around the cracks, Li favorably reacts at those points and reduces locally the fracture toughness by breaking the covalent Si bonds [228, 229]. Looking at the capacity of cycle 130, the fading is not reversible - the anode is irreversibly destroyed. Normally, the capacity should increase again, when cycled at room temperature.

When discussing temperature effects, not only the electrode structure suffers, but also the surrounding electrolyte. These tests are performed with the standard electrolyte Selectilyte LP30. Those electrolytes slightly increase their ionic conductivity by 63 % or in the case of PC electrolytes by more than twice the initial value (LP30=11.3 mS/cm at room temperature, PC/EC/DMC=15 mS/cm). Due to the coupling to the diffusion, the enhanced reaction rate is evident. The high performance cycling tests are still performed in the "safe" electrolyte range (see chapter 3.4). Below 85-90 °C, the electrolyte remains stable. Above these critical temperatures, anyhow, the PF_5 begins to decompose further under CO_2 evolution in LiF and HF and Li_2CO_3. Anyhow, the complete wire destruction may be a result of the imperfect SEI layer, which also reacts and starts to dissolve with temperature. The continuous reaction of the SEI layer with the "hot" electrolyte leads to a periodic re-arrangement of the SEI layer. As the homogeneity of the SEI layer is a requirement, as discussed in chapter

5.2, for a successful cycling, strong hints lead to the conclusion that this is at least one possible failure mode. The viscosity of the electrolyte was found to be equally important for the performance. With increasing temperature, some processes inside the electrolyte start because they are thermally activated, especially, an increased ring-opening process is noticed. Consequently, a higher degree of polymerization is observed. Due to the complex interaction between the sheer stress and the cohesive forces inside viscous fluids, no viscosity increase follows the enhanced polymerization at elevated temperatures. Instead the electrolyte is even more liquid-like. It is even more pronounced in the high performance electrolyte with the addition of PC, which shows severe capacity loss. Figuratively, the approach is to improve the thermal stability of the silicon microwire array anodes and to keep the kinetic limitation to a minimum. Therefore, Figure 5.29 shows the improved cycling behavior with boron nitride infiltration As indicated, the BN flakes are not completely integrated or coated along the wire walls but only the wire tips are covered with this nano-composite. Subsequent EDX analysis indicate that also the first 10 µm are covered with a thin boron layer. This infiltration enables a) a capacity increase by a factor of 2 with a C-rate increase by a factor of 10, b) a stable capacity also at 40 °C without irreversible losses, c) hardly any capacity loss when cycling with 1 C and d) a stable capacity at 80 °C. Reference measurements at room temperatures with BN, anyhow, indicate a rapid capacity decrease from the beginning.

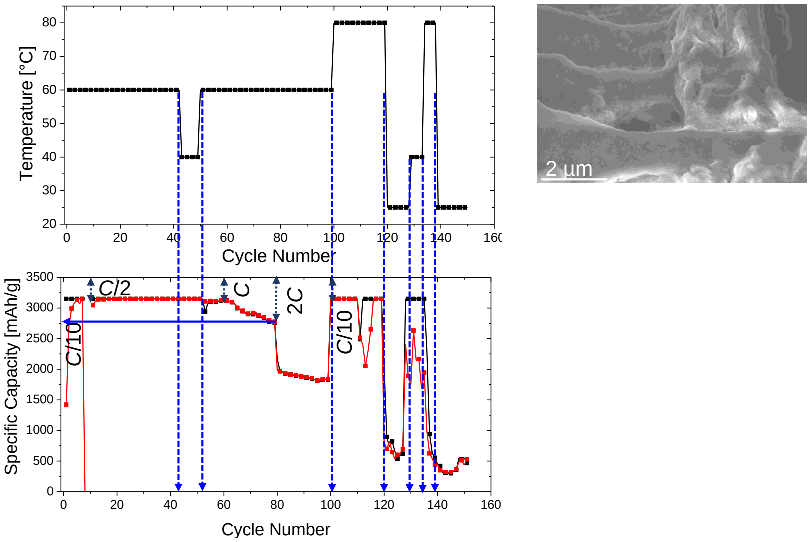

Figure 5.29: Improved high-temperature cycling of silicon microwire arrays with additional BN nano-composites. The benefit of BN is clearly seen with C-rate variation, also at 2 C.

The capacity decrease at 2 C in Figure 5.29 at 60 °C is the result of kinetic limitation. The enhanced diffusion leads to kinetic limitation, in order to prevent the structure from mechanical failure. The subsequent capacity increase re-establishes exactly that: the structure is still perfectly intact. Thus, the positive effect of BN is attributed to the improved mechanical stability of the wires due to the additional stabilizing plane and the high specific thermal capacity. The high thermal capacity $C_p = \delta Q/\delta T$ allows to transfer the amount of heat outwards, directing it away from the wires. Of course, additional layers always add to the total series resistance of the system. It slightly increases the necessary voltage for the incorporation at 2 C with every new cycle, i.e. with every cycle the voltage limitation during cycling is reached earlier and the total time of cycling increases. Thereby, the C-rate is reduced to only 2.5 C^*. Nevertheless, the question is whether charging at higher C-rates in this temperature range is necessary.

The most important part is that the tips are covered. TEM experiments show that the small tips start to amorphize at first [192], see Appendix A3, which indicate diffusional problems inside the electrolyte. By protecting these tips from the electrolyte influence and thereby slowing down the amorphization process, the high degree of crystallinity is maintained, which allows to form highly lithiated phases. It is likely that the formation of the metastable $Li_{15}Si_4$ phase is prevented. This directs the discussion to another point: The temperature at the interface is dissipated in a more efficient way, having the same temperature at every point. As a consequence, there will not be any local temperature difference at the silicon-electrolyte interface, which would lead to temperature-induced stress and cracks (unidirectional thermal expansion). In

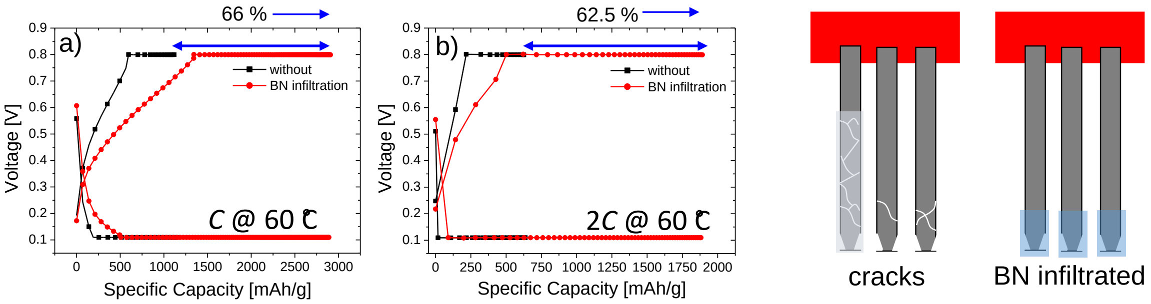

Figure 5.30: Efficiency increase at higher C-rates with BN infiltration. Without BN, the capacity drops to a third. With higher thermal capacity, an increase in heat will not directly relate to an increase in temperature, thus acting as buffer to the wires. Both schematics illustrate the power of the BN nano-composites. It does not lead to temperature induced cracks, maybe also because the temperature is dissipated in a more controlled way due to the good thermal properties of BN.

summary, the silicon microwire arrays perform exceptionally well also at elevated temperatures by enhancing the mechanical properties of the electrode with BN flakes using the high thermal capacity. This coating enabled a total capacity increase of over 70 % at standard C-rates, independent of the temperature, and an increase of 67 % for higher C-rates like 1 *C*. In order to get a feeling for the dimensions: Suppose that the 60 kWh battery of the Tesla S has a driving range of 100 km at a surrounding temperature 40 °C. An efficiency increase of 70 % would lead to a driving range of 300 km.

Chapter 6

Summary & Outlook

This work emphasizes the large potential of silicon microwire anodes for lithium-ion batteries and discusses several improvements to reach stable anodes, based on a fundamental understanding of the interaction of the electrolyte, the SEI, and the mechanical stability of the silicon wires. It indicates the potential of the anode, but more importantly, it can also be seen as a guideline or schedule, what to do to successfully fabricate highly-stable electrodes. The results are not limited to silicon, but can be applied to all systems with a high degree of order. The most important results are highlighted and summarized again throughout this summary:

Highly-ordered structure with optimal geometry, like size, length, thickness and shape

In this thesis, it was demonstrated how important the correct size and length is and how it influences the lithiation potential and voltage ranges during galvanostatic charging processes. Correct thicknesses for anodes have been discussed for a very long time in literature, e.g. nano- or micro-sized structures are more favorable for lithiation. This thesis with its publications gives a first, clear indication about the optimal thicknesses and lengths for silicon wire anodes. The entropy minimization is crucial in the different existing anode geometries. Paste electrodes mostly suffer from the interaction of the structures with each other, creating voids around the active material. Due to the random distribution of the silicon inside these anodes, the particle-particle interaction is enhanced and the volume expansion could be performed to every direction. Consequently, the void formation leads to a mechanical loss of the active material to the current collector and most commonly to pulverization and disintegration of the complete anode. If, on the other hand, the volume expansion could be restricted in advance, like for the silicon microwires, the disintegration could be minimized.

Correct charging rates and deliberate capacity (SOC) limitations during charging.

This thesis successfully showed that the correct cycling parameters are crucial to obtain a high cycling stability. Because of the precise and detailed understanding of the impact of cycling rates and SOC limitations on the formation of the SEI and consequently on the silicon anode, the anode could be successfully charged in only 12 minutes, a decrease in charging time by a factor of 10, while maintaining the stability of the anode. Reducing the C-rate in the beginning allows to establish a stable SEI layer, which is a direct requirement to enhance C-rates during cycling. Like that, a high degree of crystallization is established, responsible for the stable capacity.

Viscosity and ionic conductivity of an electrolyte.

FFT-IS analysis demonstrated how the viscosity changes for a high-performance electrolyte leading to high-performance electrodes. The viscosity (together with the ionic conductivity, connected by the Walden rule) is decisive to intrinsically establish an additional mechanical support for the active material. The mechanical support is produced in form of the SEI layer. Passivating SEI layers always form at the electrolyte/electrode interface. Due to the fact that they always form, they cannot be neglected in all of the discussions; otherwise, the models would be falsified. The SEI layer is made out of polymeric and lithiated products of the electrolytes and is a direct result of change in viscosity of the electrolyte. It is quite difficult to characterize only passivating layers around materials. In-situ FFT-IS analysis is very sensitive to diffusion phenomena. They can reproduce and model this behavior in direct dependency on voltage and time. The addition of PC to the standard electrolytes allows a very long-term stable electrolyte and tends to chemically retard further electrolyte decomposition. Consequently, an anode can be cycled much longer because electrolyte aging could be minimized.

For complete full cells, it was demonstrated that the viscosity here is even more important. There, electrolytes contain salts which negatively influence the SEI layer and the performance. If those negative influences can be avoided in such a way that the basic SEI layer is thick and elastic, the direct interaction between co-salts and electrode are buffered.

Mechanical stabilization by elastic SEI during lithiation

By adding PC into the electrolyte, the SEI layer was similar to a viscous fishing net. It can move and expand, with the silicon wire still inside. During lithiation, compressive stresses are put upon the wires, reducing the driving forces for further lithiation, leading to amorphization or disintegration of the anode. By systematically modifying the properties of the SEI layer, these stresses could be reduced and the crystallinity is maintained. Such a modified SEI layer enhances the mechanical stability of the free-standing electrode and can protect it from mechanical failure due to large changes in current density.

Self-stabilization by single crystal growth

The crystal growth needs a permanent and surviving seed crystal. The architecture of the anode is designed in such a way that parts of the wires are embedded and electrochemically inert during lithiation having a reservoir of seed crystals. The elasticity of the SEI layer, thereby, creates enough force on the individual silicon wire to support the single crystal growth and equalizing the partial pressure difference due to an increase in pressure during lithium incorporation. Consequently, the SEI keeps the crystal structure and the solid solution together. In case of an amorphization process, the SEI layer has to be even more elastic because the partial pressure difference between a perfect single crystal and a solid solution is even larger.

The excellent performance, the long-term stability as well as the fast charging could be attributed to the re-crystallization and single crystal silicon growth. The wires are etched and aligned in the <100> direction. Lithium diffusion and the single crystal growth of silicon are anisotropic processes. Lithium diffusion is slowest, and the crystal growth are fastest in the exact same direction, as the wires are etched. Thus, the analysis showed that this direction is essential for the good performance of the silicon wire arrays.

FFT-IS as tool to analyze processes inside the electrodes.

FFT-IS is used throughout this thesis in order to study in-situ the voltage and time dependent processes which limit and trigger the phase transformations inside the silicon wire arrays. Future work will concentrate on the cathode research in order to use the potential of the here-proposed silicon wire array anode. The anode has a very high areal capacity which is beneficial. Unfortunately, no compatible and comparable cathodes with equal areal capacities exist up to now. Combining the anodes with cathodes of smaller areal capacity would lead to a full cell with very low capacity. The recipe for the electrolyte compatibility was covered in this thesis, where the viscosity of the aprotic solvents has to be adjusted in order to allow for a thicker SEI formation.

On the anode side, future research will concentrate on adapting the findings and recipes of this thesis to an electrode system which can be made commercially available and cheaper than this approach. The approach is based on a porous thin film, which is electrochemically etched on a large area etching tool. In order to characterize this electrode system on a large area, a new large area diagnostic tool is developed during this thesis [230]. Compared to the array anodes, this approach is an industry-related approach where time and money play a crucial role. Therefore the etching process itself is adapted to the time scale of solar cell production. One wafer of large area $(15 \times 15\,cm^2)$ can be etched within 30 minutes, depending on the pore size, distribution, and thickness. The guideline of this thesis helps to transfer the important parameters for a successful electrode to this porous layer electrode system to replace existing electrodes.

This summary and conclusion visualizes how important it is to understand each individual component of a battery system, because they interact with each other and influence one another. Therefore, it is not enough to know every detail about one component. Furthermore, it is essential to analyze the interface and the interplay between the components. The reactions at these interfaces are the limiting factors of a battery and have to be understood. With a profound understanding of these interfaces, especially the complex interaction between the silicon and the electrolyte, the cycling performance was successfully increased by a factor of 10. The SEI layer is the gear between the electrodes and the electrolytes and got too little attention. By keeping the gear lubricated, the electrode works. If, on the other hand, the lubricant gets lost, the electrode will lose its functionality. By understanding these interactions, a new electrolyte is designed with increasing viscosity during lithiation and a stable electrochemical dynamic. It is well known that electrolytes can improve the cycling performance, but the electrolytes themselves are hardly electrochemically investigated. A specially designed impedance spectroscopy method demonstrate how electrolytes can be studied quantitatively, acknowledging the necessary parameters for a high-performance anode, even prior to a complete battery test run.

Appendix A

Electrolyte variation

The properties of the used salts as well as lithium salts are summarized in Table A.1:

Solvent	Viscosity cP	Dielectric Constant
1,3-Dioxolan (DOL)	0.59	7.1
Propylene Carbonate (PC)	2.53	64.92
Ethylene Carbonate (EC)	1.9	89.78
Diethylene Carbonate (DEC)	0.75	2.8
Dimethyle Carbonate (DMC)	0.59	3.11
1,2-Dimethoxyethan (DME)	0.46	7.2

Table A.1: Overview of used solvents and lithium salts used in this thesis depending on the viscosity and dielectric constants [77, 94, 95].

The sulfur electrolytes all contain the basic lithium salt with varying concentrations, summarized in Table A.2:

Lithium salt	Solvent 1	Solvent 2	Additive
0.7 M LiTFSi	Dol (1)	DME (2)	
0.7 M LiTFSi	Dol (1)	DME (5)	
0.7 M LiTFSi	Dol (1)	DME (2)	0.1 M $LiNO_3$
0.7 M LiTFSi	Dol (1)	DME (2)	0.25 M $LiNO_3$
1 M LiTFSi	Dol (1)	DME (1)	0.1 M $LiNO_3$

Table A.2: Overview of solvent and lithium salt composition for sulfur electrolytes. In brackets, the individual ratios are indicated [66, 181, 216].

A.1 Electrolyte Aging

When adding DOL to the standard Selectrolyte LP30, the $LiPF_6$ is completely consumed and decomposed. The aging of the electrolyte means that after six days a complete precipitation occurs. This precipitation is studied by Raman spectroscopy in Figure A.1. The peaks of the solvents are completely missing.

Upon mixing both electrolyte components together, an exothermic reaction occurs with heat generation. This exothermic reaction leads to a complete hardening of the electrolyte. Such electrolytes lead to a pore blocking or void volume blocking between the individual silicon wires, as indicated by the SEM images. DOL as such is not very viscous, but may lead under exothermic reaction to cationic polymerization. For an electrolyte it is not very suitable because it is necessary that the lithium salt stays constantly inside the electrolyte. And not only that, for a long-term cycling experiment, it has to be stable the complete time because it has severe consequences on the SEI formation as well as SEI dissolution in combination with the degradation products and precipitations. The purpose of this electrolyte mixing is to underline the electrochemical stability of the electrolyte in the impedance data, in correlation to chapter 5.2.3. The region 3 indicates the electrochemical stability. With this electrolyte, the periodic maxima and minima are separated in additional peaks, indicating that there are additional reactions continuing because of the decomposed electrolyte.

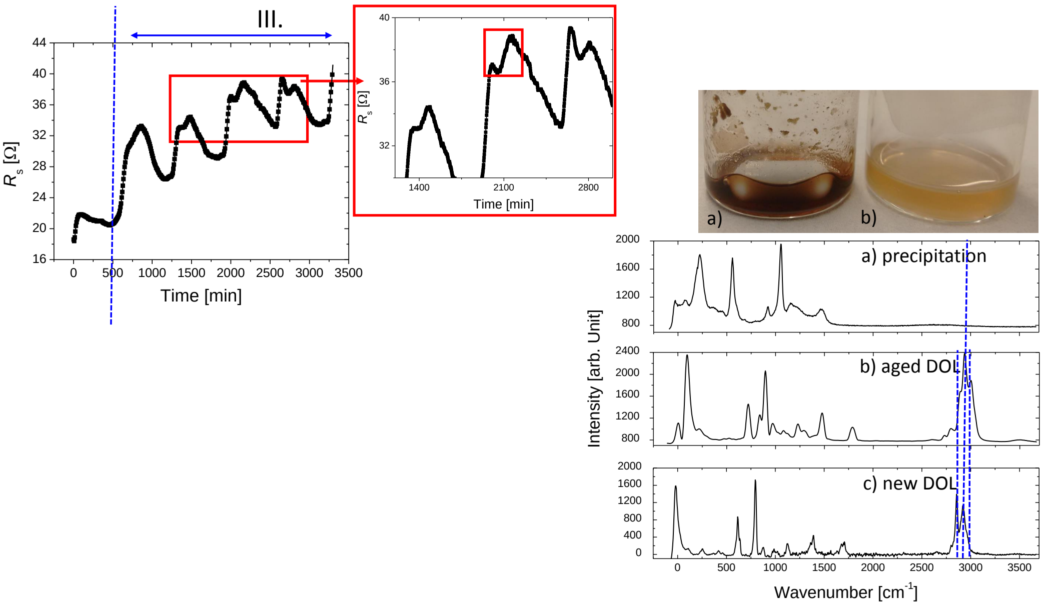

Figure A.1: Electrolyte aging with DOL electrolytes. An exothermic reaction inside the electrolyte leads to a complete polymerization of the electrolyte. Nevertheless, it is not stable and a precipitation of the reduced $LiPF_6$ occurs. Raman spectroscopy measurements compare the three electrolytes, upon which it is emphasized that the complete solvent is missing after aging.

A.2 High Temperature cycling

The infiltration with BN showed the stabilization of the structure (refer to chapter 5.5). The corresponding EDX analysis (Figure A.2 and A.3) indicate that boron and nitrides are also found at the walls of the wires up to 10 µm from the tips. This helps to dissipate the generated heat at the silicon-electrolyte interface and avoids the amorphization process. The TEM analysis emphasize the cracks induced by temperature. The diffraction pattern indicates as well that the structure is almost completely amorphous. The BN can be assumed to be "self-healing".

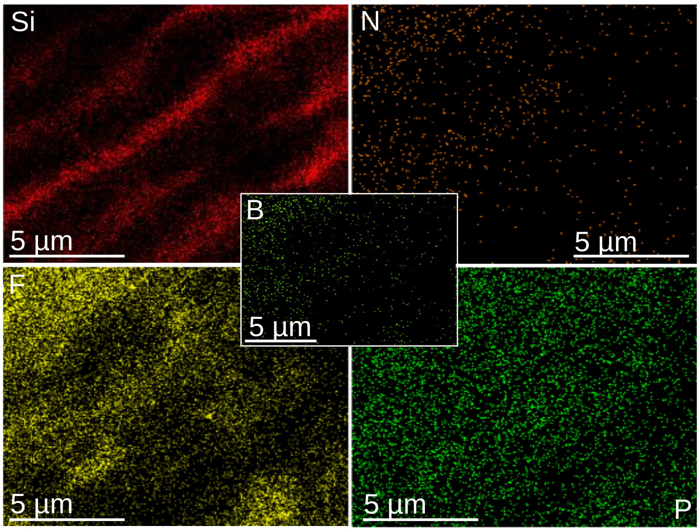

Figure A.2: EDX postmortem analysis of the BN infiltrated silicon wires. It is beneficial that not the complete wire is covered with BN because it is electronically insulating and would limit the capacity rather than contributing positively to it.

A.3 Chemo-mechanical interactions depending on binding material

The fundamental analysis of paste electrodes revealed void formation around silicon wires due to the interaction of the binder, the conductive carbon and the silicon wires. Thereby, it was revealed that the materials used in the paste have to be considered in their interaction with the active material. As a comparison, Figure A.4 shows the three time constants for polyvinyldifluoride (PVDF) as binder material. The basic difference between both materials is their interaction with the electrolyte and

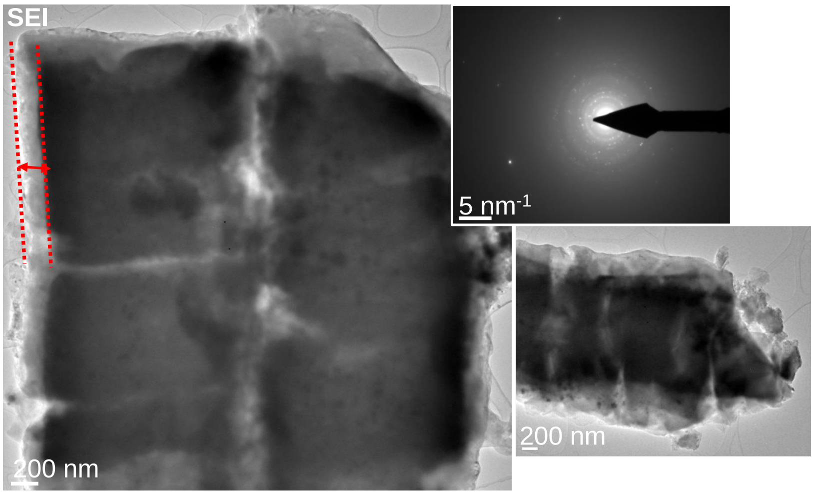

Figure A.3: TEM analysis of the silicon wires cycled with temperature. The induced cracks indicate a mechanical failure of the wires and loss of active material for cycling.

the material. This is clearly seen in the time constants, especially in the first cycle during the SEI formation. The comparison of the time constants show the difference of magnitude between τ_2 and τ_3. The recorded current of the voltammogram shows at 0.8 V (50 minutes) a clear defined maximum, which indicates the formation of the SEI. Astonishingly, the charge transfer process inside the paste with PVDF is three times slower than with CMC, as discussed in the manuscript. PVDF does not chemically bind on the silicon. Furthermore, upon volume expansion it is known that it cannot

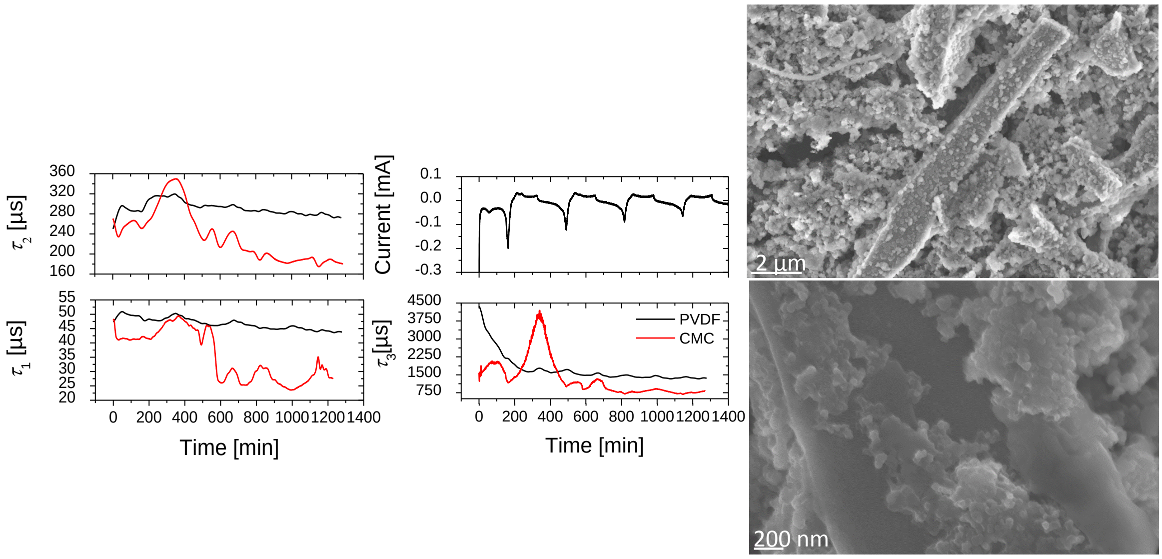

Figure A.4: Chemo-mechanical interactions in paste electrodes with PVDF binder analyzed with impedance spectroscopy, in analogy to 4.2

accommodate the volume expansions without leading to disintegration of the silicon particles [154, 163, 231, 153]. Upon contact with the electrolyte, Che et al. stated that the mechanical properties change significantly, which are demonstrated in the time dependent behavior of the first and fastest time constant τ_1. PVDF adsorbs the electrolyte and swells up. Thus, the bonds, which are already weak due to weak van der Whaals forces, lose their boning strength even more. Consequently, if the silicon wires expand during volume expansion, the tensile and adhesion forces of the binder towards the silicon interface are not adequate to maintain good mechanical stability. The binder has a poor restoring force, which leads to a fast disintegration and pulverization of the paste electrode with this type of binder [154, 231, 153]. Here, the steady increase of the time constant up to the first delithiation peak indicates the interaction of the silicon with the paste. Postmortem SEM analysis in Figure A5 reveals the voids i.e. the disintegration of the wires from the paste. (This behavior is not a preparation artefact, but due to the cycling of the paste electrode.) At the phase transformations, specified by the dashed line, the series resistance losses decrease which is accounted for the stabilization of the SEI. In comparison, the hydrogen bonds of the cellulose interact and adsorb on the silicon surface. Therefore, the adhesion strength at the interface is enhanced. As a consequence, paste electrodes with cellulose show better performance. Nevertheless, as this impedance study showed both binding materials impede limitations on paste electrodes [154, 231, 153].

Another important parameter is the influence on the charge transfer kinetics. While τ_1 and τ_2 follow the same behavior with time, τ_3, on the other hand, shows completely different behavior. Exactly during the first lithiation process, the charge transfer is severely slowed down by the use of a different binder. Also here it shows a stabilization of the behavior when the phase transformations appear. The influence of the SEI formation slows down every process in the paste electrode. This is more pronounced in the paste where PVDF is used. On the other hand, if the first contact with the electrolyte slows down the charge transfer of the ions into the silicon, a slow lithiation process encounters the disintegration due to the volume expansion.

In summary, a binder should show good adhesion strength towards the silicon interface and also towards the current collector. If these adhesion forces are reduced, the active material suffers from void formation. With ongoing cycling, a complete disintegration is observed due to the mechanical failure of the binding material.

A.4 FFT-IS with varying state of charge (SOC)

As previously discussed in section 5.3.3, thin and longer wires show better lithiation and delithiation behavior. Simultaneous FFT-IS analysis gave additional information about diffusional and kinetical limitations, if the C-rate is increased and the SOC as well. Figure A.5 shows in a matrix-like representation the change in time constants with the parameter increasing SOC. This analysis allows to track the history of the previous experiments. Any lithiation will change the state of charge of the anode. Therefore, the FFT-IS measurements show only the first cycle, in order to reproduce what happens when cycling the anodes. TEM analysis showed that the inner core of the wires stays crystalline, which has an impact on the charge transfer kinetics. As shown in Figure 5.20, the movement of the lithiated phase produces compressive stress. This stress and the driving forces for the lithiated phases do not necessarily reduce, especially not, if the stress is transferred form the inside to the outside due to an elastic SEI layer. (These measurements are still performed with the standard

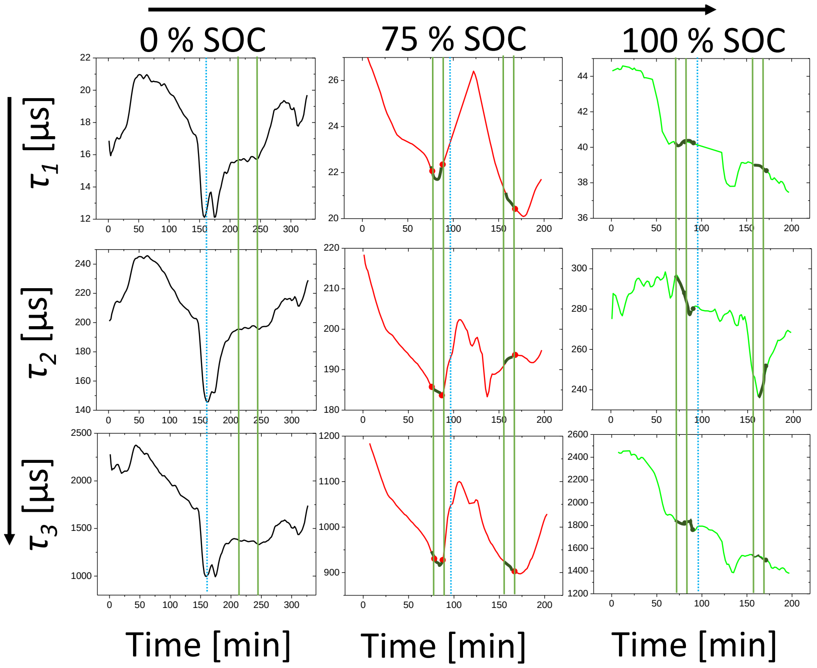

Figure A.5: FFT-IS analysis after pre-lithiation of silicon microwire arrays with varying state-of-charge. The time constants change upon changing the SOC for the wire arrays. The cycling conditions are the same as for the structural characterization. The SOC ranges from no pre-lithiation (0 %) to absolutely no capacity limitation (100 % SOC). The wires in the array electrode have a thickness of 1.2 µm and are 60 µm long. They can be directly compared to the individual study above.

electrolyte system to identify the charge transfer kinetics and correlate them to the XRD and TEM results.)

A.5 Electrolyte variation and influence on crystallinity

As discussed, different cyclic and linear carbonates are tested throughout this thesis. In addition, even esters and ethers are investigated in addition to the standard electrolyte. Figure A.6 summaries the cycling performance with carying cyclic carbonate as well as linear carbonates, esters and ethers. Electrolytes commonly used for sulfur electrodes, it is necessary to investigate the influence of the electrolyte and its components on the silicon performance, as discussed in section 5.3. The first row is attributed to the anode electrolytes and its components. The second row summarizes the different sulfur (cathode electrolytes), even adding sulfur to the electrolyte, which is commonly known as catholyte. Not only the anode electrolyte, but also the single components of the sulfur electrolyte is tested in order to check for the compatibility of the silicon anode with a suitable sulfur cathode. For the anode electrolytes, it is evident that adding PC to the electrolyte and even interchanging a third, linear carbonate DME

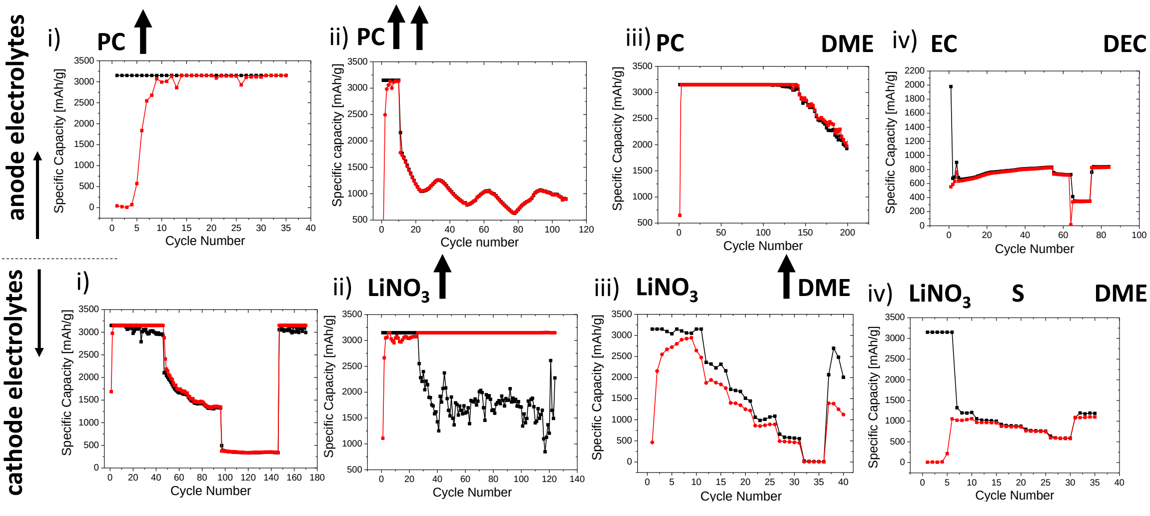

Figure A.6: Cycling performance with varying electrolytes divided in anode and cathode electrolytes indicating the changes to the individual electrolyte systems. anode electrolyte: i) C-rate increase every 5 cycles; ii-iii) same C-rate variation $5C$-$1C$; iv) C-rate variation every 10/0/60/20/20/0. sulfur electrolytes: i) 4/20/20/50/50/50, ii) 4/4/100/4/4/4, iii-iv) every 5 cycles.

will result in good long term stability, but most importantly, to the reported high charging rate. iii) indicates repeatedly this behavior with a charging rate of only 12 minutes. The step behavior in the cycling curves, which is seen in almost all of the tested electrolytes, is the result of the C-rate increase. Typically, the electrolytes are tested between $C/10$, $C/5$, $C/2$, C, $2C$ and $5C$.

The individual electrolyte components have an influence on the crystallinity and thereby on the mechanical stability of the wires. As discussed, the restoring force of the SEI layer on the wires has to be large enough to maintain the single crystal. In other words, if the SEI layer cannot withstand the partial pressure difference due to the large volume expansion and C-rate, the crystallinity of the wires changes drastically. As an example, four differently cycled silicon microwire anodes are investigated with ex-situ TEM and summarized in Figure A.7. The differences are evident in the corresponding SEM and TEM images. The difference between the standard and the PC electrolyte are discussed in detail in this work. The elasticity of the PC SEI layer is very high and enough (the correct amount of force) is implemented on the wire, in order to maintain the crystallinity even after high charging rates. In contrary, $LiNO_3$ additive on the sulfur electrolytes results in an almost complete amorphization of the silicon wire. The SEI layer in these electrolytes is very thin and not very elastic, as indicated by the SEM image as well as by the FFT-IS measurements. Consequently, the wires are prone for mechanical failure and cannot carry as much current as the PC cycled

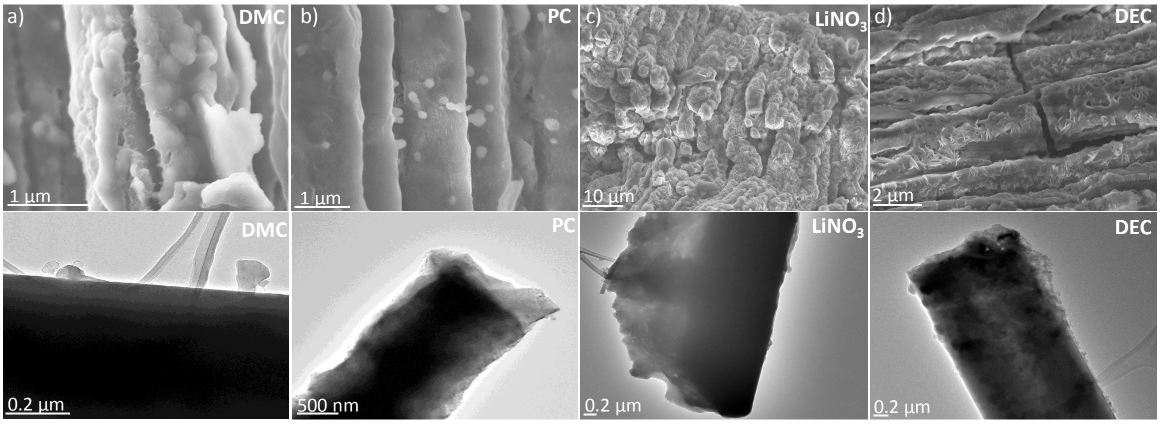

Figure A.7: TEM investigation on differently cycled wires with the corresponding SEM and TEM images a) the standard electrolyte , b) PC electrolytes, c) $LiNO_3$ and d) DEC electrolytes.

wires. The same holds for the DEC samples. Here, the surface oxidation is not as severe as for the previously discussed samples. Nevertheless, the amount of oxygen is enough to lead to a very thin SEI layer and cracks inside the silicon.

Acknowledgement

My special thanks belong to Professor Dr. Föll and Professor Dr. Adelung in equal parts for giving me the opportunity to work scientifically in the field of electrochemistry of silicon and battery technology. Over the past four years, I have learned many things about myself and grown on the subjects. I had the opportunity to fabricate silicon anodes for Li ion batteries, starting from silicon wafers and ending up with finished batteries. Having the responsibility and research opportunity to optimize every single step during the production line enabled far-reaching understanding about the contributions for good electrode material. They allowed me to travel to Stanford University, to get a deeper insight in our anodes. Thanks for letting me talk about my research at different world leading conferences.

I thank Enrique Quiroga-González, who has been my mentor and friend throughout the last years. Although he left me in my first year of my PhD, we overcame the distance between Mexico and Germany. The internet makes it work, and he always listened to my fears, problems and we had fruitful discussions via Skype. I was also very keen on teaching his exchange student Oscar our lithography process, to optimize his work in Mexico. Muchos corazones gracias a toda mi.

I am most grateful to Jürgen Carstensen, without him all the work and discussions would be useless and fruitless. He carved my personality and my scientific work, by throwing me in cold water, after Enrique was gone back to Mexico. I had to give a very important closing presentation in front of financial sponsors of the BMBF. He always trusted in me and my abilities and allowed me thereby to trust myself. I cannot thank him enough for all the work we did together.

Among one of my closest friends and colleges, I thank Andreas Schütt. Andreas has the ability to have a higher (different) perspective on things, relaxing my fear in the last month of my thesis, creating a very nice atmosphere to work with. Due to his background in the solar cell industry and his start-up company, we created successfully two different measurement techniques, based on which, we published papers and convinced industrial cooperation partners to trust our battery abilities. Both Andreas and his wife grew very close to me, being very good friends at work is very important. He always had an open ear for me and our discussion helped me during the writing of my thesis.

I also thank Fabian Schütt for collaborating on the cathode side of the battery and being there to have fruitful discussions to push our technique forward. I thank him for being there for me at difficult times. Many thanks go to Sindu Shree as well for helping with the chemistry of the electrolytes and for performing both Raman and IR-spectroscopy analysis. With that, I thank the complete Functional Nanomaterials and General Materials Science group for the nice working environment. Many thanks go also to Gero Neubüser for making all the TEM analysis for the different questions under investigation.

Another thanks go to Antonio Malavé, who made me responsible for the lithography in the clean room. With this responsibility, I got to know lots of nice and friendly colleagues of every chair of the faculty of engineering, allowing me to cooperate with different projects. The largest contribution and thanks go to my parents and my husband. My family and the love and gratitude of my husband allowed me to believe in myself, to overcome difficult times during my thesis, to just be myself and let me identify that work is not everything in life. He always reminded me on my abilities and calmed my panic with pure and uttermost love, letting me relax in the evening to catch some breath. The support of my family created a lovable backbone in my life. My parents raised me to be honest, supportive and showed me that I could always rely on them.

Thank you all for everything.

Eidesstattliche Erklärung

Hiermit erkläre ich:

Diese Dissertation mit dem Titel "**On the stabilization mechanisms of Silicon Microwire Array Anodes for Li-Ion Batteries**" habe ich noch nie, weder ganz noch teilweise im Rahmen eines anderen Promotionsverfahrens vorgelegt oder veröffentlicht. Ich habe mich bislang noch keiner mündlichen Prüfung im Rahmen eines Promotionsverfahrens unterzogen. Die vorliegende Arbeit habe ich ohne unzulässige Hilfe Dritter und ohne Benutzung anderer als der angegebenen Hilfsmittel angefertigt; die aus fremden Quellen direkt oder indirekt übernommenen Gedanken sind als solche kenntlich gemacht. Die Arbeit ist unter Einhaltung der Regeln guter wissenschaftlicher Praxis der Deutschen Forschungsgemeinschaft entstanden. Bei der Auswahl und Auswertung des Materials sowie bei der Herstellung des Manuskripts habe ich Unterstützungsleistungen von folgenden Personen erhalten:
Dr. Jürgen Carstensen, Lehrstuhl für Funktionale Nanomaterialien, CAU zu Kiel
Weitere Personen waren an der geistigen Herstellung der vorliegenden Arbeit nicht beteiligt. Insbesondere habe ich nicht die Hilfe eines Promotionsberaters in Anspruch genommen. Dritte haben von mir weder unmittelbar noch mittelbar geldwerte Leistungen für Arbeiten erhalten, die im Zusammenhang mit dem Inhalt der vorgelegten Dissertation stehen.

Parts of this here presented work were previously published in the following journals:

Publications

1. S. Nöhren, E. Quiroga-González, J. Carstensen and H. Föll, "Fabrication and Characterization of Silicon Microwire Anodes by Electrochemical Etching Techniques", in *ECS Transactions*, 66 (6), 27-38, (2015).
2. S. Nöhren, E. Quiroga-González, J. Carstensen and H. Föll, "Dependence of the lithiation/delithiation potentials of silicon microwire anodes on their state of charge and sizes"', in *ECS Transactions*, 64 (23), 1-10, (2015).

3. S. Hansen, E. Quiroga-González, J. Carstensen and H. Föll, "Size-dependent cyclic voltammetry study of silicon microwire anodes for lithium ion batteries", in *Electrochimica Acta*, 27, 283-291, (2016).
4. S. Nöhren, E. Quiroga-González, J. Carstensen and H. Föll "Electrochemical Fabrication and Characterization of Silicon Microwire Anodes for Li Ion Batteries", in *J.Electrochem.Soc.*, 163 (6), A1-A7, (2016).
5. S. Hansen, A. Schütt, J. Carstensen and R. Adelung "Local transmittance measurements as large area diagnostic tool for the optimization of porous Si foils as Li-ion battery anodes", in *J.Electrochem.Soc*, 163 (14), A3036-A3045, (2016).
6. S. Nöhren, J. Bahr and J. Carstensen, "Method for producing surface discharge electrodes and semifinished product for carrying out the method", in *International Patent, WIPO*, **WO 2016/037610 A1**, (2016).
7. S. Hansen, E. Quiroga-González, J. Carstensen, R. Adelung and H. Föll, "Size-dependent physicochemical and mechanical interactions in battery paste anodes of Si-microwires revealed by Fast-Fourier-Transform Impedance Spectroscopy", in *J. Power Sources*, 349, 1-10, (2017).
8. G. Neubüser, S. Hansen, V. Duppel, R. Adelung and L. Kienle, "(Re-) crystallization mechanism of highly-oriented Si-microwire arrays by TEM analysis", in *J.Solid State Electrochem.*, DOI: 10.1007/s10008-017-3672-6, 21, 3421-3427 (2017).
9. S. Hansen, F. Schütt, J. Carstensen, J. Marx, V. Kaidas, N. Stock and R. Adelung, "On the mechanisms for resistive switching at local point contacts for 3D Si-nano-architectures", *in preparation*, (2017/18).
10. S. Hansen, S. Shree, G. Neubüser, J. Carstensen, L. Kienle, R. Adelung, "Corset-like solid electrolyte interface for fast charging of silicon wire anodes", in *submitted Journal of Power Sources*, (2017).

Scientific Talks

1. S. Nöhren, E. Quiroga-González, J. Carstensen and H. Föll, "Electrochemical study of size effects in Si microwire anodes for Li ion batteries", Euro Intelligent Materials, Kiel (2013).

2. S. Nöhren, E. Quiroga-González, J. Carstensen and H. Föll, "Dependence of the lithiation/delithiation potentials of Si microwire anodes on their state of charge and sizes", 226th Meeting of the Electrochemical Society (ECS), Cancun, Mexico (2014).
3. S. Nöhren, E. Quiroga-González, J. Carstensen, H. Föll and R. Adelung, "Electrochemical characterization of different carbon additives in silicon microwire anodes", SPIE Microtechnologies, Barcelona, Spain (2015).
4. S. Nöhren, E. Quiroga-González, J. Carstensen, J. Weker, H. Föll and R. Adelung, "Structural characterization of Si microwire anodes by in-situ synchrotron radiation", Advanced Materials World Congress (AMWC), Advanced Materials, Stockholm, Sweden, (2015).
5. S. Hansen, J. Carstensen, A. Schütt and R. Adelung, "Li-ion battery performance of silicon microwire array anodes unter extreme conditions", Spie Microtechnologies, Barcelona, Spain (2017).

Posters

1. S. Nöhren, E. Quiroga-González, J. Carstensen and H. Föll, "Size dependency study of Si microwire anodes by cyclic voltammetry"', 5th Kraftwerk Batterie, Advanced Battery Power, Poster, Session PA 4 (2013).
2. S. Nöhren, E. Quiroga-González, J. Carstensen and H. Föll, "Dependency of the lithiation/delithiation susceptibility and cycling stabillity of Si microwire anodes on their state of charge (SOC), 6th Kraftwerk Batterie, Advanced Battery Power, Poster, Session P2/3 (2014).

Sandra Hansen, geb. Nöhren

Curriculum Vitae

Personal

Name:	Sandra Hansen, geb. Nöhren
Adress:	Kanalredder 29, 24783 Osterrönfeld
Date / Place of Birth:	01/08/1987 in Rendsburg
Marriage status:	married
Nationality:	German
Parents:	Renate and Klaus Nöhren

Education

1994-1998	Grundschule Schacht-Audorf
1998-2007	Helene-Lange-Gynasium Rendsburg
June 2007	graduation (Abitur) Helene-Lange-Gynasium Rendsburg

University Education

10/2007–10/2010	Study of Bachelor Course of Materials Science at the Kiel University (Germany) - mark very good (1.9), number of semester: 6
10/2010–12/2012	Study of Master Course of Materials Science at the Kiel University (Germany) - mark excellent (1.4), number of semester: 4
05/2012–12/2012	Master Thesis: Study of Si Microwire Slurry - Anodes by Cyclovoltammetry Methods at Chair of General Materials Science, CAU, Germany (Prof. Föll) (1.1)
12/2012 – present	PhD. student / research scientist of Prof. Dr. Helmut Föll (AMAT) and Prof. Dr. Rainer Adelung (FUN) at the Kiel University, CAU, Germany

List of Figures

List of Tables

Bibliography

[1] Vereinte Nationen Generalversammlung Siebzigste Tagung (Tagungsordnungspunkte 15 und 16). Transformation unserer Welt: die Agenda 2030 für nachhaltige Entwicklung. *Vereinte Nationen*, 2015. 1.1, 1.2

[2] Lazard Group. Lazard's Levelized Cost of Storage Analysis - Version 1.0. *Lazard Report*, page 29, 2015. 1.1, 1.2

[3] www.welt.de AFP/dpa/Reuters/ott. Die 17 UN-Ziele für eine bessere Welt - kurz erklärt. *https://www.welt.de/politik/ausland/article146885469/Die-17-UN-Ziele-fuer-eine-bessere-Welt-kurz-erklaert.html*, 2015. 1.2

[4] F. Cuenot. Road transport: The cost of renvewable solutions. Technical report, IRENA - International Renewable Energy Agency, 2013. 1.2, 1.2

[5] Umwelt Bundesamt AGEE-Stat. Entwicklung der erneuerbaren Energien in Deutschland im Jahr 2016, Quartalsbericht der AGEE-Stat. *Umwelt Bundesamt*, page 8, 2016. 1.2

[6] G. Sachs Albemarle. Global Lithium Market Outlook - HCID Conference. *www.albemarle.com*, page 30, 2016. 1.2

[7] J. Aspa. Lithium Outlook 2017: Analysts Weigh In. *http://investingnews.com/daily/resource-investing/energy-investing/lithium-investing/lithium-outlook/*, 2016. 1.2

[8] A. Home and D. Goodman. What Price Lithium, the Metal of the Future? *http://www.reuters.com/article/lithium-batteries-ahome-idUSL8N18Y2P6*, 2016. 1.2

[9] C. Morris. New study: Lithium cost swings unlikely to impact battery prices. *https://chargedevs.com/newswire/new-study-lithium-cost-swings-unlikely-to-impact-battery-prices/*, 2016. 1.2

[10] R.E. Ciez and J.F. Whitacre. The cost of lithium is unlikely to upend the price of Li-ion storage systems. *J.Power Sourc.*, 320:310–313, 2016. 1.2

[11] Columbia University. How Better Battery Storage Will Expedite Renewable Energy. *http://www.ecowatch.com/how-better-battery-storage-will-expedite-renewable-energy-1882097909.html*, 2015. 1.2

[12] X. Gong and C. C. Mi. Temperature-dependent performance of lithium ion batteries in electric vehicles. In *2015 IEEE Applied Power Electronics Conference and Exposition (APEC)*, pages 1065–1072, March 2015. 1.2, 5.6

[13] T. Yuksel and J. J. Michalek. Effects of Regional Temperature on Electric Vehicle Efficiency, Range, and Emissions in the United States. *Environmental Science & Technology*, 49(6):3974–3980, 2015. PMID: 25671586. 1.2, 5.6

[14] Lazard Group. Lazard's Levelized Cost of Energy Analysis - Version 8.0. *Lazard Report*, page 19, 2014. 1.2, 1.2

[15] R.v. Noorden. A better battery. *Nature*, 507:26–28, 2014. 1.2

[16] D.L. Wood, J. Li, and C. Daniel. Prospects for reducing the processing cost of lithium ion batteries. *J.Power Sourc.*, 275:234–242, 2015. 1.2, 1.1

[17] V. Muenzel, A.F. Hollenkamp, A.I. Bhatt, J.d. Hoog, M. Brazil, D.A. Thomas, and I. Mareels. A Comparative Testing Study of Commercial 18650-Format Lithium-Ion Battery Cells. *J.Electrochem.Soc.*, 162:A1592–A1600, 2015. 1.2, 1.1

[18] V. Muenzel, A.F. Hollenkamp, A.I. Bhatt, J.d. Hoog, M. Brazil, D.A. Thomas, and I. Mareels. Comment on "A Comparative Testing Study of Commercial 18650-Format Lithium-Ion Battery Cells". *J.Electrochem.Soc.*, 162:Y11–Y12, 2015. 1.2, 1.1

[19] C. Daniel. Materials and Processing for Lithium-Ion Batteries. *JOM*, 60:43–48, 2008. 1.2, 1.1, 1.2, 1.3

[20] C. Cluzel and C. Douglas. Cost and performance of EV batteries (Final report for The Commitee on Climate Change). *Element Energy Limited*, 2012. 1.2, 1.1

[21] O. Gröger, H.A. Gasteiger, and J.P. Suchsland. Review-Electromobility: Batteries or Fuel Cells. *J. Electrochem. Soc.*, 162:A2605–A2622, 2015. 1.2

[22] L. Gaines and R. Cuenca. Costs of Lithium-Ion Batteries for Vehicles (ANL/ESD-42). *Center for Transportation Research, Energy Systems Division, Argonne National Laboratory*, page 73, 2000. 1.1, 1.2, 1.3

[23] M. Hagen, S. Dörfler, P. Fanz, T. Berger, R. Speck, J. Tübke, H. Althues, M.J. Hoffmann, C. Scherr, and S. Kaskel. Development and costs calculation of lithium-sulfur cells with high sulfur load and binder free electrodes. *J. Power Sourc.*, 224:260, 2013. 1.1

[24] M.N. Obrovac and V.L. Chevrier. Alloy Negative Electrodes for Li-Ion Batteries. *Chem. Rev.*, 114:11444–11502, 2014. 1.2, 2.5.1.2, 4.1, 4.2, 5.2.1

[25] C. Fu, C. Song, and L. Liu. High Reversible Silicon/Graphene Nanocomposite Anode for Lithium-Ion Batteries. *Int. J. Electrochem. Sci.*, 11:154–164, 2016. 1.3, 1.2

[26] C.K. Chan, H. Peng, G. Liu, K. McIlwrath, X.F. Zhang, R.A. Huggins, and Y. Cui. High-performance lithium battery anodes using silicon nanowires. *Nat. Nanotechnol.*, 3(1):31–35, 2008. 1.3, 1.2

[27] K. Kang, H.S. Lee, D.W. Han, G.S. Kim, D. Lee, G. Lee, Y.M. Kang, and M.H. Jo. Maximum Li storage in Si nanowires for the high capacity three dimensional Li-ion battery. *Appl. Phys. Lett.*, 96:0531101–0531103, 2010. 1.3, 1.2, 2.5.2

[28] J.J. Wu and W.R. Bennett. Fundamental investigation of si anode in li-ion cells. *NASA Energytech, IEEE*, pages 1–4, 2012. 1.3, 1.2

[29] T.D. Hatchard and J.R. Dahn. In Situ XRD and Electrochemical Study of the Reaction of Lithium with Amorphous Silicon. *J. Electrochem. Soc.*, 151(6):A838–A842, 2004. 1.3, 1.2, 2.5.2

[30] M. Green, E. Fielder, B. Scrosati, M. Wachtler, and J.S. Moreno. Structured silicon anodes for lithium battery applications. *Electrochem. Solid-State Lett.*, 6(5):A75–A79, 2003. 1.3, 1.2

[31] W.R. Liu, Z.Z. Guo, W.S. Young, D.T. Shieh, H.C. Wu, M.H. Yang, and N.L. Wu. Effect of electrode structure on performance of Si anode in Li-ion batteries: Si particle size and conductive additive. *J. Power Sourc.*, 140:139–144, 2005. 1.3, 1.2

[32] S. Nöhren, E. Quiroga-González, J. Carstensen, and H. Föll. Electrochemical Fabrication and Characterization of Silicon Microwire Anodes for Li Ion Batteries. *J.Electrochem.Soc.*, 163(6):A1–A7, 2016. 1.3, 4.3

[33] S. Hansen, E. Quiroga-González, J. Carstensen, and H. Föll. Size-dependent cyclic voltammetry study of silicon microwire anodes for lithium ion batteries. *Electrochimica Acta*, 217:283–291, 2016. 1.3, 3.3, 3.2.1, 3.3, 3.3.1, 3.7, 4.2, 4.3, 4.5, 4.1.2, 4.9, 4.10

[34] G. Lee, S.L. Schweizer, and R.B. Wehrspohn. Microstructural characterization of Li insertion in individual silicon nanowires. *Appl. Phys. A*, 117:973–979, 2014. 1.2

[35] G. Korotcenkov et al. *Porous Silicon - From Formation to Application.* CRC Press - Taylor and Francis Group, Florida, 2016. 2.1, 2.1, 3.1.2.2

[36] V. Lehmann. *Electrochemistry of Silicon.* Wiley-VCH, Weinheim, 2002. 2.1, 2.1, 2.1, 2.2, 2.3.2

[37] V. Lehmann. Porous silicon preparation: alchemy or electrochemistry? *Adv. Mater.*, 4(11):762, 1992. 2.1

[38] V. Lehmann. The physics of macroporous silicon formation. *Thin Solid Films*, 225:1, 1995. 2.1

[39] V. Lehmann and S. Rönnebeck. The physics of macropore formation in low doped p-type silicon. *J. Electrochem. Soc.*, 146(8):2968–2975, 1999. 2.1, 2.2, 3.1.2.2

[40] M. Christophersen, J. Carstensen, K. Voigt, and H. Föll. Organic and aqueous electrolytes used for etching macro- and mesoporous silicon. *Phys. Status Solidi A*, 197(1):34–38, 2003. 2.1, 2.2, 3.1.2.2

[41] E. Ossei-Wusu, J. Carstensen, E. Quiroga-González, M. Amirmaleki, and H. Föll. The role of polyethylene glycol in pore diameter modulation in depth in p-type silicon. *ECS J. Solid State Sci. Technol.*, 2(6):P243–P247, 2013. 2.1, 3.1.1, 3.1.2.2, 3.1.2.2

[42] V. Kochergin and H. Föll. *Porous semiconductors: Optical properties and applications.* Springer, London, 2009. 2.1

[43] H. Föll, M. Leisner, A. Cojocaru, and J. Carstensen. Macroporous semiconductors. *Materials*, 3:3006–3076, 2010. 2.1

[44] M.J. Archer and F.S. Ligler. Fabrication and Characterization of Silicon Micro-Funnels and Tapered Micro-Channels for Stochastic Sensing Applications. *Sensors*, 8:3849–3872, 2008. 2.1

[45] H. Seidel, L. Csepregi, A. Heuberger, and H. Baumgärtel. Anisotropic etching of crystalline silicon in alkaline solutions. I. Orientation dependence and behavior of passivation layers. *J. Electrochem. Soc.*, 137(11):3612, 1990. 2.1, 2.2

[46] O. Powell and H.B. Harrison. Anisotropic etching of 100 and 110 planes in (100) silicon. *J. Micromech. Microeng.*, 11:217–220, 2001. 2.1

[47] C.H. Hamann and W. Vielstich. *Elektrochemie I.* Verlag Chemie, 1975. 2.3.1, 2.3.2, 2.7.1

[48] S.M. Sze. *Physics of semiconductor devices.* Wiley & Sons, New York, 1981. 2.3.1

[49] P. Schmuki, L. Santinacci, T. Djenizian, and D.J. Lockwood. Electrochemistry and pore formation - pore formation on n-inp. *Phys. Status Solidi A*, 182(1):51, 2000. 2.3.2, 2.2, 2.4.2, 2.4.2.1

[50] E. Gileadi. *Physical Electrochemistry - Fundamentals, Techniques and Applications.* Wiley - VCH, Weinheim, 2011. 2.3.2, 2.7.1

[51] J.P. Boddy. Impedance measurements at the semiconductor-electrolyte interface. *Surf. Sci.*, 13:52, 1969. 2.3.2

[52] G. Oskom, J.G. Long, A. Natarajan, and P.C. Searson. Electrochemical deposition of metals onto silicon. *J. Phys. D*, 31:1927–1949, 1998. 2.3.2, 2.2, 2.4.2, 2.5.3

[53] Sebastiao G. dos Santos Filho, A.A. Pasa, and C.M. Hasenack. A mechanism for electroless Cu plating onto Si. *Microelectronic Eng.*, 33:149, 1997. 2.4.1

[54] C.P. daRosa, R. Maboudian, and E. Iglesia. Copper deposition onto silicon by galvanic displacement: effect of silicon dissolution rate. *J. Electrochem. Soc.*, 155(6):E70–E78, 2008. 2.4.1, 2.3

[55] S. Zhong, Z.-G. Yang, J. Cai, H.-J. He, J.-S. Wen, and C. Liu. Electroless Cu deposition on a TiN barrier in $CuSO_4$-HF solution. *J. Electrochem. Soc.*, 152(7):C466–C473, 2005. 2.4.1

[56] G.J. Norga, M. Platero, K.A. Black, A.J. Reddy, J. Michel, and L.C. Kimerling. Mechanism of Copper Deposition on Silicon from Dilute Hydrofluoric Acid Solution. *J.Electrochem.Soc.*, 144:2801–2810, 1997. 2.4.1, 2.3

[57] M. Schlesinger and M. Paunovic. *Modern Electroplating.* John Wiley % Sons, 2010. 2.4.1, 2.4.2, 2.4.2.1

[58] G. Mallory, J.B. Hajdu, and W. Andrew. *Electroless plating: Fundamentals and Applications.* William Andrew Publishing, New York, 1990. 2.4.1

[59] C.P. daRosa, R. Maboudian, and E. Iglesia. Copper Deposition onto Silicon by Galvanic Displacement: Effect of Silicon Dissolution Rate. *J.Electrochem.Soc.*, 155:E70–E78, 2008. 2.4.1, 2.3, 3.2.1

[60] K. Kondo, N. Yamakawa, Z. Tanaka, and K. Hayashi. Copper demascene electrodeposition and additives. *J.Electroanalytical Chem.*, 559:137–142, 2003. 2.4.2

[61] D. Grujicic and B. Pesic. Electrodeposition of copper: the nucleation mechanisms. *Electrochimica Acta*, 47:2901–2912, 2002. 2.4.2, 2.4.2.1

[62] J.P. Zheng, R.Y. Liang, M. Hendrickson, and E.J. Plichta. Theoretical Energy Density of Li-Air Batteries. *J.Electrochem.Soc.*, 155:A432–A437, 2008. 2.5

[63] J. Christensen, P. Albertus, R.-S. Sanchez-Carrera, T. Lohmann, B. Kozinsky, R. Liedtke, J.-Ahmed, and A. Kojica. A critical review of li/air batteries. *J. Electrochem. Soc.*, 2:1–30, 2012. 2.5

[64] N. Imanishi and O. Yamamoto. Rechargeable lithium-air batteries: Characteristics and prospects. *Materials Today*, 17(1):24–30, 2014. 2.5

[65] K. Zaghib and K. Kinoshita. Advanced materials for negative electrodes in Li-polymer batteries. *Journal of Power Sources*, 125(2):214–220, 2004. 2.5

[66] M. Hagen, E. Quiroga-González, S. Doerfler, G. Fahrer, J. Tübke, M.J. Hoffmann, H. Althues, R. Speck, M. Krampfert, S. Kaskel, and H. Föll. Studies on preventing Li dendrite formation in Li-S batteries by using pre-lithiated Si microwire anodes. *J. Power Sourc.*, 248:1058–1066, 2014. 2.5, 5.5, 5.5.2, A.2

[67] M. Hagen, G. Feisthammel, P. Fanz, H.T. Grossmann, S. Dörfler, J. Tübke, M.J. Hoffmann, D. Börner, M. Joos, M. Althues, and S. Kaskel. Sulfur Cathodes with Carbon Current Collector for Li-S cells. *J. Electrochem. Soc.*, 160:A996, 2013. 2.5

[68] K.M. Abraham. Prospects and Limits of Energy Storage in Batteries. *J.Phys.Chem.Lett.*, 6:830–844, 2015. 2.5

[69] A. Manthiram, Sh.H. Chung, and C. Zu. Lithium-Sulfur Batteries: Progress and Prospects. *Adv.Mater.*, 27:1980–2006, 2015. 2.5

[70] B. Scrosati and J. Garche. Lithium batteries: Status, prospects and future. *J. Power Sources*, 195:2419–2430, 2010. 2.5, 2.5.1.1

[71] Y. Tang, Y. Zhang, W. Li, B. Ma, and X. Chen. Rational material design for ultrast rechargeable lithium-ion batteries. *Chem. Soc. Rev*, 44:5926, 2015. 2.5.1, 2.5.3, 2.7

[72] L. Mai, X. Tian, X. Xu, L. Chang, and L. Xu. Nanowire electrodes for electrochemical energy storage devices. *Chemical Reviews*, 114:11828, 2014. 2.5.1

[73] M.K. Song, S. Park, F.M. Alamgir, J. Cho, and M. Liu. Nanostructured electrodes for lithium-ion and lithium-air batteries: the latest developments, challenges and perspectives. *Mater. Sci. Engineering R*, 72(11):203–252, 2011. 2.5.1, 2.5.1.1

[74] C. Liu, Z. G. Neale, and G. Cao. Understanding electrochemical potentials of cathode materials in rechargeable batteries. *Materials Today*, 19(2):109–123, 2016. 2.5.1, 2.5.1.1, 2.5.3

[75] J.B. Goodenough and Y. Kim. Challenges for rechargeable li batteries. *Chem. Mater.*, 22:587–603, 2010. 2.5.1, 2.7, 2.5.3

[76] R. Huggins. *Advanced Batteries.* Springer Science & Business Media, New York, USA, 2010. 2.5.1

[77] G.A. Nazri and G. Pistoia. *Lithium Batteries: Science and Technology.* Springer, 2009. 2.5.1, 2.5.1.1, 2.5.1.2, 2.5.3, 2.5.3, 2.5.3, 2.6.1, 5.2.1, 5.2.3, A.1

[78] B. Xu, D. Qian, Z. Wang, and Y. S. Meng. Recent progress in cathode materials research for advanced lithium ion batteries. *Materials Science and Engineering R: Reports*, 73(5-6):51–65, 2012. 2.5.1.1

[79] J.W. Fergus. Recent developments in cathode materials for lithium ion batteries. *J.Power Sources*, 195:939–954, 2010. 2.5.1.1

[80] Y. Sun, Z. Chen, H. Noh, D. Lee, H. Jung, Y. Ren, D. Lee, S. Wang, Ch. yoon, S. Myung, and Kh. Amine. Nanostructured high-energy cathode materials for advanced lithium batteries. *Nature Mater.*, 11:942–947, 2012. 2.5.1.1

[81] D. Ma, Z. Cao, and A. Hu. Si-based anode materials for li-ion batteries: A mini review. *Nano-Micro Lett.*, 6(4):347–358, 2014. 2.5.1.2, 4.1, 5.2.3.2

[82] C. Daniel and J.O. Besenhard. *Handbook of Battery Materials Vol.1+2.* Wiley-VCH, Weinheim, 2011. 2.5.1.2

[83] T.B. Reddy and D. Linden. *Linden's handbook of batteries.* Mc Graw-Hill, Nex York, 2011. 2.5.1.2, 2.5.2, 2.5.2

[84] L. Liu, J. Lyu, T. Li, and T. Zhao. Well-constructed silicon-based materials as high-performance lithium-ion battery anodes. *Nanoscale*, 8(2):701–722, 2016. 2.5.1.2

[85] M.N. Obrovac and L.J. Krause. Reversible cycling of crystalline silicon powder. *J. Electrochem. Soc.*, 154(2):A103–A108, 2007. 2.5.2, 2.5.2, 5.5

[86] V. L. Chevrier, J. W. Zwanziger, and J. R. Dahn. First principles study of Li-Si crystalline phases: Charge transfer, electronic structure, and lattice vibrations. *Journal of Alloys and Compounds*, 496(1-2):25–36, 2010. 2.5.2

[87] V.L. Chevrier, H.M. Dahn, and J.R. Dahn. Activation energies of crystallization events in electrochemically lithiated silicon. *J. Electrochem. Soc.*, 158(11):A1207–A1213, 2011. 2.5.2, 3.3.1, 4.2, 5.3.2, 5.4

[88] R. Chandrasekaran, A. Magasinski, G. Yushin, and T.F. Fuller. Analysis of lithium insertion/deinsertion in a silicon electrode particle at room temperature. *J. Electrochem. Soc.*, 157(10):A1139–A1151, 2010. 2.5.2, 4.1.2

[89] Y. Kubota, M.C.S. Escano, H. Nakanishi, and H. Kasai. Crystal and electronic structure of $li_{15}si_4$. *J. Appl. Phys.*, 102:0537041–0537046, 2007. 2.5.2

[90] W. Wan, Q. Zhang, Y. Cui, and E. Wang. First principles study of lithium insertion in bulk silicon. *J. Phys. Condens. Matter*, 2010. 2.5.2, 5.4, 5.20

[91] E. Quiroga-González, J. Carstensen, and H. Föll. Good cycling performance of high-density arrays of Si microwires as anodes for Li ion batteries. *Electrochim. Acta*, 101:93–98, 2013. 2.5.2, 4.1.1, 5.1.1, 5.2, 5.2.1

[92] E. Quiroga-González, J. Carstensen, and H. Föll. Optimal conditions for fast charging and long cycling stability of silicon microwire anodes for lithium ion batteries, and comparison with the performance of other si anode concepts. *Energies*, 6(10):5145–5156, 2013. 2.5.2, 5.2.1

[93] D. Aurbach, Y. Talyosef, B. Markovsky, E. Markevich, E. Zinigrad, L. Asraf, J.S. Gnanaraj, and H.J. Kim. Design of electrolyte solutions for Li and Li-ion batteries: A review. *Electrochimica Acta*, 50:247–254, 2004. 2.5.3

[94] K. Xu. Nonaqueous liquid electrolytes for lithium-based rechargeable batteries. *Chem. Rev.*, 104:4303–4417, 2004. 2.5.3, 2.5.3, 2.6.1, 2.6.2, 5.2.3, 5.2.3.1, 5.5.2, A.1

[95] T.R. Jow, K. Xu, O. Borodin, and M. Ue. *Electrolytes for Lithium and Lithium-Ion Batteries*. Springer, New York, 2014. 2.5.3, 2.6.1, 5.2.3, 5.5.2, A.1

[96] S.S. Zhang. A review on electrolyte additives for lithium-ion batteries. *J. Power Sources*, 162:1379–1394, 2006. 2.5.3

[97] P. Verma, P.and Maire and P. Novak. A review of the features and analyses of the solid electrolyte interphase in Li-ion batteries. *Electrochimica Acta*, 55(22):6332–6341, 2010. 2.5.3, 2.6.1

[98] S.S. Zhang, K. Xu, and T.R. Jow. Eis study on the formation of solid electrolyte interphase in li-ion battery. *Electrochimica Acta*, 51:1636–1640, 2006. 2.5.3, 4.2, 5.9, 5.2.3

[99] A. N. Dey and B. P. Sullivan. The Electrochemical Decomposition of Propylene Carbonate on Graphite. *Journal of The Electrochemical Society*, 117(2):222, 1970. 2.5.3, 5.2.3.1

[100] G. V. Zhuang, K. Xu, H. Yang, T. R. Jow, and P. N. Ross. Lithium ethylene dicarbonate identified as the primary product of chemical and electrochemical reduction of EC in 1.2 M $LiPF_6$/EC:EMC electrolyte. *Journal of Physical Chemistry B*, 109(37):17567–17573, 2005. 2.5.3

[101] X. Zhang, B. Sun, H. Guo, N. Tetreault, H. Giessen, and R.H. Friend. Large-area two-dimensional photonic crystals of metallic nanocylinders based on colloidal gold nanoparticles. *Appl. Phys. Lett.*, 90:133114, 2007. 2.5.3

[102] K. Tikhonov and V.R. Koch. *Li-ion Battery Electrolytes Designed for a Wide Temperature Range*. Defense Technical Information Center, 2006. 2.5.3, 2.6.2

[103] S.S. Zhang, K. Xu, and T.R. Jow. Electrochemical impedance study on the low temperature of Li-ion batteries. *Electrochimica Acta*, 49:1057–1061, 2004. 2.5.3

[104] T.R. Jow, S.S. Zhang, K. Xu, and J.L. Allen. Electrolytes for low temperature operations of li-ion batteries. *ECS Transactions*, 3(27):51–58, 2007. 2.5.3, 2.6.2

[105] S.S. Zhang, K. Xu, J.L. Allen, and T.R. Jow. Effect of propylene carbonate on the low temperature performance of Li-ion cells. *Journal of Power Sources*, 110(1):216–221, 2002. 2.5.3

[106] T.R. Jow, J.L. Allen, M. Marx, K. Nechev, B. Deveney, and S. Rickman. Electrolytes, sei and charge discharge kinetics of li-ion batteries. *ECS Trans.*, 25(26):3–12, 2010. 2.5.3

[107] G.G. Botte, R.E. White, and Z. Zhang. Thermal stability of $LiPF_6$-EC:EMC electrolytes for lithium-ion batteries. *J.Power Soc.*, 97-98:570–575, 2001. 2.5.3

[108] J. Yamaki, Y. Shinjo, T. Doi, S. Okada, and Z. Ogumi. The Rate Equation of Decomposition for Electrolytes with $LiPF_6$ in Li-Ion Cells at Elevated Temperatures. *J.Electrochem.Soc.*, 162:A520–A530, 2015. 2.5.3, 2.6.2

[109] E. Quartarone and P. Mustarelli. Electrolytes for solid-state lithium rechargeable batteries: recent advances and perspectives. *Chem.Soc.Rev.*, 40:2525–2540, 2011. 2.5.3, 2.5.3

[110] S. H. Chung, K. Such, W. Wieczorek, and J. R. Stevens. An analysis of ionic conductivity in polymer electrolytes. *Journal of Polymer Science Part B: Polymer Physics*, 32(16):2733–2741, 1994. 2.5.3

[111] K. Hayamizu. Temperature Dependence of Self-Diffusion Coefficients of Ions and Solvents in Ethylene Carbonate, Propylene Carbonate, and Diethylene Carbonate Single Solutions and Ethylene Carbonate+Diethyl Carbonate Binary Solutions of $LiPF_6$ Studied by NMR. *J.Chem.Eng.Data*, 57:2012–2017, 2012. 2.5.3, 2.6.2, 5.2.3.1

[112] D.E. Goldsack and A.A. Franchetto. The viscosity of concentrated electrolyte solutions - iii. a mixture law. *Electrochimica Acta*, 22:1287–1294, 1977. 2.5.3

[113] R.H. Ewell. The Reaction Rate Theory of Viscosity and Some of its Applications. *J.Appl.Phys.*, 9:252, 1938. 2.5.3, 5.2.3, 5.2.3.1, 5.2.3.1

[114] M. Gauthier, T.J. Carney, A. Grimaud, L. Giordano, N. Pour, H.H. Chang, D.P. Fenning, S.F. Lux, O. Paschos, C. Bauer, F. Maglia, S. Lupart, P. Lamp, and Y. Shao-Horn. Electrode-Electrolyte Interface in Li-Ion Batteries: Current Understanding and New Insights. *J.Phys.Chem.Lett.*, 6:4653–4672, 2015. 2.7, 5.2

[115] M. Winter. The Solid Electrolyte Interphase – The Most Important and the Least Understood Solid Electrolyte in Rechargeable Li Batteries. *Zeitschrift für Physikalische Chemie*, 223(10-11):1395–1406, 2009. 2.6.1

[116] S.J. An, J. Li, C. Daniel, D. Mohanty, S. Nagpure, and D.L. Wood III. The state of understanding of the lithium-ion-battery graphite solid electrolyte interphase (SEI) and its relationship to formation cycling. *Carbon*, 105:52–76, 2016. 2.6.1, 5.2.3, 5.2.3.1

[117] T.M. Bandhauer, S. Garimella, and T.F. Fuller. A Critical Review of Thermal Issues in Lithium-IOn Batteries. *J.Electrochem.Soc.*, 158:R1–R25, 2011. 2.6.2

[118] V.J. Heinze. Elektrochemie mit Ultramikroelektroden. *Angew. Chem.*, 105:1327, 1993. 2.7.1, 2.7.2, 4.3, 5.2.1

[119] M. Lovric and J. Osteryoung. Theory of differential normal pulse voltammetry. *Electrochimica Acta*, 27:963–968, 1982. 2.7.1, 2.7.2

[120] R.G. Compton and C.E. Banks. *Understanding Voltammetry.* Imperial College Press, London, 2011. 2.7.1, 2.7.2, 4.3, 5.2.1

[121] D.R. Ferrier and R.R. Schroeder. Staircase voltammetry with varied current sampling times. *Electroanal. Chem. Interfac. Electrochem.*, 45(3):343–359, 1973. 2.7.2

[122] M.E. Orazem and B. Tribollet. *Electrochemical impedance spectroscopy*. Wiley-VCH, 2008. 2.7.3, 2.7.3

[123] V.F. Lvovich. *Impedance Spectroscopy: Applications to Electrochemical and Dielectric Phenomena*. Wiley, 2012. 2.7.3, 2.7.3, 4.2

[124] J. Carstensen, E. Foca, S. Keipert, H. Föll, M. Leisner, and A. Cojocaru. New modes of fft impedance spectroscopy applied to semiconductor pore etching and materials characterization. *Phys. Status Solidi A*, 205(11):2485–2503, 2008. 2.7.3

[125] S. Hansen, E. Quiroga-González, J. Carstensen, R. Adelung, and H. Föll. Size-dependent physicochemical and mechanical interactions in battery paste anodes of Si-microwires revealed by Fast-Fourier-Transform Impedance Spectroscopy. *J.Power Sources*, 349:1–10, 2017. 2.7.3, 3.1.1, 3.3, 3.3, 4.1.1, 4.2, 4.6, 4.2, 5.1.1

[126] E. Barsoukov and J.R. Macdonald. *Impedance Spectroscopy: Theory, Experiment, Applications*. John Wiley & Sons,Inc., New Jersey, 2005. 2.7.3

[127] P. Cloetens, R. Barrett, J. Baruchel, J.P. Guigay, and M. Schlenker. Phase objects in synchrotron radiation hard x-ray imaging. *J.Phys.D: Appl.Phys.*, 29:133–146, 1996. 2.8.1

[128] J.C. Andrews, F. Meirer, Y. Liu, Z. Mester, and P. Pianetta. Transmission X-ray microscopy for full-field nano-imaging of biomaterials. *Microsc.Res.Tech.*, 14:671–681, 2011. 2.8.1

[129] J. Nelson, S. Misra, Y. Yang, A. Jackson, Y. Liu, H. Wang, H. Dai, J.C. Andrews, Y. Cui, and M.F. Toney. In Operando X-ray Diffraction and Transmission X-ray Microscopy of Lithium Sulfur Batteries. *J.Am.Chem.Soc.*, 134:A6337–6343, 2012. 2.8.1

[130] J.C. Andrews, S. Brennan, C. Patty, K. Luening, and P. Pianetta. A high resolution, hard x-ray bio-imaging facility at SSRL. *Synchrotron Radiat. News*, 21:17–26, 2008. 2.8.1

[131] J.C. Andrews and B.M. Weckhuysen. Hard X-ray Spectroscopic Nano-Imaging of Hierarchical Functional Materials at Work. *Chem.Phys.Chem.*, 14:3655–3666, 2013. 2.8.1

[132] C. Holzner, M. Feser, S. Vogt, B. Hornberger, S. B. Baines, and C. Jacobsen. Zernike phase contrast in scanning microscopy with X-rays. *Nature Physics*, 6(11):883–887, 2010. 2.8.1

[133] S.-C. Chao, Y.-C. Yen, Y.-F. Song, H.-S. Sheu, H.-C. Wu, and N.-L. Wu. In Situ Transmission X-ray Microscopy Study on Working SnO Anode Particle of Li-Ion Batteries. *Journal of The Electrochemical Society*, 158(12):A1335–A1339, 2011. 2.8.1

[134] M. Birkholz. *Thin Film Analysis by X-Ray Scattering.* Wiley-Vch Verlag GmbH, Weinheim, Deutschland, 2006. 2.8.2

[135] Thermo ARL. Basics of X-Ray Diffraction - Introduction to powder polycrystalline diffraction. *www.thermoarl.com*, page 21, 1996. 2.8.2

[136] E.J. Mittemeijer and P. Scardi. *Diffraction Analysis of the Microstructure of Materials.* Springer Verlag, Heidelberg, 2004. 2.8.2

[137] International Union of Crystallography N.V.A. Oosthoek. Methods and Problems of Crystal Structure Analysis. *IUCr Journals - http://www.iucr.org/publ/50yearsofxraydiffraction/full-text/structure-analysis*, 1962. 2.8.2

[138] S.A. Speakman. Introduction to X-Ray Powder Diffraction Data Analysis. *MIT - http://prism.mit.edu/xray/*, page 25. 2.8.2

[139] F. Siebert and P. Hildebrandt. *Vibrational Spectroscoy in Life Science.* Wiley-VCH Verlag, Weinheim, Deutschland, 2008. 2.8.3

[140] F. Adar. Analytical Vibrational Spectroscopy - NIR, IR, and Raman. *Spectroscopy*, 26:7, 2011. 2.8.3

[141] P. Larkin. *Infrared and Raman Spectroscopy: principles and spectral interpretation.* Elsevier, USA, 2011. 2.8.3

[142] D. Boas, C. Pitris, and N. Ramanujam. *Handbook of Biomedical Optics.* CRC Press, Florida, USA, 2011. 2.8.3

[143] J.R. Ferraro, K. Nakamoto, and C.W. Brown. *Introduction Raman Spectroscopy.* Elsevier, United Kingdom, 2003. 2.8.3

[144] B. Stuart. *Infrared Spectroscopy: Fundamentals and Applications.* John Wiley & Sons, Chichester, United Kingdom, 2004. 2.8.3

[145] PerkinElmer precisely. FT-IR Spectroscopy - Attenuated Total Reflectance (ATR). *www.perkinelmer.com*, page 5, 2005. 2.8.3

[146] M. Tasumi. *Introduction to Experimental Infrared Spectroscopy.* John Wiley & Sons, United Kingdom, 2015. 2.8.3

[147] PikeTechnologies. ATR - Theory and Applications. *www.piketech.com*, page 53, 2011. 2.8.3

[148] E. Quiroga-González, E. Ossei-Wusu, J. Carstensen, and H. Föll. How to make optimized arrays of Si nanowires suitable as superior anode for Li-ion batteries. *J. Electrochem. Soc.*, 158(11):E119–E123, 2011. 3.1.1, 5.3

[149] E. Quiroga-González, J. Carstensen, and H. Föll. Structural and electrochemical investigation during the first charging cycles of silicon microwire array anodes for high capacity lithium ion batteries. *Materials*, 6:626–636, 2013. 3.3, 3.2.1, 4.2, 5.1, 5.2, 5.2.1

[150] E. Ossei-Wusu, J. Carstensen, and H. Föll. Analysis of p-Si macropore etching using FFT- impedance spectroscopy. *Nanoscale Res. Lett.*, 7:320, 2012. 3.1.2.2

[151] J. Carstensen, M. Christophersen, G. Hasse, and H. Föll. Parameter dependence of pore formation in silicon within a model of local current bursts. *Phys. Status Solidi A*, 182(1):63–69, 2000. 3.1.2.2, 3.1.3

[152] R. Taft and H. E. Messmore. The Electrodeposition of Copper in Presence of Gelatin. *The Journal of Physical Chemistry*, 35(9):2585–2618, 1931. 3.2.4

[153] L. Chen, X. Xie, J. Xie, K. Wang, and J. Yang. Binder effect on cycling performance of silicon/carbon composite anodes for lithium ion batteries. *J. Appl. Electrochem.*, 36:1099–1104, 2006. 3.3.1, 4.2, A.3

[154] A. Magasinski, B. Zdyrko, I. Kovalenko, B. Hertzberg, R. Burtovy, C.F. Huebner, T.F. Fuller, I. Luzinov, and G. Yushin. Towards efficient binders for li-ion batteries si-based anodes: Polyacrylic acid. *ACS Appl. Mater. Interfaces*, 2(11):3004, 2010. 3.3.1, 4.2, A.3

[155] S.D. Beattie, D. Larcher, M. Morcrette, B. Simon, and J.M. Tarascon. Si electrodes for li-ion batteries - a new way to look at an old problem. *J. Electrochem. Soc.*, 155(2):A158–A163, 2008. 3.3.1, 4.2

[156] N.S. Hochgatterer, M.R. Schweiger, S. Koller, P.R. Raimann, T. Wöhrle, C. Wurm, and M. Winter. Silicon/graphite composite electrodes for high-capacity anodes: Influence of binder chemistry on cycling stability. *Electrochem. Solid Stat. Lett.*, 11(5):A76–A80, 2008. 3.3.1, 4.2

[157] M. Cerbelaud, B. Lestriez, D. Guyomard, A. Videcoq, and R. Ferrando. Brownian Dynamics Simulations of Colloidal Suspensions Containing Polymers as precursors of Composite Electrodes for Lithium Batteries. *Langmuir*, 28:10713–10724, 2012. 3.3.1, 4.2, 4.7

[158] H. Haftbaradaran, H. Gao, and W.A. Curtin. A surface locking instability for atomic intercalation into a solid electrode. *Appl. Phys. Lett.*, 96:091909, 2010. 4.1.2, 5.17, 5.4, 5.20

[159] R. Ruffo, S.S. Hong, C.K. Chan, R.A. Huggins, and Y. Cui. Impedance analysis of silicon nanowire Lithium ion battery anodes. *J. Phys. Chem. C*, 113:11390–11398, 2009. 4.2

[160] M. Gaberscek, J. Moskon, B. Erjavec, and R. Dominko. The Importance of Interphase Contacts in Li Ion Electrodes: The Meaning of the High-Frequency Impedance Arc. *Electrochem. Solid State Lett.*, 11:A170–A174, 2008. 4.2, 5.2.4

[161] B. Lestriez, S. Bahri, I. Sandu, L. Roue, and D. Guyomard. On the binding mechanism of cmc in si negative electrodes for li-ion batteries. *Electrochem. Comm.*, 9:2801–2806, 2007. 4.2

[162] M. Itagaki, S. Yotsuda, N. Kobari, K. Watanabe an S. Kinoshita, and M. Ue. Electrochemical impedance of electrolyte/electrode interfaces of lithium-ion rechargeable batteries: Effect of additives to the electrolyte on negative electrodes. *Electrochimica Acta*, 51:1629–1635, 2006. 4.2, 5.2.3, 5.2.4

[163] M.N. Obrovac and L. Christensen. Structural changes in silicon anodes during lithium insertion/extraction. *Electrochem. Solid State Lett.*, 7(5):A93–A96, 2004. 4.7, 5.2.3.2, 5.5, A.3

[164] J. Li, R.B. Lewis, and J.R. Dahn. Sodium carboxymethyl cellulose a potential binder for si negative electrodes for li-ion batteries. *Electrochemical and Solid-State Letters*, 10(2):A17, 2007. 4.7

[165] E. Laborda, A. Molina, Q. Li, C. Batchelor-McAuley, and R.G. Compton. Square wave voltammetry at disc microelectrodes for characterization of two electron redox processes. *Phys. Chem. Chem. Phys.*, 14:8319–8327, 2012. 4.3

[166] B.D. Topal, S.A. Ozkan, and B. Uslu. The analytical applications of square wave voltammetry on pharmaceutical analysis. *The Open Chem. and Bio Med. Meth.*, 3:56–73, 2010. 4.3

[167] H. Wu, G. Chan, J.W. Choi, I. Ryu, Y. Yao, M.T. McDowell, S.W. Lee, A. Jackson, Y. Yang, L. Hu, and Y. Cui. Stable cycling of double-walled silicon nanotube battery anodes through solid-electrolyte interphase control. *Nature Nanotechnol.*, 7:310–315, 2012. 5.2.1

[168] A. Ostadhossein, E.D. Cubuk, G.A. Tritsaris, E. Kaxiras, S. Zhang, and A.C.T. vanDuin. Stress effects on the initial lithiation of crystalline silicon nanowires: reactive molecular dynamics simulations using ReaxFF. *Phys.Chem.Chem.Phys.*, 17:3832, 2015. 5.2.1, 5.3, 5.4, 5.5.3

[169] H. Zhao, S.J. Park, F. Shi, Y. Fu, V. Battaglia, P.N. Ross Jr, and G. Liu. Propylene Carbonate (PC)-Based Electrolytes with High Coulombic Efficiency for Lithium-Ion Batteries. *J.Electrochem.Soc.*, 161:A194–A200, 2014. 5.2.1, 5.2.3.1

[170] G.V. Zhuang, H. Yang, B. Blizanac, and P.N. Ross Jr. A Study of Electrochemical Reduction of Ethylene and Propylene Carbonate Electrolyte on Graphite Using ATR-FTIR Spectroscopy. *Electrochem. and Solid-State Lett.*, 8:A441–A445, 2005. 5.2.1, 5.2.3.1

[171] M. Nie, D.P. Abraham, D.M. Seo, Y. Chen, A. Bose, and B.L. Lucht. Role of Solution Structure in Solid Electrolyte Interphase Formation on Graphite with $LiPF_6$ in Propylene Carbonate. *J.Phys.Chem.C*, 117:25381–25389, 2013. 5.2.1, 5.2.3, 5.2.3.1, 5.2.3.1

[172] S.E. Sloop, J.B. Kerr, and K. Kinoshita. The role of Li-ion battery electrolyte reactivity in performance decline and self-discharge. *J.Power Sourc.*, 119–121:330–337, 2003. 5.2.1, 5.2.3.1

[173] C. Xu, F. Lindgren, B. Philippe, M. Gorgoi, F. Björefors, K. Edström, and T. Gustafsson. Improved Performance of the Silicon Anode for Li-Ion Batteries: Understanding the Surface Modification Mechanism of Fluoroethylene Carbonate as an Effective Electrolyte Additive. *Chem. Mater.*, 25:2591–2599, 2015. 5.2.1

[174] K. Kondo, M. Sano, A. Hiwara, T. Omi, M. Fujita, A. Kuwae, M. Iida, K. Mogi, and H. Yokoyama. Conductivity and Solvation of Li^+ Ion of $LiPF_6$ in Propylene Carbonate Solutions. *J.Phys.Chem. B*, 104:5040–5044, 2000. 5.2.1, 5.2.3.1, 5.2.3.1

[175] C.L. Campion, W. Lie, and B.L. Lucht. Thermal Decomposition of $LiPF_6$-Based Electrolytes for Lithium-Ion Batteries. *J.Electrochem.Soc.*, 152:A2327–A2334, 2005. 5.2.2, 5.2.3, 5.2.3.1, 5.5.3

[176] B. Ravdel, K. M Abraham, R. Gitzendanner, J. DiCarlo, B. Lucht, and C. Campion. Thermal stability of lithium-ion battery electrolytes. *Journal of Power Sources*, 119121:805–810, 2003. 5.2.2, 5.2.3

[177] L. Filipovic. *Topography Simulation of Novel Processing Techniques.* Dissertation, Technischen Universitt Wien, 2012. 5.2.2, 5.2.3, 5.2.3.1, 5.5.3

[178] R. Miao, J. Yang, Z. Xu, J. Wang, Y. Nuli, and L. Sun. A new ether-based electrolyte for dendrite-free lithium-metal based rechargeable batteries. *Sci. Rep.*, 21771:6, 2016. 5.2.2, 5.2.3

[179] C. Barchasz, J. Lepretre, S. Patoux, and F. Alloin. Revisiting tegdme/diox binary electrolytes for lithium/sulfur batteries: Importance of solvation ability and additives. *J. Electrochem. Soc.*, 160:A430–A436, 2013. 5.2.2

[180] M. Dahdi, F. Ghamouss, F. Tran-Van, D. Lemordant, and M. Anouti. Comparative study of EC/DMC LiTFSI and $\mathrm{LiPF_6}$ electrolytes for electrochemical storage. *J.Power Sourc*, 196:9743–9750, 2011. 5.2.2, 5.2.3

[181] N. Angulakshmi and A.M. Stephan. Efficient electrolytes for lithium-sulfur batteries. *Frontiers in Energy Research*, 3:1–8, 2015. 5.2.2, 5.5, A.2

[182] K.W. Schroder, H. Celio, L.J. Webb, and K.J. Stevenson. Examining Solid Electrolyte Interphase Formation on Crystalline Silicon Electrodes: Influence of Electrochemical Preparation and Ambient Exposure Conditions. *J. Phys. Chem. C*, 116:19737–19747, 2012. 5.2.3, 5.2.3.1

[183] X. B. Cheng, R. Zhang, C. Z. Zhao, F. Wei, J. G. Zhang, and Q. Zhang. A review of solid electrolyte interphases on lithium metal anode. *Advanced Science*, 3(3):1–20, 2015. 5.2.3.1

[184] D. M. Seo, D. Chalasani, B. S. Parimalam, R. Kadam, M. Nie, and B. L. Lucht. Reduction Reactions of Carbonate Solvents for Lithium Ion Batteries. *ECS Electrochemistry Letters*, 3(9):A91–A93, 2014. 5.2.3.1

[185] S. Koltzenburg and O. Nuyken. *Polymere - Synthese, Eigenschaften und Anwendungen.* Springer Spektrum, 2014. 5.2.3.1, 5.5.2

[186] O. Nuyken and S.D. Pask. Ring-Opening Polymerization - An Introductory Review. *Polymers*, 5:361–403, 2013. 5.2.3.1, 5.5.2

[187] H.P. Latscha, U. Kazmaier, and H.A.. Klein. *Organische Chemie.* Springer-Verlag, Berlin Heidelberg, 2016. 5.2.3.1

[188] R. E. Jones, D. K. Ward, F. S. Gittleson, and M. E. Foster. Assessing Electrolyte Transport Properties with Molecular Dynamics. *Journal of The Electrochemical Society*, 164(6):A1258–A1267, 2017. 5.2.3.1

[189] J.J. Fontanella, M.C. Wintersgill, and J.J. Immel. Dynamics in propylene carbonate and propylene carbonate containing in $LiPF_6$. *J.Chem.Pys.*, 110:5392–5402, 1999. 5.2.3.1

[190] J.M. Martnez de la Hoz and P.B. Balbuena. Reduction mechanisms of additives on Si anodes of Li-ion batteries. *Phys.Chem.Chem.Phys.*, 16:17091, 2014. 5.2.3.1

[191] E. Radvanyi, K.V. Havenbergh, W. Porcher, S. Jouanneau, J.S. Bridel, S. Put, and S. Franger. Study and modeling of the Solid Electrolyte Interphase behavior on nano-silicon anodes by Electrochemical Impedance Spectroscopy. *Electrochimica Acta*, 137:751–757, 2014. 5.2.4

[192] G. Neubüser, S. Hansen, R. Adelung V. Duppel, and L. Kienle. (Re-) crystallization mechanism of highly-oriented Si-microwire arrays by TEM analysis. *J.Solid State Electrochem., accepted*, 2017. 5.3, 5.15, 5.6

[193] S. Hansen, S. Shree, G. Neubüser J. Carstensen, and R. Adelung. Diffusion limited control at the Solid Electrolyte Interface – Realization of high charging rates for Si Microwire Array Electrodes. submitted, 2017, Chemistry of Materials. 5.3

[194] G. Eranna. *Crystal Growth and Evaluation of Silicon for VLSI and ULSI.* Taylor & Francis, 2014. 5.3.2, 5.17

[195] K. Nakajima and N. Usami. *Crystal Growth of Silicon for Solar Cells.* Advances in Materials Research. Springer Berlin Heidelberg, 2010. 5.3.2

[196] J. Safarian, G. Tranell, and M. Tangstad. Processes for Upgrading Metallurgical Grade Silicon to Solar Grade Silicon. *Energy Procedia*, 20:88 – 97, 2012. Technoport 2012 - Sharing Possibilities and 2nd Renewable Energy Research Conference (RERC2012). 5.3.2

[197] H. Wang, X. Ji, C. Chen, K. Xu, and L. Miao. Lithium diffusion in silicon and induced structure disorder: A molecular dynamics study. *AIP Advances*, 3(11), 2013. 5.17, 5.3.2

[198] Q. Zhang, Y. Cui, and E. Wang. First-principle approaches to simulate lithiation in sililcon electrodes. *Modelling Simul. Mater. Sci. Eng.*, 21:04001, 2013. 5.17

[199] M. Pharr, K. Zhao, X. Wang, Z. Suo, and J.J. Vlassak. Kinetics of initial lithiation of crystalline silicon electrodes of lithium-ion batteries. *Nano Lett.*, 12(9):5039–5047, 2012. 5.17, 5.3.2, 5.4, 5.20, 5.4, 5.5.3

[200] G. Gottstein. *Physikalische Grundlagen der Materialkunde.* Springer-Lehrbuch. Springer Berlin Heidelberg, 2013. 5.17

[201] M.H. Braga, A. Debski, and W. Gasior. Li-Si phase diagram: Enthalpy of mixing, thermodynamic stability, and coherent assessment. *Journal of Alloys and Compounds*, 616:581–593, 2014. 5.3.2

[202] M. McDowell, S.W. Lee, W.D. Nix, and Y. Cui. 25th Anniversary Article: Understanding the Lithiation of Silicon and Other Alloying Anodes for Lihtium-Ion Batteries. *Adv. Mater.*, 25:4966, 2013. 5.3.2

[203] S. Nöhren, E. Quiroga-González, J. Carstensen, and H. Föll. Dependence of the lithiation/delithiation potentials of silicon microwire anodes on their state of charge and sizes. *ECS Transactions*, 64(23):1–10, 2015. 5.3.3, 5.3.3

[204] S. Nöhren, E. Quiroga-González, J. Carstensen, and H. Föll. Fabrication and Characterization of Silicon Microwire Anodes by Electrochemical Etching Techniques. *ECS Transactions*, 66(6):27–38, 2015. 5.3.3

[205] Y. Ko, C. Hwang, and H. K. Song. Investigation on silicon alloying kinetics during lithiation by galvanostatic impedance spectroscopy. *Journal of Power Sources*, 315:145–151, 2016. 5.4, 5.20

[206] Z. Xie, Z. Ma, Y. Wang, Y. Zhou, and C. Lu. A kinetic model for diffusion and chemical reaction of silicon anode lithiation in lithium io batteries. *RSC Adv.*, 6:22383, 2016. 5.4, 5.5.3

[207] S. W. Lee, H.-W. Lee, I. Ryu, W. D. Nix, H. Gao, and Y. Cui. Kinetics and fracture resistance of lithiated silicon nanostructure pairs controlled by their mechanical interaction. *Nature Communications*, 6:7533, 2015. 5.4

[208] V. Ramadesigan, P.W.C. Northrop, S. De, S. Santhanagopalan, R.D. Braatz, and V.R. Subramanian. Modeling and Simulation of Lithium-Ion Batteries from a Systems Engineering Perspective. *J.Electrochem. Soc.*, 159:R31–R45, 2012. 5.4, 5.21

[209] Y. S. Meng and M. E. Arroyo-de Dompablo. First principles computational materials design for energy storage materials in lithium ion batteries. *Energy & Environmental Science*, 2(6):589, 2009. 5.4, 5.21

[210] R. Younesi, G.M. Veith, P. Johannson ad K. Edström, and T. Vegge. Lithium salts for advanced lithium batteries: Li-metal, Li-O_2 and Li-S. *Energy Environ.Sci.*, 68:1908, 2015. 5.5

[211] A. Rosenman, R. Elazari, G. Salitra, E. Markevich, D. Aurbach, and A. Garsuch. The Effect of Interactions and Reduction Products of $LiNO_3$, the Anti-Shuttle Agent, in Li-S Battery Systems. *J.Electrochem. Soc.*, 162:A470–A473, 2015. 5.5

[212] J. Scheers, S. Fantini, and P. Johansson. A review of electrolytes for lithium-sulphur batteries. *J.Power Sourc.*, 255:204–218, 2014. 5.5, 5.5.2, 5.5.2

[213] H. Jha, I. Buchberger, X. Cui, S. Meini, and H.A. Gasteiger. Li-S Batteries with Li_2S Cathodes and Si-C Anodes. *J.Electrochem.Soc.*, 162:A1829–A1835, 2015. 5.5

[214] M. Vijayakumar, N. Govid, E. Walter, S.D. Burton, A. Shukla, A. Devaraj, J. Xiao, J. Liu, C. Wang, A. Karim, and S. Thevuthasan. Molecular structure and stability of dissolved lithium polysulfide species. *Green Energy & Environment*, 16:10923–10932, 2014. 5.5

[215] A. Webber. Conductivity and Viscosity of Solutions of $LiCF_3SO_3$,$Li(CF_3SO_2)_2N$, and Their Mixtures. *J.Electrochem.Soc*, 138:2586–2590, 1991. 5.5, 5.5.2

[216] S. S. Zhang. Role of $LiNO_3$ in rechargeable lithium/sulfur battery. *Electrochimica Acta*, 70:344–348, 2012. 5.5, 5.5.2, A.2

[217] T. Jauchmann, J. Balach, M. Klose, S. Ostwald, J. Eckert, and L. Giebeler. Role of 1,3-Dioxolane and $LiNO_3$ Addition on the Long Term Stability of Nanostructured silicon/carbon Anodes for Rechargeable Lithium Batteries. *J.Electrochem.Soc.*, 163:A557–A564, 2016. 5.5, 5.5.2

[218] S. Nöhren, E. Quiroga-González, J. Carstensen, and H. Föll. STROM: AlkaSuSi-Alkalimetall Schwefel und Silizium : Abschlussbericht BMBF für den Zeitraum 1.5.2011 - 31.5.2014. Technical report, TIB Hannover, 2014. DOI: 10.2314/GBV:833627732. 5.5

[219] M.R. Zamfir, H.T. Nguyen, E. Moyen, Y.H. Lee, and D. Pribat. Silicon nanowires for Li-based battery anodes: a Review. *J. Mater. Chem. A*, 1:9566, 2013. 5.5, 5.5.2

[220] V. Etacheri, U. Geiger, Y. Gofer, G.A. Roberts, I.C. Stefan, R. Fasching, and D. Aurbach. Exceptional Electrochemical Performance of Si-Nanowires in 1,3-Dioxolane Solutions: A Surface Chemical Investigation. *Langmuir*, 28:6175–6184, 2012. 5.5.2

[221] P. H. Plesch and P. H. Westermann. The polymerization of 1,3-dioxolane. I. Structure of the polymer and thermodynamics of its formation. *Journal of Polymer Science Part C: Polymer Symposia*, 16(7):3837–3843, 1967. 5.5.2

[222] L.C. Reibel, C.P. Durand, and E. Franta. Cationic polymerization of 1,3-dioxolane and 1,3-dioxepane. Application to graft and block copolymer synthesis. *Can. J. Chem.*, 63:265–269, 1985. 5.5.2

[223] D. Aurbach, E. Pollack, R. Elazari, G. Salitra, C.S. Kelley, and J. Affinito. On the surface chemical aspects of very high energy density, rechargeable li-sulfur batteries. *J. Electrochem. Soc.*, 156:A694–A702, 2009. 5.5.2

[224] U. Kasavajjula, C. Wang, and A.J. Appleby. Nano- and bulk-silicon-based insertion anodes for lithium-ion secondary cells. *J. Power Sources*, 163(2):1003–1039, 2007. 5.5.3

[225] N. Bernstein, M.J. Aziz, and E. Kaxiras. Amorphous-crystal interface in silicon: A tight-binding simulation. *Phys.Rev.B*, 58:4579, 1998. 5.5.3

[226] F. Shi, Z. Song, P.N. Ross, G.A. Somorjai, R.O. Ritchie, and K. Komvopoulos. Failure mechanisms of single-crystal silicon electrodes in lithium-ion batteries. *Nature communications*, 7:8, 2016. 5.5.3

[227] Z. Jia and T. Li. Instrinsic stress mitigation via elastic softening during two-step electrochemical lithiation of amorphous silicon. *J.Mech.Phys.Solids*, 91:278–290, 2016. 5.5.3

[228] S. Zhang. Chemomechanical modeling of lithiation-induced failure in high-volume-change electrode materials for lithium ion batteries. *npj Computational Materials*, 7:11, 2017. 5.6

[229] R. Xu and K. Zhao. Electrochemomechanics of Electrodes in Li-Ion Batteries: A Review. *J.Electrochem.En.Conv.Stor.*, 13:030803–1–030803–9, 2016. 5.6

[230] S. Hansen, A. Schütt, J. Carstensen, and R. Adelung. Local transmittance measurements as large area diagnostic tool for the optimization of porous Si foils as Li-ion battery anodes. *J.Electrochem.Soc*, 163(14):A3036–A3045, 2016. 6

[231] N.S. Choi, K.H. Yew, W.U. Choi, and S.S. Kim. Enhanced electrochemical properties of a si-based anode using an electrochemically active polyamide imide binder. *J. Power Sources*, 177:590–594, 2008. A.3